Institute of Experimental Pharmacology and Toxicology

Center for Experimental Medicine

University Medical Center Hamburg-Eppendorf

Modeling of *LMNA*-cardiomyopathy in human iPSC-derived engineered heart tissue for testing novel therapies

Dissertation

Submitted to the Department of Biology

Faculty of Mathematics, Informatics, and Natural Sciences

University of Hamburg

for the degree of

Doctor of Natural Sciences

(Dr. rer. nat.)

by

Charlotta Sophie Behrens

Hamburg, 2022

1st Referee: Prof. Dr. Thomas Eschenhagen

2nd Referee: Prof. Dr. Thomas Dobner

Date of disputation: 03.03.2023

Disputation committee:

Prof. Dr. Julia Kehr

Prof. Dr. Baris Tursun

Prof. Dr. Thomas Eschenhagen

This thesis was carried out from January 2018 until December 2022 (including maternity and parental leave from August 2021 until September 2022, with one month intermission) at the Institute of Experimental Pharmacology and Toxicology under the supervision of Prof. Dr. Thomas Eschenhagen.

Table of content

1 Introduction

1.1 Heart failure and inherited dilated cardiomyopathies

The heart is a fist-sized pump that has to contract constantly to supply the whole body with oxygen and nutrients, summing up to over 2 billion of heartbeats throughout an average human lifespan. Therefore, the heart is under constant mechanical load. The inability of the heart to meet the demand of the body for sufficient nutrients and oxygenated blood is defined as heart failure (HF; Hershberger, Morales and Siegfried, 2010). Underlying causes of HF include cardiomyopathies that affect the cardiac muscle as a result of, *e.g.* mechanical, contractile or electrophysiological defects (Maron *et al.*, 2006). Cardiomyopathies are mostly acquired due to a particular lifestyle or an infection but can be also caused by mutations in certain genes. The two most common classes are dilated (DCM) and hypertrophic cardiomyopathies (HCM), characterised by a dilated ventricle or a hypertrophic ventricle, respectively (Figure 1). Increasing amounts of myocardial fibroses with excess deposition of extracellular matrix (ECM) proteins such as collagen is one common hallmark of pathological remodelling (Eijgenraam, Silljé and de Boer, 2020). The amount of fibrosis correlates with the severity of the disease (Eijgenraam, Silljé and de Boer, 2020). DCM is characterised by left ventricular enlargement and left ventricular systolic dysfunction accompanied by a reduced ejection fraction, which is not caused by coronary artery disease or hypertension (Schultheiss *et al.*, 2019). The higher end diastolic volume (preload) and elevated stretching of the cardiac wall increases the stress subjected to the wall resulting in a vicious cycle of heart failure (Schultheiss *et al.*, 2019). Another type is the arrhythmogenic right ventricular cardiomyopathy (ACM; Figure 1), which impairs usually the right ventricle first and leads to ventricular tachycardia, fibrillation and sudden cardiac death (Hershberger, Hedges and Morales, 2013).

DCM is one of the most frequent cardiac diseases, with an estimated prevalence of ~1:250 (Hershberger, Hedges and Morales, 2013; Schultheiss *et al.*, 2019). Inherited disease-causing mutations are found in 15-40% of DCM patients (Hershberger, Hedges and Morales, 2013; Schultheiss *et al.*, 2019). Yet, for inherited DCM there is often a lack of a clear phenotype/genotype correlation: Patients can carry the same variations in the gene but show a different course and onset of DCM (Hershberger *et al.*, 2021). Both, a polygenetic interplay, or differences in the lifestyle, such as nutrition and exercise are possible explanations (Hershberger *et al.*, 2021). In contrast, pathogenic mutations in the gene *LMNA* generally cause monogenic DCM (Hershberger *et al.*, 2021; Jordan *et al.*, 2021) and account for 8% of inherited DCM (Hershberger, Hedges and Morales, 2013).

Up to now, there are no curative treatments for cardiomyopathies. Current treatment strategies aim at slowing down disease progression and reducing symptoms. In detail, this management consists of administration of angiotensin converting enzyme inhibitors, angiotensin receptor inhibitors, β-blockers, neprilysin inhibitors, sodium glucose transport 2 inhibitors and diuretics. This combination therapy improved the life expectancy of HF patients with reduced ejection fraction by around 44% over the last 20 years (McDonagh *et al.*, 2021). Still, this approach does not address the underlying cause of the disease, particularly not in inherited forms of DCM or HCM. Another strategy is the employment of devices, such as implantable defibrillators/cardioverters or biventricular pacemakers in order to stop ventricular fibrillation and to restore cardiac synchronisation, respectively. Nevertheless, disease progression can be too advanced for these strategies to apply. Hence, heart transplantation or implantation of long-term mechanical circulatory support are the remaining options (Schultheiss *et al.*, 2019).

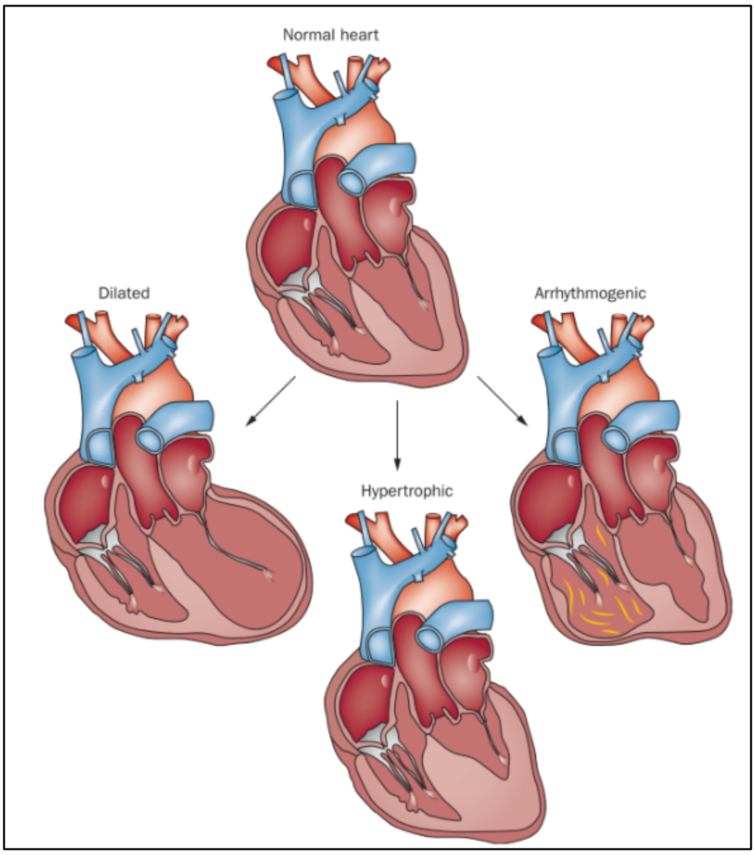

Figure 1 Illustration of the morphological changes from a normal heart (up, middle) to either a heart suffering from dilated (DCM, lower left), hypertrophic (HCM, lower middle) or arrhythmogenic right ventricular cardiomyopathy (lower right, ACM). DCM is characterised by an enlarged left ventricle, HCM by a hypertrophy of the cardiac wall, while ARVC first affects the right ventricle. Image retrieved from: (Hershberger, Hedges and Morales, 2013).

1.2 Lamins and laminopathies

1.2.1 Types and structure of nuclear lamins

Mutations in the gene *LMNA* are one of the most definite causes for inherited DCM (see 1.1) with a clear phenotype/genotype relationship. The gene *LMNA* encodes for the two isoforms lamin A and C via alternative splicing, both called A-type lamins (Lin and Worman, 1993). In addition, there are B-type lamins, encoded by the genes *LMNB1* or *LMNB2* (Höger *et al.*, 1990). In general, lamins are V type intermediate filaments, consisting of an N-terminal head and a carboxyl-terminal (C-terminal) tail domain intermitted by a rod domain of α-helical proteins (see Figure 2). The C-terminal tail domain consists of three functional components, the chromatin binding domain (CBD), the nuclear localisation signal (NLS) and the immunoglobulin (Ig)-like domain. The protein assembles in an anti-parallel fashion to a meshwork, called lamina, which is located at the nuclear periphery (Stuurman, Heins and Aebi, 1998; Dechat *et al.*, 2008).

The A-type lamins, lamin A and C share the first 9 exons, consisting of 566 amino acids (AAs), and can be distinguished by specific C-terminal regions from exon 10 onwards (Figure 2). A part of exon 10 is lamin C-specific. Lamin C consists in total of 572 AAs with 6 unique AAs at the C-terminus. Lamin A contains exclusively the other part of exon 10, exon 11 and 12 and is translated into a premature form, prelamin A. Prelamin A encompasses 664 AAs and is post translationally modified (PTM) to mature lamin A with 646 AAs. In detail, prelamin A includes a C-terminal *CaaX* box (C for cysteine, a for aliphatic amino acid and X for a hydrophobic residue) that undergoes four different PTM steps inside the nucleus (Schreiber and Kennedy, 2013). First, the farnesyltransferase (FNT) farnesylates the C-terminal cysteine of the *CaaX* motif. Second, the *aaX* motif is cleaved by the RAS-converting enzyme 1 (RCE1). Third, the remaining farnesylcyteine, is carboxylmethylated by isoprenylcysteine carboxyl methyltransferase (ICMT). In a final step, 15 AAs are cleaved from the C-terminus by the zinc metalloprotease ZMPSTE24 (Figure 2). The exact role of the PTMs is still under discussion (Schreiber and Kennedy, 2013; Al-Saaidi and Bross, 2015).

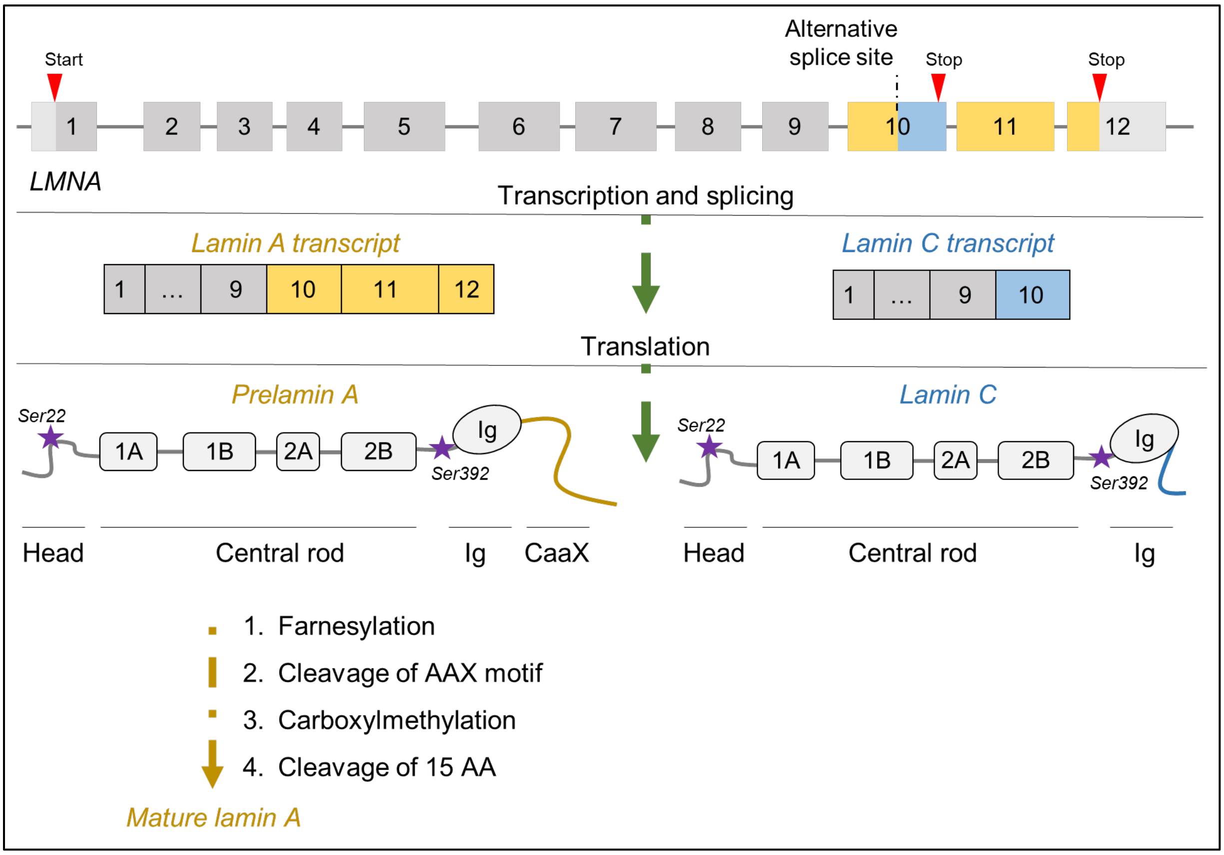

Figure 2 Schematic overview of the expression of the two different isoforms, lamin A and C from the gene *LMNA*. Alternative splicing of lamin A-specific (yellow) and lamin C-specific (blue) sequences results in two different transcripts. Translation results in prelamin A and mature lamin C sharing the head, central rod and immunoglobulin (Ig) like domains. The central rod domain consists of the four sub-domains: 1A, 1B, 2A and 2B. Two serine phosphorylation sites (Ser22 and Ser392) important for mitosis are indicated as purple asterisk. Prelamin A (664 amino acids; AAs) includes a C-terminal CaaX domain which undergoes four PTM steps to become mature lamin A (646 AAs). The figure is based on Al-Saaidi and Bross, 2015.

1.2.2 Molecular functions of A-type lamins

Lamins localise adjacent to the inner nuclear membrane (INM; Figure 3) were they form the lamina and play a pivotal role in numerous cellular properties and processes.

During cell cycle division, chromosomes are duplicated by replication. In the mitotic phase, the chromosomes are then divided into two new nuclei. For the nuclear division, the disassembly of the lamina is required, which is achieved by phosphorylation of A-type lamins (Heald and McKeon, 1990; Peter *et al.*, 1991). In detail, during the mitotic phase, cell cycle dependent kinase 2 (Cdc2) phosphorylates two serine residues (Ser22 and Ser392; Figure 2) in A-types lamins (Heald and McKeon, 1990; Peter *et al.*, 1991).

Gene expression regulation is highly complex, and one aspect of it is the spatial organisation of chromatin in territories, where A-type lamins also have a central role. They form the so-called lamina-associated domains (LADs), which are formed upon the recruitment of chromatin to the nuclear periphery (Gruenbaum and Foisner, 2015). These LADs are gene poor and consist of regions, which are transcriptionally inactive (Gruenbaum and Foisner, 2015). The human genome consists of over 1,300 LADs, and the organisation is conserved throughout mammalians (Peric-Hupkes *et al.*, 2010). Loss of lamin A and C correlates with higher expression of genes normally located in LADs (Gesson *et al.*, 2016). A direct interaction partner of A-type lamins that supports the genome organisation is the protein emerin (Figure 3) encoded by the gene *EMD* (Bione *et al.*, 1994). Emerin in turn binds the chromatin-binding molecule barrier to autointegration factor (BAF; Figure 3; Bione *et al.*, 1994). Interestingly, A-type lamins do not only organise chromatin at the nuclear periphery. Lamin A and C solubilise upon serine 22 phosphorylation (Ser22; Figure 2) and localise to the nucleoplasm, where they bind tumour suppressor p53 or lamina-associated polypeptide 2α (LAP2α). LAP2α binds in association with A-type lamins the transcriptionally active euchromatin, but without affecting overall gene expression (Gesson *et al.*, 2016).

Another important cellular function of A-type lamins is to maintain genomic stability. A-type lamins take part in the non-homologous end-joining (NHEJ) and the homologous recombination (HR). Both processes repair the genomic DNA (gDNA) upon damage through double strand breaks (DSBs). Levels of key proteins involved in NHEJ and HR are not preserved upon loss of A-type lamins, which results in a genomic instability (Redwood *et al.*, 2011).

Cellular stress induced by hypoxia or DNA damage can result in the tumour suppressor p53 dependent apoptosis. A-type lamins facilitate the process of p53-dependent apoptosis. During apoptosis, lamin A and C are cleaved at aspartic acid residue (position 230), which results in two fragments of 47 kDa and 37 kDa size, respectively (Rao, Perez and White, 1996). Failure in cleavage of A-type lamins due to a substitution of aspartic acid result in a nuclear envelope collapse with delayed apoptotic chromatin condensation and nuclear shrinkage (Rao, Perez and White, 1996).

In addition, lamin A and C are part of the so-called linker of nucleoskeleton and cytoskeleton (LINC) complex, which reaches from the INM to the outer nuclear membrane (ONM). In this complex, lamin A and C connect to SUN (Sad1p, UNC-84) domain-containing proteins on the INM, which in turn couple to integral nuclear membrane proteins, such as nesprins spanning the nuclear membrane (Figure 3). The LINC complex fulfils several functions, such as nuclear positioning, anchoring the nucleus to the cytoskeleton, mechanical force transduction and interaction with NPCs (Figure 3; Soheilypour *et al.*, 2016; Brayson and Shanahan, 2017; Kirby and Lammerding, 2018).

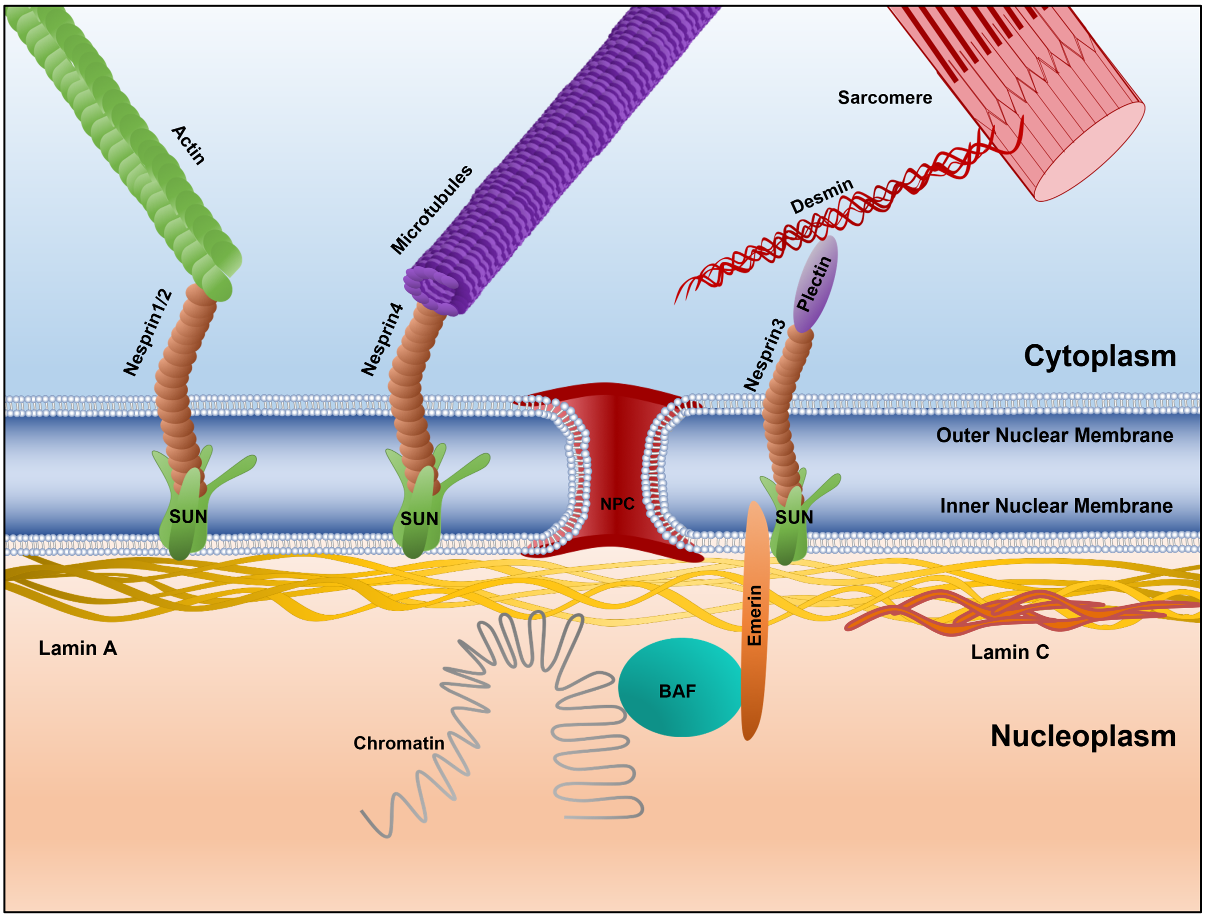

Figure 3 Lamin A (yellow) and C (red) form a meshwork, the lamina, adjacent to the inner nuclear membrane (INM). The lamina is anchored to cytoplasmic structures as actin through direct- (SUN domain-containing proteins) and indirect interaction partners (nesprin 1 to 4, actin, microtubules and desmin). In the nucleoplasm, A-type lamins bind chromatin, emerin and indirectly the chromatin-binding molecule BAF. Image drawn based on (Gruenbaum and Medalia, 2015)

Mechanical cues that are sensed on the ECM and cell adhesion complexes are transduced along the cytoskeleton and microtubules (Gruenbaum and Foisner, 2015; Heffler *et al.*, 2020). The mechanical signals reach the nucleus and A-type lamins via the LINC complex. Subsequently, A-type lamins induce transcriptomic changes to combat the mechanical cues (Heffler *et al.*, 2020). Interestingly, not only mechanical genes are upregulated in response to mechanical strain, but also A-type and (less) B-type lamins in order to gain stiffer properties (González-Cruz, Dahl and Darling, 2018). Of note, A-type but not B-type lamins contribute to the shape and stiffness properties of the nucleus (Lammerding *et al.*, 2006). Furthermore, A-type lamins protect nuclei from mechano-induced rupture and DNA damage by retaining proteins, which are required for DNA repair, in the nucleus (Cho *et al.*, 2019)

The roles in mechanotransduction and gene expression regulation of A-type lamins are important in definition and maintenance of cell fates and identity (Perovanovic *et al.*, 2016; Shah *et al.*, 2021). Fine tuning of lamin A and C protein levels can be found in different cell types, depending on their fate (Swift and Discher, 2014). Further, A-type lamins are directly involved in differentiation, exemplified by the fact that complete loss or mutations resulted in impaired differentiation (Guénantin *et al.*, 2021; Wang *et al.*, 2022). A-type lamins are abundant in almost all cell-types, but at low levels in embryonic stem cells, which increases upon differentiation and cell fate commitment (Swift *et al.*, 2013; Swift and Discher, 2014).

An important mechanotransducer is the Yes-activated protein 1 (YAP1). It transduces the mechanical signals from the outer surface of the cell (ECM) into the nucleus, *e.g.* to activate gene expression to respond to the strain. The mechanical strain is sensed via the cytoskeleton, intercalated disc and microtubular network. YAP1 then enters the nucleus in the dephosphorylated form, together with its transcriptional co-activator WW-domain-containing transcription regulator 1 (TAZ; Owens *et al.*, 2020). In the nucleus, the YAP1/TAZ complex drives transcription of gene programmes for cell proliferation or F-actin polymerisation regulation in association with the transcriptional enhancer factor domain (TEAD) family members TEAD 1 to 4 (Panciera et al., 2017). Defective mechanosensing of YAP1 can be linked to mutations in A-type lamins. *LMNA*-mutated skeletal muscle stem cells showed an unresponsiveness to the environment due to constantly elevated nuclear localisation of YAP1 (Owens *et al.*, 2020).

1.2.3 Laminopathies

1.2.3.1 Pathophysiology of laminopathies

As a consequence of the diverse role of *LMNA*, mutations in the gene affect diverse tissues. Diseases caused by *LMNA* mutations are collectively termed laminopathies. A first link of mutations in the gene *LMNA* and Emery-Dreifuss muscular dystrophy (EDMD), a skeletal muscle disorder, has been described in 1999 (Bonne *et al.*, 1999, 2000). In recent years, more than 498 different mutations have been reported, of which almost all have been inherited in an autosomal dominant fashion (Lu *et al.*, 2011; Crasto, My and Di Pasquale, 2020). Furthermore, involvement of a diverse range of tissues, for instance the adipose tissue and the cardiac muscle has been discovered (Lu *et al.*, 2011; Crasto, My and Di Pasquale, 2020). They are classified into those affecting mainly skeletal muscle (example EDMD), the heart (as DCM with conduction defects), the adipose tissue (lipodystrophy syndromes), the neurons (peripheral neuropathy) and connective tissues (as accelerated aging disorders; Figure 4; Lu *et al.*, 2011). Of note, every laminopathy results in a severe form of DCM, most frequently associated with primary arrhythmia (Bécane *et al.*, 2000; Crasto, My and Di Pasquale, 2020; Hershberger *et al.*, 2021). In a cohort study, patients diagnosed with *LMNA*-associated DCM and aged over 30 years developed dysrhythmia in 92% of cases (Van Berlo *et al.*, 2005). Cardiac arrhythmia can include atrioventricular (AV) block, atrial fibrillation, or ventricular arrhythmias (Fatkin *et al.*, 1999; Arbustini *et al.*, 2002). When patients reach the age of 50 years, 64% acquire HF (Van Berlo *et al.*, 2005; Hershberger *et al.*, 2021).

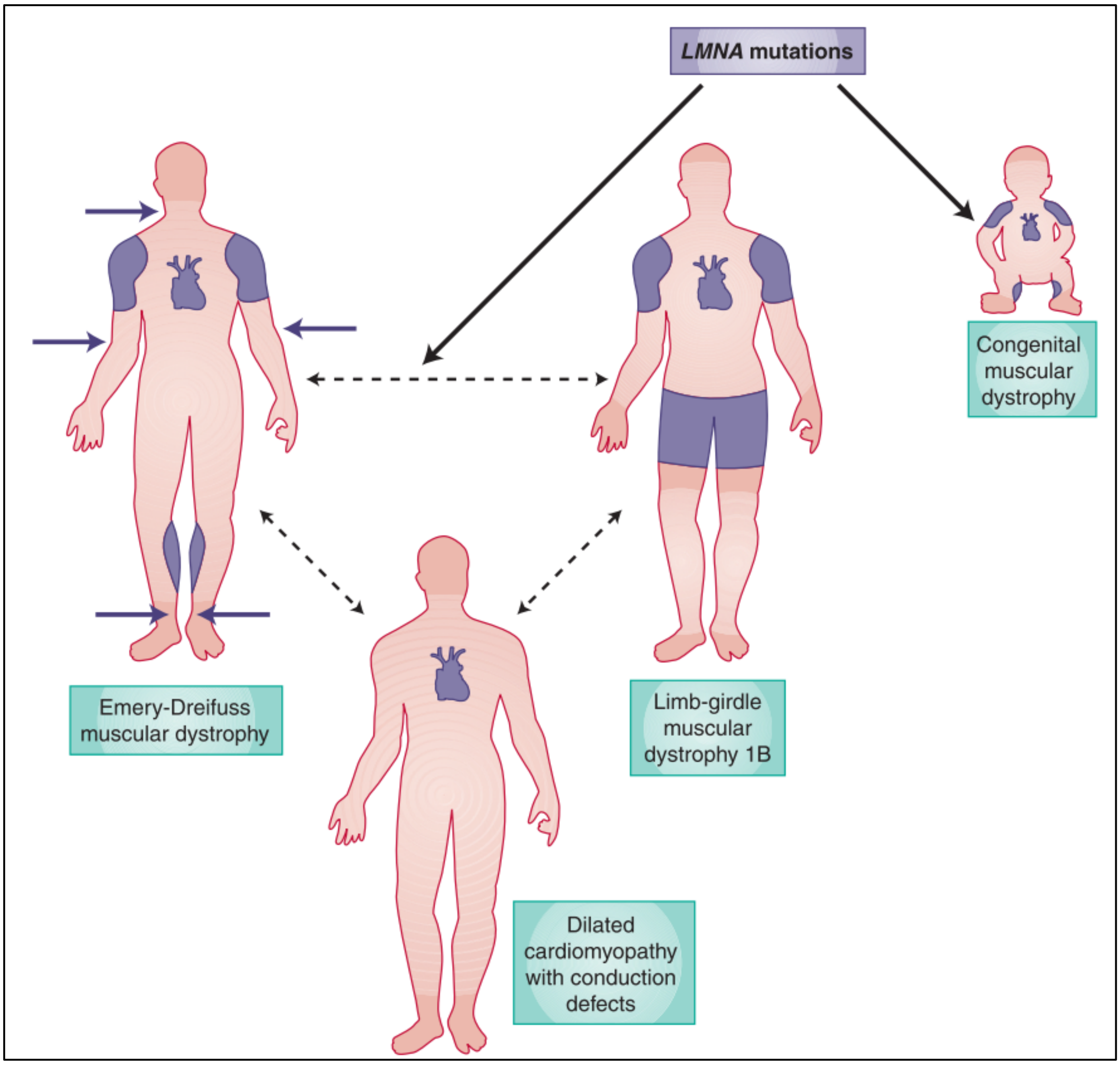

Figure 4 Examples of laminopathy classification based on the affected tissue, indicating the involvement of DCM in all types of tissue disorders. Image retrieved from (Lu *et al.*, 2011).

Treatment of laminopathies pose an enormous challenge in clinics. Conventional therapeutic strategies such as β-blockers do not even prevent cardiac disease progression (Brull *et al.*, 2018; McDonagh *et al.*, 2021). Given the lack of a curative treatment of *LMNA*-associated DCM, 55% of patients aged over 60 years received a heart transplantation or suffered from cardiovascular death (Taylor *et al.*, 2003; Lu *et al.*, 2011). Recent preclinical studies suggested novel strategies, such as the inhibition of kinase pathways (Choi and Worman, 2013; Brull *et al.*, 2018; Lee *et al.*, 2019). However, these are global approaches that entail unpredictable consequences. A clinical trial of Pfizer, REALM-DCM (NCT03439514), that used a mitogen activated protein kinase 38 (MAPK38) inhibitor was recently discontinued (*Pfizer to Discontinue Development Program for PF-07265803 for LMNA-Related Dilated*

Cardiomyopathy, 2022). Therefore, there is an increasing interest in a therapeutic strategy acting on the underlying pathogenic mechanism, instead of effected downstream pathways.

1.2.3.2 Reported patient mutations

165 of the 498 different mutations in *LMNA* are associated with DCM (Crasto, My and Di Pasquale, 2020). Two mutations are discussed at more detail: (i) pH222.P and (ii) p.Y259X.

(i) The missense mutation p.H222P (c.665 A >C) is one of the first described *LMNA* mutations to cause familial EDMD (Bonne *et al.*, 1999, 2000). The two male mutation carriers of the family showed arrhythmia, the youngest being only 23 years old (Bonne *et al.*, 2000). In contrast, the female mutation carrier showed typical symptoms of EDMD on skeletal muscle, but no arrhythmia at the age of 25 years yet (Bonne *et al.*, 2000). Despite the clear association in the EDMD family study, p.H222P is not classified as pathogenic in the database ClinVar (Landrum *et al.*, 2018), providing some ambiguity as to its severity.

(ii) p.Y259X is a nonsense mutation that leads to a premature stop codon with a predicted truncated protein (Van Engelen *et al.*, 2005). The p.Y259X is classified as likely pathogenic in the ClinVar database (Landrum *et al.*, 2018). All members of a five generations family carrying this mutation in the heterozygous state exhibited cardiac conduction defects (Van Engelen *et al.*, 2005). In one case, the mutation was present in the homozygous state, which resulted in new-born death due to respiratory insufficiency (Van Engelen *et al.*, 2005).

Taken together, *LMNA* mutations cause a wide spectrum of human diseases summarised as laminopathies. The commonly observed *LMNA*-associated DCM is characterized by a severe clinical course, high prevalence of ventricular arrhythmias and sudden cardiac death. *LMNA* mutations in DCM are the only established indication for the prophylactic implantation of intracardiac defibrillator/cardioverters (ICD; McDonagh *et al.*, 2021). The number of different mutations, the variability in the affection of tissues and the severity of the disease phenotype pose a challenge for the design of a therapeutic strategy for all laminopathy patients.

1.2.4 *In vivo* and *in vitro* laminopathy models

In the last two decades, many laminopathy models have been established to study the underlying pathomechanism, so far mainly in mice.

1.2.4.1 LMNA knockout mouse models (LMNA$^{-/-}$ and LMNA$^{GT-/-}$)

To generate a full-length knockout two different strategies were employed: LMNA$^{-/-}$ (or LMNA$^{\Delta 8-11)}$ mice depict a large genomic deletion. The LMNA$^{GT-/-}$ mouse model carries a promoter trap construct that leads to a complete lack of A-type lamins (Kubben *et al.*, 2011).

Heterozygous *LMNA* knockout mice (LMNA$^{+/-}$) exhibited only 50% of lamin A and C compared to wild-type (WT) mice (Wolf *et al.*, 2007). LMNA$^{+/-}$ developed ventricular dilation only after 50 weeks of age and had a normal lifespan (Wolf *et al.*, 2007). Homozygous LMNA$^{-/-}$ showed severe growth retardation already two weeks after birth and encompassed hallmarks of DCM, such as lower left ventricular (LV) wall thickness/chamber radius ratio and LV dysfunction (Nikolova *et al.*, 2004). All mice died after 8 weeks of age (Nikolova *et al.*, 2004). Of note, data obtained in the LMNA$^{-/-}$ mouse model (hereafter termed LMNA$^{\Delta 8-11}$) have to be interpreted carefully, because this strain expresses a truncated form, lamin A Δ8–11, on transcript and protein level (Sullivan *et al.*, 1999; Jahn *et al.*, 2012).

The LMNA$^{GT-/-}$ mouse model carries a promoter trap construct and probably better reflects a true, full-length *LMNA* knockout (Kubben *et al.*, 2011). The complete lack of A-type lamins resulted in defective adipose-, cardiac- and skeletal muscle post-natal development (Kubben *et al.*, 2011). Homozygous LMNA$^{GT-/-}$ mice died between 16 and 18 days post-partum (Kubben *et al.*, 2011). In contrast to the LMNA$^{\Delta 8-11}$ model, no signs of DCM were noted (Kubben *et al.*, 2011), possibly because the early death preceded the development of a cardiac phenotype.

1.2.4.2 LMNA p.H222P mouse model (LMNA$^{H222P/222P}$)

In addition to the complete knockout or nonsense mutated lamins, missense mutations in mice have been investigated too. One example for a well-studied missense model is the LMNA$^{H222P/222P}$ mouse carrying the mutation p.H222P (Arimura *et al.*, 2005). While mice with a heterozygous p.H222P mutation exhibited a normal lifespan without any cardiac phenotype, the life expectancy of mice with a homozygous mutation was reduced. Male homozygous mice died between 4 to 9 months and female between 7 to 13 months (Arimura *et al.*, 2005). Furthermore, male and female mice developed hallmarks of DCM, as LV dilation and decreased LV fractional shortening (LVFS), with a later onset for females (Arimura *et al.*, 2005). Additionally, AV conduction defects were reported in males at 3 months of age (Arimura *et al.*, 2005). All mice showed enlarged hearts with dilation of atrial

and ventricular chambers, as well as an increased fibrosis and arrays of degeneration and necrosis (Arimura *et al.*, 2005).
On the molecular level, several signalling pathways were altered in the hearts of mice with homozygous p.H222P mutation (summarised in Figure 5). Autophagy activity was reduced and its re-activation had a positive effect on disease progression (Choi *et al.*, 2012). The WNT/β-catenin signalling was reduced and its activation had beneficial effects, suggesting a potential therapeutic target (Le Dour *et al.*, 2017). Conversely, the activity of three MAPK signalling cascades was increased in LMNA$^{H222P/222P}$ mice hearts compared to WT, extracellular signal-regulated kinases 1/2 (ERK1/2), c-Jun N-terminal kinase (JNK) and MAPK p38α (Muchir *et al.*, 2007, 2012; Wu *et al.*, 2010). Pharmacological inhibition of ERK1/2 or JNK resulted in prolonged lifespan, reduced fibrosis and restored LV fractional shortening (Muchir *et al.*, 2009; Wu *et al.*, 2010, 2011).

Several molecular consequences of elevated ERK1/2 phosphorylation were unravelled. For example, increased ERK1/2 activity in LMNA$^{H222P/222P}$ affected the actin cytoskeleton, which has been linked to higher phosphorylation of cofilin-1, an F-actin depolymerisation factor (Chatzifrangkeskou *et al.*, 2018). In addition, increased ERK signalling caused elevated expression levels of sarcolipin, which inhibited the sarcoplasmic reticulum (SR) calcium ATPase (SERCA) and thus resulted in prolonged calcium uptake and decay time (Morales Rodriguez *et al.*, 2020). These data formed the basis of the above-mentioned clinical trial with ARRY-371797 (PF-07265803), a potent, selective, oral, small-molecule inhibitor of the MAPK p38α pathway (Judge *et al.*, 2022). The apparent lack of efficacy in the Phase III trial (see above) exemplifies the difficulties to directly translate findings from mouse models into clinical practise.

Interestingly, the desmin network, pivotal for linking sarcomeres, Z-discs and the intercalated discs, nuclei and mitochondria, is also involved in the p.H222P laminopathy mouse model (Galata *et al.*, 2018). In hearts of these mice, desmin aggregates were detected and were absent of their usual localisation at the Z-disc and intercalated disc (Galata *et al.*, 2018). Further, the disrupted desmin network resulted in mislocalised intercalated disc proteins, desmoplakin, plakoglobin and connexin 43 (Galata *et al.*, 2018). Given the detection of abnormal aggregates, overexpression of the most abundant cardiac chaperone αB-chain crystallin (αBCry), rescued the cardiac phenotype in LMNA$^{H222P/222P}$ mice, not only in terms of the intercalated disc but also on ERK1/2 signalling (Galata *et al.*, 2018). Disorganisation of connexin 43 in LMNA$^{H222P/222P}$ hearts was not only due to a disruption of the desmin network, but also caused by an alteration in the microtubular network. Increasing the acetylated form α-tubulin by paclitaxel restored localisation and functioning of connexin 43 (Cx43) and rescued cardiac conduction defects in LMNA$^{H222P/222P}$ mice (Macquart *et al.*, 2018).

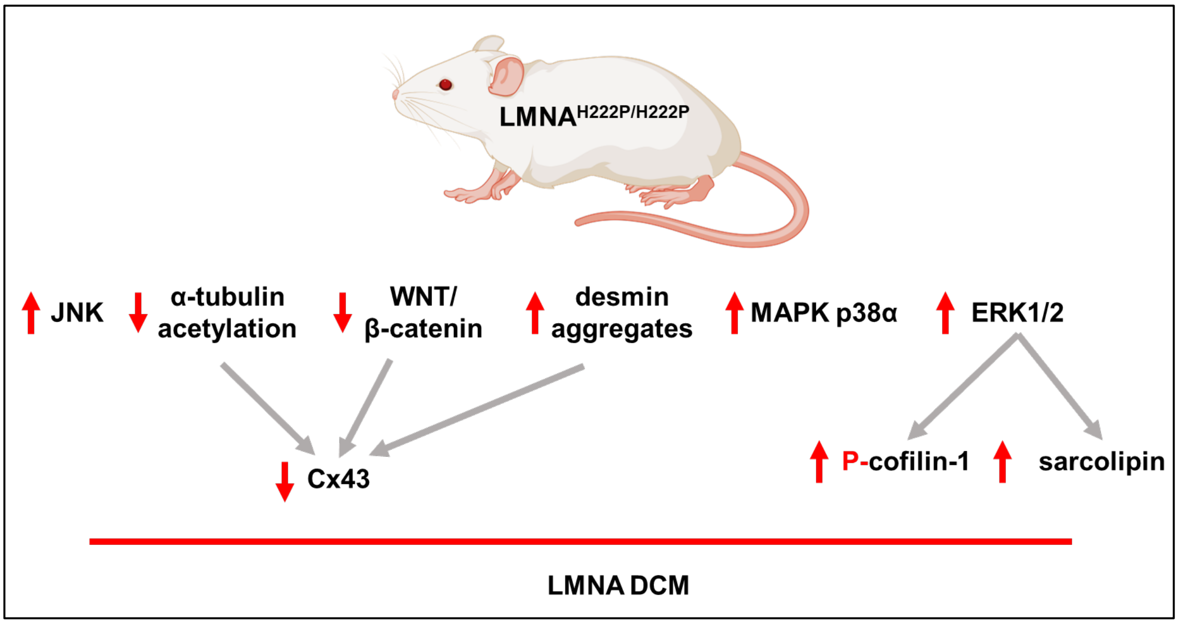

Figure 5 Signalling pathways altered in LMNA$^{H222P/H222P}$ mice hearts in comparison to WT mice that may contribute to *LMNA*-associated DCM (*LMNA*-DCM). The three mitogen activated protein kinase (MAPK) pathways are upregulated, extracellular signal-regulated kinases 1/2 (ERK1/2), c-Jun N-terminal kinase (JNK) and MAPK p38α. Elevated ERK1/2 results in increased phosphorylation of cofilin-1 (p-cofilin-1) and higher levels of sarcolipin. Lower acetylation of α-tubulin, decreased Wnt/β-catenin and increased desmin aggregates caused mislocalisation of connexin 43 (Cx43). Image based on (Gerbino *et al.*, 2018) and one element retrieved from BioRender.com.

1.2.4.3 Human induced pluripotent stem cell (hiPSC)-derived laminopathy models

The advent of the human induced pluripotent stem cell (hiPSC) technology (Takahashi *et al.*, 2007) opened the possibility to model laminopathy patient-specific hiPSC (explanation see sections 1.3.1 and 1.3.2). Two studies focussed on the altered genome upon the *LMNA* mutations, p.K219T and p.R225X (Bertero *et al.*, 2019; Salvarani *et al.*, 2019). hiPSC Cardiomyocytes (hiPSC-CMs) with a heterozygous p.K219T mutation exhibited action potential (AP) abnormalities as a result of lower sodium peak current (Salvarani *et al.*, 2019). The reduced sodium current resulted in lower conduction velocity, which facilitates arrhythmic events via re-entry circuits. One key finding was that mutated A-type lamins showed elevated binding affinity to the promotor of the *SCN5A* gene and thus recruited the functional region to the LADs (Salvarani *et al.*, 2019). Mutated lamin A and C repressed the transcription of *SCN5A* in cooperation with a Polycomb Repressive Complex 2 (PRC2) at the nuclear periphery (Salvarani *et al.*, 2019). This pathogenic mode of action was corrected in hiPSC-CMs upon CRISPR/Cas9-mediated *LMNA* mutation correction (Salvarani *et al.*, 2019). In contrast, myocytes with a heterozygous p.R225X mutation showed normal sodium currents, but abnormal AP prolongation, caused by a stronger and prolonged calcium influx (Bertero *et al.*, 2019). In the p.R225X model, the genome architecture was assessed on different levels, indicating a massive change in chromosomal topology, but only mild effects on chromatin compartmentalisation in mutated hiPSC-CMs. Still, altered architecture resulted *e.g.* in activation of neuronal genes, such as *CACNA1A*, which participated in AP alteration (Bertero *et al.*, 2019). A third study, investigating a p.K117fs laminopathy model, linked aberrant calcium homeostasis and cellular arrhythmia to altered platelet-derived growth factor (PDGF) signalling pathway. The observed pathogenic phenotype was rescued upon pharmacological inhibition (Lee *et al.*, 2019).

To sum up, current findings in mice and hiPSC-CM studies recapitulated important features of laminopathies in patients and identified several alterations of signalling pathways and electrophysiological consequences critical in the pathogenesis of *LMNA*-DCM. However, a wide variety of different mechanisms is notable. This may partially reflect model- and mutation-specific aspects, but most likely relates to the broad range of biological function of A-type lamins as described in this chapter. It appears unlikely that therapeutic targeting of any single pathway can be sufficiently effective in a mixed cohort of patients.

1.3 Cardiac disease modelling making use of hiPSCs

1.3.1 Discovery and challenges of hiPSCs

Recapitulating cardiac disease mechanisms in a model is challenging. Discrepancies between animal models and patient or patient-derived models have been reported, not only for laminopathies but for many other cardiac diseases (Eschenhagen and Carrier, 2019). Animal models, such as mice, are valuable with regards to studying the whole organism. However, the large differences in cardiac physiology between mice and human makes interpretations challenging (Milani-Nejad and Janssen, 2014; Bruyneel *et al.*, 2018). For example, the resting heart rate of mice is several-fold higher than that of humans (300-800 versus 50-180 beats per minute). Further, APs are very short in mice with a dominant early repolarisation, in contrast to a long plateau with small contribution of early repolarisation in humans (Kaese and Verheule, 2012). In combination with the smaller size of the mouse heart, mice are relatively resistant to cardiac arrhythmia, while the larger human heart is prone to arrhythmia (Kaese and Verheule, 2012). It may therefore not come as a surprise that mice develop hallmarks of laminopathy-associated DCM only in a homozygous, but not in a heterozygous state (Arimura *et al.*, 2005; Chandar *et al.*, 2010; Cattin *et al.*, 2013), while heterozygous *LMNA* mutations cause DCM in humans.

A first step towards human disease modelling was the isolation of embryonic stem cells (ESCs) from human blastocysts (Thomson *et al.*, 1998). ESCs serve as an unlimited source of cells and have the potential to differentiate into any cell-type of interest. However, the requirement for human blastocyst raised several ethical concerns (King and Perrin, 2014). Therefore, the discovery in 2006 to reprogram adult fibroblasts of mice to iPSC served as a steppingstone to revolutionise the field (Takahashi and Yamanaka, 2006). Upon retroviral infection of the four transcription factors Oct3/4, Sox2, c-Myc and Klf4 and culture in ES media, iPSC gained similar morphology, self-renewal properties and ability to commit to all embryonic germ layers as ESCs (Takahashi and Yamanaka, 2006). The application of this reprogramming method from human fibroblast into hiPSCs was reported only one year later (Takahashi *et al.*, 2007). This method enables to issue consent of the donor from the biological material for different concerns, thus circumventing ethical issues, and studying disease in a human model at the same time (King and Perrin, 2014).

The hiPSC based technologies have been considerably improved in recent years. A key problem was the delivery of the reprogramming factors since the lentivirus has integrating properties (Schlaeger *et al.*, 2014). Even delivery via the non-integrating Sendai virus resulted in unexpected integration events in up to 13% of analysed cell lines (Shibamiya *et al.*, 2020). A potential solution can be the use of small-molecule mediated reprogramming (Kim, Jeong and Choi, 2020). Another optimisation which was investigated was the source of biological material for reprogramming. Fibroblasts are gained by skin biopsies, which is an invasive procedure. Furthermore, dermal fibroblasts are prone to genetic damage due to their exposure to sunlight during lifetime. Both problems could be overcome by the development of protocols for the generation of hiPSC from urine or peripheral blood mononuclear cells (PBMCs; Zhou *et al.*, 2011; Kim *et al.*, 2016; Okumura *et al.*, 2019).

Another challenge in the hiPSC field is the maintenance of an optimal cell quality and reproducibility. Given the natural propensity of pluripotent cells for self-renewal, clonal variation and genetic shifts can be observed during culture time (Paull *et al.*, 2015; Musunuru *et al.*, 2018). For example, karyotype abnormalities occur frequently (Taapken *et al.*, 2011). Therefore, hiPSCs should not be propagated for unnecessarily high number of passages, especially due to the potential incidence of one clone overgrowing cultured cells (Brenière-Letuffe *et al.*, 2018). A major challenge of hiPSC based disease models are batch-to-batch variations. Clone-to-clone variations have been observed, which can be reduced upon usage of a pool of clones, instead of selecting one clone for disease studies (Paull *et al.*, 2015). Further, the combination of cell banking and quality controls for starting material can increase reproducibility (Shibamiya *et al.*, 2020).

1.3.2 *In vitro* cardiac differentiation

Early after the establishment of the first human ESCs, cardiac differentiation protocols were developed that mimic key events in cardiac embryonic development *in vitro* (Kehat *et al.*, 2001; Mummery *et al.*, 2002). These protocols were very inefficient but paved the way for improved protocols that generate over 90% cardiomyocytes from hiPSCs (Kattman *et al.*, 2011; Burridge *et al.*, 2014; Breckwoldt *et al.*, 2017; Lee *et al.*, 2017; Mosqueira *et al.*, 2018). They share the same principle: an initial mesodermal induction phase via activation of wingless-related integration site (Wnt) signalling and a second phase inducing cardiac differentiation by inhibition of Wnt. Wnt signalling is activated either by growth factors (Activin A and bone morphogenetic protein 4; BMP4) or small molecule inhibitors (CHIR99021) of the glycogen synthase kinase 3 (Gsk3). Differentiation can either be accomplished in monolayer (2D) or embryoid bodies (EB; 3D), as pluripotent cells have already the property of self-assembly resulting in aggregates (Mummery *et al.*, 2012). These aggregates, also known as EB, already tend to differentiate and spontaneous contraction can be observed (Mummery *et al.*, 2012). Several three-dimensional differentiation protocols have been established, which allows up-scaling (Burridge *et al.*, 2007; Breckwoldt *et al.*, 2017). Alternatively, two-dimensional differentiation protocols allow handling in a smaller scale (Burridge *et al.*, 2014; Mosqueira *et al.*, 2018).

However, several limitations for cardiac differentiations have been reported. For example, differentiations often result in a mixture of cells, consisting of *e.g.,* fibroblasts, cardiac progenitors, epicardial or epithelial cells (Jiang *et al.*, 2022). Furthermore, cell line specific inconsistencies in differentiation efficiencies occur and need to be tackled by testing different activin A and bone morphogenetic protein 4 (BMP4) concentrations for the mesodermal induction (Kattman *et al.*, 2011; Sa and McCloskey, 2012).

The hiPSC-CMs are great tools to recapitulate human cardiac diseases in a dish and have therefore gained wide acceptance in the biomedical field (Denning *et al.*, 2016). However, the limited maturation status of hiPSC-CMs compared to adult CMs remains an important limitation and needs to be taken into account when interpreting data (Guo and Pu, 2020). Examples of immaturity include a lower mitochondrial content per cell, i.e. lower mitochondrial DNA to gDNA, associated with less fatty acid metabolism (Ulmer and Eschenhagen, 2020) or a lower than normal expression of key sarcomeric protein such as myosin heavy chain 7 (*MYH7*; Guo and Pu, 2020) , lack of a fully developed intercalated disc (Lemoine *et al.*, 2017; Gilbert *et al.*, 2021), lack of mature T-tubuli, smaller size, a round shape (Hwang *et al.*, 2015), a less negative resting membrane potential (RMP) and a shorter plateau phase due to lower expression of calcium channels (Guo and Pu, 2020). As explained later, further culture in micro physiological systems like engineered heart tissues (EHTs), or specific media compositions are utilized to increase maturation status of hiPSC-CMs.

1.3.3 CRISPR/Cas9-mediated gene editing

Another molecular biological tool, which revolutionised the disease modelling field as much as the hiPSC technology, was the discovery of the genome editing machinery, clustered regularly interspaced short palindromic repeats (CRISPR)- associated Cas system (Haurwitz *et al.*, 2010; Deltcheva *et al.*, 2011). The CRISPR/Cas system is part of the adaptive immune system of bacteria to combat viral infection. Fragments of foreign DNA are integrated into the bacterial genome between clustered repeats and serve as a template for CRISPR-RNA (crRNA). The guide RNA (gRNA) consists of the two independently expressed crRNA and trans-activating crRNA (tracrRNA). The gRNA binds the Cas enzyme (here Cas9) via the tracrRNA and forms a ribonucleoprotein complex (RNP; Jinek *et al.*, 2013). The crRNA guides the RNP towards the foreign locus (Jinek *et al.*, 2013). The Cas9 requires a PAM (protospacer adjacent motif; 5'-NGG) adjacent to the crRNA sequence in the genome to become active and induces a double strand break (DSB). This system can be exploited for targeted gene editing in eukaryotic cells in two ways. DNA repair upon DSB occur either in NHEJ or the less frequent homology directed repair (HDR). The latter requires the presence of double- (dsODNs) or single-stranded oligonucleotides (ssODNs) as a repair template (Ran *et al.*, 2013). NHEJ results in insertion or deletions (indels) and can therefore serve as a tool for functional inactivation of a gene (=knockout). HDR can be exploited for targeted insertions or corrections as shown in Figure 6 (Ran *et al.*, 2013). This can be used in hiPSCs to generate isogenic lines that just differ by the mutation of interest: Either pathogenic mutations in hiPSCs from patients are repaired to generate an isogenic control, or mutations are introduced. These isogenic pairs of cell lines are powerful tools in functional experiments to understand the effect of a single mutation without genetic confounders.

Two main challenges in the CRISPR/Cas9 technology are the variability of Cas9 efficiency and unintended off-target (OT) effects. It can take several designs to reach the desired precise gene editing, due to the low chance of HDR. Thus, having a lower Cas9 cleavage activity makes it work intensive to gain an edited clone. One reason for the variation in success is a reduced chromatin accessibility, which lowers Cas9 efficiency (Uusi-Mäkelä *et al.*, 2018; Liu *et al.*, 2019; Jain *et al.*, 2021). Another reason is the absence of suitable PAM sequences close to the intended cleavage site (Schubert *et al.*, 2021). The unintended OT effects were primarily thought to occur at loci carrying a similar sequence to the crRNA. However, recent studies identified larger deletions and even chromosome rearrangements as consequences of CRISPR/Cas9 interventions (Kosicki, Tomberg and Bradley, 2018). Thus, careful long-range genetic analyses are needed to exclude such unintended side effects with their obvious potential for obscuring any cause-effect relationships.

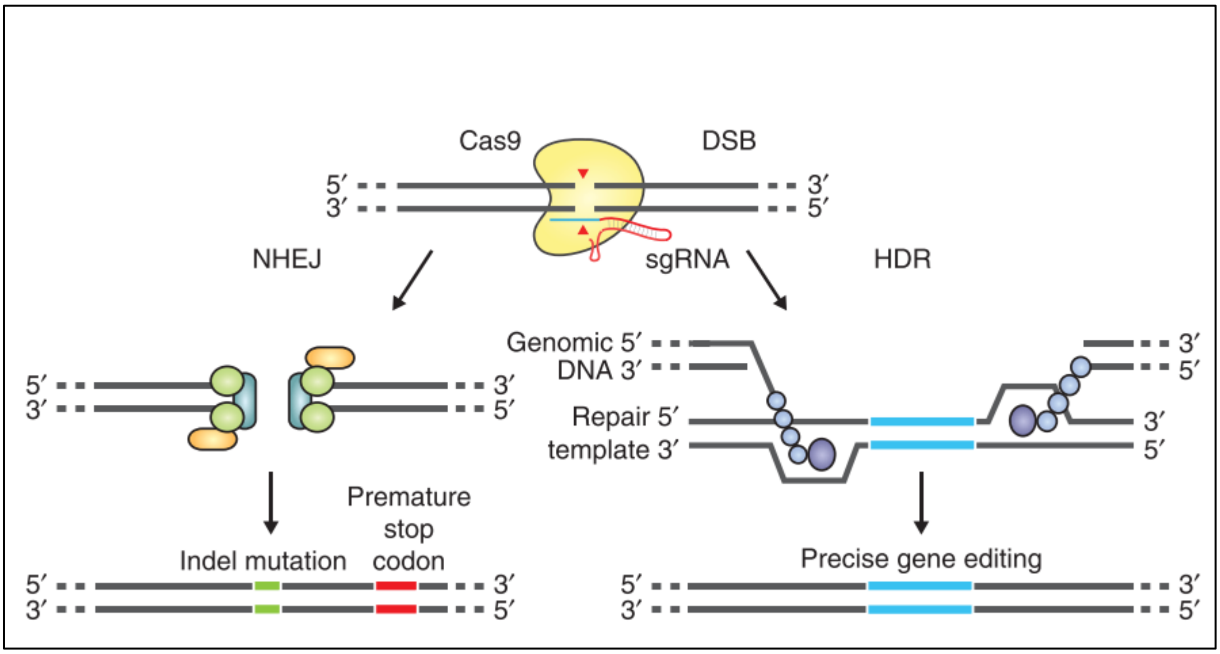

Figure 6 Cas9 recruited by single guide RNA (sgRNA) to genomic DNA locus induces a double strand break (DSB). Two repair mechanisms occur upon DSB; either non-homologous end joining (NHEJ) which results in insertion or deletions or homology-directed repair (HDR) that results in precise gene editing with the help of a repair template. Figure retrieved from (Ran *et al.*, 2013).

1.3.4 Engineered heart tissues (EHTs)

Preceding the discovery of the isolation of human pluripotent cells, another approach paving the way away from the animal disease models was the development of a technique to generate spontaneously beating 3-dimensional heart tissues in the dish (engineered heart tissue, EHT; Eschenhagen *et al.*, 1997). Embryonic chicken CMs were cultured within a collagen matrix and started to beat spontaneously, allowing force measurements (Eschenhagen *et al.*, 1997). In the recent two decades, the system has been extensively developed further and optimised. First, the system was adapted for the use of neonatal rat CMs and efficient adenovirus-mediated gene transfer was validated (Zimmermann *et al.*, 2000). In order to allow more standardised and also miniaturised EHTs, the shape was changed to stripe instead of ring format and the matrix changed from collagen to fibrin (Hansen *et al.*, 2010). In 2011, the first EHTs were made from human ESC-derived CMs (Schaaf *et al.*, 2011) and in 2014 the first EHTs from hiPSC-CMs (Stoehr *et al.*, 2014). Protocol optimisations for cardiac differentiation from hiPSCs and generation of human EHTs were published 2017 (Breckwoldt *et al.*, 2017). Another milestone for the EHT disease modelling set up (Figure 7) was the establishment of an automated video optical recording system, allowing standardised measurements under defined gas supply, humidity and temperature conditions (Hansen *et al.*, 2010). Furthermore, the system allows external manipulations via *e.g.* stiffening of the posts, inducing acute afterload enhancement in rat derived EHTs subsequently resulting in hypertrophy (Hirt *et al.*, 2012; Rodriguez *et al.*, 2019). Several studies have shown that maturation of hiPSC-CMs advances in the EHT format in terms of metabolism, contraction of force, sodium channel density and upstroke velocity of APs, but still does not reach a full adult state (Lemoine *et al.*, 2017; Ulmer *et al.*, 2018; Ulmer and Eschenhagen, 2020).

EHTs can be employed for different purposes. For example, the tissue derived from healthy control donors as a starting material might serve as a cardiac repair tissue for surgeries (Querdel *et al.*, 2021; Köhne *et al.*, 2022). In addition, EHTs with hiPSC-CMs derived from healthy donors can be used for drug screening of intentional or unintentional side effects (Eder *et al.*, 2014; Mannhardt *et al.*, 2016; Saleem *et al.*, 2020). Finally, as shown in Figure 7 patient derived hiPSC can be corrected for their mutation via CRISPR/Cas9 gene editing and underlying pathogenic mechanisms of the mutations can be studied in EHTs when differentiated to CMs (Prondzynski *et al.*, 2019; Cuello *et al.*, 2021; Zech *et al.*, 2022).

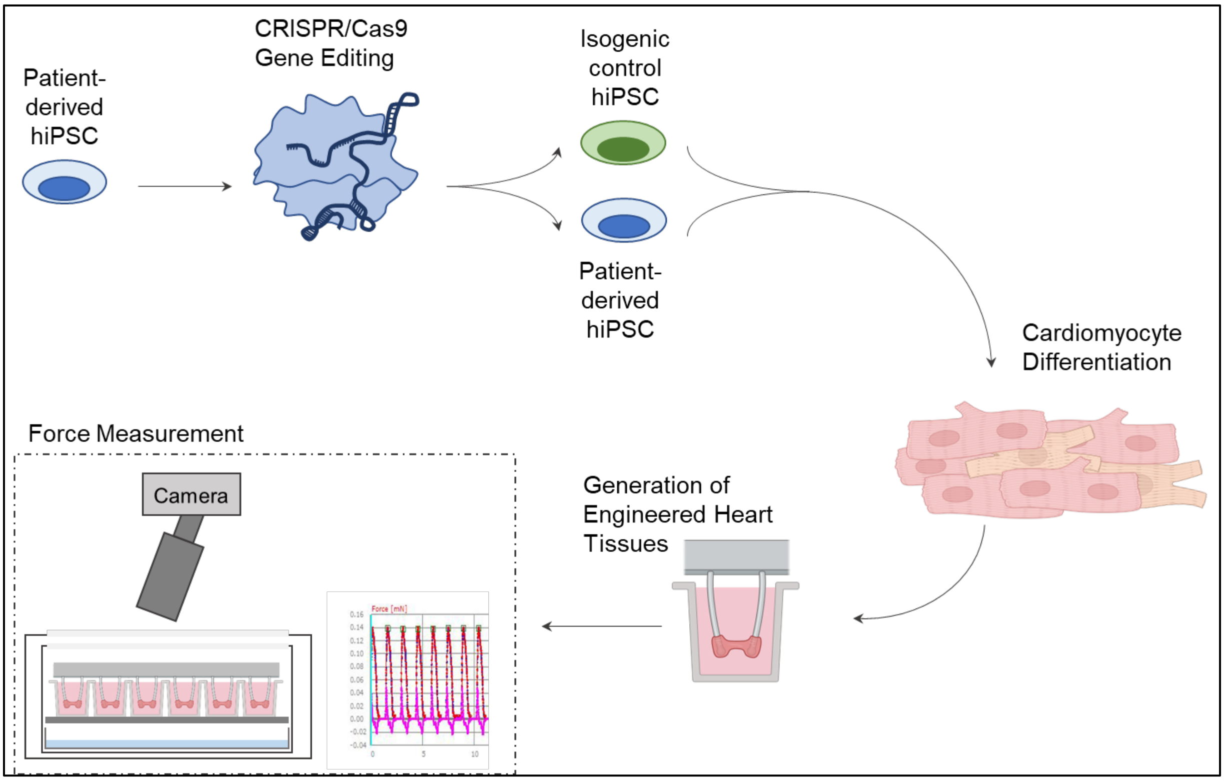

Figure 7 Disease modelling platform to study patient-derived hiPSC-CMs in the EHT format. Using video optical recording unit allows force of contraction measurement under defined culture conditions. Adapted from (Hansen *et al.*, 2010) and segments were retrieved from Biorender.com

In conclusion, the implementation of patient-derived hiPSC-CMs and the possibility to precisely target mutations with CRISPR/Cas9 added a new perspective for cardiac disease modelling. However, immaturity of hiPSC-CMs still pose one of the biggest challenges to gain understanding of pathological mechanisms. A disease modelling setup that makes use of EHTs allows hiPSC-CMs to reach a more mature state, to manipulate the tissues *in vitro* and thus facilitate to explore disease mechanisms.

1.4 Gene therapies as novel therapeutic approaches

Current therapies of HF target secondary changes such as the neurohumoral activation. They delay HF progression and provide symptomatic relief, but do not address the underlying pathogenic mechanisms. Therefore, gene therapies are a promising field to explore, particularly for inherited cardiomyopathies with a defined pathogenic mutation. Several strategies can be pursued that depend on the disease mechanism: (i) lack of protein *e.g.*, for heterozygous mutation haploinsufficiency or (ii) the dominant-negative effect of a poison peptide.

(i) Haploinsufficiency is often caused by a situation in which the mutation leads to a truncated protein that is rapidly degraded, leading to a lower-than-normal protein concentration. A simple overexpression of exogenous WT transcript can be employed. An example is HCM on the basis of *MYBPC3* mutations that are commonly truncating (Mearini *et al.*, 2014; Prondzynski *et al.*, 2017). Gene replacement strategy by adeno-associated virus (AAV)-mediated transfer of WT *MYBPC3* transcript rescued cardiac hypertrophy in a *MYBPC3* mouse and hiPSC-CM model (Mearini *et al.*, 2014; Prondzynski *et al.*, 2017). Similarly, transgenic cardiomyocyte-specific expression of WT lamin A rescued the phenotype in LMNA$^{-/-}$ mice, while overexpression in WT mice induced arrhythmia (Frock *et al.*, 2012).

Another strategy is *trans*-splicing, which can be useful if the full-length cDNA is too long for the vector. The fragment delivered by the vector carries a part of the transcript with the WT exonic and intronic sequence as well as a specific complementary sequence in order to hybridise with the target pre-mRNA. Thus, it competes with *cis*-splicing, resulting in a corrected mature mRNA and protein (Prondzynski, Mearini and Carrier, 2019). *Trans*-splicing strategies have been reported in *MYBPC3* and *LMNA* models, both with relatively low efficiency (Prondzynski *et al.*, 2017; Azibani *et al.*, 2018).

A third strategy for treating haploinsufficiency is exon-skipping of the mutation. In the case of a frameshift mutation the transcript carrying the mutation is degraded. Inducing skipping of the exon with the mutation, *e.g.* by CRISPR/Cas9 technology or antisense oligo nucleotides, can restore the reading frame and the production of a stable albeit shorter protein (Prondzynski, Mearini and Carrier, 2019). A well-studied example is the treatment of Duchenne muscular dystrophy, which reached approval by the Food and Drug Administration (FDA) following clinical trials (Eser and Topaloğlu, 2022). Not only haploinsufficiency has been proposed to be targeted, also missense mutations in *LMNA* might be treated by skipping of exon 5, without altering the alpha-helix of the rod domain (Scharner *et al.*, 2015). The beneficial effect can be explained in this case by a prevention of a poison peptide effect (“gain-of-function”) of the mutated lamin A.

In case of a (ii) dominant-negative gain-of-function mechanism as cause of the disease, an allele-specific knockdown can be the strategy of choice. Therefore, RNA interference can be exploited to silence the mutated allele. An allele-specific knockdown mediated by an siRNA has been reported to cure long QT syndrome in hiPSC-CMs carrying a *KCNH2* mutation

(Matsa *et al.*, 2014). Another possibility is to a combine silencing of the mutated gene with replacement of the WT cDNA. This “suppression replacement strategy” has been successfully applied in hiPSC-CMs from a patient with long QT type 1 syndrome caused by a loss-of-function in the gene *KCNQ1* encoding a potassium channel (Dotzler *et al.*, 2021).

Taken together, different strategies have been developed to target the underlying causes of cardiomyopathies. Current roadblocks towards clinical application include the efficiency of gene delivery as well as the immunogenicity and liver toxicity of AAV vectors, which may be reduced by finding AAV vectors with better cell-type and/or organ specificity of promoters and means to apply AAV in a loco-regional manner.

2 Aim of study

The first aim of the thesis was to establish a human *in vitro* p.H222P laminopathy model. This model allowed the investigation of the interplay of altered gene expression and mechanical coupling defect under external mechanical manipulation in EHT format in comparison to an isogenic control. The experiments were designed to tackle the question of why tissues under high mechanical strain are affected the most in laminopathies.

The second aim of this thesis was the development of a therapeutic strategy. It addresses a conceptional problem in the development of molecular therapies of laminopathies, namely the large diversity of *LMNA* mutations, which impedes the design of mutation-specific approaches. Thus, the aim was to establish an AAV-based therapy of a lamin A cDNA replacement strategy that could, theoretically, target all cases of LMNA haploinsufficiency by restoring normal lamin A levels. This strategy was tested in a homozygous LMNA-KO hiPSC-CM model exhibiting a complete lack of A-type lamin. The readouts of this test were contractile function of EHTs as well as structural parameters, the transcriptome, and the proteome.

3 Material and methods

3.1 Culture media

3.1.1 Stem cell culture media

FTDA	**Concentration**
DMEM/F-12 without Glutamine	1X
L-glutamine	2 mM
Transferrin	5 mg/L
Sodium selenite	5 µg/L
Human serum albumin	0.1% (v/v)
Lipid mix	0.1% (v/v)
Human recombinant insulin	5 mg/L
Dorsomorphin	50 nM
Activin A	2.5 ng/mL
Transforming growth factor-β 1 (TGFß1)	0.5 ng/mL
bFGF (freshly added)	30 ng/mL
Conditioned medium	**Concentration**
DMEM/F-12 without Glutamine	1X
Non-essential amino acids (NEAA)	1% (v/v)
L-glutamine	1% (v/v)
Penicillin/streptomycin	0.5% (v/v)
2-Mercaptoethanol	3.5 µL/500 mL
Knockout serum replacement	20% (v/v)

3.1.2 Monolayer differentiation media

Stage 0 medium	**Concentration**
StemPro®-34 SFM Complete Medium	1X
StemPro®-34 SFM-34 Nutrient Supplement	26 µL/mL
Matrigel® (for EHT generation)	1% (v/v)
BMP4	1 ng/mL
L-glutamine	1% (v/v)
Stage 1 medium	**Concentration**
StemPro®-34 SFM Complete Medium	1X
StemPro®-34 SFM-34 Nutrient Supplement	26 µL/mL

Activin A BMP4 L-glutamine	8 ng/mL 10 ng/mL 1% (v/v)
Stage 2.1 medium	**Concentration**
RPMI 1640 B27 minus insulin KY 02111 XAV 939	1X 2% (v/v) 10 µM 10 µM
Stage 2.2 medium	**Concentration**
RPMI 1640 B27 with insulin (0.156 mg/mL B27) KY 02111 XAV 939	1X 2% (v/v) 10 µM 10 µM
Regular daily medium (RDM)	**Concentration**
RPMI 1640 B27 with insulin (0.156 mg/mL B27)	1X 2% (v/v)

3.1.3 Embryoid body (EB) based differentiation media

Stage 0 medium	**Concentration**
FTDA (without bFGF) Polyvinyl alcohol Y-27632 bFGF	1X 4 mg/mL 10 µM 30 ng/mL
Stage 1 medium	**Concentration**
RPMI 1640 Polyvinyl alcohol HEPES (pH7.4) Human serum albumin Phosphoascorbate Transferrin Sodium selenite Lipid mix Activin A BMP 4 bFGF	1X 4 mg/mL 10 mM 0.05% (v/v) 250 µM 5 mg/L 5 µg/L 0.1% (v/v) 3 ng/mL 10 ng/mL 5 ng/mL

Y-27632	10 µM
Stage 1 washing medium	**Concentration**
RPMI 1640	1X
Polyvinyl alcohol	4 mg/mL
HEPES (pH7.4)	10 mM
Stage 2.1 medium	**Concentration**
RPMI 1640	1X
Polyvinyl alcohol	4 mg/mL
HEPES (pH7.4)	10 mM
Human serum albumin	0.05% (v/v)
Phosphoascorbate	250 µM
Transferrin	5 mg/L
Sodium selenite	5 µg/L
Lipid mix	0.1% (v/v)
XAV 939	1 µM
Y-27632	1 µM
Penicillin/streptomycin	0.5% (v/v)
Stage 2.1 washing medium	**Concentration**
RPMI 1640	1X
Polyvinyl alcohol	4 mg/mL
Penicillin/streptomycin	0.5% (v/v)
Stage 2.2 medium	**Concentration**
RPMI 1640	1X
B27 plus insulin	2% (v/v)
HEPES (pH7.4)	10 mM
1-Thioglycerol	500 µM
XAV 939	1 µM
Y-27632	1 µM
Penicillin/streptomycin	0.5% (v/v)
Stage 2.3 medium	**Concentration**
RPMI 1640	1X
B27 plus insulin	2% (v/v)
HEPES (pH7.4)	10 mM
1-Thioglycerol	500 µM
Y-27632	1 µM
Penicillin/streptomycin	0.5% (v/v)

3.1.4 Media for engineered heart tissue (EHT) culture

EHT casting medium	**Concentration**
DMEM	1X
Horse serum	10% (v/v)
L-glutamine	2 mM
Penicillin/streptomycin	1% (v/v)
EHT complete medium	**Concentration**
DMEM	1X
Horse serum	10% (v/v)
Insulin	10 µg/mL
Aprotinin	33 µg/mL
Penicillin/streptomycin	1% (v/v)
EHT maturation medium	**Concentration**
DMEM without glucose	1X
Glucose	3 mM
L-lactate	10 mM
Vitamin B12	5 µg/mL
Biotin	0.82 µM
Ascorbic acid	0.5 mM
NEAA	1X
Albumax	0.5% (w/v)
B27	1X
Knockout serum	1% (v/v)
Penicillin/streptomycin	1%

3.2 HiPSCs

3.2.1 Generation of p.H222P hiPSCs

Fibroblasts were retrieved from a skin biopsy of a male patient, who carried the mutation p.H222P in the gene *LMNA* in the heterozygous state. The fibroblasts were kindly provided by the laboratories of Gisèle Bonne and Antoine Muchir at INSERM Paris. The donor gave informed consent, and all methods were approved by the local ethics committee in Hamburg (PV3501). The HEXT stem cell core facility at the university medical center Eppendorf (UKE) Hamburg reprogrammed these fibroblasts at passage 7 upon Sendai viral transduction according to the manufacturer's protocol CytoTune-iPS Sendai Reprogramming Kit (Product No. A1377801, Life Technologies). Clones were cultured in conditioned medium (CDM;

murine embryonic fibroblasts) under the usage of bFGF (30 ng/mL). Confluent cells were then passaged with EDTA (0.5 mM) in PBS and under the treatment with Y-27632 (10 µM). Mycoplasma contamination tests were kindly performed by June Uebeler at the Institute of Experimental Pharmacology and Toxicology (IEPT), UKE Hamburg (see 3.2.3.4). All p.H222P stored clones were mycoplasma positive. Mycoplasma treatment occurred at passage 9 making use of BIOMYC antibiotics (1:100; PromoCell) according to manufacturer's protocol. After successful treatment hiPSCs were propagated and CDM medium was exchanged gradually in 25% steps with every passage to the chemically defined FTDA (bFGF, TGFβ1, dorsomorphin and activin A-based hiPSC culture) media (Frank *et al.*, 2012). Cells were propagated according to section 3.2.2 when they reached 100% FTDA media culture conditions.

3.2.2 Culture of hiPSCs

HiPSCs were cultured and expanded according to a published protocol (Shibamiya *et al.*, 2020). In short, hiPSCs were seeded on Geltrex® (1:100; Thermo Fisher Scientific) coated 6-well plates (Nunc) in a density between 50,000 and 60,000 cells/cm^2 and fed daily with FTDA media supplemented with bFGF (30 ng/mL). For singularisation on the day of passaging, hiPSCs were washed two times with 1X PBS, incubated with Accutase® (Sigma Aldrich) for 10 minutes (37 °C, 5% CO2, 20% O2) and detached with FTDA. Centrifugation was performed according to media volume for 3 (up to 10 mL) or 5 minutes (up to 50 mL) at 200 x g. On the day of passaging, all substances except PBS were supplemented with Y-27632 (10 µM). The hiPSCs were propagated until passage 18 for generation of a master cell bank (MCB). Therefore, hiPSCs were cryopreserved in a freezing medium that consisted of foetal calf serum (FCS; Biochrom) supplemented with Dimethylsulfoxide (DMSO; 10%; Sigma-Aldrich) and Y-27632 (10 µM; Biobyrt). The freezing step of the 1x10^6 cell vials was carried out in an isopropanol container at -80 °C prior to final storage at -150 °C. Thawed vials were then expanded until passage 22 to create a working cell bank.

3.2.3 Quality controls of hiPSCs

3.2.3.1 Pluripotency via stage-specific embryonic antigen 3 (SSEA3)

Before making use of the hiPSCs in experiments, their quality in terms of pluripotency was assessed with fluorescent labelled stage-specific embryonic antigen 3 (SSEA3) following the reported protocol (Shibamiya *et al.*, 2020). In brief, 0.5 to 1x10^6 detached hiPSCs were blocked with foetal bovine serum (FBS) for a minimum of 15 minutes up to overnight. Then, cells were washed under the usage of SSEA3 staining buffer (PBS + 5% FBS) and centrifugation steps out at 200 x g. Cells were then stained in 100 µL SSEA3 staining buffer (1:50; SSEA3 antibody) for 45 minutes followed by two washing steps and final resuspension in 200 µL PBS. The analysis of pluripotency positivity of hiPSCs was performed according to a staining with isotypic control antibody for human recombinant engineered antibodies (REA) via a flow cytometry (FC). FC was carried out under the usage of Canto II (BD Biosciences) at FACS Core Facility at the UKE Hamburg. Other pluripotency markers were analysed as described in section 3.2.3.3.

3.2.3.2 Karyotype analysis

The karyotype analysis of hiPSC MCB was kindly conducted by Lisa Krämer and Dr. Giulia Mearini from the NanoString facility at the IEPT at the UKE Hamburg (Shibamiya *et al.*, 2020). In short, gDNA was extracted from all clones used in this study following the DNeasy Blood & Tissue Kit (QIAGEN) manufacturer's protocol. For analysis, 250 µg gDNA was enzymatically digested, followed by a hybridisation step at 65 °C overnight and subsequent loading into the nCounter cartridge (Nanostring). Detection of probes were performed using the nCounter$^{\text{SPRINT™}}$ Profiler (Nanostring) and analysed making use of the nCounter CNV Collector Tool (Nanostring).

3.2.3.3 Germ layer differentiation

Maximilian Kolbe (UKE Hamburg) kindly conducted the already published protocol (Warnecke *et al.*, 2021) for spontaneous germ layer differentiation for all three hiPSC clones that were used in this study. Further, Maximilian Kolbe provided the quantitative PCR (qPCR) data for the analysis of pluripotency markers (*NANOG* and *SOX2*), as well as ectodermal (*NCAM1* and *PAX6*) and endodermal (*SOX17*) markers (Warnecke *et al.*, 2021). In brief, hiPSCs of MCB vials were propagated for three passages until performing the germ layer differentiation following STEMdiff Trilineage Differentiation Kit (StemCell Technologies) manufacturer's protocol for endoderm and ectoderm commitment. RNA of hiPSCs were extracted as described in section 3.5.6 and were reverse transcribed to cDNA following Superscript IV (Thermo Fisher Scientific) manufacturers protocol. A reaction mix was pipetted, which consisted of 1 µL cDNA (1:10 diluted), the corresponding primers (Table S 4) and the Maxima SYBR Green/ROX qPCR Master Mix (Thermo Fisher Scientific). Reactionmix assembly and qPCR were performed according to manufacturer's protocol and using the AbiPrism 7900HT Fast Real-Time PCR System (Applied Biosystems).

3.2.3.4 Contamination test

When hiPSCs reached confluency, 200 µL of media was aspirated and stored at 4 °C until mycoplasma testing via PCR. The PCR was carried out as described previously under the usage of primers, which sequence can be found in Table S 4 (Breckwoldt *et al.*, 2017).

For visual assessment of sterility, one vial of MCB and WCB per cell line were thawed as described in section 3.2.2 without changing the media for 10 days, but regular microscopic evaluation of contaminants.

3.2.4 CRISPR/Cas9-mediated gene editing in p.H222P

3.2.4.1 Validation of targeted genomic locus and allelic discrimination

Genomic DNA was isolated from a p.H222P hiPSC pellet making use of the DNeasy Blood & Tissue Kit (QIAGEN; according to manufacturer's protocol). A PCR reaction mix was assembled with the primer Exon-4-in-Fwd and SNP-Rev (Table S 2) and according to Table 1. The PCR program was set according to Table 2.

Table 1 PCR reaction mix assembled based on PrimeSTAR protocol.

Substance	**Stock Concentration**	**Volume for 1 X**
PrimeStar Buffer	5X	10 µL
dNTPs	2.5 mM	4 µL
DMSO		1 µL
PrimeSTAR Polymerase	100 X	0.5 µL
PrimerPair	10 µM	0.5 µL
Genomic DNA	34 ng/µL	1 µL
H_2O		33 µL

Table 2 Cycle program run for PrimeStar PCR. * indicates -0.5 °C per cycle.

Step	Duration	Cycles
98 °C	00:10	x13
67°C*	00:30	
72 °C	03:00	
98 °C	00:10	x24
57 °C	00:30	
72 °C	03:00	
72 °C	07:00	
4 °C	∞	

The PCR product was analysed on a 1% agarose 1X TAE gel stained with Midori Green Advance DNA Stain (Nippon Genetics Europe; 3 µL for a small 50 mL agarose gel). Subsequently, the PCR product was purified following the manufacturer’s protocol QIAquick PCR Purification Kit (QIAGEN). Further, the purified product was ligated into the CloneJET pJET1.2/blunt plasmid according to the manufacturer’s instructions of the CloneJET PCR Cloning Kit (Thermo Fisher Scientific). In brief, the reaction mix was assembled according to Table 3 and briefly vortexed. Then the reaction was incubated at room temperature (RT) for 15 to 20 minutes.

Table 3 Reaction mixture assembled for CloneJET ligation.

Substance	Volume for 1 X
Reaction Buffer	10 µL
PCR Product	8.2 µL
pJET1.2/blunt Plasmid	1 µL
T4 DNA Ligase	1 µL
Nuclease-free H_2O	0.8µL

To select later single-ligated plasmids, TOP10 heat shock competent *E. coli* were transformed with the reaction mix. Therefore, 100 µL *E. coli* cells were thawed on ice prior to the addition of either 3 µL ligation mix or empty control. Cells were incubated on ice for 30 minutes before a heat shock at 42 °C for 45 seconds was performed. Subsequently, cells were chilled on ice followed by the addition of 200 µL S.O.C. media. An outgrowth was performed for 1 hour with 200 rpm at 37 °C and subsequent plating of 250 µL cell onto

Ampicillin-containing agar plates. Plates incubated overnight at 37 °C. Next day, 10 tubes with 3 mL of LB media containing Ampicillin were inoculated with colonies picked from the agar plate and incubated at 37 °C with 200 rpm overnight. The next day, *E. coli* cultures were centrifuged at 11,000 x g at 4 °C for 10 minutes. Then the supernatant was discarded, and plasmid DNA was isolated from cell pellets according to manufacturer's instructions (NucleoSpin Plasmid Miniprep kit, Macherey-Nagel) and eluted in 30 µL nuclease-free water. The 10 plasmids were sent for Sanger sequencing at MWG/Eurofins.

.

3.2.4.2 CRISPR/Cas9 gene editing approach

To generate an isogenic control (IsoC) derived from p.H222P hiPSCs, several runs (I to V) were conducted. Different crRNA and ssODN HDR templates were designed due to the success of the experiments (runs reviewed and analysed in section 4.1.2; shown in Figure 8; Table 4). It is speculated that secondary structure might have an influence on HDR efficiencies. The ssODN HDR template 3.2 was designed based on a hairpin prediction in comparison to the template 3.1 making use of an *in silico* secondary structure prediction tool (http://rna.urmc.rochester.edu/RNAstructureWeb/Servers/Predict1/Predict1.html; Mathews, Turner and Zuker, 2007). The crRNAs were selected based on the CRISPOR *in silico* tool and predicted potential OT size (http://crispor.tefor.net/).

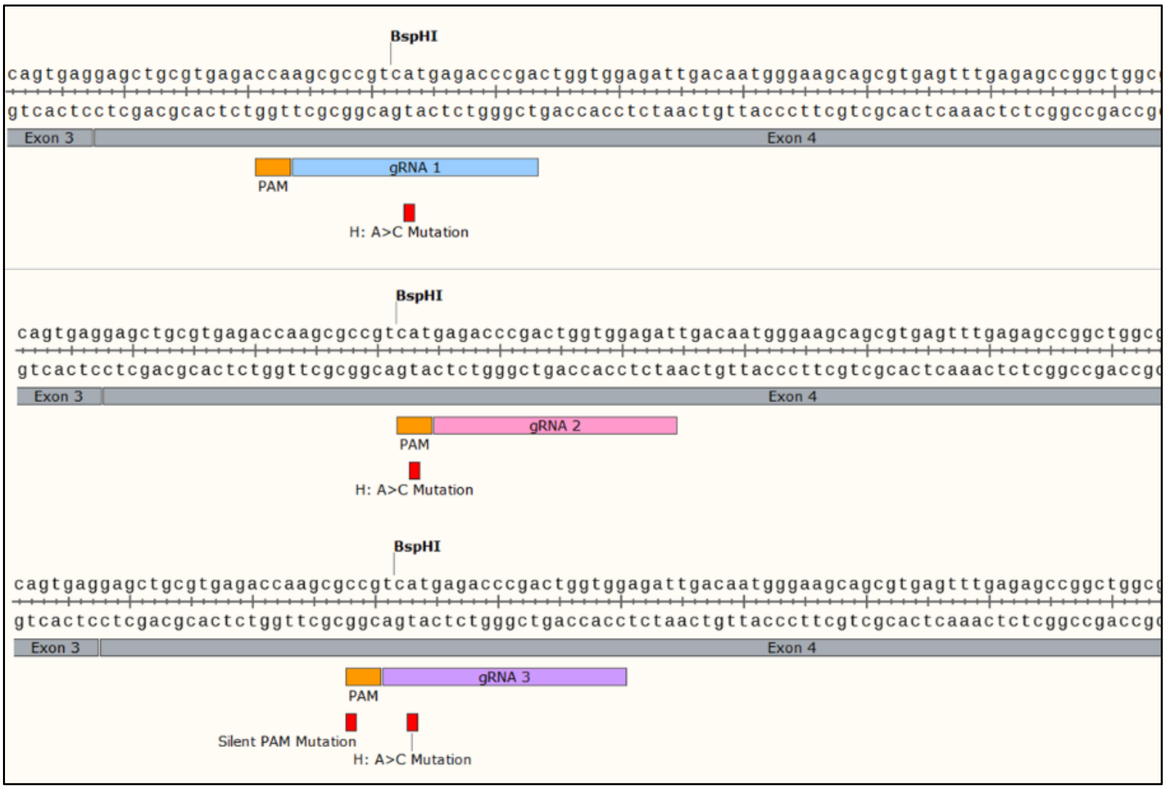

Figure 8 Overview of the three different gRNAs (1 to 3) predicted *in silico* according to the CRISPOR tool (http://crispor.tefor.net/) to correct the p.H222P mutation in exon four of the gene *LMNA*. The three gRNAs were used in five different CRISPR/Cas9 experiments.

Table 4 Sequences of crRNA and ssODN used for different CRISPR/Cas9 experiments.

CRISPR Run	**crRNA (5’-3’)**	**ssODN (5’-3’)**
I + III	TCGGGTCTCAGGACGGCGCT	tctgattttggtttctgtgtccttcctccaacccttccagGAGCTGCGTGAGACGAAGCGCCGTCATGAGACCCGACTGGTGGAGATTGACAATGGGAAGCAGCGTGAGTTTGAGAGCCG
II + III	ATCTCCACCAGTCGGGTCTC	tctgattttggtttctgtgtccttcctccaacccttccagGAGCTGCGTGAGACGAAGCGCCGTCATGAGACCCGACTGGTGGAGATTGACAATGGGAAGCAGCGTGAGTTTGAGAGCCG
IV	CCACCAGTCGGGTCTCAGGA	CCAGGAGCTGCGTGAGACGAAGCGGCGTCATGAGACCCGACTGGTGGAGATTGACAATGG
V	CCACCAGTCGGGTCTCAGGA	tctgtgtccttcctccaacccttccagGAGCTGCGTGAGACCAAGCGACGTCATGAGACCCGACTGGTGGAGATTGACAATGGGAAGCAGCGTGAGTTTGAGAGCCGGCTGGC

For each run hiPSCs were expanded as explained in section 3.2.2. until passage 21. Reaching an 80-90% confluency in 6-well format, p.H222P hiPSCs were treated with FTDA supplemented with Y-27632 (10 µM; Biobyrt) and bFGF (30 ng/mL) for one hour. Then, crRNA (according to CRISPR run; Table 4) and tracrRNA (fluorescence-labeled tracrRNA-ATTO 550; IDT) were resuspended in RNAse-free IDTE Buffer (100 µM; IDT) and annealed at 95 °C for 5 minutes to a gRNA and cooled down at room temperature. Further for ribonucleic acid protein (RNP) complex formation, Cas9 3NLS (61 µM; IDT) and sgRNA (according to CRISPR run; Table 4) were pipetted in 1:1 relation at room temperature for one hour protected from light. After one hour incubation of hiPSCs, p.H222P were first washed with PBS, treated with Accutase® (Sigma Aldrich) and incubated (10 min, 37 °C, 5% CO2, 20% O2) for single cell dissociation. After counting with CASY cell counter, 800,000 hiPSCs were resuspended for each approach in 100 µL Nucleofector solution (82 µL P3 Amaxa Solution and 18 µL Supplement). Further, 4 µL of ssODN (4 µM; according to CRISPR run; Table 4) produced by IDT and 1 µL RNP complex were added prior to the nucleofection making use of the Amaxa nucleofection cassette and the 4D-NucleofectorTM (Lonza) according to manufacturer’s instructions (program CA137). After nucleofection 500 µL CDM media supplemented with Y-27632 (10 µM; Biobyrt) and bFGF (30 ng/mL) was added to the cells, which were then seeded on Matrigel (1:60; Corning®) coated 12-well. Following 48 hours, cells were cultured in CDM supplemented with Y-27632 (10 µM) and bFGF (30 ng/mL), hiPSCs were singularised as described above and seeded as 200, 400 and 600 cells per 6-well format and maintained until clonal growth was evident. Single clones were picked using a 100 µL pipette under the microscope (EVOS FL Cell Imaging System) and transferred to 48-well format plate for subsequent culture and cryo-preservation.

3.2.4.3 Molecular analysis of CRISPR clones

For analysing the CRISPR/Cas9 experiments gDNA was extracted from frozen hiPSC clones pellets making use of the QIAcube HT System (Qiagen) and QIAamp 96 DNA QIAcube HT kit (Qiagen). A PCR reaction mix was assembled with the primers Exon-3-in-Fwd and Exon-5-in-Rev (Table S 2) and was based on Phusion HF (Thermo Fisher Scientific) as shown in Table 5 and performed according to Table 6.

Table 5 PCR reaction mix assembled based on Phusion HF Ready Mix protocol.

Substance	**Volume for 1 X**
2X Phusion Master Mix with HF Buffer	25 µL
DMSO	1 µL
Primer Pair	2.5 µL
Nuclease-free H_2O	20.5 µL
gDNA	2 µL

Table 6 Cycle program run for Phusion HF Ready Mix PCR. * indicates -0.5 °C per cycle.

Step	**Duration**	**Cycles**
98 °C	00:30	x1
98 °C	00:10	x13
70 °C*	00:30	
72 °C	00:45	
98 °C	00:10	x27
65 °C	00:30	
72 °C	00:45	
72 °C	07:00	
4 °C	∞	

Primers (Table S 3) were designed for the OT analysis and used for the top 10 most likely OT sequences (Table S 1) according to CRISPOR *in silico* tool (http://crispor.tefor.net/;. The PCR reaction component composition was as described in Table 7 and the PCR ran according to Table 8.

Table 7 PCR reaction mix assembled based on Phusion HF Ready Mix protocol.

Substance	**Volume for 1 X**
2X Phusion Master Mix with HF Buffer	25 µL
DMSO	1 µL
Primer Pair	2.5 µL
Nuclease Free H_2O	20.5 µL
gDNA	0.5 µL

Table 8 Cycle program run for Phusion HF Ready Mix PCR. * Indicates -0.5 °C per cycle.

Step	**Duration**	**Cycles**
98 °C	00:30	x1
98 °C	00:10	x13
64 °C*	00:30	
72 °C	01:30	
98 °C	00:10	x18
58 °C	00:30	
72 °C	01:30	
72 °C	07:00	
4 °C	∞	

All PCR products were then analysed along the 1 kb DNA Ladder (5 µL; Thermo Fisher Scientific) on a 1% agarose 1X TAE gel stained with Midori Green Advance DNA Stain (Nippon Genetics Europe; 7 µL for a large 150 mL gel). Upon positive clear bands, PCR products were purified following the QIAquick PCR Purification Kit (QIAGEN) and sent for Sanger sequencing at MWG/Eurofins.

3.2.4.4 Large fragment PCR of clone #1 CRISPR run IV

For large fragment PCR, the primers Intronic-Fwd-1 and Exon-5-in-Rev for an expected amplification length of 2,201 bp were used (Table S 2) and PCR was performed as stated in Table 9 and Table 10.

Table 9 Reaction mix assembled based on PrimeSTAR protocol for long-range PCR.

Substance	**Stock Concentration**	**Volume for 1 X**
PrimeStar Buffer	5X	10 µL
dNTPs	2.5 mM	4 µL
DMSO		1 µL
PrimeSTAR Polymerase	100 X	0.5 µL
PrimerPair	10 µM	0.5 µL
Genomic DNA	34 ng/µL	0.1 µL
H_2O		33.9 µL

Table 10 Cycle program run for long-range PrimeStar based PCR. * indicates -0.5 °C per cycle.

Step	**Duration**	**Cycles**
98 °C	00:10	x13
66 °C*	00:30	
72 °C	03:00	
98 °C	00:10	x24
57 °C	00:30	
72 °C	03:00	
72 °C	07:00	
4 °C	∞	

PCR products were then analysed along the 1 kb DNA Ladder (5 µL; Thermo Fisher Scientific) on a 1% agarose 1X TAE gel stained with Midori Green Advance DNA Stain (Nippon Genetics Europe; 3 µL for a small gel).

3.3 HiPSC-derived CMs

3.3.1 Cardiac monolayer differentiation

Frozen vials of stored hiPSC WCBs were thawed and propagated for three passages as mentioned in section 3.2.2. Upon reaching confluency, hiPSCs were seeded in a density 50,000-60,000 cells/cm^2 and subjected to an already published 2D monolayer differentiation protocol (Mosqueira *et al.*, 2018). Differentiation was initiated, when hiPSCs reached 60 to 70 % confluency, by the addition of Stage 0 media and transfer from hypoxic to normoxic incubation conditions. After 12 to 16 hours, media was exchanged to Stage 1. Next stages were induced every 48-hour by media exchange. Here, the protocol was modified by an additional washing step with prewarmed RPMI between Stage 1 and Stage 2.1 (Mosqueira *et al.*, 2018).

Beating CMs were dissociated with collagenase II (200 units/mL; Worthington) for 1 hour and analysed with an intracellular cardiac troponin T (cTnT) staining via FC as recently described (Breckwoldt *et al.*, 2017). Remaining cells were either directly used for following experiments or frozen as vials in foetal calf serum (FCS; Biochrom) supplemented with Dimethylsulfoxide (DMSO; 10%; Sigma-Aldrich) and Y-27632 (10 µM; Biobyrt).

3.3.2 Cardiac EB based differentiation

For three differentiation batches and one EHT batch of p.H222P and IsoC, hiPSCs were differentiated according to the published 3D EB-based protocol (Breckwoldt *et al.*, 2017).

In short, hiPSCs were propagated and expanded to a minimum of 8 confluent Geltrex-coated T75 cell culture flasks. Prior to an EDTA dissociation, hiPSCs were treated with 1 µM Y-27632 for one hour. Subsequently, dissociated 30 million hiPSCs per 100 mL Stage 0 medium were transferred to a spinner flask, which was placed on a magnetic stirrer and were incubated under hypoxic conditions overnight. Next day, EB volume was assessed and 180 to 250 µL were transferred to Pluronic F-127 treated T175 cell culture flasks containing Stage 1 medium and incubated under hypoxic conditions. The following two days half of the medium was exchanged. After that, EBs were washed and again their volume was assessed and 180 to 250 µL EBs per T175 flask were incubated with Stage 2.1 medium under normoxic conditions. The three following days half of the medium was exchanged. After that, medium was exchanged completely to Stage 2.2 medium. The next four days half of the medium was exchanged until a complete medium exchange to Stage 2.3 medium was performed.

Beating EBs were cultivated for some more days and then dissociated with collagenase II (200 units/mL; Worthington) for 3 to 4 hours (3D EB-based differentiation) and analysed with an intracellular cardiac troponin T (cTnT) staining via FC and cryopreserved as recently described (Breckwoldt *et al.*, 2017).

3.3.3 Cultivation of CM in 2D

Dissociated CMs were seeded on Geltrex® (1:100; Thermo Fisher Scientific) coated 12-well plates (Nunc) in a density of 50,000 cells/cm^2. The seeded CMs were cultured in complete medium under normoxic conditions at 37 °C (5% CO2). Media exchange occurred every two to three days with 1 mL complete medium. On the final day of culture after around 28 days, hiPSC-CMs were washed two times with PBS prior to dissociation with 0.5 mL Accutase® (Sigma Aldrich; 10 minutes). After resuspension of the cells in Accutase® with a 1000 µL pipette, wells were washed with 500 µL RPMI and centrifuged with 100 x g at 4 °C for 10 minutes. Pellets were subsequently washed in PBS and centrifuged again. In a final step the PBS was aspirated, the pellets were snap-frozen in liquid nitrogen and finally stored at -80 °C until further processing.

3.3.4 Inhibition of nonsense-mediated mRNA decay (NMD)

Cultured CMs were treated on day 30 in culture either with the nonsense-mediated mRNA decay (NMD) inhibitors or DMSO as a control in complete medium (Table 11). After 4 hours of incubation, CMs were harvested as described in section 3.3.3. and analysed by PCR as described in section 3.5.2. Experiments were kindly performed by Julia Freese (UKE Hamburg).

Table 11 Administration of NMD inhibitors or DMSO in culture media.

Substance	**Final concentration in media**
Emetine	900 µg/mL
Puromycin	130 µg/mL
DMSO	0.1 %

3.3.5 Transduction of CM in 2D

Cultured 2D hiPSC-CMs were transduced on day 15 in culture by the addition *AAV6-pCMV-GFP-2A-cLMNA* (Figure S 1) viral particles at an MOI of 30,000. For the transduction a centrifugation step at 2500 rpm at 30 °C was carried out for 30 min.

3.4 Engineered heart tissues (EHTs)

3.4.1 Generation, cultivation, and baseline measurements of EHTs

Singularised hiPSC-CMs being at least 80% cTnT positive according to FC were used for EHT generation. EHT generation was performed as previously described with some exceptions for the master mix, which contained only DMEM medium (PAN BioTech), supplemented with heat-inactivated horse serum (10%; Thermo Fisher), penicillin/streptomycin (1%; PEST, Gibco), GlutaMAX™ (1X; Gibco), Y-27632 and 5mg/mL fibrinogen (Sigma #F8630) and one million hiPSC-CMs (Mannhardt *et al.*, 2016; Breckwoldt *et al.*, 2017). All EHTs were casted on normal silicon posts, except p.H222P and IsoC EHTs subjected to mechanical stress intervention of acute AE, which were casted on “white” hollow posts as previously published (Hirt *et al.*, 2012; Rodriguez *et al.*, 2019).

All EHTs were cultured in the so-called “complete medium” consisting of DMEM medium (PAN BioTech) supplemented with heat-inactivated horse serum (10%; Thermo Fisher), penicillin/streptomycin (1%; PEST, Gibco), insulin (0.1%; Sigma Aldrich) and aprotinin (0.1%; Sigma Aldrich). Medium was changed every two to three days. Contraction parameters were recorded every two to three days using the equipment (A003 and A004) purchased from EHT Technologies GmbH (Hamburg, Germany) and analysed as previously published for baseline development making use of the CTMV software (Hansen *et al.*, 2010).

On final day of culture, EHTs were washed two times in 1 mL PBS and either prepared for immunofluorescence or other molecular analyses. For immunofluorescence analysis, washed EHTs were incubated in 1.5 mL ice-cold Histofix® (Carl Roth) at 4 °C overnight. Next day, EHTs were washed again with PBS and stored in PBS or TBS-azide at 4 °C until further experiments. Other washed EHTs were snap-frozen in liquid nitrogen and stored at -80 °C for further molecular experiments.

3.4.2 Electrical pacing of EHTs

Electrical pacing occurred in serum-free medium with defined calcium concentration. EHTs were washed in DMEM medium (1.8 mM calcium; 25 mM HEPES) and incubated for 30 minutes. Subsequently, EHTs were transferred to a second plate containing 2 mL in DMEM medium (1.8 mM calcium; 25 mM HEPES) and in which custom-made graphite electrodes were placed (Hirt *et al.*, 2014). EHTs were then electrically stimulated via graphite electrodes with the use of a Grass S88X Dual Output Square stimulator (Natus Neurology

Incorporated). The stimulation was set at an output voltage of 2 V in biphasic pulses of 4 milliseconds.

3.4.3 Functional experiments

On day 46 in culture, the effect of two different drugs, 4-aminopyridine (4-AP), a selective blocker for voltage-gated potassium channels, and Bay K8644, a calcium channel agonist, on contraction parameters were tested in one EHT batch. Therefore, EHTs were washed in DMEM medium (1.8 mM calcium; 25 mM HEPES) and incubated for 30 minutes. Then, EHTs were transferred to a second DMEM medium (1.8 mM calcium; 25 mM HEPES) plate. After measuring baseline conditions, 50 µM 4-AP and 100 nM Bay K8644 were added to the medium.

An experiment to assess a calcium response of IsoC and p.H222P EHTs was conducted. Prior to the experiment, EHTs were transferred to a DMEM medium plate (1.8 mM calcium; 25 mM HEPES) and incubated for 30 minutes, until baseline parameters were recorded as described above (see section 3.4.1). Then, EHTs were washed two times in DMEM medium (0.1 mM calcium; 25 mM HEPES) for one hour. When EHTs decreased in force of contraction, the calcium concentration was stepwise increased ranging from 0.3 mM (0.1 mM steps till 0.6 mM) to 3.3 mM (0.2 steps from 0.6 mM) and the final steps been 1.4 mM, 1.8 mM, 2.4 mM and 3.0 mM. Contractile force was then normalised to each EHTs own maximum value and median effective concentration (EC_{50}) values were calculated with the GraphPad Prism software 8.3.0 and selection of the “Dose-response – Stimulation” equation for a nonlinear regression (curve fit).

3.4.4 Afterload enhancement

EHTs were casted onto white hollow post as previously described (see section 3.4.1) and were changed to the defined medium lacking serum, termed maturation media, after 21 days in culture (Feyen *et al.*, 2020). After 28 days in culture, EHTs were randomised according to their force and split into groups with time-matched controls (TC) and acute afterload enhancement (AE). Prior to the experiments, 5 mm metal braces were covered with a silicon layer. These metal braces were inserted into the hollow post. EHTs were then measured regularly to assess the effect after four or five hours and after five or six days. For subsequent analysis, EHTs were either snap frozen as described above or fixed for immunofluorescence (see section 3.4.1).

3.4.5 Sharp microelectrode action potential recordings

Sharp microelectrode action potential recordings were kindly performed and analysed by Jascha Sani, Carl Schulz and Anna Steenpaß from AG Christ at the IEPT at UKE Hamburg. EHTs were subjected to the previously published protocol for action potential measurements. In short, EHTs were transferred to Tyrode's solution and were impaled by a sharp microelectrode to conduct recordings (Lemoine *et al.*, 2017; Prondzynski *et al.*, 2019).

3.4.6 Transduction of EHTs

For the therapeutic intervention, EHTs were randomised according to their force development on day 14 or 15 in culture. EHTs were transduced on day 15 in culture with the *AAV6-pCMV-GFP-2A-cLMNA* virus (Figure S 1) at MOI of 30,000 or 60,000. The viral particles were added directly to the complete media and EHTs incubated under continuous shaking for 72 hours (37 °C, 7% CO_2, 40% O_2).

3.4.7 Medium contamination test

LMNA-KO EHTs were incubated for three days in complete medium. The medium was then aliquoted and kindly analysed by the Institute of Medical Microbiology, Virology and Hygiene at the UKE Hamburg to exclude any contaminations.

3.4.8 Troponin I and NT pro-BNP media test

Complete media in which EHTs were cultivated and negative controls, were aliquoted and snap frozen. The media samples were kindly analysed for NT-proBNP (Abbott) and cardiac Troponin I (Abbott) according to manufacturer's protocols by AG Zeller (UKE Hamburg).

3.5 Molecular analysis

3.5.1 Isolation of RNA

Snap-frozen EHTs were thawed on ice and RNA was extracted with TRIzol® Reagent. In brief, EHTs were resuspended in 300 µL cold TRIzol® Reagent under shear stress applied first by a P1000 pipette followed by P100 and then a 1 mL RNase-free (B.Braun) syringe with different needles diameters of 0.9 mm and 0.4 mm (B-Braun). The resuspended EHTs were then further processed following the manufacturer's protocol with adjusted volumes according to resuspension volume. Finally, RNA was resuspended in 20 µL nuclease free water, concentrations were measured with Nanodrop, and samples were snap frozen in liquid nitrogen and stored at -80 °C for further experiments.

3.5.2 Validation of *LMNA*-knockout on RNA level

In order to validate, whether lamin A and C transcripts were absent in LMNA-KO CMs and arise upon NMD inhibition, RNA was isolated as described above (see 3.5.1) from treated and harvested CMs (see section 3.3.4). Subsequently the 500 ng of isolated RNA was reverse transcribed to cDNA by Superscript IV (Thermo Fisher Scientific) following manufacturer's protocol. Then either lamin A or lamin C transcripts were amplified by PCR, which made use of LMN_Fwd and LMNA_Rev or LMNC_Rev primers, respectively (Table S 2). The master mix was assembled as shown in Table 12 and PCR run following the program shown in Table 13. The success of the PCR was assessed on 1% agarose gel electrophoresis (see section). The experiment was kindly performed by Julia Freese (UKE Hamburg).

Table 12 PCR reaction mix assembled based on Phusion HF Ready Mix protocol.

Substance	**Volume for 1 X**
2X Phusion Master Mix with HF Buffer	25 µL
DMSO	1 µL
Primer Pair	2.5 µL
Nuclease Free H_2O	20.5 µL
cDNA	1 µL

Table 13 Cycle program run for Phusion HF Ready Mix PCR. * indicates -0.5 °C per cycle.

Step	**Duration**	**Cycles**
98 °C	00:30	x13
70 °C*	00:30	
72 °C	00:45	
98 °C	00:10	x27
65 °C	00:30	
72 °C	00:45	
72 °C	07:00	
4 °C	∞	

3.5.3 Restriction enzyme digestion

For the verification of the absence of the p.H222P mutation in IsoC hiPSCs, Julia Freese (UKE Hamburg) kindly assessed whether a restriction site for BSPHI in the region of the mutation was now in the homozygous state. Previously, isolated RNA was gained of CMs of all three cell lines (see 3.5.1) and reverse transcribed to cDNA by Superscript IV (Thermo Fisher) following manufacturer's protocol. A PCR was performed to amplify lamin A and lamin C transcripts, as described above (see section 3.5.2).

After checking the success of the PCR via 1% agarose gel electrophoresis, PCR products were purified following QIAquick PCR Purification Kit (QIAGEN) manufacturer's protocol. 100 ng of purified PCR product was digested with BspHI (PagI; Thermo Fisher). Therefore, digestion mix was assembled as shown in Table 14 and incubated at 37 °C for 10 minutes followed by a termination step at 80 °C for 5 minutes. Efficiency of restriction digestion was analysed in a 1% agarose gel electrophoresis.

Table 14 Reaction mixture assembled for restriction digestion of cDNA PCR product.

Substance	**Volume for 1 X**
FD Green Buffer (10X)	1.5 µL
PagI (BspHI) Enzyme	0.5 µL
DNA	X µL
Nuclease Free H_2O	Fill up to 15 µL

3.5.4 Isolation of proteins

The protein-containing phase was extracted with TRIzol® Reagent as described in section 3.5.1. The protein-containing phase was then further processed according to manufacturer's protocol. The protein pellet was then resuspended in 100 µL Kranias buffer (1 mM DTT). For -20 °C sample storage, 20 µL 6x Laemmli buffer was added to the resuspended protein and boiled at 95 °C for 5 min (Wenzel et al., 2021).

3.5.5 Western blot analysis

Protein lysates already diluted in Laemmli buffer were thawed and shortly spun down. Subsequently 12 µL of each sample were loaded onto either 10% SDS PAGE gel or a 4-15% Miniprotean TGX gel (BioRad; #4561083) along a 5 µL protein standard (Precision Plus Dual Color Standard; Biorad) and run at 80 V for 10 min following 110 V for 100 minutes.

Separated proteins were transferred from the gel on a nitrocellulose membrane at 300 mA for 90 min. Subsequently, the membrane was washed in TBS-T and stained with Ponceau S solution (Sigma-Aldrich) and was imaged using ChemiDoc™ Touch Imaging System (Bio-Rad) to validate the successful transfer. After two washing steps in TBS-T, the membrane was blocked in 5% milk TBS-T at room temperature for 1 hour. After three washing steps, incubation with the primary antibodies anti-lamin A/C (Santa Cruz, sc-376248 E-1; 1:500), anti-MYBPC3 (Santa Cruz, sc-137181, F-1, 1:1,000), anti-GFP (Abcam, ab290; 1:2,000) in 5% milk TBS-T occurred at 4 °C overnight. Next day, the membrane was washed in three steps in TBS-T followed by incubation with secondary antibodies conjugated with peroxidase directed against mouse (Sigma Aldrich, A9044; 1:6,000) and rabbit (Sigma Aldrich A0545; 1:5,000) at room temperature for 1 hour. Again, after three washing steps in TBS-T signals were detected by applying the Clarity™ Western ECL Substrate (1:1; Bio-Rad) and imaging with a ChemiDoc™ Touch Imaging System (Bio-Rad). Signals were then quantified utilising the Image Lab™ 5.2.1 software (Bio-Rad).

3.5.6 Western blot - antibody dilution series

The binding affinity of anti-lamin A/C antibody (1:500; Santa Cruz, sc-376248 E-1) was assessed in a Western blot of UKEi1 and p.H222P hiPSC-CM protein lysates. Therefore, protein concentrations were determined using the Qubit 3.0 Fluorometer (Thermo Fisher Scientific) according to manufacturer’s protocol. A 10% SDS-PAGE gel was loaded with increasing volume between 8 µL and 18 µL (in 2 µL steps) with the samples UKEi1 (0.264 µg/ µL) and p.H222P (0.263 µg/ µL), diluted in Laemmli as described above (3.5.5).

3.6 Immunofluorescence

3.6.1 Staining of 2D cultured CMs

For 2D immunofluorescence experiments, dissociated hiPSC-CMs were seeded as single cells (5,000 and 10,000 per well) as described previously cells on Geltrex® coated 96-well plates in 100 µL per well complete media (Prondzynski *et al.*, 2017). Every two to three days complete media was exchanged and the wells for gene replacement therapy (GT) were transduced as described in section 0 on day 15 in culture. Finally, cultured CMs were fixed with pre-cooled 4 % PFA in PBS for immunofluorescence as previously reported (Prondzynski et al., 2017). Following two washing steps in PBS, fixed hiPSC-CMs were stained in blocking solution (1X PBS [Gibco], 3% w/v milk powder [Carl Roth], 0.1% Triton X-100 [Roth 3051.3]) supplemented with primary antibodies agitating at 4 °C overnight. Next day, well were washed twice with 1X PBS and subsequently stained with secondary antibodies (Table S 5) in 50 µL blocking solution per well agitating at RT for one hour. Hoechst (1:2,000; Thermo Fisher Scientific, 33352) was added to staining solution for the last 20 minutes of the staining incubation period. Finally, wells were washed twice with PBS and stored in PBS at 4 °C until further imaging.

3.6.2 Staining of EHTs

Fixed and stored EHTs as described in section 3.4.1 were washed with 1 mL 1X PBS (Gibco) per EHT sample prior to the staining procedure. As a next step, blocking of EHTs was achieved in 500 µL blocking solution (1X PBS [Gibco], 3% w/v milk powder [Carl Roth], 0.1% Triton X-100 [Roth 3051.3]) per sample agitating at 4 °C overnight. The next day, EHT samples were washed hourly three to four times in 1x PBS (Gibco). Immunostaining occurred in 500 µL blocking solution per sample supplemented with primary antibodies of Table S 5 and Hoechst (1:2,000; Thermo Fisher Scientific, 33352). Samples incubated in solution agitating at 4 °C overnight. The following day, the washing procedure was performed as described before and EHTs were subsequently incubated in 500 µL blocking solution per sample supplemented with secondary antibodies (Table S 5) agitating at 4 °C overnight. On the final day, EHTs were washed and then mounted onto coverslips in Fluoromount-G (Southern Biotech) and analysed by confocal microscopy (Zeiss LSM 800 microscope). The images were processed with the ZEN (2012) Blue Edition software for tiff export, ImageJ for analysing particles and immunofluorescence positive areas (Fiji software) and Imaris (Bitplane) for the 3D reconstruction and length measurement of nuclei.

3.7 Omics analysis

3.7.1 Transcriptome analysis of EHTs

RNA was isolated from snap frozen EHTs as described in section 3.5.1. and 500 ng were sent for bulk RNA sequencing to Münster. The Core Facility Genomics of the Medical Faculty Münster kindly performed the following steps for bulk RNA sequencing. The integrity and quality of total RNA was assessed on Agilent Technologies 2100 Bioanalyzer (Agilent Technologies; Waldbronn, Germany). 150 ng of total RNA was purified using the NEBNext rRNA Depletion Kit (NEB E6310, New England Biolabs). The RNA Sequencing library was set up with NEBNext® Ultra™ II Directional RNA Library Prep Kit for Illumina® (New England Biolabs). The libraries were sequenced on Illumina Nextseq 2000 using NextSeq2000 P3 Reagent Kit (200 cycles, paired end run 2x 111 bp) with an average of 37.9 M reads per RNA sample. The samples were demultiplexed (bcl2fastq2) molecular barcode to fastq data and quality controlled (FastQC). Trimmomatic was used for adapter trimming and read filtering (Bolger, Lohse and Usadel, 2014). Using HISAT2, the resulting reads were aligned to the Ensembl GRCh38 reference genome (Kim, Langmead and Salzberg, 2015). The aligned reads were sorted using samtools (Li, 2011) and were subsequently counted into genes using HTSeq-Counts (Anders, Pyl and Huber, 2015). The test for differential expression were conducted with the r-package DESeq2 (Love, Huber and Anders, 2014). The gene set enrichment analysis was performed with the GSEA software, a joint project of UC San Diego and Broad Institute and the Gene Ontology gene sets c5.go.v7.4.symbols from the Broad Institute (Subramanian et al., 2005; Goswami et al., 2019).

3.7.2 Proteome analysis of EHTs

EHTs were lysed in 100 mM triethyl ammonium bicarbonate (TEAB) and 1% w/w sodium deoxycholate (SDC) buffer, and subsequently boiled at 95 °C for 5 minutes. Samples were sonicated with a probe sonicator for 6 pulses to break DNA and RNA. For proteome analysis 20 µg of protein of each sample was retrieved and disulfide bonds were reduced in the presence of 10 mM dithiothreitol (DTT) at 60 °C for 30 minutes. Cysteine residues were alkylated using 20 mM iodoacetamide at 37 °C in the dark for 30 minutes. Tryptic digestion (sequencing grade, Promega) was conducted with a protein-to-enzyme ratio of 100:1 at 37 °C overnight. Digestion was terminated and SDC precipitated by the addition of 1% v/v formic acid (FA). Subsequently, samples were centrifuged at 16,000 x g for 5 minutes and the supernatant was transferred into a new tube. Finally, samples were dried in a vacuum centrifuge.

Samples were resuspended in 0.1% FA and transferred into a full recovery autosampler vial (Waters). Chromatographic separation was performed on a nano- ultra performance liquid chromatography (UPLC) system (Dionex Ultimate 3000 UPLC system, Thermo Fisher Scientific) with a two-buffer system (buffer A: 0.1% FA in water, buffer B: 0.1% FA in ACN). For desalting a reversed phase trapping column (Acclaim PepMap 100 C18 trap; 100 µm x 2 cm, 100 Å pore size, 5 µm particle size, Waters) was attached to the UPLC. Following, a purification was performed by a reversed-phase capillary column (nanoEase M/Z peptide BEH130 C18 column; 75 µm x 25 cm, 130 Å pore size, 1.7 µm particle size, Waters). Separation of peptides was achieved with a 60 min gradient of increasing ACN concentration from 2% - 30% ACN. The peptides that were eluted were analysed on a quadrupole orbitrap ion trap tribrid mass spectrometer (Fusion, Thermo Fisher Scientific) in data-dependent acquisition (DDA) mode. The fusion was operated at top speed mode with the most intense ions per precursor scan (2x105 ions, 120,000 Resolution, 120 milli seconds fill time) within 3 seconds and MS/MS in the ion trap (HCD at 30 normalised collision energy, 1x104 ions, 60 milli seconds fill time) was analysed in a range of 400 – 1300 m/z. A dynamic precursor exclusion of 20 seconds was used.

Acquired DDA LC-MS/MS data was analysed making use of the reviewed human protein database downloaded from Uniprot (release April 2020, 20,365 protein entries) and all lamin A and C proteolytic and splice variants derived from search engine algorithm (Sequest) integrated in the Proteome Discoverer software version 2.4. Label-free quantification mode with match between runs and performing chromatographic retention re-calibration for precursors with a 5-minute retention time tolerance enabled no scaling, and no normalisation for extracted peptide areas. Mass tolerances for precursors was set to 10 ppm and 0.6 Da for fragments. Carbamidomethylation was set as a fixed modification for cysteine residues and the oxidation of methionine, pyro-glutamate formation at glutamine residues at the peptide N-terminus, acetylation of the protein N-terminus, methionine loss at the protein N-terminus and the acetylation after methionine loss at the protein N-terminus were allowed as variable modifications. Only peptides with a high confidence (false discovery rate < 1% using a decoy data base approach) were taken into consideration. Peptide areas were summed to protein areas and used for quantitative analysis. Protein areas were imported into Perseus software version 1.5.8 for statistical analysis.

3.8 Adeno-associated virus production and purification

The cloning and the production of adeno-associated virus (AAV) particles were kindly performed by Dr. Ingke Braren at the HEXT vector facility at the UKE Hamburg. AAV vector particles were produced as recently published with some adaptions (Saleem et al., 2020). For the construct, GFP and lamin A (*LMNA*) cDNA were linked via a 2A peptide and ligated into pFBGR under control of a Cytomegalovirus (*CMV*) enhanced promoter by InFusion cloning. Therefore, two PCRs were performed using PrimeStar GLX Polymerase (Clontech). In the first PCR, *GFP* was amplified from pCW57-GFP-2A-MCS (Addgene Plasmid #71783) using the primers 5´-GTCAGATCCGCTAGCGCTaccATGGTGAGCAAGGGC and 5´-gtctccatGCTAGCcggTGCag. In the second PCR, *LMNA* was amplified from PA-mCherry1-LaminA-C-18 (Addgene, plasmid #57185) using the primers 5´- gGCTAGCatggagaccccgtccc and 5´- tatagggcgaattgggtaccttacatgatgctgcagttctggggg. The pFBGR-Ultra CMVenh-GFP plasmid was cut with AfeI and KpnI and both PCR products were inserted simultaneously using the InFusion HD Cloning Kit (Takara Clontech) according to the recommendations of the manufacturer to generate the AAV transfer plasmid pFBGR CMVenh GFP-2A-LMNA. Final AAV transfer plasmids were confirmed by restriction digest, by PCR using the specific primers mentioned above and by sequencing.

3.9 Data analysis

Visualisation in graphs and statistical analysis of the data was carried out in GraphPad Prism software 8.3.0. Gene ontology enrichment analysis was performed with String database version 11.5 (Szklarczyk *et al.*, 2021).

4 Results

4.1 Generation and characterisation of p.H222P derived isogenic cell lines for establishing the disease model

A hiPSC line and corresponding isogenic control and knockout lines were generated to model human laminopathy *in vitro*. These lines underwent quality controls and served as a basis for subsequent disease modelling experiments.

4.1.1 Validation of a patient-derived hiPSC line

Fibroblasts from a male patient with a clinically overt EDMD and cardiac arrhythmia were reprogrammed by the HEXT stem cell core facility at the UKE Hamburg. The patient carried a heterozygous missense mutation c.665A>C (rs58034145) resulting in the change in amino acid 222 from histidine to proline (p.H222P). The mutation is located in exon 4, within the linker domain L12 between the two rod domains 1B and 2A (Figure 9). The successfully reprogrammed clone p.H222P sv1122 was chosen to validate the mutation p.H222P. Therefore, gDNA was isolated from hiPSCs, and the region of interest (ROI) was analysed by PCR and subsequent Sanger sequencing (Figure 9).

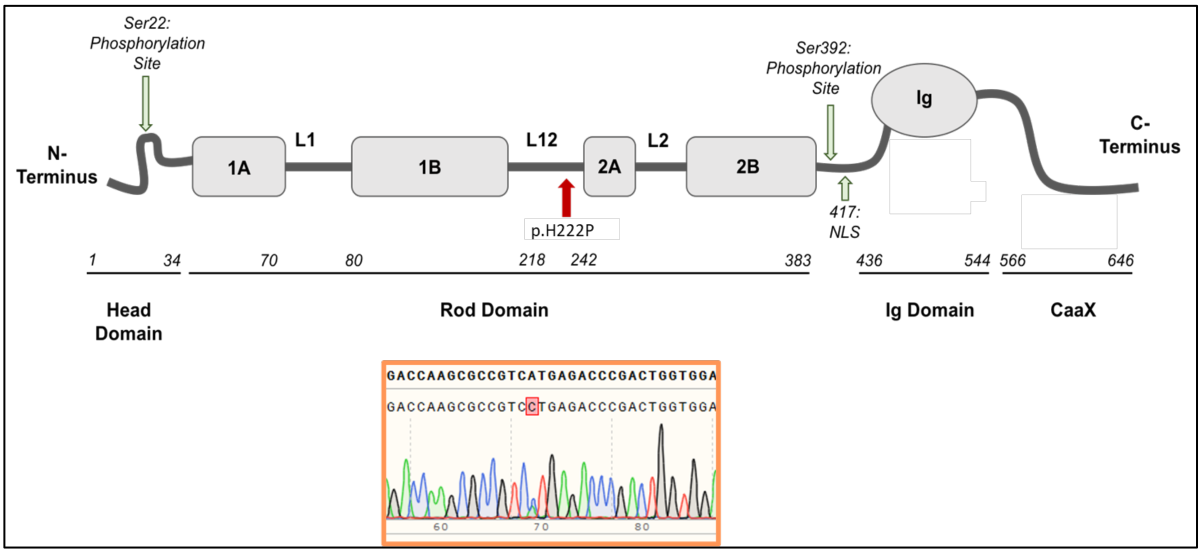

Figure 9 Schematic overview of Lamin A/C domain organisation, phosphorylation sites and localisation of the patient-derived missense mutation p.H222P. Isolated gDNA of patient-derived hiPSC was PCR amplified and the resulting DNA fragment was sequenced by Sanger sequencing. Alignment was performed with SnapGene. The orange box shows part of the sequence with the heterozygous mutation A>C at position 69 of the sequencing trace.

A single nucleotide polymorphism (SNP), rs4641, that results in a C>T transition, was detected at heterozygous state in the p.H222P hiPSC line by PCR amplification of a 3,181-base pair (bp) containing region and subsequent Sanger sequencing (Figure 10 A and B). To further discriminate on which allele the SNP was located, the purified PCR product was ligated into a blunt plasmid, and *E. coli* were transformed to analyse single plasmids. For example, the mutation p.H222P and SNP rs4641 were detected in clone 10 (Figure 10 C and D) verifying the localisation of the mutation and the SNP on the same allele.

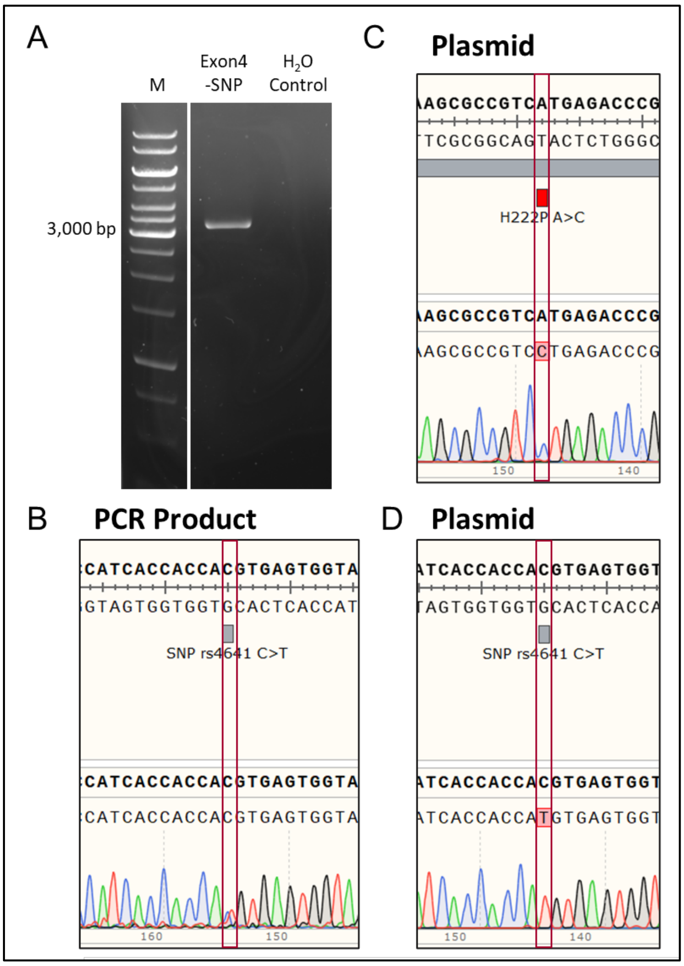

Figure 10 Allelic discrimination of SNP rs4641 and p.H222P mutation. **A** PCR product of a region spanning from exon 4 to exon 10 on gDNA isolated from p.H222P hiPSCs and a negative H_2O control loaded onto a 1% agarose gel. Expected size of the PCR product was 3,181 bp (M= marker; DNA 1 kb ladder ([Generuler]). **B** Sanger sequencing of a PCR product around the SNP rs4641 (C>T transition). **C** Sanger sequencing of clone 10 carrying the PCR product ligated into a plasmid around the region of the p.H222P mutation (A>C transversion). **D** Sanger sequencing of clone 10 carrying the PCR product ligated into a plasmid around the region of the SNP rs4641 (C>T transition). Alignment was performed in SnapGene.

4.1.2 Generation of an isogenic control cell line (IsoC)

In order to generate an isogenic control cell line, the mutation in the patient cell line p.H222P was corrected by protein based CRISPR/Cas9 gene editing. In total, five experiments were performed until a corrected clone was received (Figure 11). In detail, in the first experiment (run I) 32% of clones remained unedited, whereas the majority of 59% clones showed CRISPR/Cas9 activity with insertions or deletions (Indels) resulting in a shift in Sanger sequencing reads. This first experimental design achieved 10% of homology-directed repair (HDR), but on the wrong allele. This can be seen by the insertion of a silent PAM mutation to prevent the Cas9 of further cutting activity (Figure 11). In a second experimental setup (run II), using a new lot of Cas9 and a newly designed gRNA (gRNA 2), no Cas9 activity was observed, as all clones remained unedited. For run III, two reactions were set up using either gRNA1 or 2, a new lot of Cas9 and a higher concentration of ssODN. This resulted in a Cas9 activity of less than 50% of the clones, and if HDR occurred, then on the wrong, wild-type (WT) allele. As a consequence, a third gRNA (gRNA 3) was designed, which was used for the run IV. This run resulted in the highest Cas9 activity of 86% so far, but not in HDR that is required for correction.

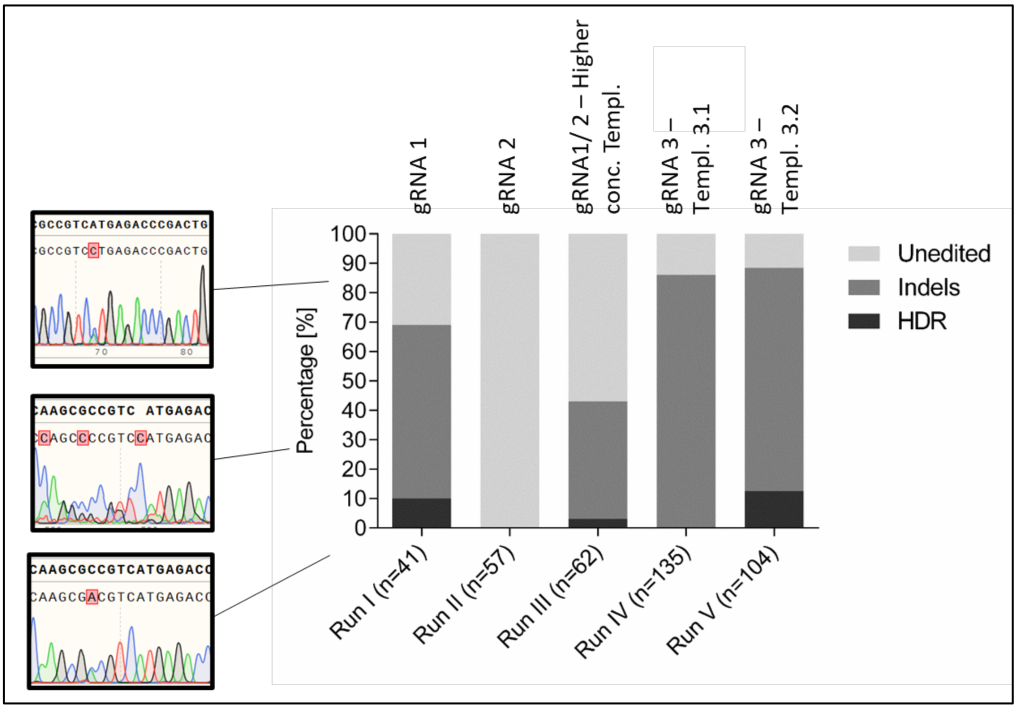

Figure 11 Summary of CRISPR/Cas9 gene editing runs (I to V) showing the different strategies and number of analysed clones indicated in brackets (x-axis), which resulted in either unedited sequences, insertion or deletions mutations (Indels) and homology directed repair (HDR). The clonal outcome of each CRISPR run is expressed in % (y-axis). Example sequence traces of unedited (top), Indels (middle) and HDR (bottom) are shown on the left.

Sequencing of clone #1 of run IV revealed the disappearance of the mutation (Figure 12 B; A>C; red box), indicating a putative correction of the mutation. However, the silent PAM mutation was missing. A PCR around the known heterozygous SNP and the mutation was performed, and its subsequent sequencing disclosed the disappearance of the SNP too (Figure 12, A green primers, C green box). Nonetheless, a PCR solely covering the SNP region still validated the presence of the SNP (Figure 12, A blue primers, D blue box), implying that only one allele was amplified in the larger fragment (green primers).

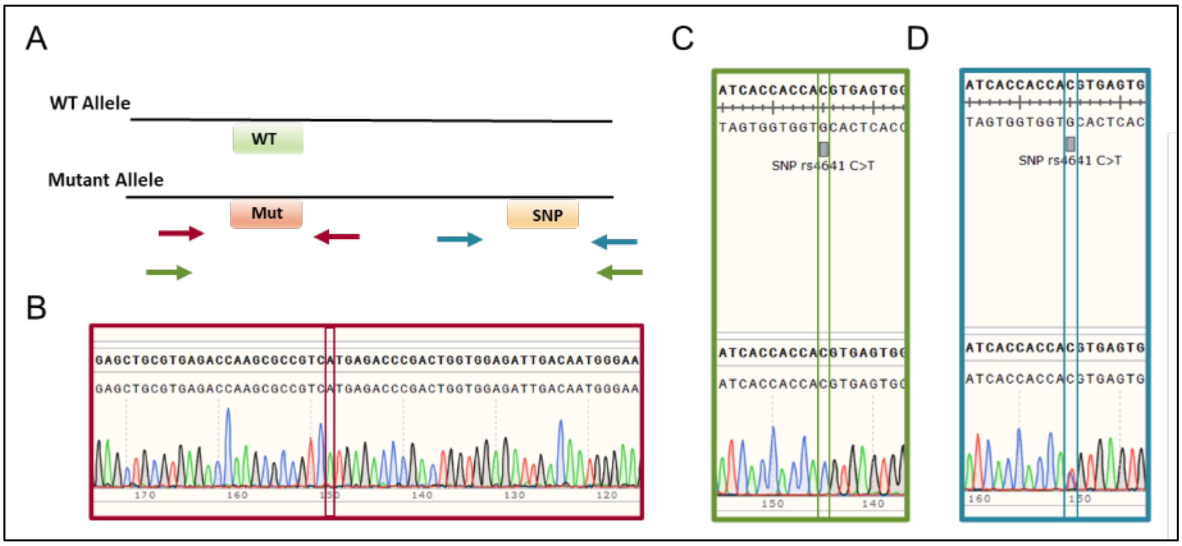

Figure 12 **A** Schematic overview of the wild-type (WT) and mutant allele (Mut), carrying a single nucleotide polymorphism (SNP). **B** When amplifying the sequence around the mutation (Mut; red arrows indicate primers), sequencing results showed homozygous WT sequence (red box). **C** Amplification of the sequence including Mut and SNP (green arrows indicate primers) and sequencing the SNP region (green box). **D** Amplification of the sequence around the region of the SNP (blue arrows indicate primers) and sequencing of the SNP region (blue box).

A long-range PCR was conducted spanning from intron 2 to intron 5, thus covering over 2,201 bp, on gDNA lysate of clone #1 and of unedited cells (UE) as shown in Figure 13. Subsequently, the PCR products were analysed on an agarose gel, whereby the product of clone #1 showed an equal distribution between two bands, one below and one above 2,000 bp. In contrast, the UE derived product showed a prominent band of over 2,000 bp (Figure 13). The results indicate that the gene editing had led to the deletion of a large fragment containing the original mutation on one of the alleles, a known on-target artefact of CRISPR/Cas 9 gene editing (Kosicki, Tomberg and Bradley, 2018).

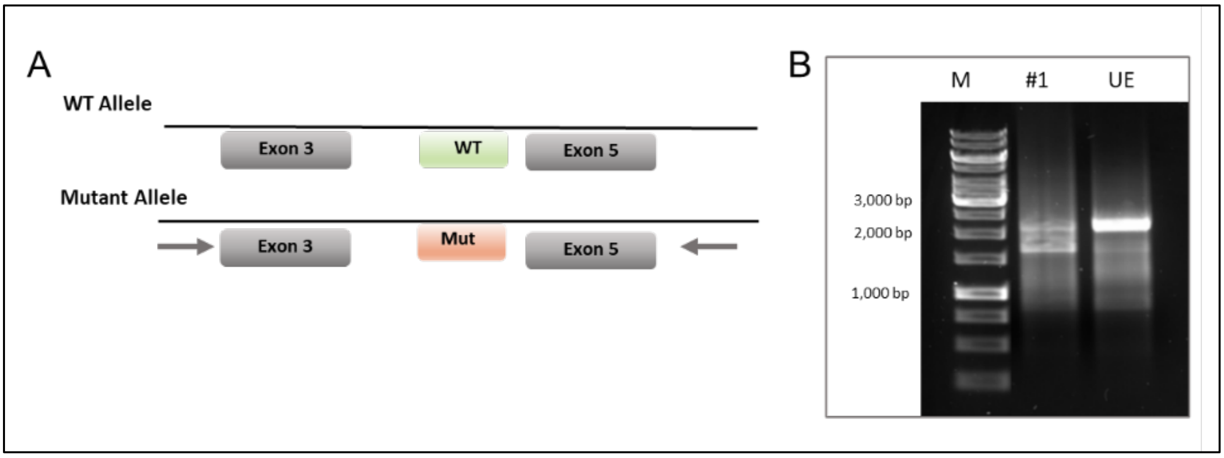

Figure 13 **A** Schematic overview of the amplified region that covers intron 2 to 5 on *LMNA* gDNA of wild-type (WT) and mutated allele. **B** Long-range PCR product of ROI with an expected size of 2,201 bp on gDNA lysate from CRISPR clone Run IV #1 and gDNA of unedited cells (UE) loaded on 1% agarose gel and M= marker: 1kb DNA ladder (Generuler).

For the final CRISPR run (V), the corresponding ssODN for gRNA3 as the repair template was redesigned. In the first set up, the ssODN (template 1) corresponding to gRNA1 was longer in nucleotides and was successfully incorporated. Thus, an *in silico* analysis to predict the folding of the template 3.1 showed a high probability (over 90%) for a hairpin structure around the ROI (red circle; Figure 14 A). The new template 3.2 was designed based on the length of template 1, which resulted in a slightly lower probability for hairpin structure around ROI (red circle; Figure 14 A). The CRISPR run V resulted in an 88.5% Cas9 cutting activity, since 76% of the clones carried indels mutations and 12.5% of the clones showed HDR (Figure 11). In total, 13 clones of run V carried the silent PAM mutation A>C (blue box; Figure 14 B) and showed an absence of the p.H222P mutation (c.665A>C; red box; Figure 14 B) as shown in the sequence trace of IsoC (Figure 14 B).

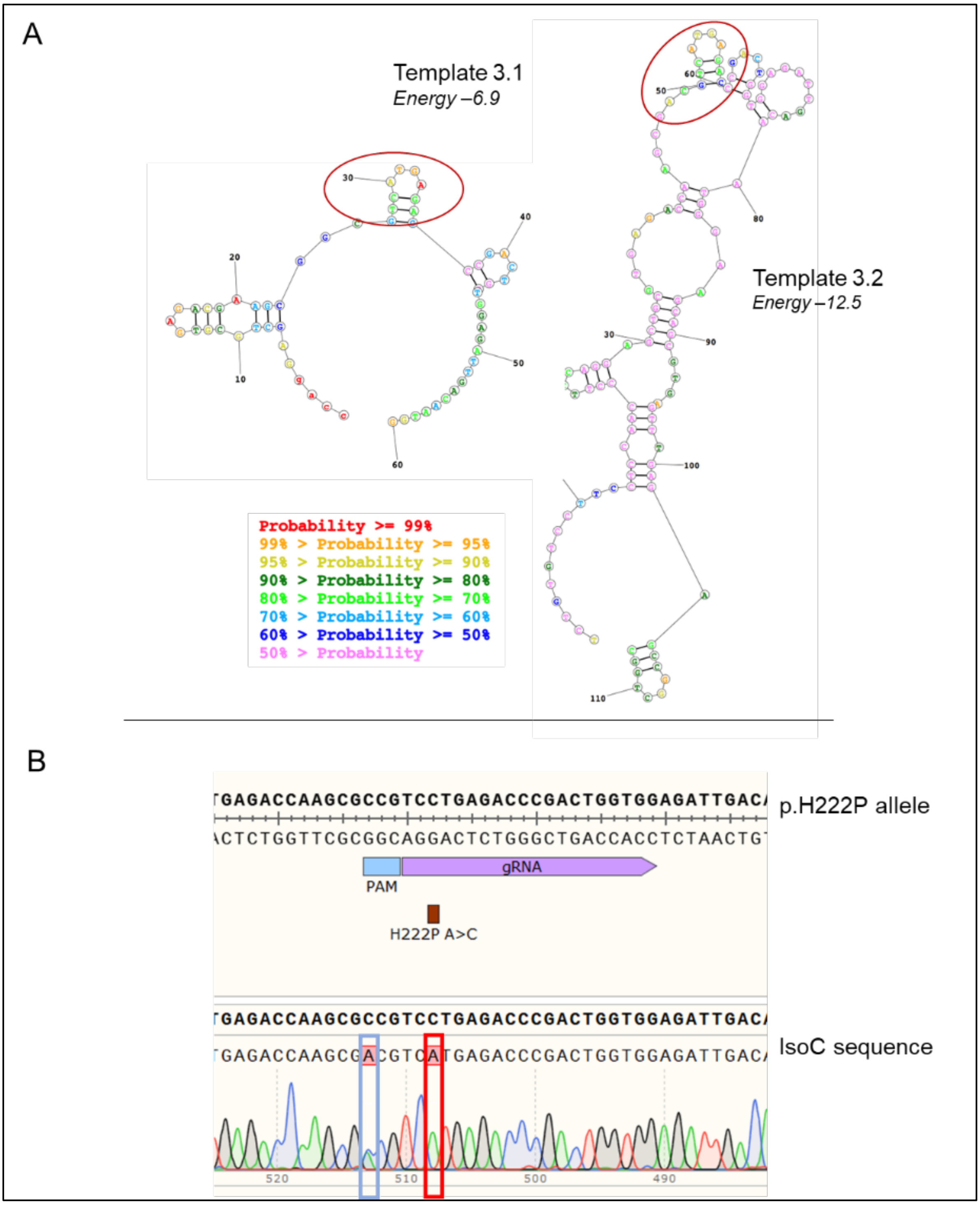

Figure 14 **A** The single stranded oligonucleotides (ssODNs) 3.1 and 3.2 that were used as repair templates for gRNA 3 in CRISPR run IV and V, respectively. *In silico* prediction of enthalpy (energy) and probability for secondary folding of ssODNs. Colour coding indicates the folding probability for the single nucleotides. Red circles mark the region of the ssODN containing the silent PAM mutation and the nucleotide required for correction of the p.H222P mutation. **B** IsoC sequencing trace aligned to P.H222P allele sequence and gRNA 3 showing the correction from A>C to C>A (red box) and the silent PAM mutation C>A (blue box).

4.1.3 Generation of an isogenic homozygous *LMNA*-knockout cell line

After CRISPR/Cas9-mediated gene editing of the p.H222P hiPSC line, a clone #139 of run V was analysed by Sanger sequencing and showed a homozygous T insertion (c.666_667insT) downstream of the heterozygous mutation (c.665A>C; Figure 15). As a consequence of the T insertion, the codon for glutamic acid (position 223) changed to a premature stop codon (*TGA*; Figure 15). The premature stop codon was located in exon 4, which is present in the two isoforms lamin A and C and thus expected to similarly affect both lamins. The clone #139 is hereafter called LMNA-KO.

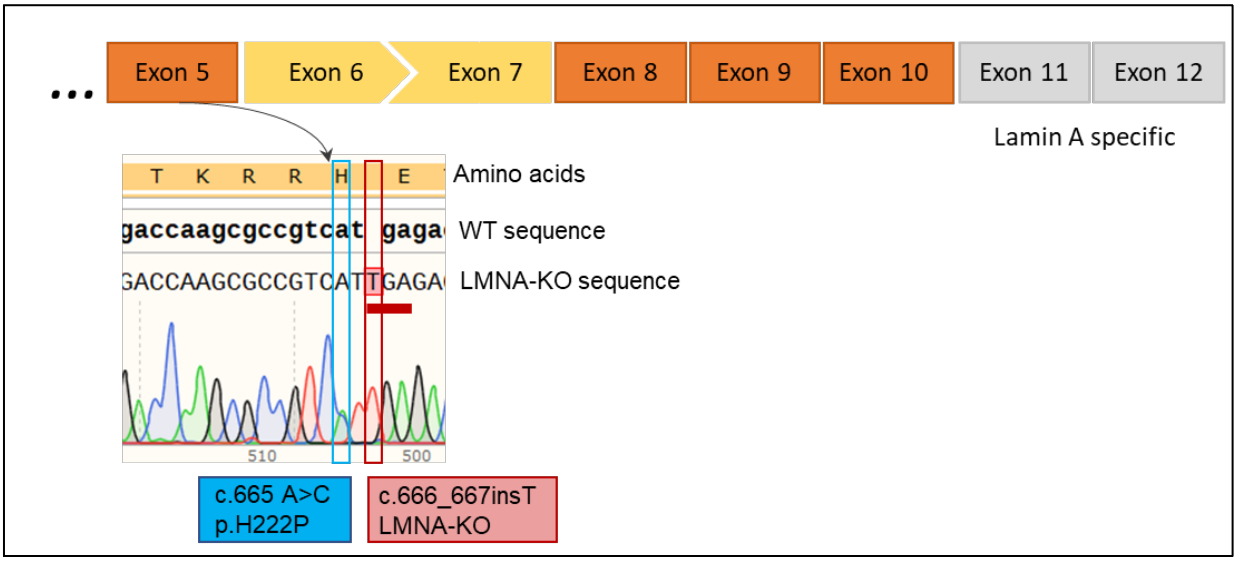

Figure 15 CRISPR/Cas9-mediated genome editing in hiPSC p.H222P resulted, besides others, in clone #139 (LMNA-KO), which was heterozygous for mutation c.665A>C (blue box) and 2 bases downstream of this mutation homozygous for a T insertion (c.666_667insT) in exon 4, and thus present in lamin A and C. The homozygous T insertion results in a premature stop codon (*TGA* underlined in red).

4.1.4 Purity of hiPSC clones

The underlying mutation c.665A>C of p.H222P induces a disruption of a BspHI restriction site, allowing the analysis of the purity and success of gene editing of hiPSC clones. Reverse transcribed mRNA was amplified for the region of lamin A (1,493 bp) and C (1,416 bp). Nonsense-mediated mRNA decay (NMD) is known to cause degradation of transcripts carrying a nonsense mutation (Vignier *et al.*, 2009; Kato *et al.*, 2020). No PCR product for lamin A mRNA was detectable in the LMNA-KO sample (not shown), indicating that the NMD indeed resulted in complete degradation of the lamin A transcript in LMNA-KO. However, a faint band was detected for lamin C in the LMNA-KO sample (Figure 16). All PCR products were purified and digested with BspHI, which should result in the case of complete digestion in two fragments of lamin A (286 bp and 1,207 bp) and lamin C (286 bp and 1,130 bp). Agarose gel electrophoresis showed complete digestion in case of IsoC and, thus verified the expected loss of the c.665A>C mutation and the presence of the respective restriction site. This result demonstrated the successful gene editing and purity of the clone (Figure 16). In contrast, in the p.H222P line three bands were detected, corresponding to the mentioned two digested fragments for lamin A and C of the WT allele and the full-length p.H222P amplicon (Figure 16). In LMNA-KO no cleaved PCR product was detected for lamin C, but a faint full-length band (Figure 16). The identity of the latter is unknown.

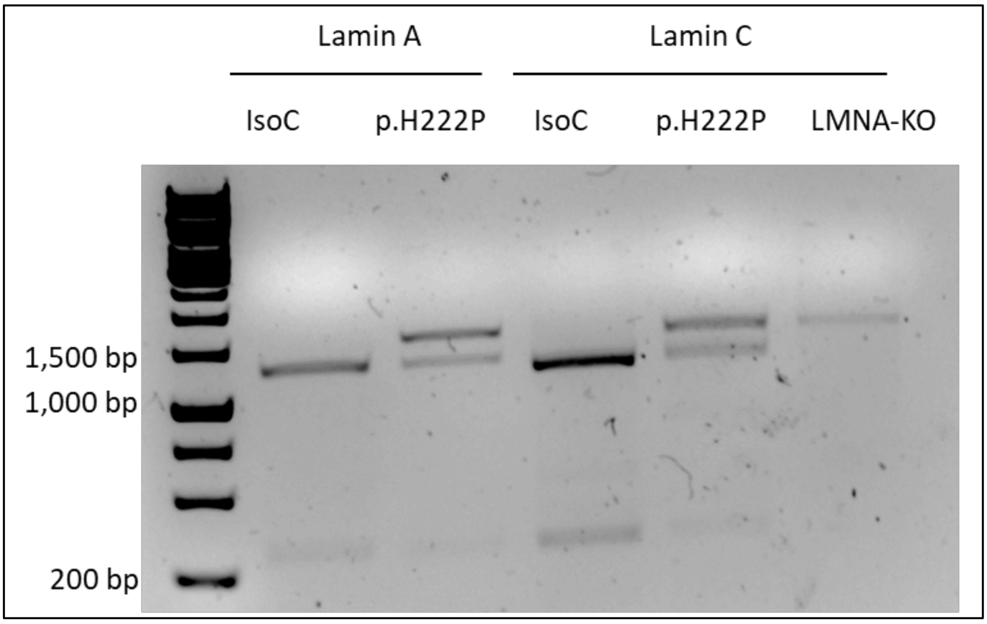

Figure 16 Reverse transcribed mRNA and PCR products of lamin A (1,493 bp) and C (1,416 bp) from the patient cell line p.H222P and its subclones, control IsoC and knockout LMNA-KO, digested with BspHI. Digestion with BspHI should result in two fragments of lamin A (286 bp and 1,207 bp) and lamin C (286 bp and 1,130 bp) if the p.H222P mutation c.665 A>C is not present and thus is not disrupting the restriction site.

4.1.5 Quality control of hiPSC

Given the propensity of fast proliferating hiPSC lines to easily change characteristics such as pluripotency or chromosome integrity, master and working cell banks were collected and characterised. As part of the quality control, all three hiPSC lines were analysed for marker of stemness and pluripotency. Therefore, hiPSCs were passaged and stained either for the surface marker *stage-specific embryonic antigen 3* (SSEA-3) or an isotypic control antibody for human recombinant engineered antibodies (REA). Subsequent flow cytometry analysis with gates, which were set according to the control antibody, verified a high level of pluripotency for all hiPSC lines. For example, SSEA-3 positivity was above 94% (Figure 17).

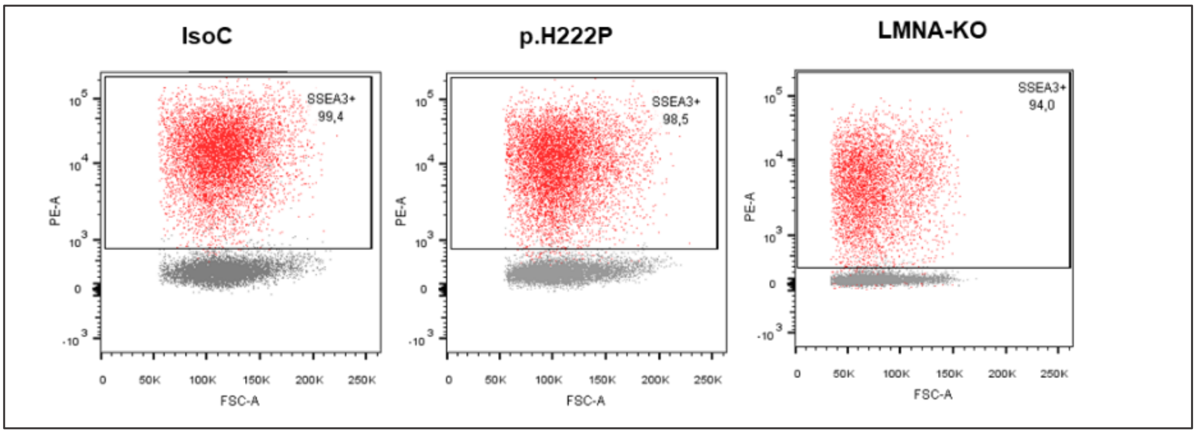

Figure 17 Representative plots of flow cytometry analysis of the three hiPSC lines, IsoC (left), p.H222P (middle) and LMNA-KO (right) stained for the stemness marker SSEA3, positive cells depicted in red. Populations were distinguished by the area of the forward scatter (FSC-A; x-axis) and the area of the antibody dye phycoerythrin (PE-A; y-axis)

As a second quality control, hiPSCs were subjected to a differentiation protocol that is expected to give rise to all three germ layers. Samples were analysed for the pluripotency marker *NANOG* and *SOX2,* the ectodermal marker *NCAM1* and *PAX16,* and the endodermal marker *SOX17* on mRNA level via RT-qPCR. HiPSCs of all three lines were strongly and almost exclusively positive for *NANOG*, however, expression of *SOX2* was strongest in the ectodermal samples (Figure 18 A and B). Ectodermal and endodermal marker confirmed the success of the capability of hiPSCs to commit the two fates (Figure 18 C - E). Mesodermal induction was demonstrated in the following experiments of direct-cardiac differentiation (section 3.3.1).

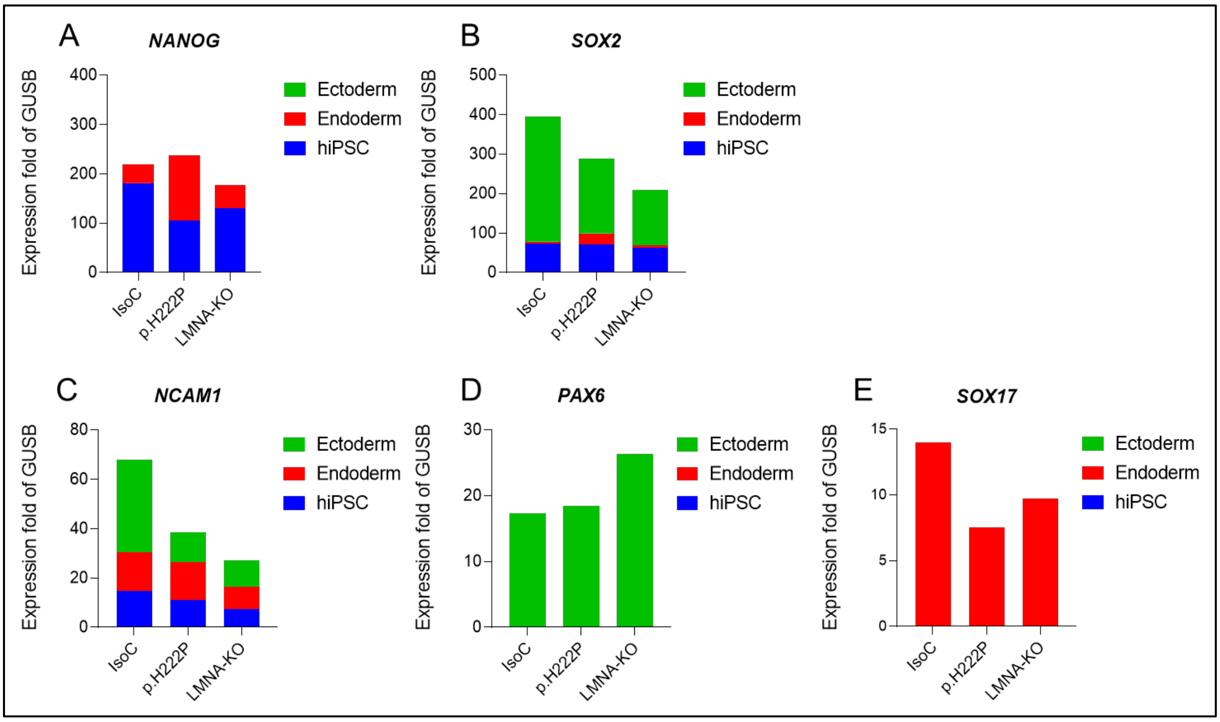

Figure 18 Expression analysis of the three cell lines, p.H222P, IsoC and LMNA-KO (x-axis) for the pluripotency marker **A-B** *NANOG* and *SOX2,* **C-D** ectodermal marker *NCAM1* and *PAX6* and **E** the endodermal marker *SOX17* in hiPSC (blue), endodermal (red) and ectodermal state (green) normalised to the housekeeping gene *GUSB* via qPCR (y-axis).

As a third quality control, gDNA of each clone was isolated and analysed for karyotype integrity by the Nanostring Core Facility of the UKE. This assay determines copy numbers of several regions per chromosome and showed consistently two copies, verifying chromosomal integrity for each clone (Figure 19). The single-copy results for X- and Y-chromosome genes (right side) verified the male sex of the proband (Figure 19).

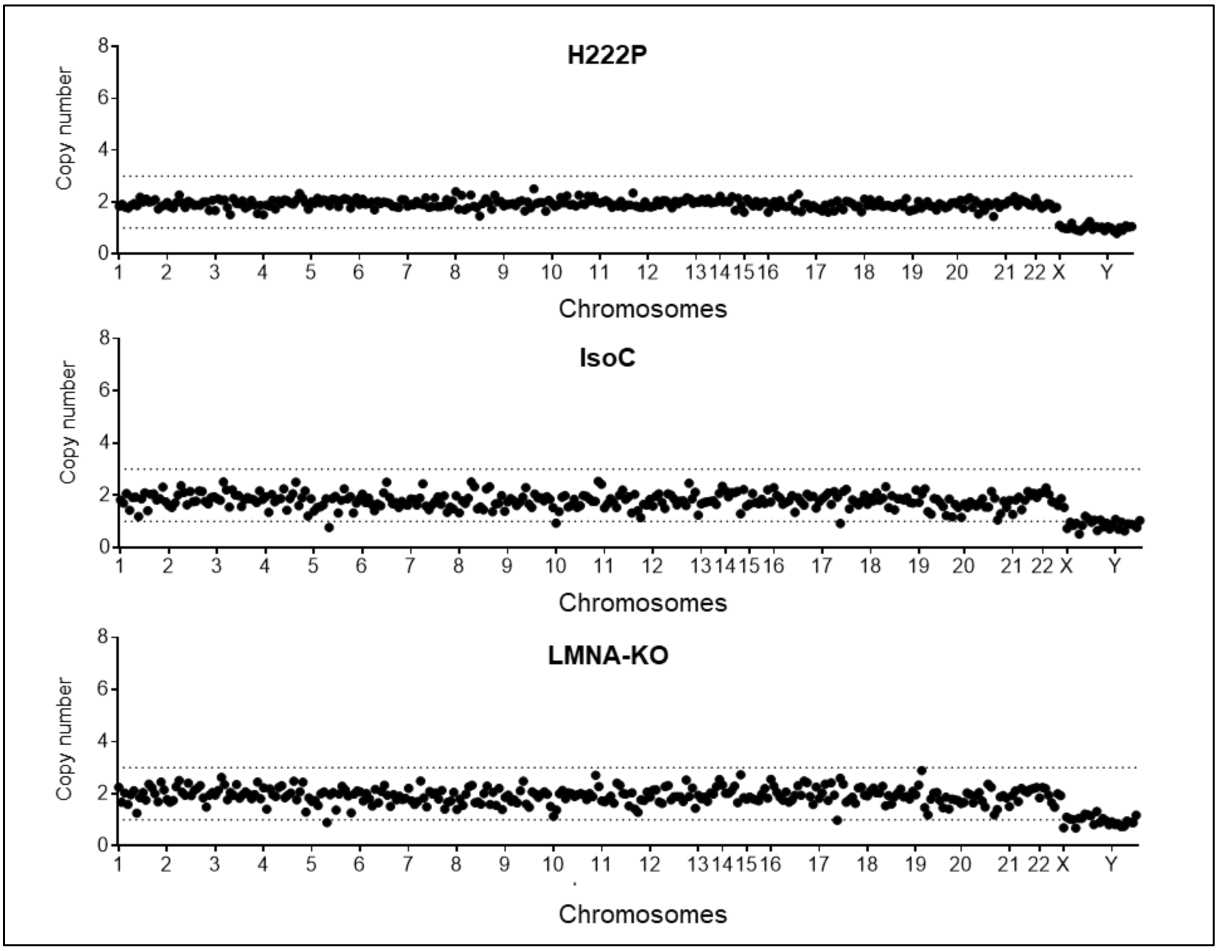

Figure 19 Assessment of karyotype integrity via Nanostring Technology by analysing copy numbers (y-axis) per chromosome (x-axis) of the original clone p.H222P sv1122 and the derived CRISPR/Cas9 gene-edited clones IsoC and LMNA-KO.

4.2 Cardiac differentiation

4.2.1 Cardiac differentiation efficiencies

In order to cast EHTs, hiPSCs of the different cell lines were expanded and subsequently differentiated either by a 2D monolayer or a 3D EB-based protocol. CMs were dissociated and permeabilised, stained for cardiac troponin T (cTnT) and subsequently analysed via flow cytometry in order to assess the purity of the cell populations. IsoC differentiation runs resulted in a mean of 66% (n= 21), p.H222P of 47% (n= 30) and LMNA-KO of 87% (n= 6) cTnT positive populations (Figure 20 A). A large scatter of differentiation efficiency was noted particularly in p.H222P. The yield of each differentiation run was calculated by dividing the output number of CMs with the input number of hiPSCs seeded. The 2D monolayer differentiation resulted in a higher yield than the 3D EB-based approach for p.H222P and

IsoC (Figure 20 B). For LMNA-KO only 2D monolayer differentiations were performed since all cells were lost in EB formation step in an initial 3D EB-based experiment.

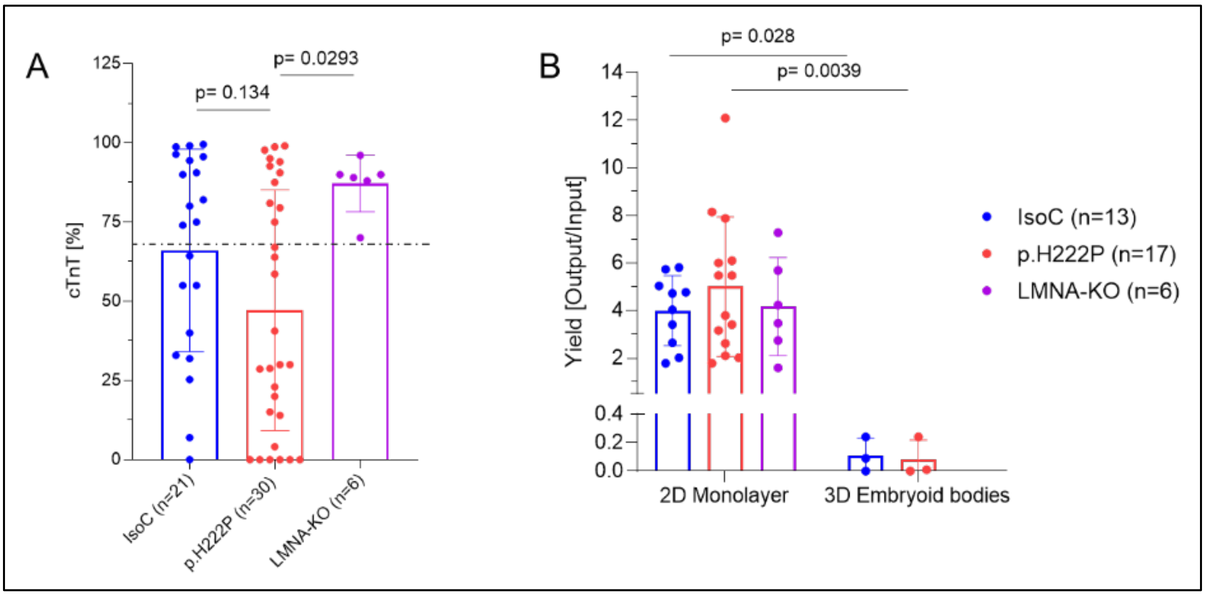

Figure 20 **A** Flow cytometry analysis of cTnT (y-axis) of each cardiac differentiation run (each dot one batch) per cell line IsoC, p.H222P and LMNA-KO (x-axis; one-way ANOVA). **B** Yield (y-axis; number of cell output divided with number of cell input) of each differentiation run grouped by cell lines IsoC, p.H222P and LMNA-KO and differentiation method, either 2D monolayer protocol or 3D EB-based (x-axis; 2-way ANOVA Sidak's multiple comparison test). n= number of differentiation runs.

4.2.2 Differentiation optimisation

To address the varying differentiation success, particularly for p.H222P, differentiation conditions were optimised. Initial seeding density was lowered, concentrations of activin A or BMP4 were doubled and stage 1 prolonged. Interestingly, in this test run, the regular differentiation conditions were the most suitable ones for p.H222P since CM population was above 90% and lower in the other conditions (Figure 21). In contrast, IsoC showed high cardiac differentiation efficiency under all, but one conditions, a prolongation of stage 1 in combination with unmodified media conditions (Figure 21). The data indicate more stable differentiation efficiency in IsoC than in p.H222P.

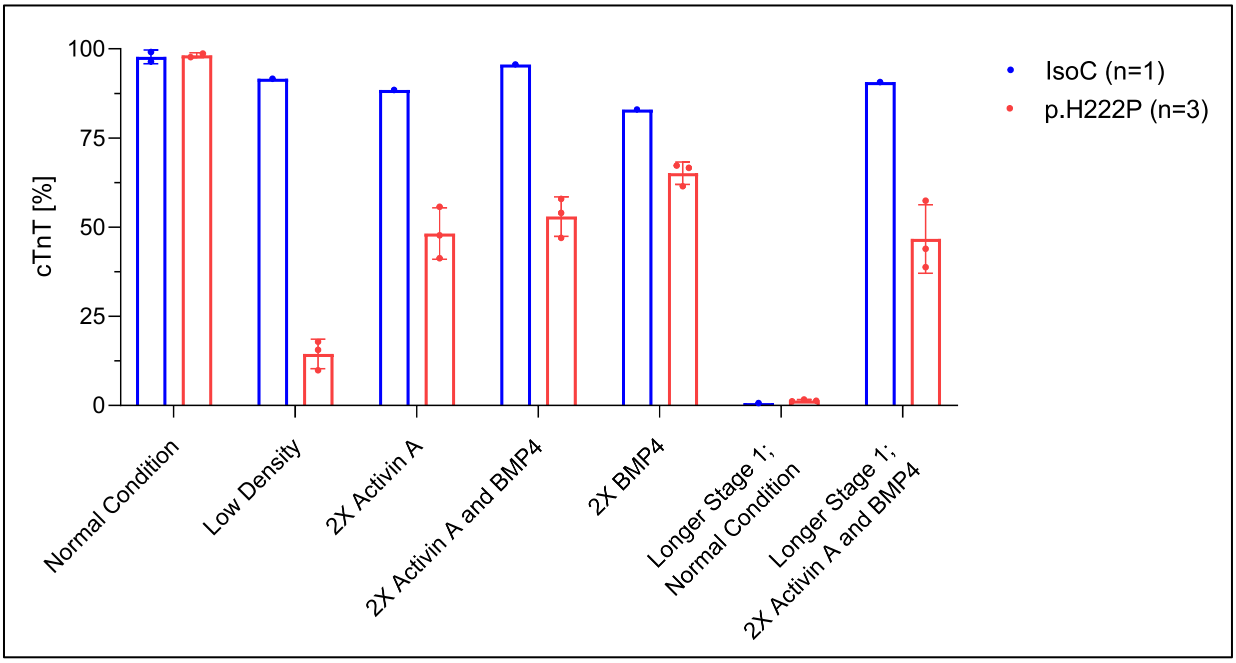

Figure 21 Optimisation of cardiac differentiation conditions by testing different activin A and BMP4 concentrations, as well as a lower seeding density or longer stage 1 (x-axis) in IsoC (n= 1 sample/ N= 1 batch) and p.H222P (n=3 samples/ 1 batch) and the corresponding positivity of cTnT (y-axis) via flow cytometry.

4.3 Characterisation of the patient-derived p.H222P heterozygous model

The central aim of the project was to investigate the mechanisms by which the p.H222P mutation in *LMNA* lead to a cardiomyopathy phenotype. Therefore, hiPSC-CMs of p.H222P and its corresponding IsoC were analysed in the EHT format that allows in-depth functional assessment under defined conditions.

4.3.1 Evaluation of the functional phenotype in EHTs

4.3.1.1 Contraction parameters under baseline conditions

EHTs were generated from differentiated CMs with a purity of at least 70% cTnT-positive cells, to investigate the role of mutated A-type lamins on the functional level. Force development and the kinetics of the EHTs were tracked over time via video-optical recordings in culture medium. Overall, different parameters of 7 independent batches of p.H222P and 5 of IsoC EHTs were compared on their final day of culture (up to 7 weeks; Figure 22). The parameters differed between the batches, of which single EHTs are represented by dots and batches by the colour-coding (Figure 22). For example, the turquoise batch of IsoC and the two beige-coloured batches of p.H222P appear to be outlier batches in terms of force and contraction velocity (Figure 22 A and C). A correlation of the cTnT and force on their final day of culture (Figure S 8) shows that the turquoise batch might indeed be an outlier. The two beige coloured batches of p.H222P appear to be outliers in terms of frequency, too (Figure 22 D). On the final day of culture, p.H222P EHTs showed a tendency towards lower force of contraction, lower contraction and relaxation velocity and shorter time to peak ($TTP_{80\%}$) than IsoC EHTs, but the differences did not reach statistical significance (Figure 22 A-C, F). Beating frequencies of p.H222P EHTs were significantly different and almost two-fold higher than of IsoC (mean 43 vs. 25 BPM; Figure 22 D). In addition, the relaxation time was significantly shorter in p.H222P than in IsoC EHTs (Figure 22 E).

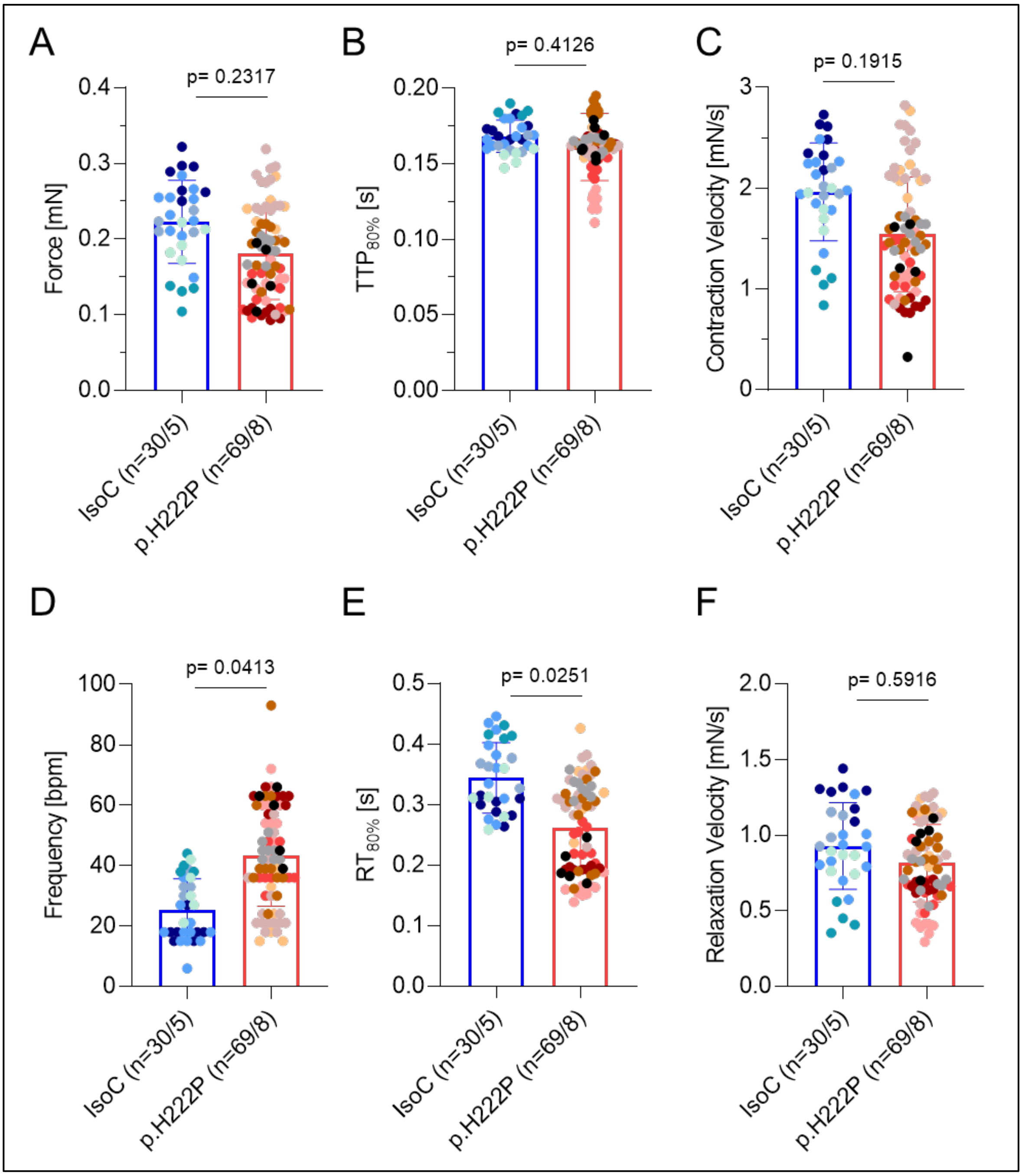

Figure 22 Functional parameters, including relaxation time (RT) and time to peak (TTP) of patient-derived p.H222P and corresponding IsoC EHTs measured under baseline conditions on last day of culture (up to 7 weeks). Each dot represents a single EHT (n=31, n=64 for IsoC and p.H222P) and each dot colour one batch (n=5, n=7 for IsoC and p.H222P). P-values were calculated by nested t-test.

The shorter relaxation time has to be interpreted with caution since relaxation time is frequency-dependent with lower values at higher frequencies. Pearson correlation confirmed the frequency dependency for the p.H222P samples (Figure 23), but not for IsoC, underlining a definite shorter relaxation time in p.H222P. Taken together, the contractile function of p.H222P EHTs showed overall a large scatter with no major statistically significant differences to IsoC under baseline conditions.

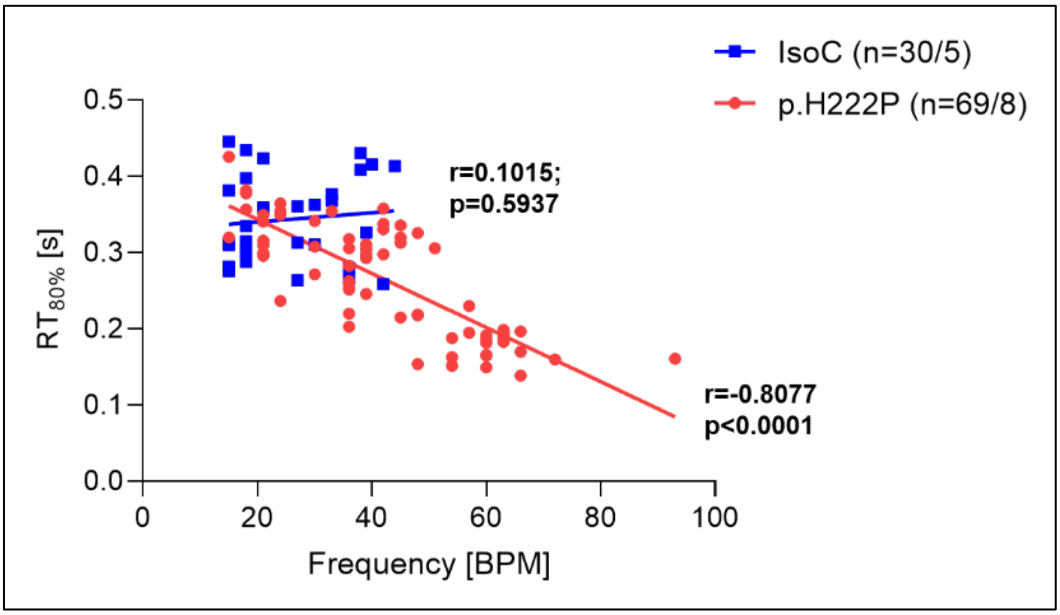

Figure 23 Pearson correlation of relaxation time ($RT_{80\%}$; y-axis) and frequency (BPM; x-axis) in IsoC and p.H222P EHTs under baseline conditions. **A** Correlation with all measured EHTs and thus larger ranges of frequencies. n= number of EHTs/ number of batches.

4.3.1.2 Average contraction peaks of paced EHTs

Two batches of p.H222P and IsoC EHTs were electrically paced in order to analyse whether the higher mean of spontaneous beating frequency caused the shorter relaxation time ($RT_{80\%}$) in p.H222P EHTs. Average contraction peaks were normalised to its maximum force and the mean of EHTs are shown in an overlay per batch (Figure 24 A and B). In one differentiation batch, EHTs were paced at 1.5 Hz and still, the relaxation time of p.H222P EHTs was shorter (mean 0.210 seconds; Figure 24 A) than of IsoC (mean 0.291 seconds; Figure 24 A). In a second batch EHTs were paced at 1.5 Hz and this time p.H222P (mean 0.185 seconds; Figure 24 B) did not differ in relaxation time from IsoC EHTs (mean 0.187 seconds; Figure 24 B). IsoC EHTs showed a higher variation in relaxation time per batch, which is demonstrated by the colour-coding and error bars (Figure 24 C). The relaxation time in p.H222P EHTs was not significantly shorter according to a nested t-test (Figure 24 C), however, more biological replicates are required to draw firm conclusions.

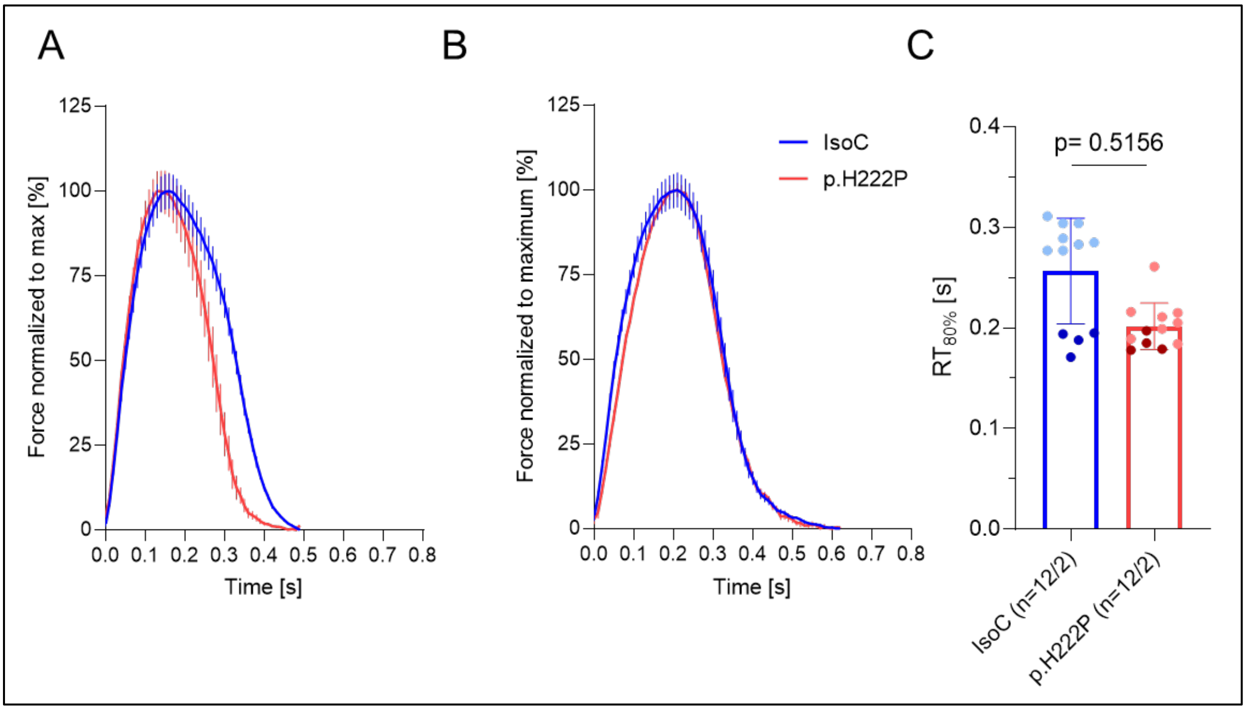

Figure 24 **A** Average normalised contraction peaks of IsoC (blue) and p.H222P (red) derived EHTs in 1.8 mM Ca^{2+} DMEM F12. EHTs were electrically paced at 1.5 Hz. n= 7-8 EHTs / N= 1 batch. **B** Average normalised contraction peaks of IsoC (blue) and p.H222P (red) derived EHTs in 1.8 mM Ca^{2+} DMEM F12. EHTs were electrically paced at 1.5 Hz. Error bars represent standard error mean (SEM). n= 3-4 EHTs / n= 1 batch. **C** Relaxation time ($RT_{80\%}$; y-axis) of IsoC and p.H222P EHTs from two different batches. Two batches electrically paced at 1.5 Hz (x-axis). Error bars represent standard deviation (SD).

4.3.1.3 Drug testing to provoke a disease phenotype

To test the hypothesis that contractile abnormalities may be more pronounced under conditions that reduce repolarisation reserve, EHTs were exposed to two drugs that inhibit repolarising potassium currents and stimulate calcium influx, respectively, 4-aminopyridine (4-AP), a selective blocker of voltage-gated potassium channels, and Bay K8644, a calcium channel agonist. Their effects on the contraction kinetics were assessed, given the previously observed shorter relaxation time in p.H222P EHTs (Figure 22 E and Figure 24). Therefore, 8 EHTs from one differentiation batch per group were washed and incubated in serum-free based medium with 1.8 mM calcium. Average absolute peaks of EHTs were measured under baseline conditions and their overlay showed a lower peak force and a shorter relaxation time in p.H222P EHTs than in IsoC (Figure 25 A). Normalisation of average peaks illustrated the shorter relaxation time of spontaneously beating p.H222P EHTs better (Figure 25 B). Subsequently, a subgroup of 4 EHTs per cell line was treated with

4-AP and Bay K8644 (Treatment) and the remaining EHTs were analysed as time controls (TC). The mean beating frequencies under baseline conditions of IsoC (TC and Treatment) was 24 and 23 BPM, respectively, and of p.H222P (TC and Treatment) 62 and 50 BPM, respectively. Upon treatment beating frequency of p.H222P (TC and Treatment) were 35 and 27 BPM, respectively, and 19 and 12 BPM of IsoC EHTs (TC and Treatment) respectively. All EHTs of both genotypes reacted with a prolongation of relaxation time upon treatment. However, the delta of absolute relaxation time was significantly smaller in p.H222P than in IsoC EHTs (Figure 25 G), resulting in exaggeration of differences between p.H222P and IsoC under baseline conditions. When extrapolating from the measured relaxation time to repolarisation, the experiments point to differences in the repolarisation reserve between the two lines with a higher repolarisation reserve and/or lower depolarisation currents in p.H222P than in IsoC.

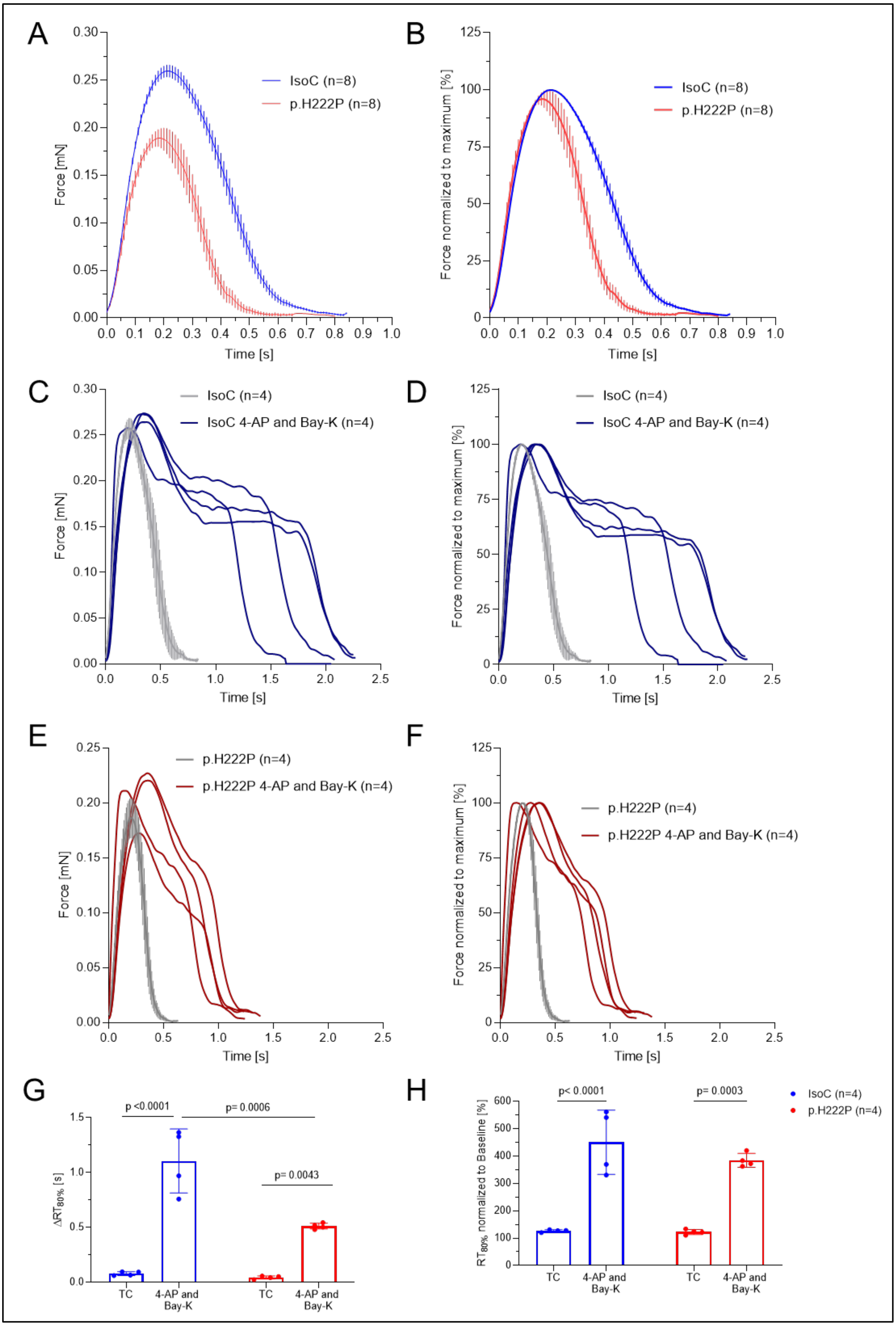
A
Force [mN]
0.30
0.25
0.20
0.15
0.10
0.05
0.00
Time [s]
0.0 0.1 0.2 0.3 0.4 0.5 0.6 0.7 0.8 0.9 1.0
IsoC (n=8)
p.H222P (n=8)
B
Force normalized to maximum [%]
125
100
75
50
25
0
Time [s]
0.0 0.1 0.2 0.3 0.4 0.5 0.6 0.7 0.8 0.9 1.0
IsoC (n=8)
p.H222P (n=8)
C
Force [mN]
0.30
0.25
0.20
0.15
0.10
0.05
0.00
Time [s]
0.0 0.5 1.0 1.5 2.0 2.5
IsoC (n=4)
IsoC 4-AP and Bay-K (n=4)
D
Force normalized to maximum [%]
125
100
75
50
25
0
Time [s]
0.0 0.5 1.0 1.5 2.0 2.5
IsoC (n=4)
IsoC 4-AP and Bay-K (n=4)
E
Force [mN]
0.25
0.20
0.15
0.10
0.05
0.00
Time [s]
0.0 0.5 1.0 1.5 2.0 2.5
p.H222P (n=4)
p.H222P 4-AP and Bay-K (n=4)
F
Force normalized to maximum [%]
125
100
75
50
25
0
Time [s]
0.0 0.5 1.0 1.5 2.0 2.5
p.H222P (n=4)
p.H222P 4-AP and Bay-K (n=4)
G
ΔRT80% [s]
1.5
1.0
0.5
0.0
p <0.0001
p= 0.0006
p= 0.0043
TC
4-AP and Bay-K
TC
4-AP and Bay-K
H
RT80% normalized to Baseline [%]
600
500
400
300
200
100
0
p< 0.0001
p= 0.0003
TC
4-AP and Bay-K
TC
4-AP and Bay-K
IsoC (n=4)
p.H222P (n=4)

Figure 25 Pharmacological intervention to block potassium channels with 4-Aminopyridin (4-AP; 50 µM) and activate calcium channels with Bay-K (100 nM) in p.H222P and IsoC EHTs **A-B** Average peaks of IsoC (blue) and p.H222P (red) derived EHTs spontaneously beating in 1.8 mM Ca^{2+} DMEM F12 of absolute and normalised values. **C-D** Absolute and normalised average peaks of spontaneously beating IsoC EHTs treated with 4-APand Bay-K or untreated as time matched controls. **E-F** Absolute and normalised average peaks of spontaneously beating p.H222P EHTs treated with 4-AP and Bay-K or untreated as time matched controls. **H** Delta of absolute $RT_{80\%}$ values (Intervention $RT_{80\%}$ - BL $RT_{80\%}$). **G** Relaxation time of IsoC and p.H222P either as time controls (TC) or treated with 4-AP and Bay-K normalised to baseline value (y-axis). Error bars represent standard deviation (SD). n= number of EHTs. Statistics calculated by 2-Way ANOVA with Tukey's post-test.

4.3.1.4 Calcium concentration response curve

Altered myofilament calcium sensitivity plays a causal role in HCM and DCM (Chung *et al.*, 2016). In standard EHTs, indirect evidence for such alterations can be obtained by constructing calcium response curves. EHTs of p.H222P and IsoC were analysed in a calcium concentration response curve to assess their sensitivity to increasing external calcium concentrations under electrical pacing at 1.5 Hz (Figure 26 A). P.H222P EHTs exhibited a mean effective concentration (EC_{50}) of 0.54 mM calcium, while IsoC EHTs had an EC_{50} of 0.08 mM calcium (Figure 26 B). Thus, p.H222P EHTs showed a rightward shift of the calcium-response curve compared to IsoC EHTs, indicating a reduced calcium sensitivity and cooperativity in p.H222P EHTs. Of note, the interpretation of this data is limited by the fact that the sensitivity to external calcium concentrations can be affected not only by the calcium binding affinity of myofilaments, but also by differences in calcium handling.

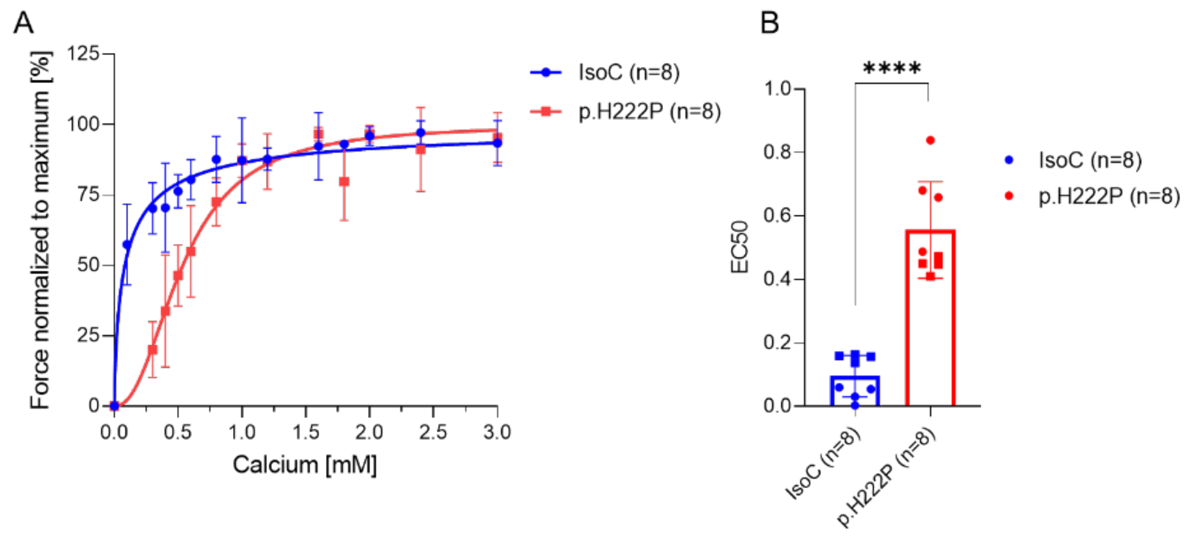

Figure 26 **A** Calcium concentration response curve of IsoC (blue) and p.H222P (red) EHTs. Calcium concentrations are shown on the x-axis and force normalised to maximum on the y-axis. Lines result of non-linear regression curve. Dots represent the means (n=number of EHTs) and error bars standard deviation (SD). **B** Mean effective concentration (EC_{50}) of the non-linear regression curve of single EHTs. Statistics calculated by Welch's t-test (**** p value <0.0001).

4.3.1.5 Electrophysiological characterisation

A typical manifestation in laminopathy patients is arrhythmia, hence patient specific EHTs were subjected to action potential (AP) measurements by sharp microelectrodes. The experiments were limited by difficulties to reach stable recording conditions. APs in p.H222P showed lower amplitudes (APA; Figure 27 A) and a significantly less negative resting membrane potential (RMP; Figure 27 B) than IsoC EHTs. Further, p.H222P exhibited a lower maximal upstroke velocity than IsoC EHTs, but differences did not reach statistical significance (Figure 27 C). Action potential duration (APD20 and APD90) showed a non-significant tendency towards a shorter duration (Figure 27 D and E). Both parameters, shorter APD20 and APD90 are in line with the shorter relaxation time in p.H222P EHTs observed in Figure 22 and Figure 24. Overall, it has to be noted that there was a large scatter for the different parameters, which suggests that more biological samples are required for conclusions.

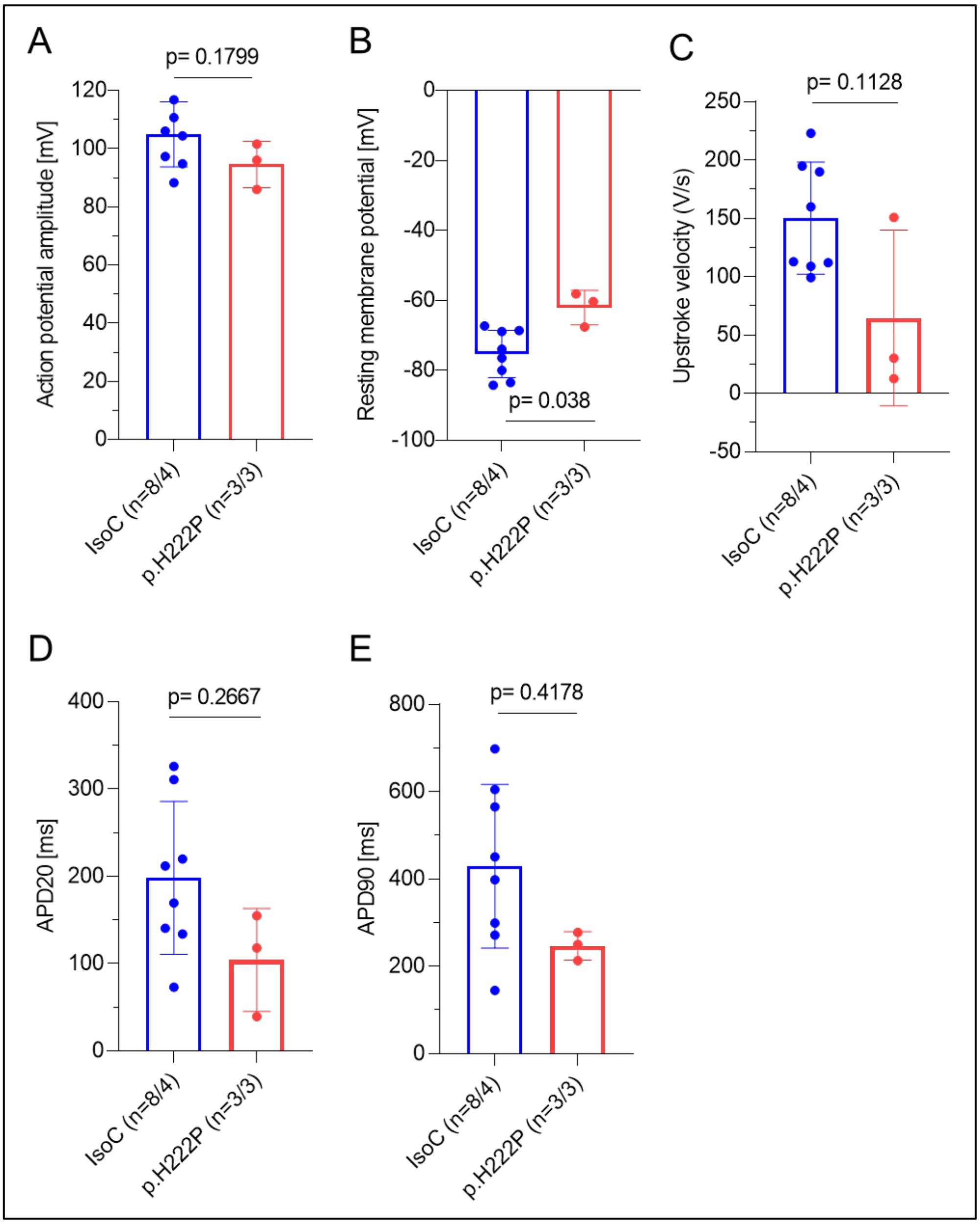

Figure 27 Statistical analysis of action potentials that were measured with a sharp microelectrode of spontaneously beating IsoC and p.H222P EHTs. Measurement parameters included **A** action potential amplitude (APA; y-axis), **B** resting membrane potential (RMP; y-axis), **C** maximal upstroke velocity (y-axis) **D** action potential duration (APD20; y-axis) and **E** action potential duration (APD90; y-axis). Measurements were conducted under basal conditions (1.8 mM Ca^{2+} Tyrode). n=number of EHTs / batches. P-values were calculated by nested t-test.

4.3.1.6 Afterload enhancement

Mechanical coupling defects are assumed to be a key pathogenic mechanism of laminopathies. Therefore, EHTs were subjected to acute afterload enhancement (AE) for four hours (4h) by inserting 5 mm metal braces into the hollow posts, the EHTs were cultivated on. This intervention increases the stiffness of the posts and thereby enhances the afterload against which the EHTs need to contract. Previous experiments in control EHTs showed that AE up to a certain degree does not reduce fractional shortening (FS), i.e. EHTs develop higher force on stiffer posts (Rodriguez *et al.*, 2019) Upon increasing stiffness 1.68-fold, FS dropped in p.H222P EHTs in comparison to time matched controls (TC; -28.8%; p <0.05; nested one-way ANOVA), but non-significantly in IsoC EHTs (Figure 28). Thus, mechanical stress unmasked a contractile deficit in p.H222P.

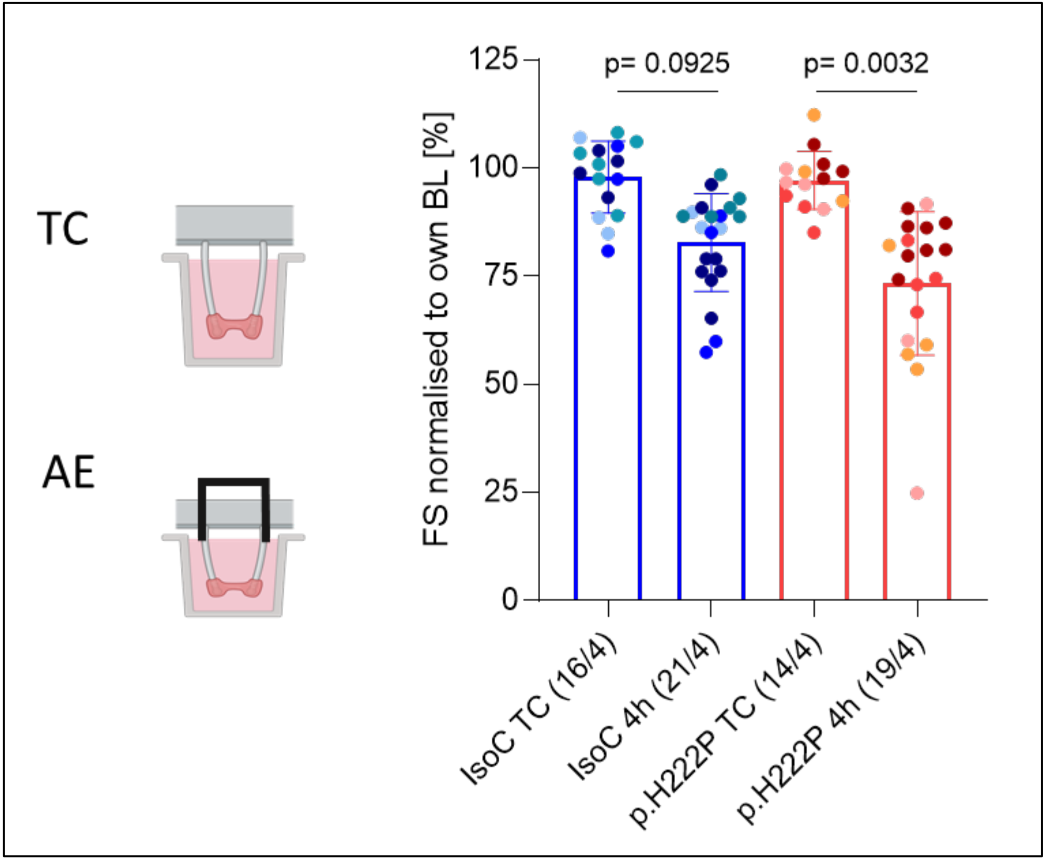

Figure 28 Fractional shortening of IsoC and p.H222P EHTs with induced afterload enhancement over 4 hours (4h) or time matched controls (TC). Each dot represents a single EHT and each colour of dot one batch (n=number of EHTs/batches). FS are expressed as percent of pre-intervention baseline values (y-axis). P-values were calculated by nested one-way ANOVA and Tukey's post-test.

4.3.2 Changes of the transcriptome

4.3.2.1 EB-based differentiation and complete media versus Monolayer differentiation and maturation media

A-type lamins play an important role in the regulation of gene expression. Thus, EHTs were subjected to bulk RNA sequencing. This was done on EHTs from two batches to reflect the different conditions under which EHTs were functionally analysed. Specifically, the functional experiments under basal conditions were done with one batch of EB-based differentiated CMs and several batches with CMs differentiated in monolayer format. All measurements were done on standard low-stiffness posts (“transparent posts”) and in complete medium. EHTs that were subjected to AE were made from CMs differentiated in monolayer format, were cultured on hollow posts with higher basal stiffness (“white posts”) and cultured in maturation media. Therefore, bulk RNA sequencing was done on EHTs from EB-based differentiation cultured on low-stiffness posts in complete media (condition I; Figure 29 A) and on EHTs from monolayer differentiated CMs cultured on stiffer posts and in maturation media (condition II; Figure 29 B). The fold change of the differentially expressed genes (DEGs; p.H222P versus IsoC) was plotted against the adjusted p value (Figure 29). To reduce the complexity and overall number of DEGs, this analysis was done only in genes with a base mean of 100. The analysis showed striking differences in the number of DEGs between p.H222P and IsoC in the two conditions. In condition I, 323 transcripts were less abundant in p.H222P and 616 more abundant, while numbers in condition II were 33 and 124, respectively (Figure 29 A). Also, the degree of regulation and the p-values were much lower in condition II than I (Figure 29 B). The data show that the culture conditions have major impact on the molecular disease phenotype.

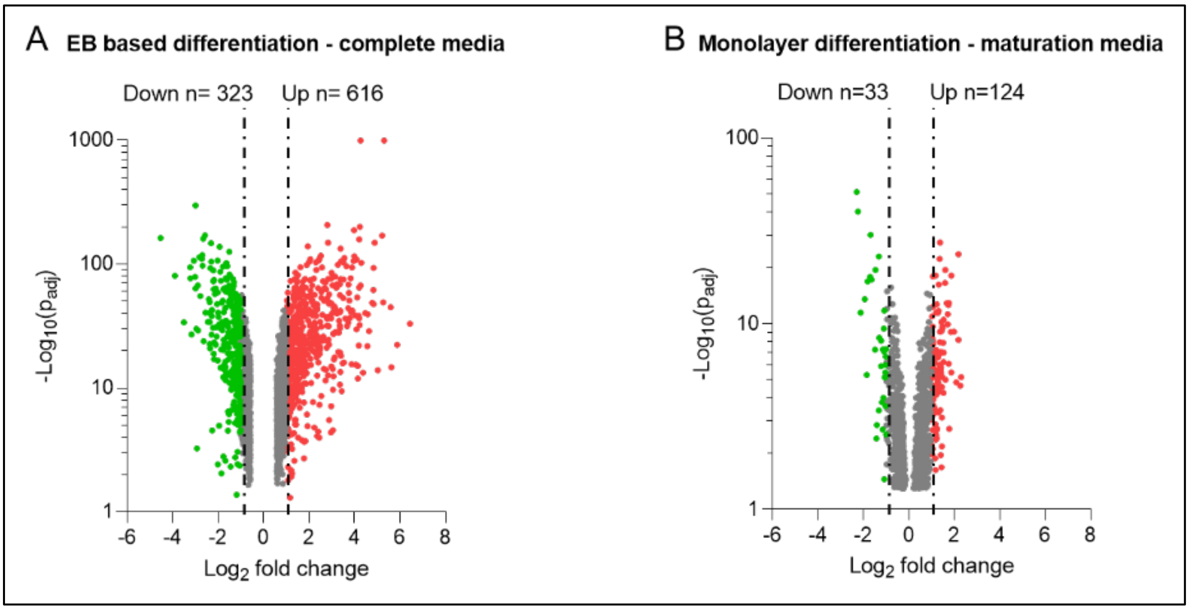

Figure 29 Comparison of DEGs (-Log$_{10}$(p$_{adj}$); y-axis) between p.H222P versus IsoC derived from the two bulk RNA sequencing experiments in two volcano plots (Log$_2$ fold change; x-axis). Genes with a minimum of 100 base mean and which were at least 2-fold up or down regulated were considered for comparison. The first experiment **A** was done on EHTs from CMs differentiated in EB format, casted on low stiffness transparent posts and cultured in complete medium (condition I). The second experiment **B** was done on EHTs from CMs differentiated in a monolayer format, casted on stiffer white posts and cultured in maturation medium (condition II).

The top 300 DEGs with the highest number of reads were analysed in a gene ontology (GO) enrichment to examine to which extent the conditions impacted the phenotype in p.H222P. Interestingly, p.H222P EHTs of condition I showed upregulation of *e.g.*, actin filament fragmentation, sequestering of TGFβ and PDGF pathways models (Figure 30), which have been reported in laminopathy disease (Chatzifrangkeskou *et al.*, 2016, 2018; Bernasconi *et al.*, 2018; Lee *et al.*, 2019).

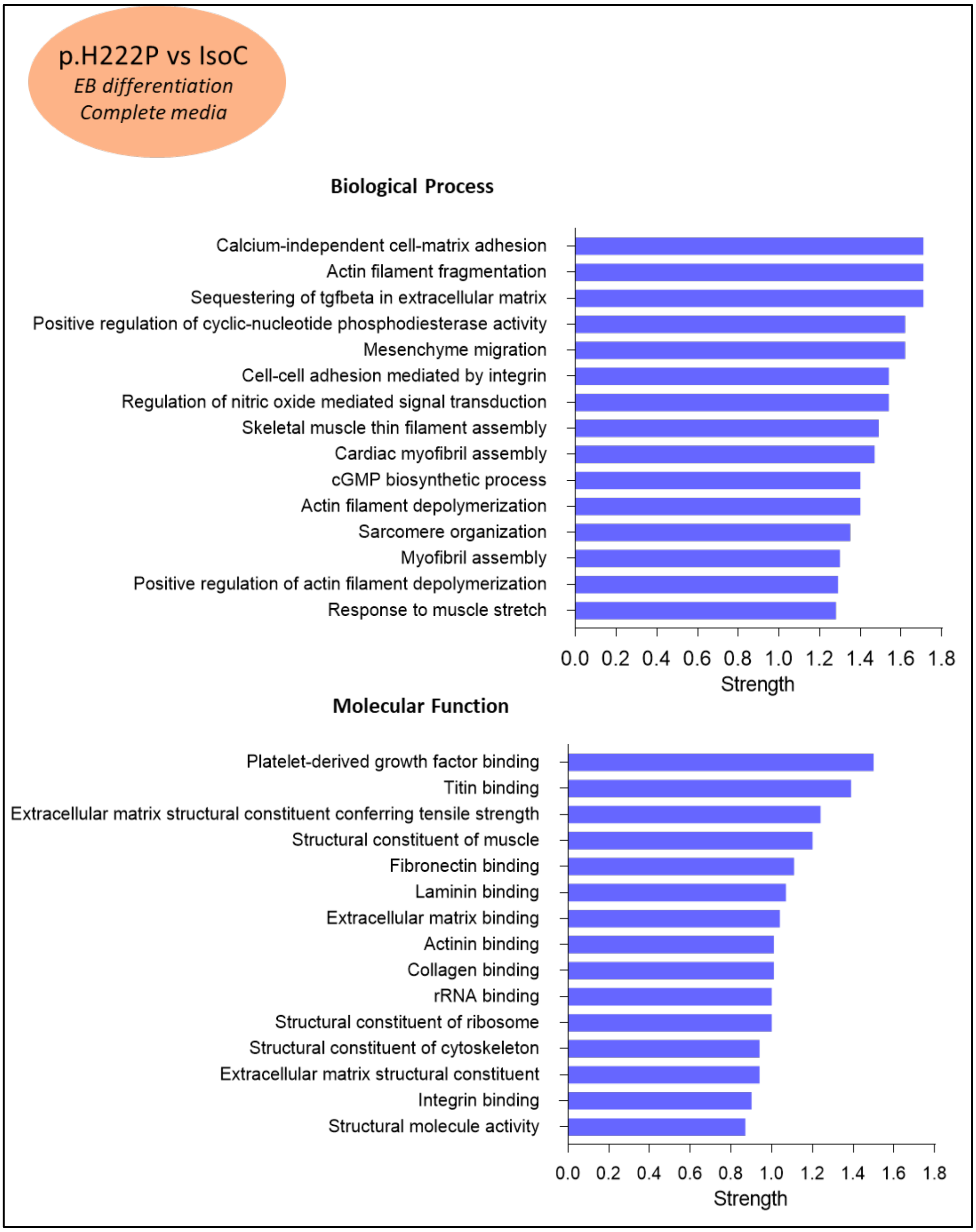

Figure 30 The top 300 DEGs of p.H222P versus IsoC EHTs differentiated in EB format and cultured in complete media (condition I) with highest read count analysed in a GO pathway enrichment of biological process and molecular function. The strength of the pathways, calculated by Log_{10}(observed/expected), is depicted on the x-axis. Query setting was adjusted to stringent (1%).

In contrast, p.H222P EHTs of condition II showed mainly an upregulation of contraction, conduction and calcium handling GO pathways (Figure 31). This might have facilitated the provocation of a contractile phenotype in AE experiments, which were conducted under these conditions.

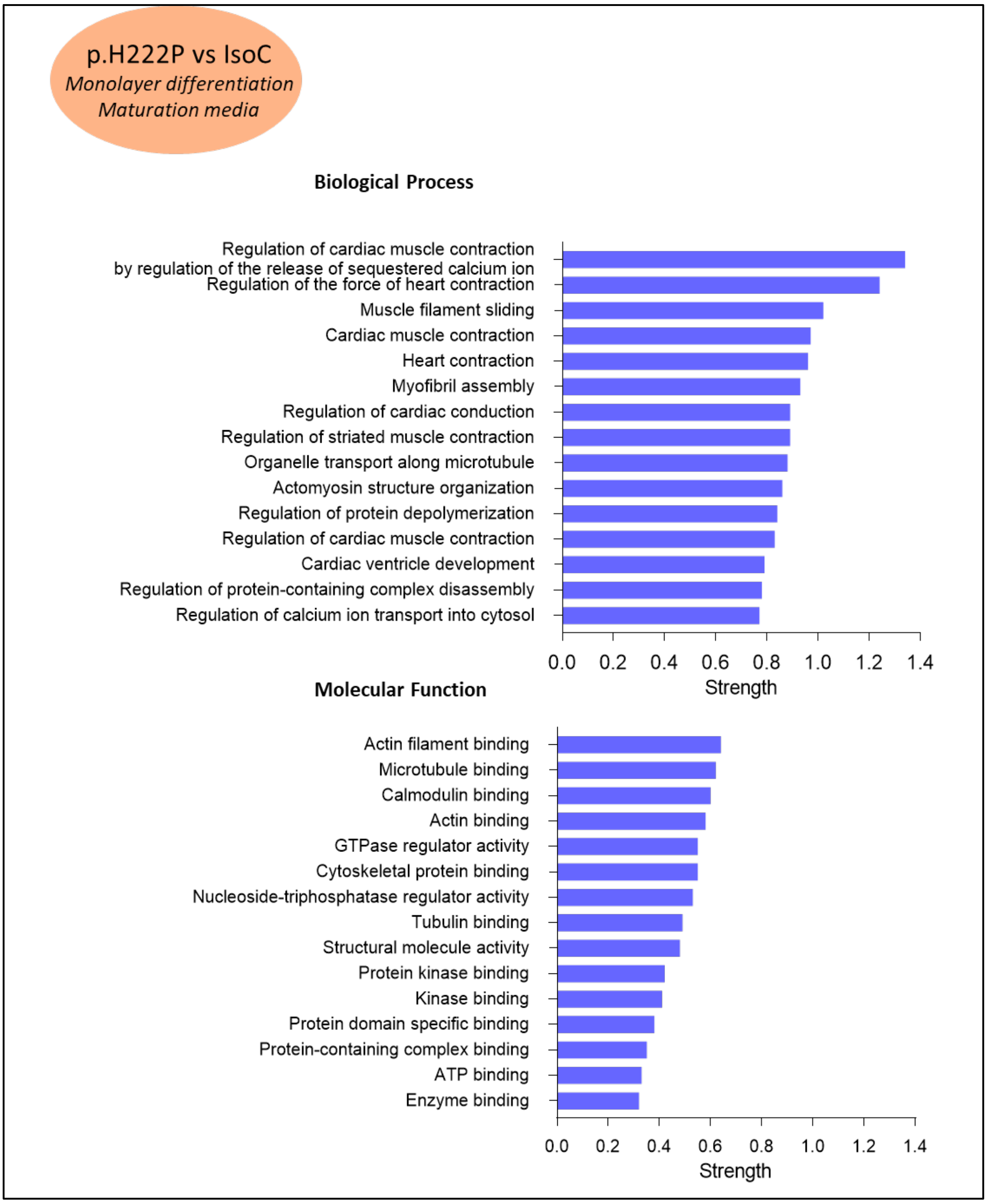

Figure 31 The top 300 DEGs of p.H222P versus IsoC EHTs differentiated in monolayer format and cultured in maturation media on stiffer posts (condition II) with highest read count analysed in a GO pathway enrichment of biological process and molecular function. The strength of the pathways, calculated by Log_{10}(observed/expected), is depicted on the x-axis. Query setting was adjusted to stringent (1%).

4.3.2.2 Differential expression of ion channels

The two RNA sequencing experiments showed altered expression patterns of various ion channel genes, which differed also depending on the condition (Figure 32 and Figure 33). In condition I, the main sodium channel Nav1.5 (*SCN5A*) that is responsible for the depolarisation in phase 1 of the ventricular action potential was not differentially expressed in p.H222P EHTs. This is at variance with another hiPSC laminopathy model (Salvarani *et al.*, 2019). However, p.H222P EHTs exhibited lower abundance of another pore forming α-subunit (*SCN1A;* Nav1.1) than IsoC EHTs. Nav1.1 is located in the t-tubules (Maier *et al.*, 2004) but plays a minor role in cardiomyocytes.

CMs express, in addition to the pore forming subunits, several auxiliary and regulatory β-subunits of which two β-subunits (*SCN3B* and *SCN4B*) were downregulated in p.H222P compared to IsoC EHTs. Another β-subunit (*SCN1B*) that is normally expressed in adult human CMs (Makita, Bennett and George, 1996), was upregulated in p.H222P EHTs (Figure 32).

T-type calcium channels (*CACNA1G* and *CACNA1H*) were downregulated in p.H222P. These channels are expressed at very low levels in the adult heart, but play an important role in excitation-contraction coupling (Ono and Iijima, 2010) and have been shown to be more prominent in hiPSC-CMs (Uzun *et al.*, 2016). P.H222P EHTs also exhibited slightly lower expression (-0.6 Log_2 fold change; Figure 32) of the main L-type calcium channel (*CACNA1C*) than IsoC EHTs. L-type calcium channels take predominantly part in depolarisation during the second phase of ventricular action potentials (Antzelevitch *et al.*, 2007).

Potassium channels made up the majority of ion channel DEGs. *KCND2* and *KCND3* encode for two channels that contribute to the potassium outward current during phase 1 of the ventricular action potential (Ito,f). This current induces the typical notch and contributes to the repolarisation. P.H222P EHTs exhibited for both genes higher expression levels.

Upregulation of *KCNA5* (forming $I_{Kur;}$ Kv1.5/3.1, normally only in atria;(Chen, Sampson and Kass, 2016) and two less prominent genes (*KCNK1* and *KCNK6*) that encode for potassium channels activated upon cellular stretching within all phases of the action potential (Grant, 2009) might contribute to this phenotype.

Two β-subunits (*KCNMB1* and *KCNMB4*) of the big conductance calcium activated potassium channel (BK_{Ca}) were also upregulated in p.H222P. The subunit 4 is predominantly expressed in brain but at low levels in heart (Meera, Wallner and Toro, 2000). The subunit 1 is mostly expressed in smooth muscle cells, but also found in immature CMs (Long *et al.*, 2009). The role in immature CMs is poorly understood, but higher expression levels of these subunits in p.H222P might contribute to the observed shortening of APD in this model.

The potassium channel Kir2.1 (*KCNJ2*) is responsible for maintaining the negative resting membrane potential (I_{K1}) during phase 3 and 4. Interestingly, p.H222P EHTs exhibited a lower expression of this channel, which might well contribute to the less negative RMP in p.H222P EHTs (Figure 27).

The potassium channels Kir6.1 (*KCNJ8*) and Kir6.2 (*KCNJ11*), which form the ATP-sensitive I_{KATP}, are usually closed and become active upon metabolic stress (Nichols, 2016). Upon metabolic stress (*e.g.* ischemia), opening of these channels shorten APD and, subsequently reduce calcium influx to sustain stress (Kane *et al.*, 2006). These channels were both downregulated in p.H222P EHTs.

Several other potassium channels were found to be up- or downregulated in p.H222P in condition I and it is difficult to predict functional consequences. Of note, the potassium channel that forms the major repolarizing current I_{Kr} in the heart and in hiPSC-CMs (KCNH2) was found not be regulated.

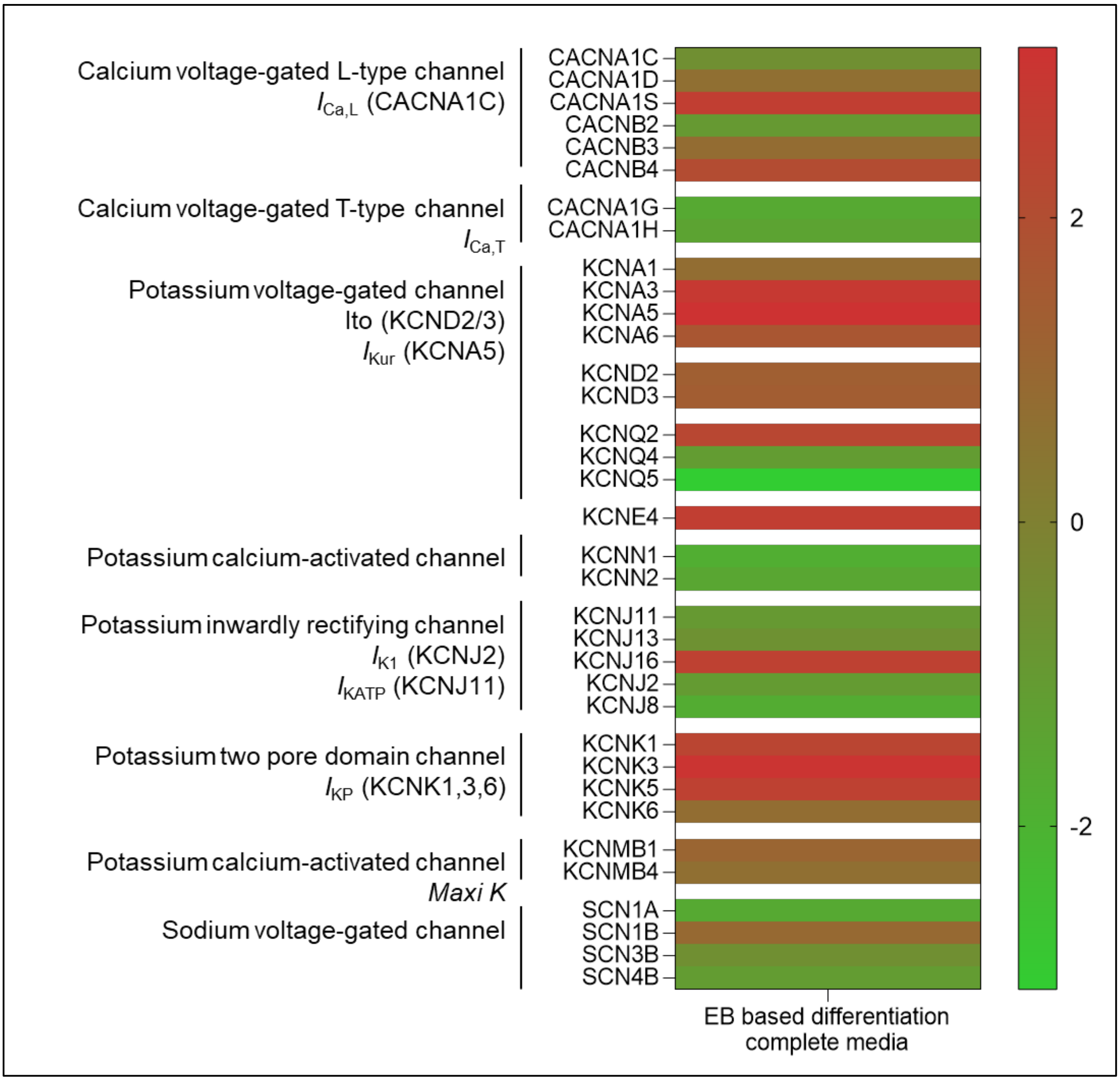

Figure 32 DEGs from bulk RNA sequencing of p.H222P versus IsoC in an EB based differentiation and EHT complete media culture experiment (condition I) that encode for different ion channels. Ion channels are classified by their function and important gene responsible for known currents are indicated in brackets. Colour coding indicates the Log_2 fold change of the genes between the two genotypes. 3 EHTs from one batch per group.

Interestingly, the differentially expressed ion channels in condition II (Figure 33) differed largely from those in condition I (Figure 32). For example, *KCNJ2* and *KCNJ8* (both of lower abundance in condition I) were more abundant in p.H222P than in IsoC in condition II, and *KCNA5* (higher in condition I) was lower in p.H222P than in IsoC in condition II. The sodium channel β unit *SCN1B* was upregulated in both batches. The subunit *KCNMB4* of BK_{Ca} was also upregulated in both batches. Further, p.H222P EHTs exhibited higher expression of the stretch-activated potassium channel (*KCNK1*) than IsoC in both conditions.

Another interesting gene is *KCNQ1*, which encodes the voltage gated potassium channel Kv7.1 and forms I_{Ks}. The expression of *KCNQ1* was solely upregulated in this batch and might contribute to more potassium outward current during plateau phase and shortening of APD. However, no action potentials were measured under condition II, making any relationship speculative.

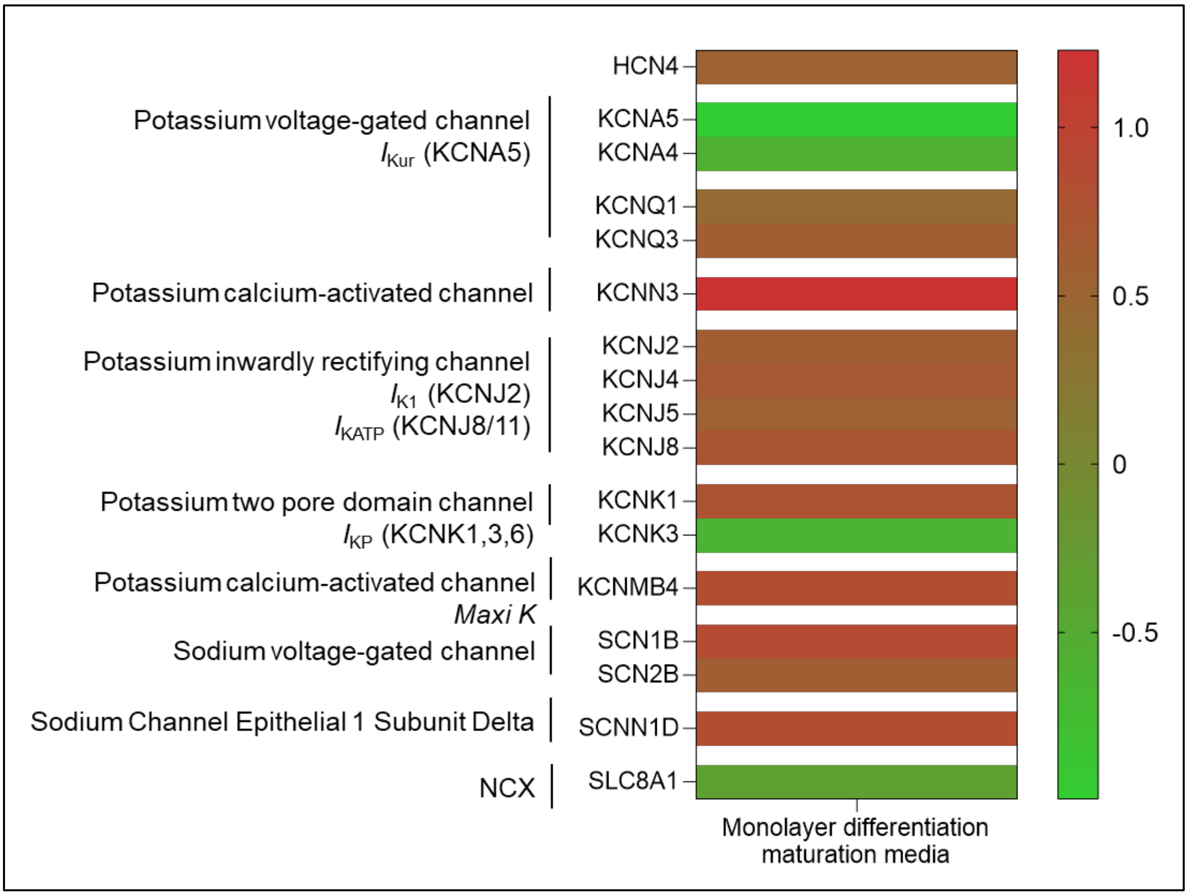

Figure 33 DEGs from bulk RNA sequencing of p.H222P versus IsoC in a monolayer based differentiation and EHT maturation media culture experiment that encode for different ion channels. Ion channels are classified by their function and important gene responsible for known currents are indicated in brackets. Colour coding indicates the Log_2 fold change of the genes. 3 EHTs from one batch per group.

To summarise, many ion channel genes belonged to the DEGs in p.H222P under both conditions, but the affected genes and also the direction of change were condition dependent. Overall, a higher expression of potassium channels and lower expression of calcium channels (condition I) might contribute to the tendency towards a shorter APD in p.H222P EHTs observed in condition I.

4.3.2.3 Lamin A on transcript level

Lamin A was quantified in the first bulk RNA sequencing experiment in order to investigate whether the p.H222P mutation causes lower lamin A transcript levels. P.H222P EHTs exhibited significantly lower lamin A transcripts per million reads (TPM) than IsoC EHTs (Figure 34), indicating that indeed the mutation affected the lamin A transcript level.

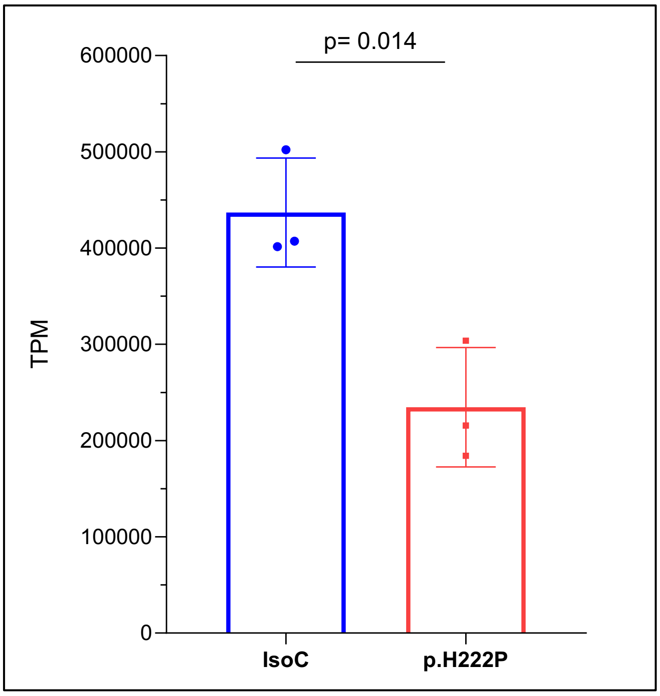

Figure 34 Balance of the isoform lamin A (x-axis) on the transcript level (Transcript per million, TPM; y-axis) in IsoC and p.H222P EHTs analysed in the bulk RNA sequencing experiment based on condition I. Statistics were calculated by unpaired t-test. n= 3 EHTs / 1 batch.

4.3.2.4 Transcriptome profile upon AE

A-type lamins play an important role in mechanotransduction, i.e. they transmit mechanical signals in changes of gene expression. Thus, EHTs subjected to 4 hours AE and their time matched controls were also analysed by bulk RNA sequencing to investigate a potential interplay as an underlying pathomechanism. The principal component analysis (PCA) revealed closest clustering of cell lines by genotypes, but AE induced a shift of IsoC EHTs to the left towards p.H222P EHTs. In p.H222P the intervention induced a shift even further to the left (Figure 35 A). Analysis of significant DEGs (without a cut off for the base mean as in section 4.3.2.1) showed that most genes (2115) were affected between p.H222P and IsoC already under basal conditions (TC). AE intervention in IsoC only led to 107 DEGs, while it induced 829 DEGs in p.H222P. Thus, the transcriptomic response to mechanical cues was exaggerated in the diseased tissues (Figure 35 B).

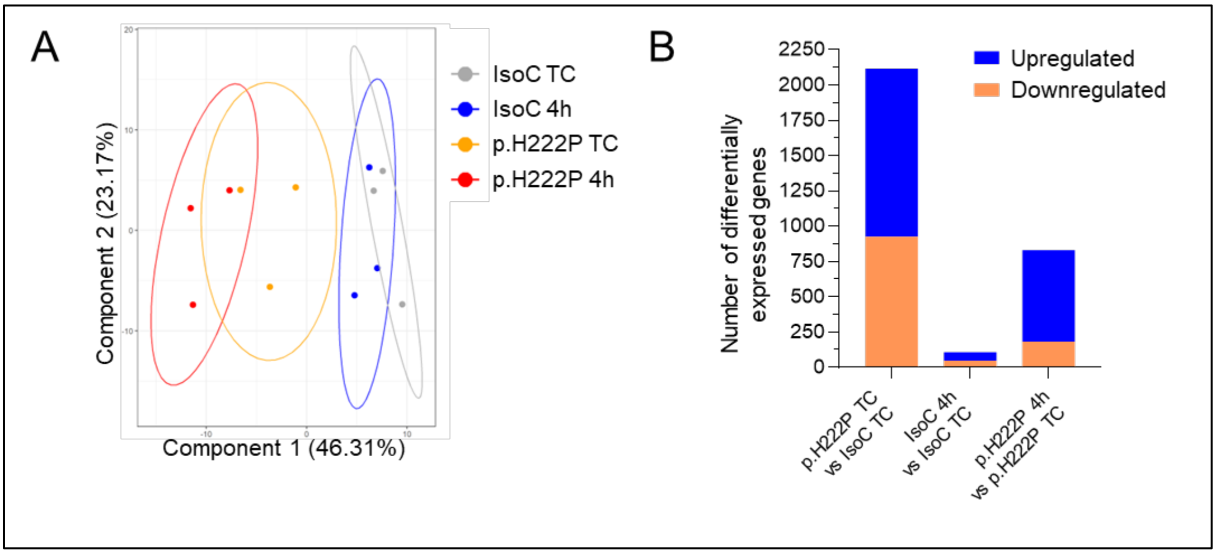

Figure 35 Analysis of the effect of acute AE on the transcriptomic level. **A** Principal component analysis showing clustering of IsoC time controls (TC) and IsoC subjected to acute AE for 4 hours (4h) as well as for p.H222P tissue TC and 4h. Component 1 depicted on x-axis and component 2 on y-axis. **B** Number of significantly differentially expressed genes (DEGs; y-axis), that were either up- (blue) or downregulated (orange) when comparing different groups (x-axis). FDR<0.05. Three EHTs per group from one differentiation batch.

Of the 829 DEGs in AE-exposed p.H222P 4h (versus p.H222P TC), 20% were overlapping with DEGs already differing between p.H222P and IsoC TC DEGs, which suggests worsening of the laminopathy phenotype under mechanical stress (Figure 36 up). However, only 7% of DEGs in stressed p.H222P were overlapping with stressed IsoC versus IsoC TC (Figure 36 bottom), indicating a differential gene expression response upon mechanical load in p.H222P and IsoC EHTs.

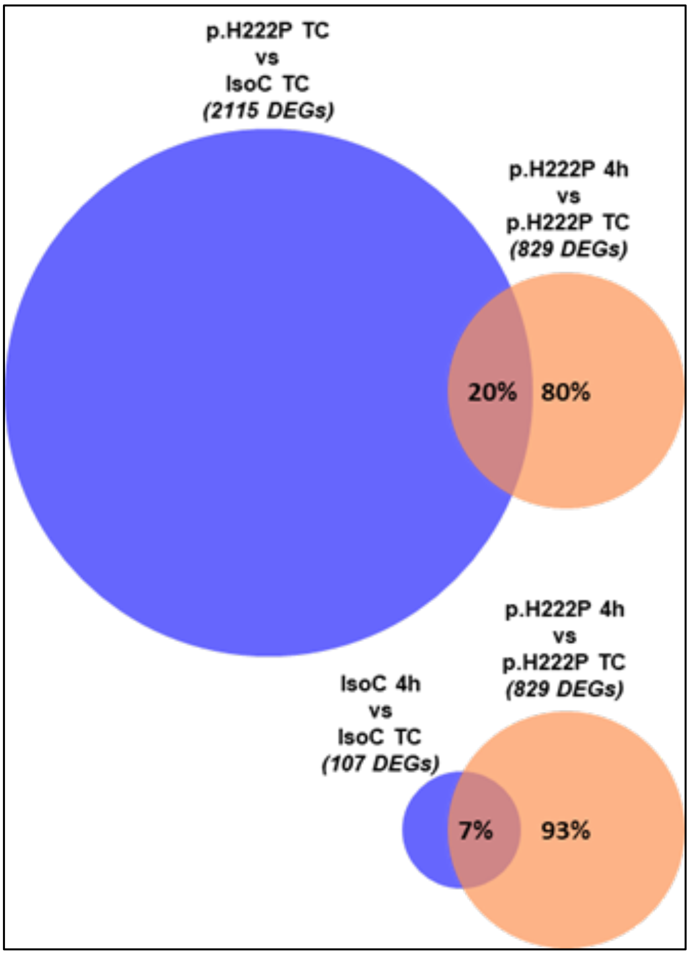

Figure 36 Venn diagram showing overlaps of DEGs when comparing (i) p.H222P time matched controls (TC) to IsoC TC and p.H222P subjected to 4 hours of acute AE (4h) to p.H222P TC (orange data set = 100%) or comparing (ii) IsoC 4h versus TC and p.H222P 4h versus TC (orange data set = 100%). All DEGs FDR<0.05.

The DEGs between p.H222P and IsoC under basal conditions (TC) were classified by gene ontology (GO) enrichment analysis. The pathways accounted mainly for chromosome organisation, mitotic, fibrotic, cytoskeletal and microtubular gene expression programmes (Figure 37). Further, p.H222P EHTs exhibited upregulation in PDGF pathway as described for another laminopathy hiPSC-CM model (Lee *et al.*, 2019).

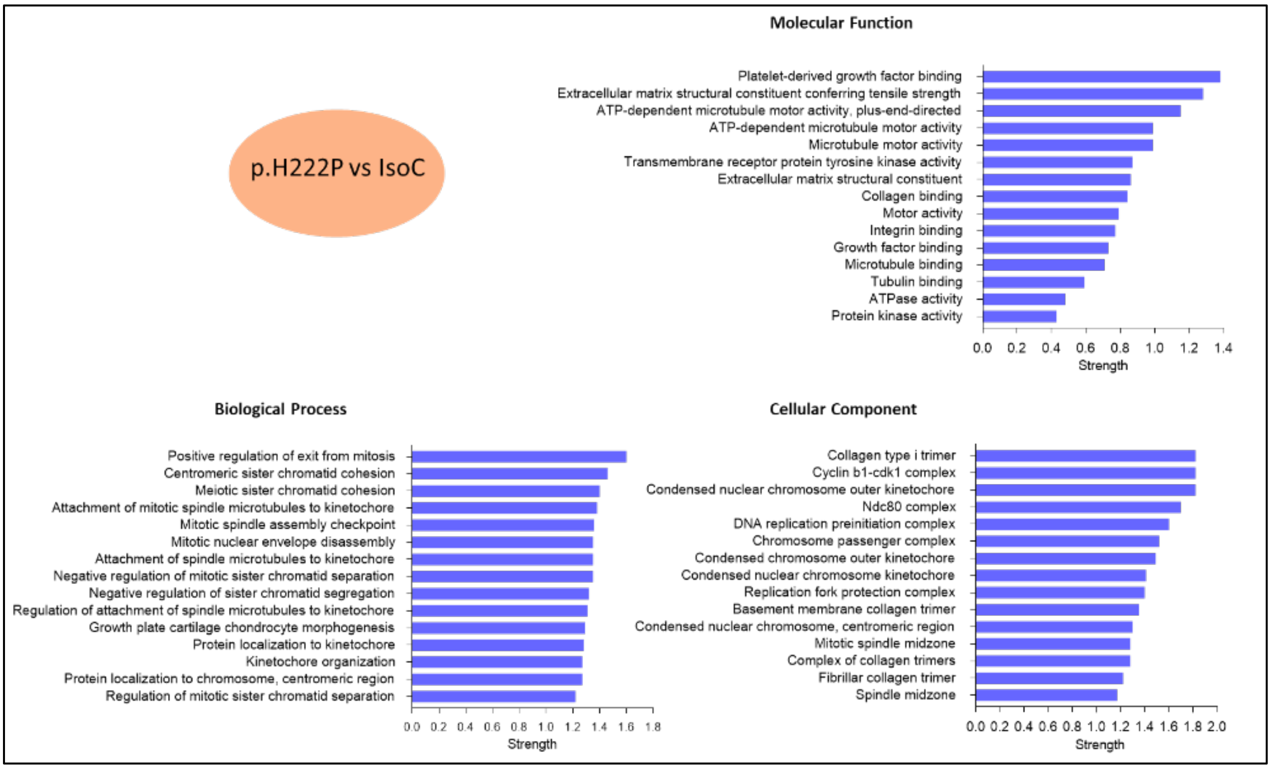

Figure 37 Gene ontology (GO) enrichment analysis of DEGs comparing p.H222P versus IsoC under basal conditions (without cut-of in basemean). Top 15 terms for molecular function, biological process and cellular component, sorted by the strength.

A deeper analysis of the upregulated genes in mechanically stressed p.H222P EHTs over TC p.H222P EHTs revealed that sarcomeric, cell-cell junction, Z-disc and transcriptional components were mainly affected (Figure 38). Pathways such as response to muscle stretch or again of PDGF confirm the successful exaggeration of phenotype upon AE (Figure 38).

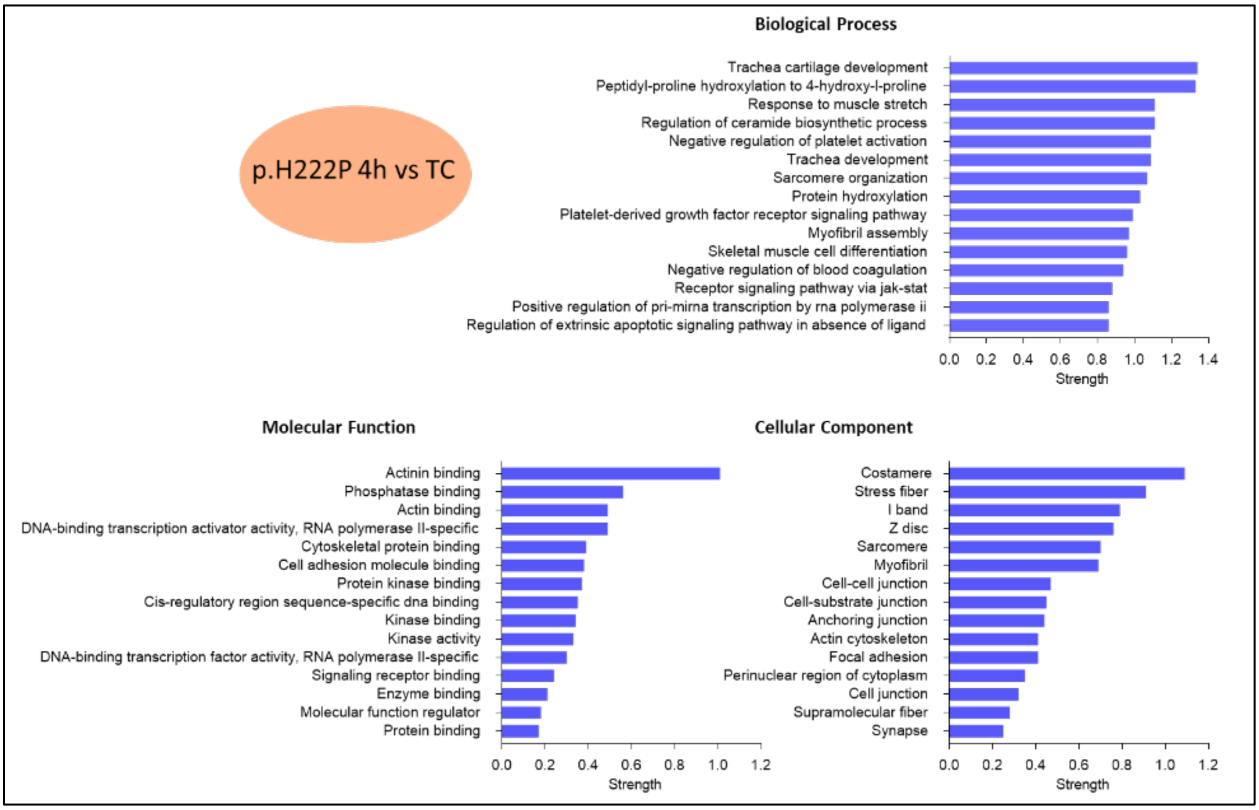

Figure 38 GO enrichment analysis of DEGs comparing p.H222P subjected to 4 hours acute AE (4h) versus controls (TC). Top 15 terms for biological process, molecular function and cellular component, sorted by the strength.

Several genes encoding components of the ECM, the cytoskeleton or transcriptional regulation are known to play a role in mechanotransduction and are being targets of YAP1. In a study, loss of YAP1 in adipose-tissue derived mesenchymal stem cells resulted in downregulation of 41 genes, which have thus been described as YAP1 target genes (Nardone *et al.*, 2017). 21 out of these 41 genes were found to be significantly more abundant in p.H222P EHTs than in IsoC under basal conditions (Figure 39 A). Some of them such as *ITGB1* and *COL12A1* were further upregulated upon mechanical intervention in p.H222P EHTs (Figure 39 B). Thus, YAP1 might be involved in a mechanical coupling defect in p.H222P EHTs.

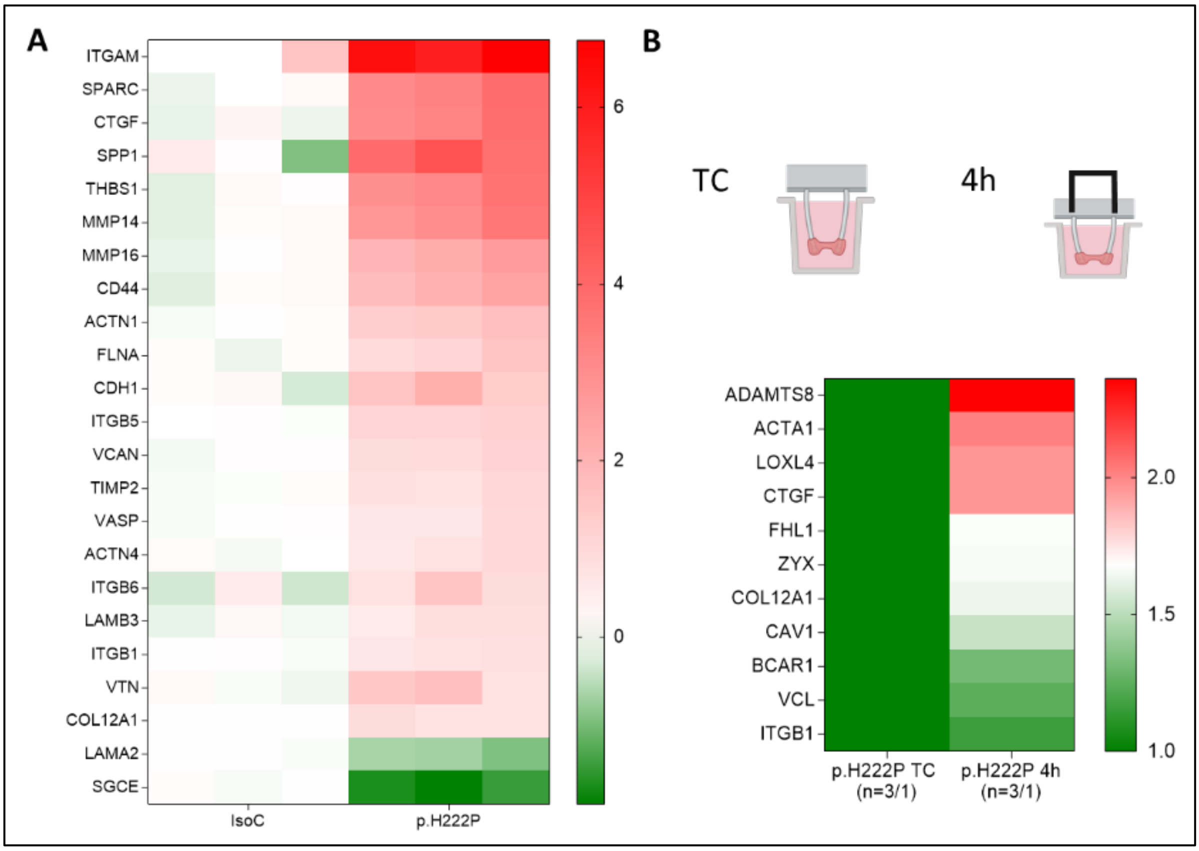

Figure 39 Loss of YAP1 resulted in the downregulation of 41 genes, which were idientified as YAP1 targets by Nardone *et al.*, 2017. **A** 21 of these genes were up- and 2 downregulated in p.H222P and IsoC EHTs under basal conditions and cultured in complete medium (condition I). **B** 12 genes of the target list were found to be upregulateed in the DEGs in p.H222P subjected to acute AE for 4 hours versus time matched controls (TC). FDR<0.05. n=number of EHTs / batches. Colour coding indicates Log_2 fold change.

4.3.3 Changes on the protein level

The protein expression of lamin A and C was assessed by Western blot. Western blots of protein lysates of TC and AE EHTs were stained for lamin A and C as well as MYBPC3 as a cardiac housekeeping protein. A high signal of MYBPC3 was especially detected in the last p.H222P 6 days (6d) sample. The Western blots showed two bands around 70 kDa, of which the band with a smaller apparent molecular weight represents lamin C (62 kDa) and the upper band lamin A (74 kDa; Figure 40 A). The lamin C band was much stronger than the lamin A band (Figure 40 A). Lamin A and C signals were quantified, normalised to MYBP3 signal and subsequently expressed as fold of IsoC TC. Under basal conditions, lamin A and C signals were approximately 50% lower in p.H222P than in IsoC EHTs (Figure 40 A and B). The AE intervention led to further reductions in lamin A and C levels particularly after 6 days

(Figure 40 A and B). Overall, the loading of protein differed, which can be seen by different intensities of MYBPC3 signal. Of note, the analysis was performed in only one to three replicates per group and therefore has to be considered preliminary.

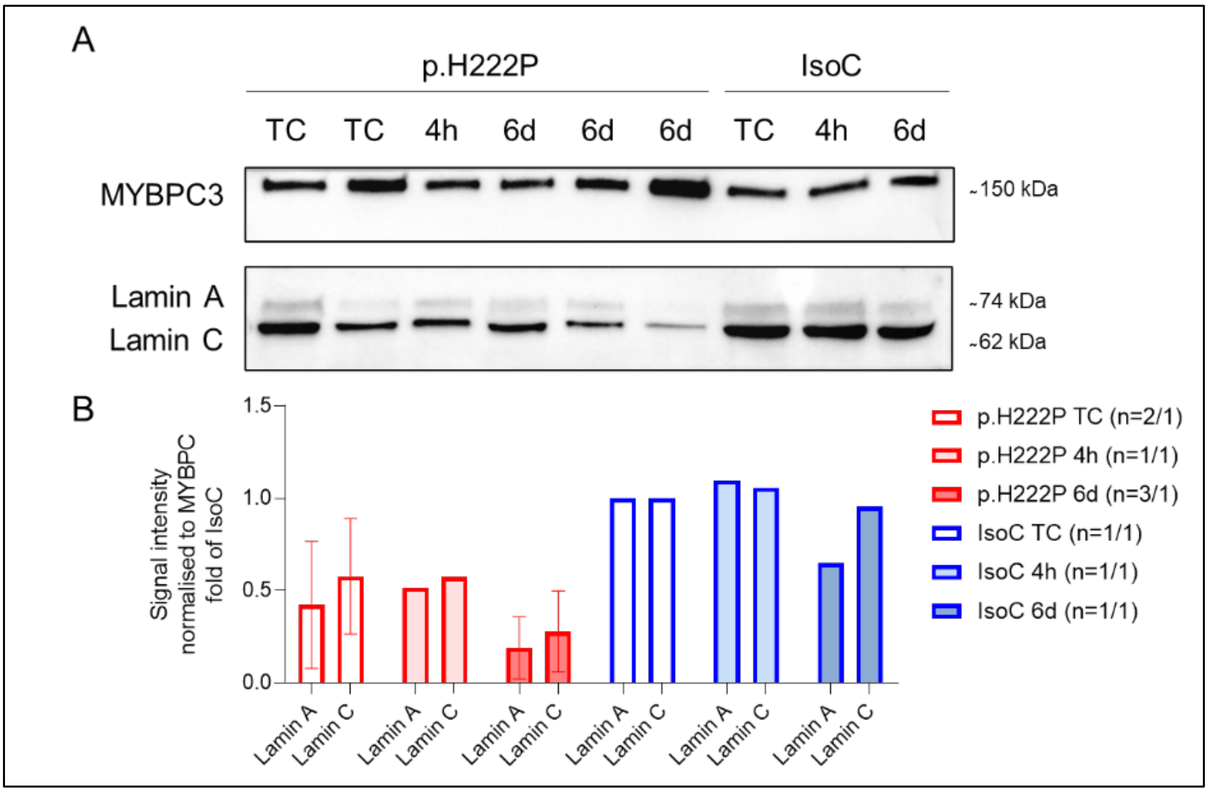

Figure 40 **A** Western blot analysis of IsoC and p.H222P EHTs controls (TC), 4 hours acute AE (4h) and 6 days AE (6d) stained for cardiac myosin binding protein C (*MYBPC3*) and lamin A and C. **B** Corresponding quantification of lamin A and C signal normalised to the signal of loading control MYBPC3. n=number of EHTs / batches.

The determination of total protein content in the EHT lysates was difficult due to the high fibrinogen concentrations in the matrix. Thus, difficulties in quantification makes equal loading on SDS PAGE gel challenging. In Western blot experiments, different loading resulted in varying lamin A to C ratios, which was unexpected (Figure 40 and Figure S 9). This prompted us to explore the possibility that the affinity of the antibody for lamin A and C may differ, and lead to apparently differing ratios depending on the amount of total protein loaded. A preferential binding of antibody to lamin C would result in a saturation of antibody binding at a lower protein content for lamin C compared to lamin A. Therefore, EHT protein lysates of an unrelated control cell line (UKEi1-A), since the isogenic control was not generated by then, and p.H222P were loaded at increasing amounts on an SDS PAGE gel.

Lamin A signals were several times lower than lamin C signals in the low protein loading sample (Figure 41 A). Lamin A and lamin C signals increased with increasing amounts of protein lysates as expected (Figure 41 A). After performing a linear regression, the signal intensity of the lamin C increases with a lower slope and has a higher y-intercept, while the lamin A signal increases dramatically from almost no detectable signal to about $8x10^6$ for UKEi1-A (Figure 41 B). Nevertheless, goodness of fit of lamin C linear regression was not indicating any oversaturation nor loss of linearity for lamin C (R^2= 0.92). The linear regression rather demonstrates that lamin C abundancy was generally higher in the sample itself. Further, performing a linear regression for the protein lysates of both genotypes resulted in two different slopes (1.473 for UKEi1-A and 0.766 for p.H222P; Figure 41 C). The lower slope in p.H222P suggests a lower absolute lamin A to C protein ratio in p.H222P EHTs than in UKEi1-A EHTs. However, this analysis was performed only in protein lysate of one EHT and thus has to be considered as preliminary (Figure 41 A and C).

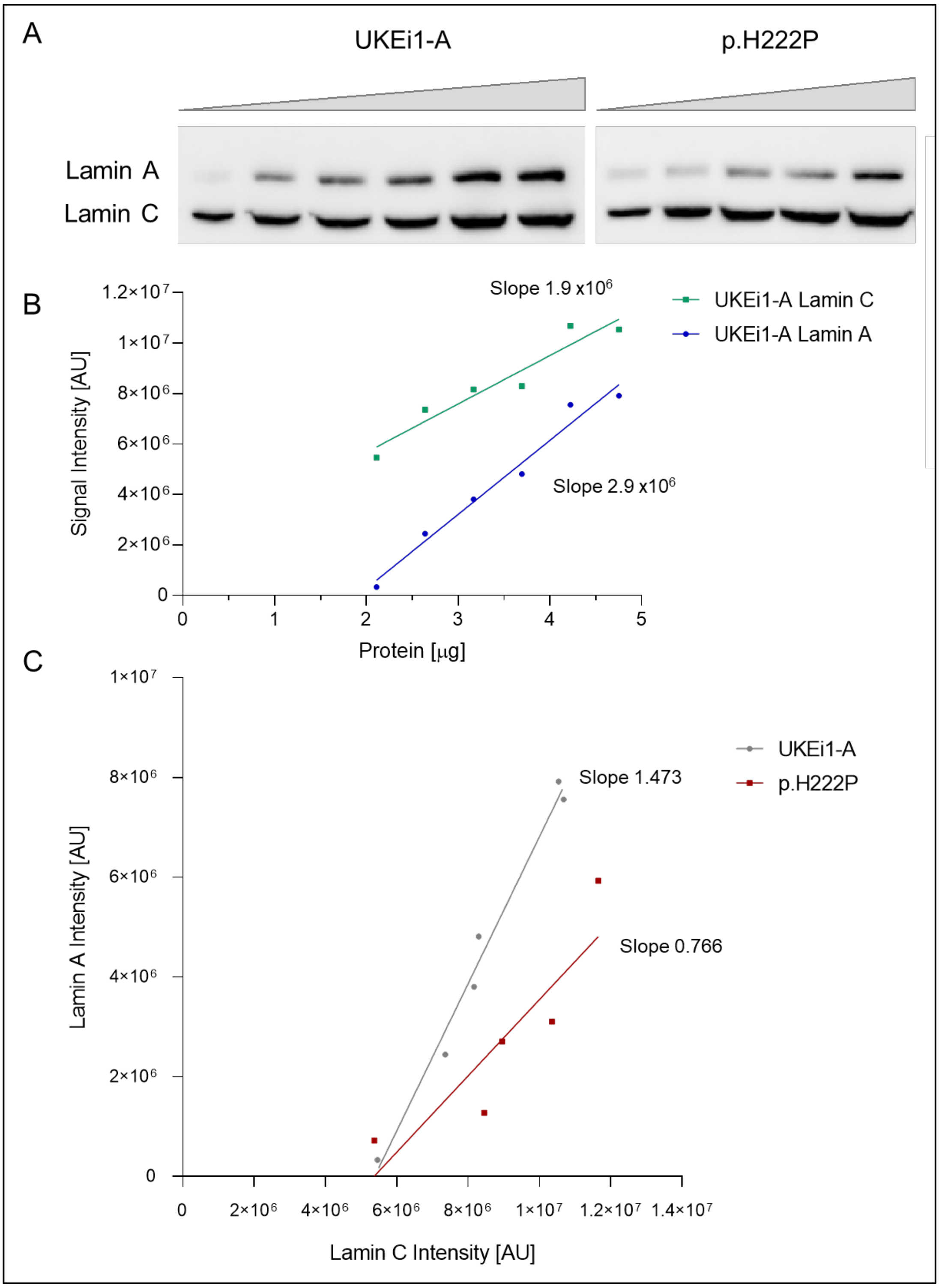

Figure 41 **A** Western blot of a dilution series of EHT lysates of an unrelated control line UKEi1-A and p.H222P stained for lamin A and C. **B** Linear regression of lamin A and C (y-axis) over the amount of protein loaded (x-axis) for UKEi1-A and their respective slope. **C** Linear regression of lamin A (y-axis) over lamin C (x-axis) intensity for both genotypes and their respective slope. Protein lysates from a single EHT per genotype.

4.3.4 Morphological changes

4.3.4.1 Nuclear elongation

Laminopathies are typically associated with elongation and/or blebbing of the nuclei (DuBose *et al.*, 2018). To test whether this phenomenon is present in p.H222P hiPSC-CM EHTs, fixed tissues of p.H222P and an unrelated control cell line UKEi1-A, since IsoC was not generated by that time, were stained in an initial experiment for lamin A and C and imaged as a Z-stack. Subsequently, Z-stacks were 3D reconstructed and the longest axes of the nuclei were measured in a blinder manner as shown in Figure 42 A. Nuclei of p.H222P EHTs showed a significantly greater length above the mean, several nuclei were even elongated to 47 µm (Figure 42 B). Nuclear blebbing was not evident but was also not systematically analysed in p.H222P hiPSC-CM EHTs. The initial experiment has to be repeated with IsoC, which was not generated by that time, to draw firm conclusions.

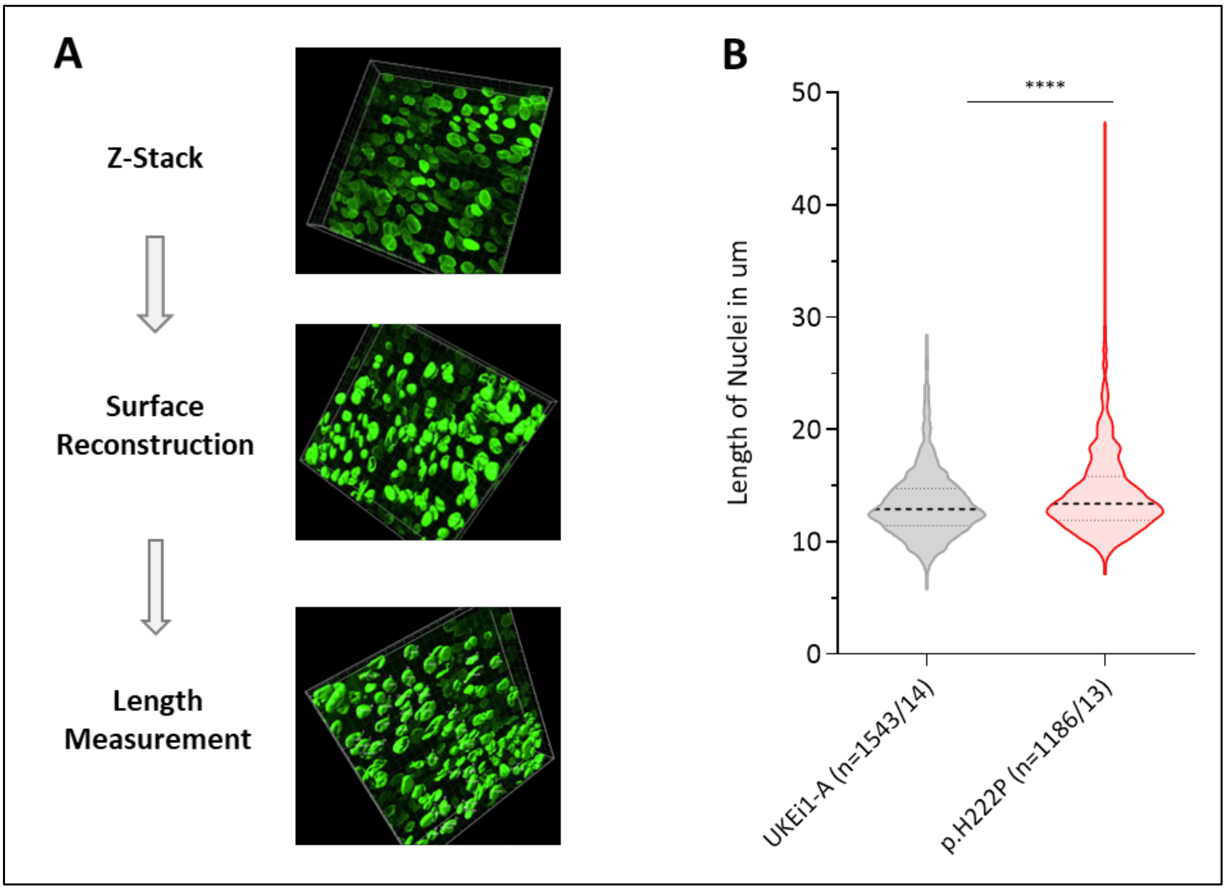

Figure 42 **A** Schematic workflow of acquiring Z-stacks of lamin A and C-stained nuclei and its subsequent surface reconstruction to obtain the length of the longest axis. **B** Length (y-axis) of single nuclei stained for lamin A and C in fixed EHTs of the unrelated control cell line UKEi1-A and p.H222P (x-axis). n= nuclei/confocal images of 3 to 4 EHTs. Blinded analysis; unpaired t-test; p-value <0.0001.

4.3.4.2 YAP and Ki67 translocation

The findings described above led to the hypothesis that altered YAP1 signalling could play a role in mechanotransduction of p.H222P EHTs already under basal conditions and exaggerated in AE-exposed EHTs (4h). YAP1 is not only involved in transduction of mechanical cues into changes of gene expression of proteins involved in mechanoresponses, but also of genes involved in proliferation (Panciera *et al.*, 2017). As an initial test to investigate whether YAP1 and associated proliferation underlies the mechanical coupling defect in p.H222P, fixed tissues of TC and 4h intervention were stained for YAP1 and the proliferation marker Ki-67 (marker of proliferation Ki-67; *MKI67*). Indeed, YAP1 and the cell cycle marker Ki-67 appeared to show more pronounced nuclear rather than cytosolic localisation (Figure 43). Of note, systematic quantification between the two genotypes was not performed yet and would require careful analysis of 3D images to account for effects of different planes. Thus, the data has to be considered preliminary at this point.

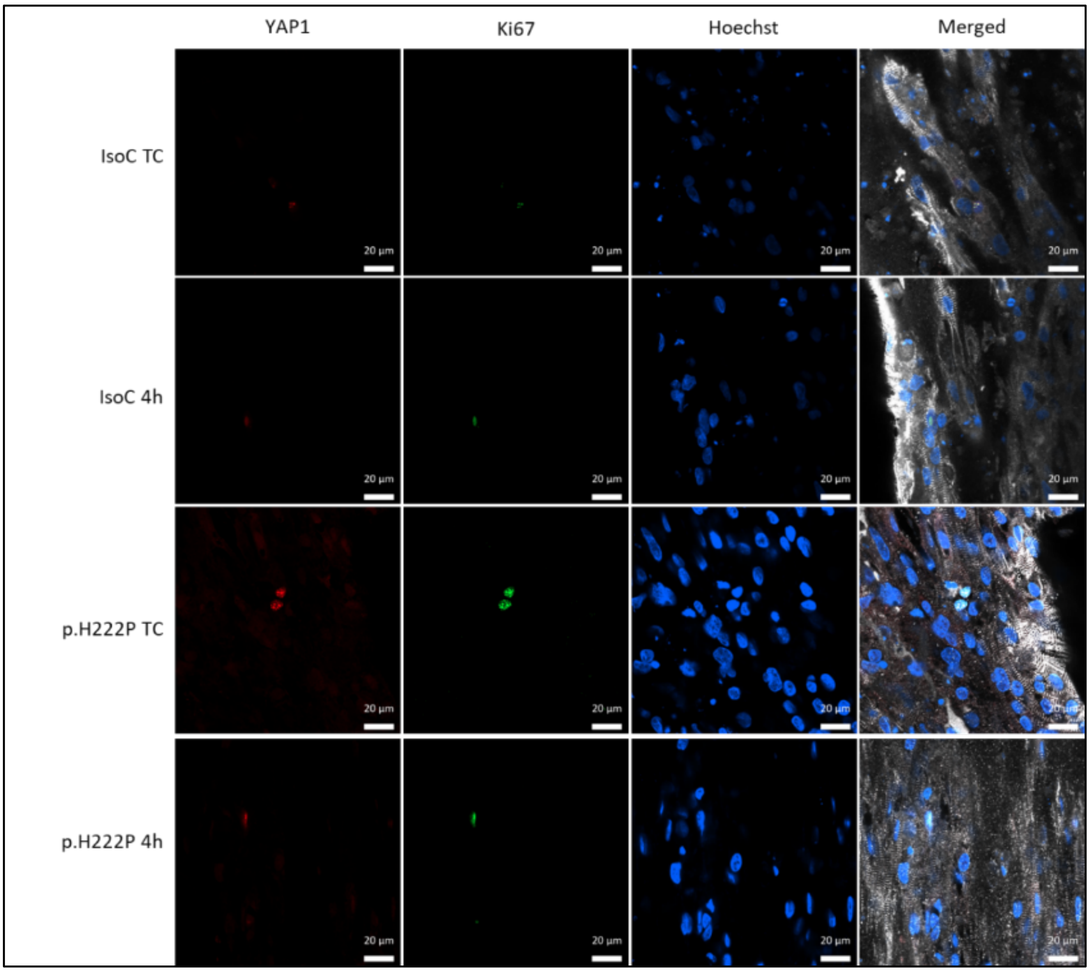

Figure 43 Fixed EHTs subjected to AE (4h) or as TC stained for YAP1 (red), the proliferation marker Ki67 (green), Hoechst (blue) and α-actinin 2 (grey). Representative pictures of individual EHTs. Scale bar 20 µm.

4.3.5 Summary of p.H222P characterisation

To summarise, the functional phenotype of p.H222P EHTs was rather mild under baseline conditions. EHTs of p.H222P CMs showed a tendency towards lower force of contraction, higher beating frequency and shorter relaxation time compared to the isogenic control IsoC. The sensitivity of p.H222P EHTs to external calcium was reduced in one batch in comparison to IsoC. Furthermore, the RMP of p.H222P was significantly less negative in several batches of EHTs than of IsoC. Several ion channels were differentially expressed on transcriptomic level between the two genotypes. However, the fold change of ion channel expression differed between differentiation and culture media conditions. A functional phenotype was successfully provoked by the insertion of metal braces for AE, which induced a drop in fractional shortening. In addition, p.H222P exhibited a larger gene expression response to mechanical stress than IsoC. Further, in one batch p.H222P EHTs lamin A to C ratio was altered, which was confirmed on RNA level. Finally, nuclear elongation could be detected in p.H222P but not in an unrelated control line (UKEi1-A) under baseline conditions.

4.4 Characterisation and partial rescue of the human LMNA-KO model

As described in the earlier part of this thesis, a LMNA-KO cell line was generated from the p.H222P line by CRISPR/Cas9 (Figure 15). It was used as a more severe laminopathy model. First, the molecular consequences of the mutation were explored in 2D culture, and its phenotypic consequences in the human 3D EHT model. Second, a gene replacement therapy was tested by transducing lamin A cDNA with an *AAV6-pCMV-GFP-2A-cLMNA* construct.

4.4.1 Design of the lamin A gene replacement vector

An AAV6 construct (*AAV6-pCMV-GFP-2A-cLMNA;* Figure S 1) was designed to transduce hiPSC-CMs and drive exogenous lamin A expression as a gene replacement therapy (GT). Dr. Ingke Braren from the HEXT vector facility at the UKE Hamburg kindly cloned the vector and produced the viral particles. The cytomegalovirus promoter (pCMV), which was known to drive strong expression in hiPSC-CM EHTs (Saleem *et al.*, 2020), was selected as promotor in this construct. The pCMV was cloned upstream to enhanced green fluorescent protein (GFP) and a two amino acid (2A) peptide that should result in cleavage of the following downstream human prelamin A cDNA (Figure 44; Figure S 1). The cleavage of GFP from exogenous lamin A by the 2A peptide was intended with regard to the structural importance of lamin A to assemble to the complex nuclear meshwork. The structural consequence of tagged lamin A is to our knowledge not thoroughly investigated. In the following experiments EHTs were transduced with a multiplicity of infection (MOI) of 30,000, which is below the range (70,000 to 700,000) of other studies in EHTs (Saleem *et al.*, 2020), but 3-fold higher than in a *MYBPC3* gene replacement therapy (MOI 10,000) in 2D hiPSC-CMs (Prondzynski *et al.*, 2017).

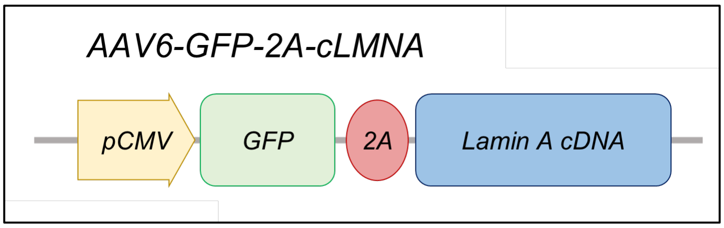

Figure 44 Schematic overview of the plasmid *AAV6-pCMV-GFP-2A-cLMNA* that was used for lamin A gene replacement therapy showing features of Cytomegalovirus promoter (pCMV) driving expression of enhanced green fluorescent protein (GFP) and human lamin A cDNA intermitted by a two amino acid (2A) peptide signal.

4.4.2 Verification of the absence of A-type lamins

A homozygous T insertion should result in a premature stop codon in all transcribed RNA. Further, NMD of pathological RNA should result in a complete absence of lamin A and C. To study this hypothesis, IsoC and LMNA-KO hiPSCs were differentiated to CMs and treated with the NMD inhibitors puromycin (Kosmidis *et al.*, 2016) or emetine (Vignier *et al.*, 2009) or DMSO as a control. Subsequently, mRNA was extracted, reverse transcribed to cDNA and amplified for lamin A and C transcript. Lamin A and C bands were detected in IsoC under all conditions at the expected size of 1,493 and 1,416 bp, respectively. Approximately similar band intensities of lamin A and C indicated the expected equal transcript levels of the two isoforms (Figure 45 A) Limitations due to the semi-quantitative approach have to be considered. In contrast to IsoC, a faint lamin A band was detected in one DMSO- and one puromycin-treated LMNA-KO sample. Treatment with emetine but not puromycin led to a more intense appearance of lamin A bands, indicating major degradation of the mutated mRNA via NMD (Figure 45 B). The lack of effect of puromycin suggests that the treatment conditions were not sufficient. Unexpectedly, lamin C was detected in all LMNA-KO samples. The band for lamin C has not been further characterised yet. Nevertheless, bands were considerably more pronounced in the emetine samples, underlining the impact of NMD on lamin C transcript as well (Figure 45 B).

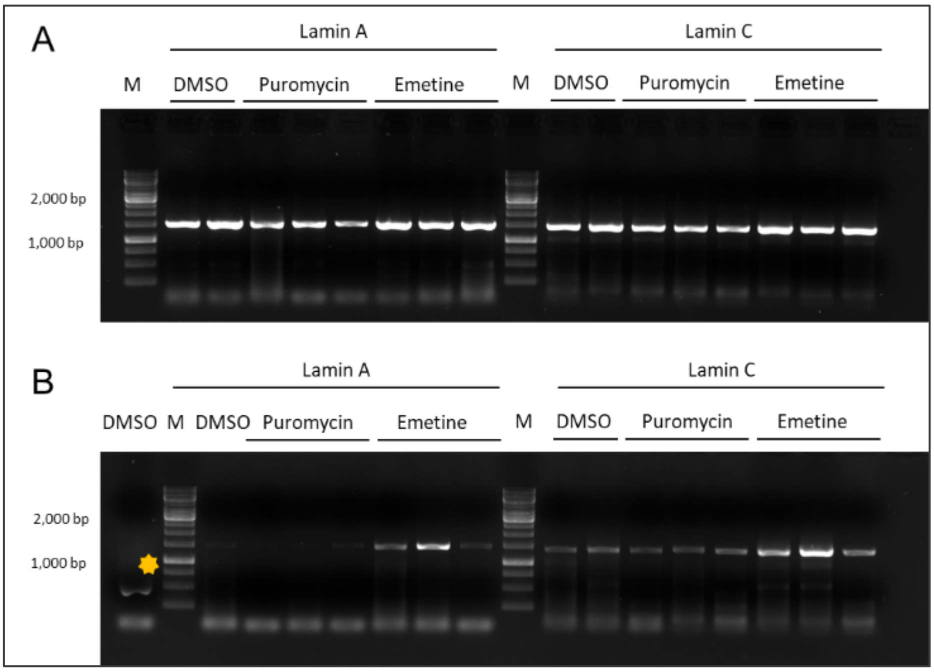

Figure 45 PCR products of lamin A and lamin C transcripts on cDNA isolated from IsoC (**A**) and LMNA-KO (**B**) hiPSC-CMs and treated with DMSO as vehicle or puromycin (130 µg/mL) and emetine (900 µg/mL) to inhibit nonsense-mediated mRNA decay. Asterisk indicates non-specific contamination in the sample.

Western blot analysis was performed to evaluate the consequence of the absence of lamin A mRNA on protein level. Moreover, the success of a restoration of lamin A on protein level was assessed in GT treated EHTs. Therefore, IsoC and LMNA-KO EHTs were either left non-transduced as control (NT) or transduced (GT) with *AAV6-pCMV-GFP-2A-cLMN*A (Figure S 1). EHT lysates of all groups were analysed by Western blot. Staining with an anti-GFP antibody revealed bands at approximately 31 kDa only in the GT groups, verifying successful transduction in both, IsoC and p.H222P (Figure 46 A). Staining with MYBPC3 as a loading control, revealed bands at approximately 150 kDa, but with lower intensity for LMNA-KO groups than for IsoC samples (Figure 46 A). The MYBPC signal was slightly higher in LMNA-KO GT samples than in LMNA-KO NT. Finally, staining with anti-lamin A and C gave rise to bands at 74 and 62 kDa in IsoC, as seen before, and no signal in LMNA-KO NT, as expected (Figure 46 A). In both GT groups, strong lamin A signal intensities were detected, which confirms successful overexpression. LMNA-KO GT and IsoC GT EHTs exhibited 8-fold higher lamin A signals than IsoC NT EHTs, when normalising lamin A level to the loading control MYBPC3 (Figure 46 B). Lamin C signals in IsoC were mainly unaffected by the GT and remained absent in LMNA-KO. Faint bands with an apparent MW less than expected for lamin C were detected in both LMNA-KO groups but were not further characterised.

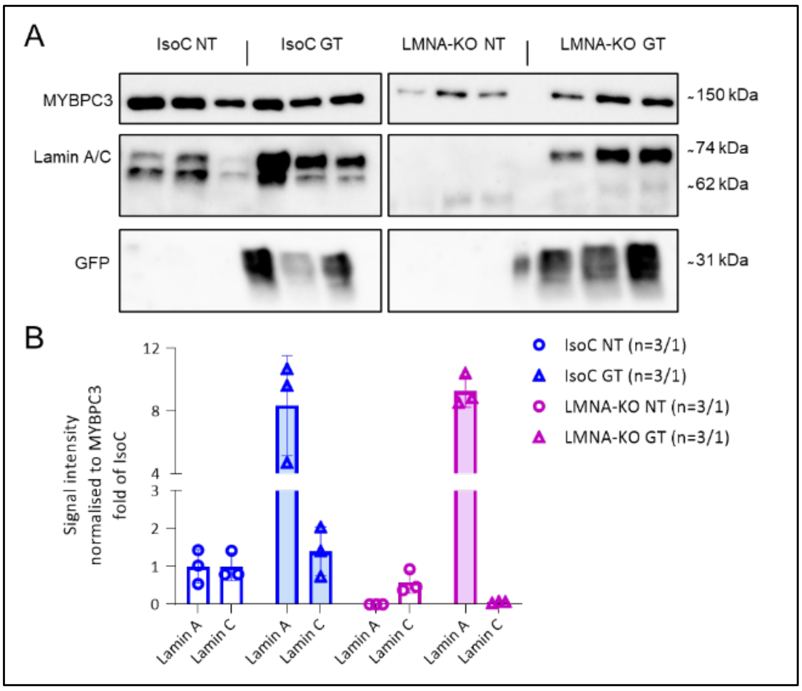

Figure 46 **A** Representative western blot of IsoC non-transduced (NT), IsoC transduced with gene replacement therapy (GT), LMNA-KO NT and LMNA-KO GT EHT lysates, stained for lamin A and C, GFP and MYBPC3 as loading control. **B** Quantification of signal intensity of lamin A and C as fold change compared to IsoC, normalised to MYBPC3.

4.4.3 Functional phenotype of LMNA-KO EHTs

To characterise the functional phenotype of the LMNA-KO disease model, differentiated CMs of IsoC and LMNA-KO were casted to EHTs, and contraction parameters were compared on day 19 or 20 in culture (Figure 47). It was not feasible to perform analysis on a later time point due to a collapse in force of LMNA-KO EHTs (Figure 50 C). LMNA-KO EHTs presented significantly lower force of contraction, contraction velocity and relaxation time than IsoC EHTs (Figure 47 A, B and C; nested t-test). Resting length was significantly higher in LMNA-KO EHTs than IsoC EHTs (Figure 47 D; nested t-test), indicating incomplete remodelling.

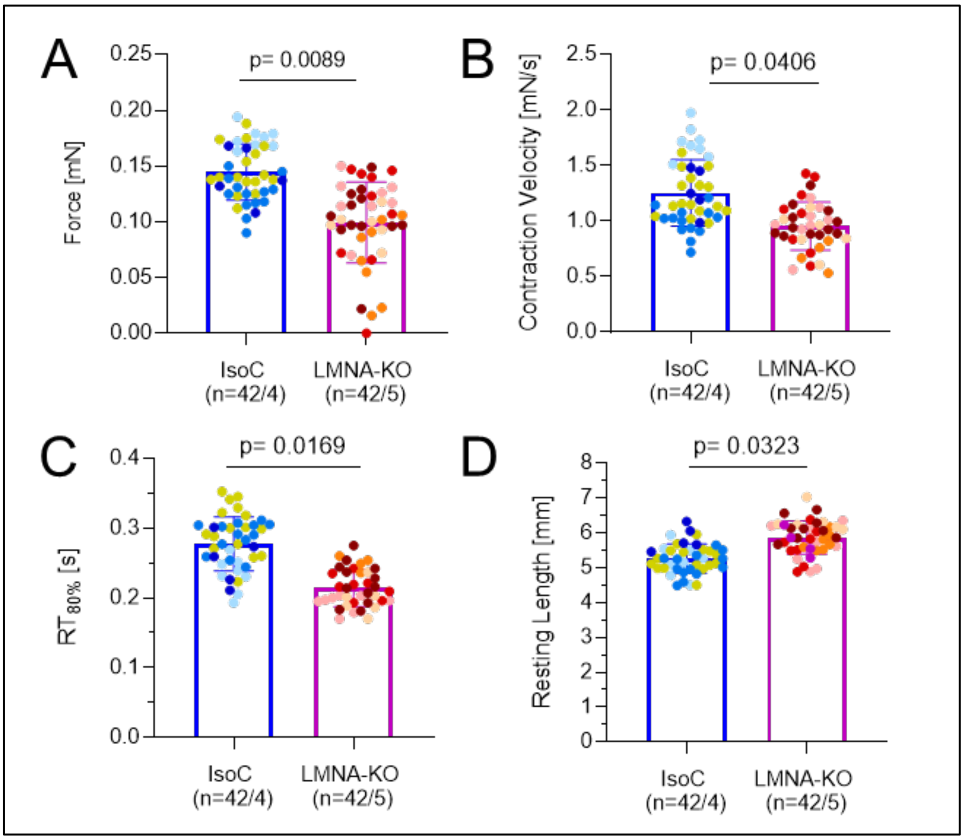

Figure 47 Functional parameters, such as relaxation time (RT) of full-length LMNA-KO and corresponding IsoC EHTs measured under baseline conditions on day 19 or 20 of culture. Each dot represents a single EHT and each colour of dot one batch. P-values were calculated based on nested t-test. n=number of EHTs / batches.

Beating frequency (Figure 48 A) appeared higher in LMNA-KO EHTs but the difference did not reach significance. LMNA-KO EHTs also showed a tendency towards a higher irregular beating pattern (RR-scatter; Figure 48 B), but the difference was not large and not significant. Overall, LMNA-KO EHTs showed a similar, but more pronounced contractile phenotype than p.H222P (see Figure 22).

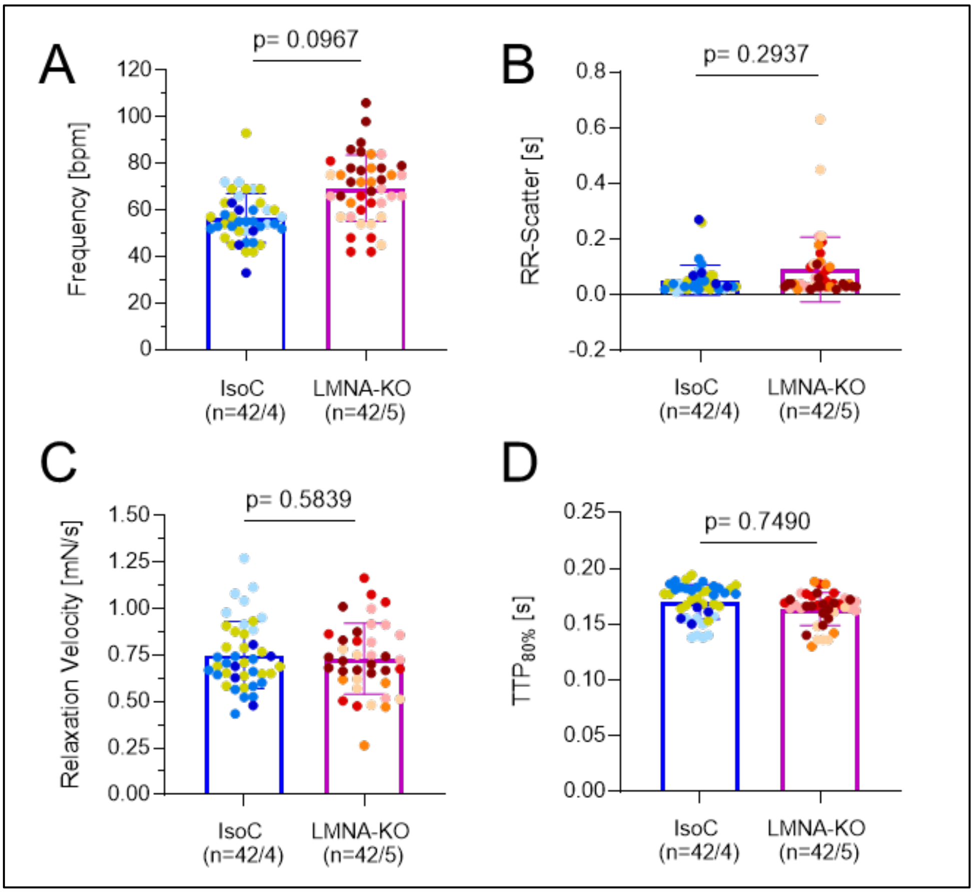

Figure 48 Functional parameters, such as time to peak ($TTP_{80\%}$) of full-length LMNA-KO and corresponding IsoC EHTs measured under baseline conditions on day 19 or 20 of culture. Each dot represents a single EHT and each colour of dot one batch. P-values were calculated by nested t-test. n=number of EHTs / batches.

4.4.4 Gene replacement therapy in LMNA-KO EHTs

On day 15 of culture, half of LMNA-KO and IsoC EHTs were transduced with *AAV6-pCMV-GFP-2A-cLMNA* at a MOI of 30,000 (GT), the other half was left non-transduced as control (NT). Remodelling of the EHTs was assessed by the measurement of the width of the EHTs in a blinded manner on the last day of culture (Figure 49 A). This revealed a non-significant tendency towards a reduced remodelling capacity in NT LMNA-KO EHTs, represented as a higher width than all other groups (Figure 49 B).

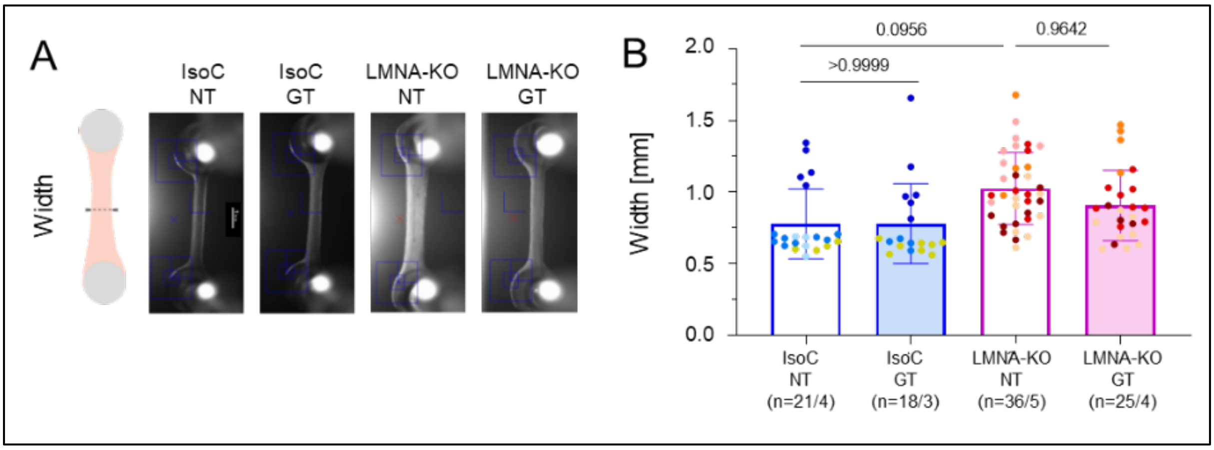

Figure 49 **A** Schematic overview with a dotted line indicating the location for width measurements. Representative images of EHTs of the groups IsoC NT, IsoC GT, LMNA-KO NT and LMNA-KO GT. Scale bar 1 mm. **B** Blinded measurements of EHT width (y-axis) of all groups (x-axis). Each dot represents one EHT and each colour one batch. n=number of EHTs / batches. Blinded analysis; nested one-way ANOVA.

Force development of all groups was tracked over time with spontaneously contracting EHTs measured in complete culture medium. A representative batch is shown in Figure 50 A. IsoC EHTs continuously increased in force over the whole culture period. LMNA-KO EHTs started delayed, reached their maximal force on day 19 (75% of IsoC maximal force) and steeply declined in force to 13% of maximal force of IsoC on day 30. This decline in force was less pronounced in LMNA-KO GT EHTs that only slowly declined in force to 61% of maximal force of IsoC on day 30 (Figure 50 A). A summary of all analysed batches on day 28 to 31 in culture showed that collapse in force could be partially prevented upon therapeutic intervention on day 15. Indeed, final force of each LMNA-KO NT EHT was less than half of its own maximum during culture time (Figure 50 C and D; mean 0.046 mN and 40.06%). Upon therapy LMNA-KO GT EHTs were at 77.92% (0.091 mN) of their maximum force during culture time (Figure 50 C and D). Compared to the generally stable IsoC (97.70%; 0.194 mN) and IsoC GT (100.00%), LMNA-KO NT, but not LMNA-KO GT showed a significant lower final force, verifying the partial reversion of the disease phenotype upon gene therapy.

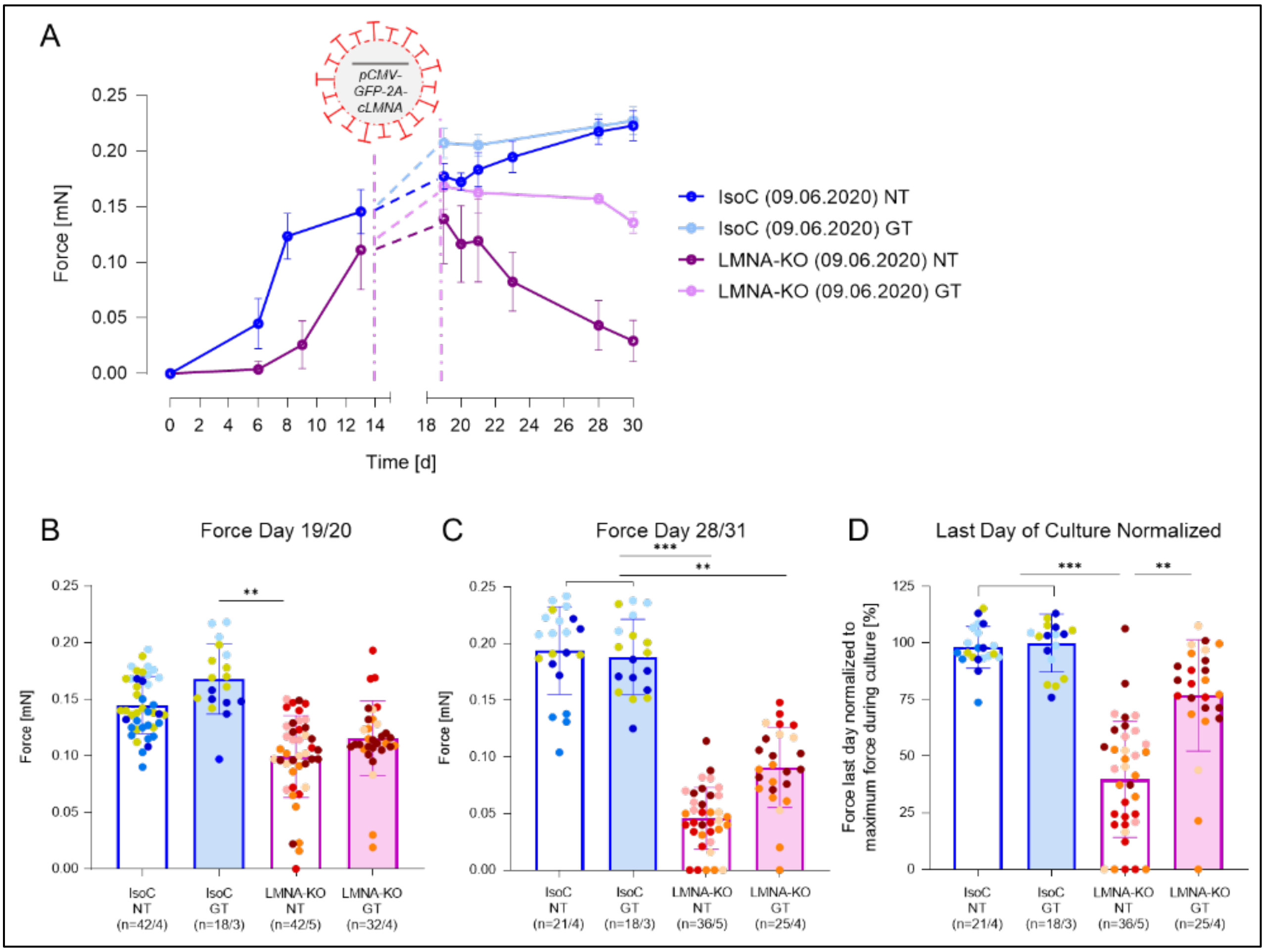

Figure 50 **A** Representative force development of one batch of EHTs of IsoC and LMNA-KO, GT group transduced on day 15 with *AAV6-pCMV-GFP-2A-cLMN*A. (dotted lines indicate transduction incubation time und continuous shaking) **B** and **C** Absolut force of EHTs on day 19/20 and final day of culture (day 28/31) and **D** force last day of culture normalised to maximum force during culture. Each dot represents one EHT and each colour one batch. n=number of EHTs / batches. Blinded analysis; nested one-way ANOVA, p-value ** <0.01 *** <0.001.

4.4.5 Toxicity studies of gene replacement therapy

The complex and critical roles of lamin A in various biological processes indicate that balanced protein levels of lamin A are important. Indeed, transgenic cardiac-specific overexpression of lamin A in WT mice had some poorly characterised adverse effects (Frock *et al.*, 2012). This question was therefore studied by overexpressing lamin A at increasing doses (MOI) in IsoC, p.H222P and an unrelated control line (UKEi3), i.e. on the background of normal or reduced endogenous lamin A levels.

4.4.5.1 Functional contractile parameters in GT IsoC versus IsoC

Putative adverse effects of the GT on contraction pattern or kinetics were assessed in three batches of IsoC EHTs. To visualise potential changes the fold-difference of each individual EHT compared to the mean of all EHTs was plotted as a heat map (Figure 51). Overall, all parameters for all EHTs were in the range between 0.5 and 2-fold, depicting low overall scatter and the absence of systematic differences between all EHTs. Only the RR-scatter that is indicating arrhythmogenicity showed an overall higher scatter. Interestingly, no clustering upon GT, rather individual outliers were observed (Figure 51), indicating that GT had no effect on EHT function in these batches.

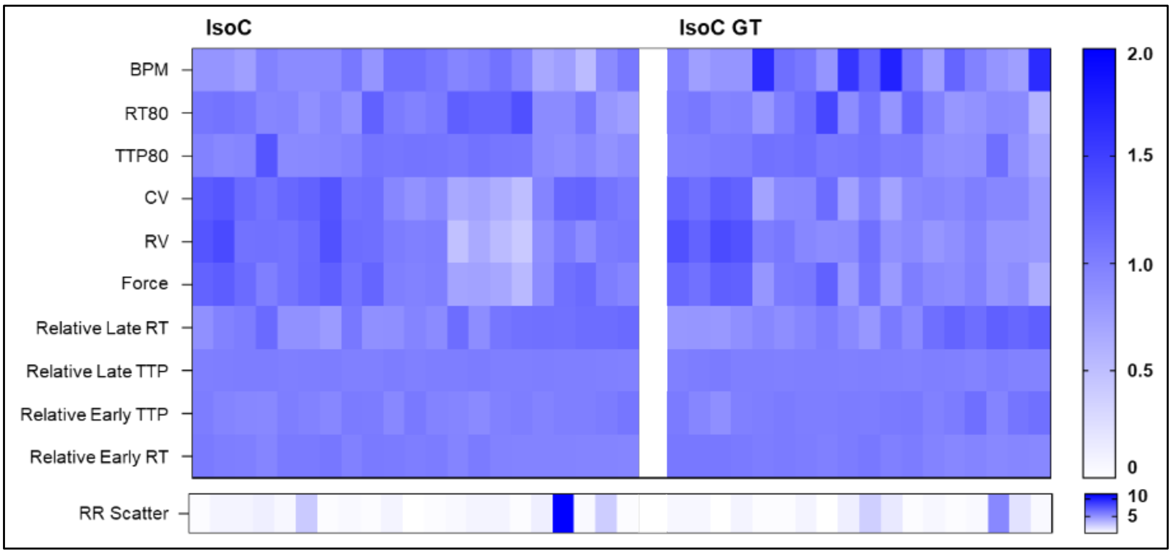

Figure 51 Effect of GT (MOI 30,000 on day 15, analysis day 30/31) on contractile parameters in IsoC EHTs, shown as single EHTs of IsoC (21/4) and IsoC GT (18/3) normalised to the mean of all values. Beats per minute (BPM), relaxation time 80% (RT80), time to peak -80% (TTP80), contraction velocity (CV), relaxation velocity (RV), force, relative late relaxation time, relative late time to peak, relative early time to peak, relative early relaxation time and RR scatter (variability of R-R/beat-to-beat distance).

4.4.5.2 Dose effect of gene replacement therapy

To further evaluate the toxic ranges of lamin A overexpression in the background of reduced and mutated lamin as well as normal WT lamin, EHTs of both p.H222P and IsoC were transduced with *AAV6-pCMV-GFP-2A-cLMN*A at MOIs ranging from 30,000 to 300,000 on day 18 in culture (Figure 52 and Figure 53). Development of absolute force of contraction was examined and normalised to the day of transduction. Non-transduced IsoC (NT) almost doubled their force until the end of culture (Figure 52). In contrast, the groups transduced with *AAV6-pCMV-GFP-2A-cLMNA* showed either slightly increasing forces (mean 151% of transduction at day 15; MOI 30,000) or a decline. In the MOI of 100,000 group, force gradually decreased after transduction and reached 40% of their initial force on day 60. In the MOI 300,000 group, force drastically decreased and completely ceased on day 48 (Figure 52). The data indicate a marked, dose-dependent toxicity of lamin A overexpression in this model.

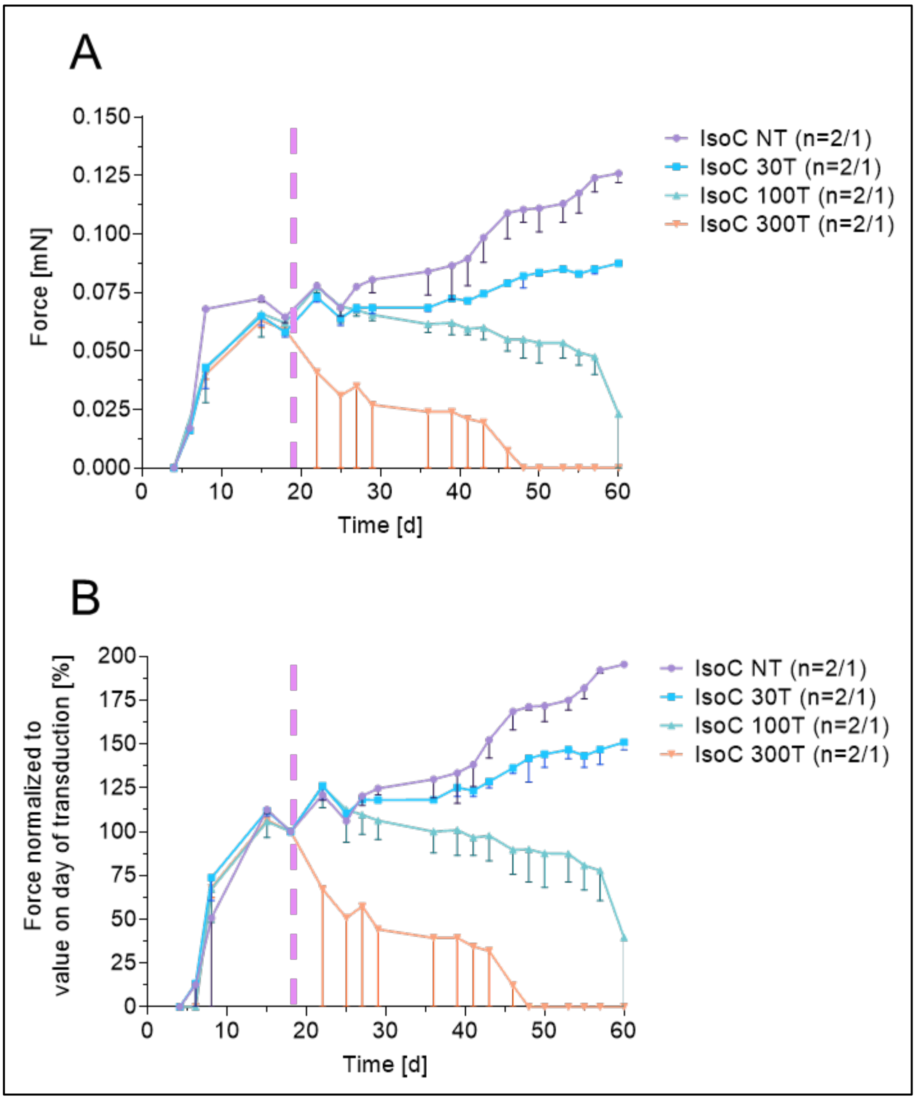

Figure 52 IsoC EHTs transduced on day 18 (dotted line) in culture with doses of MOI 30,000 (30T), 100,000 (100T) and 300,000 (300T) of the GT. Force development of the groups as **A** absolute and **B** normalised force. Error bars represent -SEM. n=number of EHTs / batches.

Non-transduced p.H222P EHTs dropped in force preceding the day of transduction but stabilised over the culture period (Figure 53). EHTs transduced at MOI of 30,000 did not differ from NT (Figure 53). In the MOI 100,000 group, force declined to approximately 86% of their initial force (Figure 53 B), in the MOI 300,000 group in p.H222P to 34% of their initial force (Figure 53 B). The GT induced drop in force was thus less pronounced than in IsoC EHTs (Figure 52 B), but still marked and dose dependent. The low replicate number in this series (n=2) makes the observation preliminary.

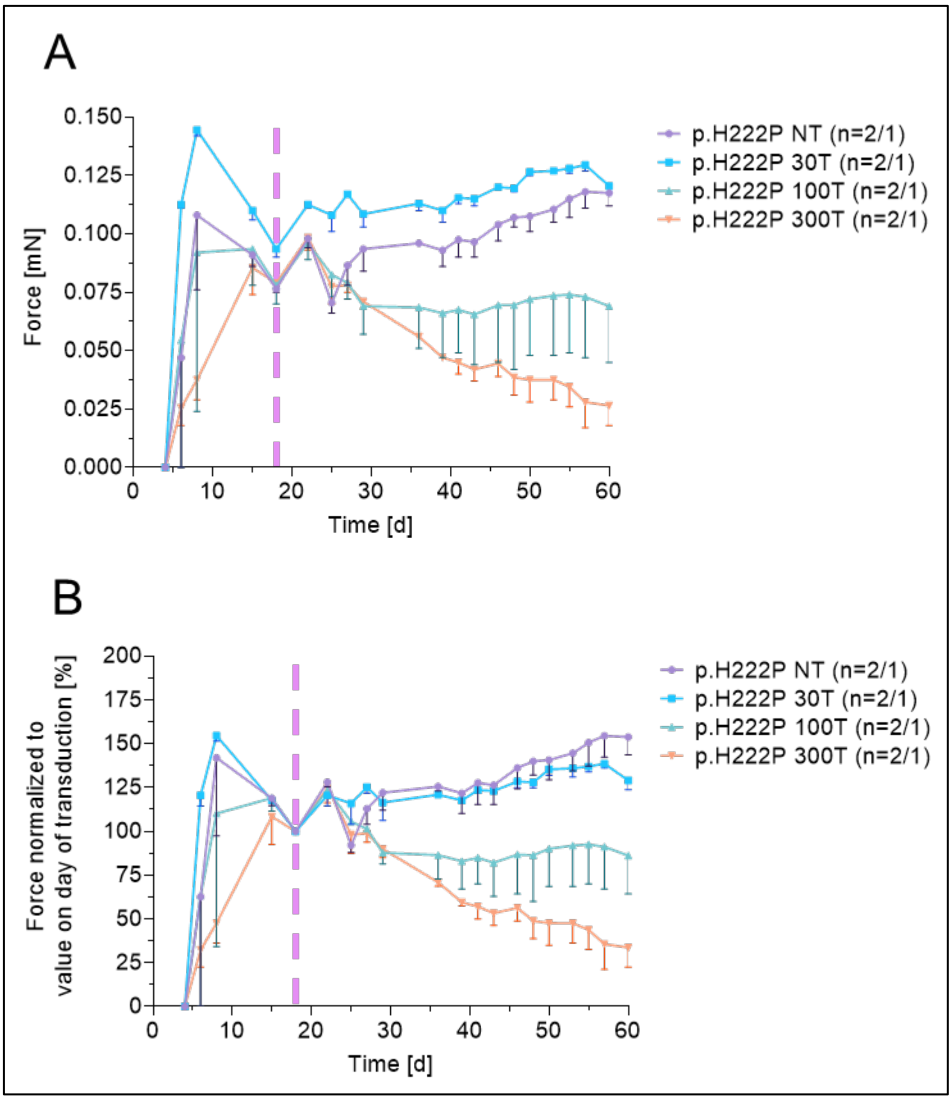

Figure 53 p.H222P EHTs transduced on day 18 (dotted line) in culture with doses of MOI 30,000 (30T), 100,000 (100T) and 300,000 (300T) of the GT. Force development of the groups as **A** absolute and **B** normalised force. Error bars represent -SEM. n=number of EHTs / batches.

Given the breakdown of force in lamin A-overexpressing EHTs, classical biomarkers of heart HF were analysed in culture media. Concentrations of cardiac troponin I and N-terminal prohormone of brain natriuretic peptide (NT-proBNP) were determined in culture media of EHTs after therapeutic intervention (Figure 54). The first samples were taken three days after transduction and the second 7 days after transduction, in which EHTs have been cultured only for two days. Troponin I levels were overall higher in the media samples of the 3-day group compared to the 7-day group, regardless of being transduced or non-transduced EHTs. The difference might occur due to the time span the EHT were incubated in the media and had time to release troponin I. Unexpectedly, the GT intervention had no clear effect on troponin I media concentrations nor NT-pro-BNP media concentrations (Figure 54 A - D). The lack of effect indicates that the functional toxicity (Figure 52 and Figure 53) was not simply due to death of CMs.

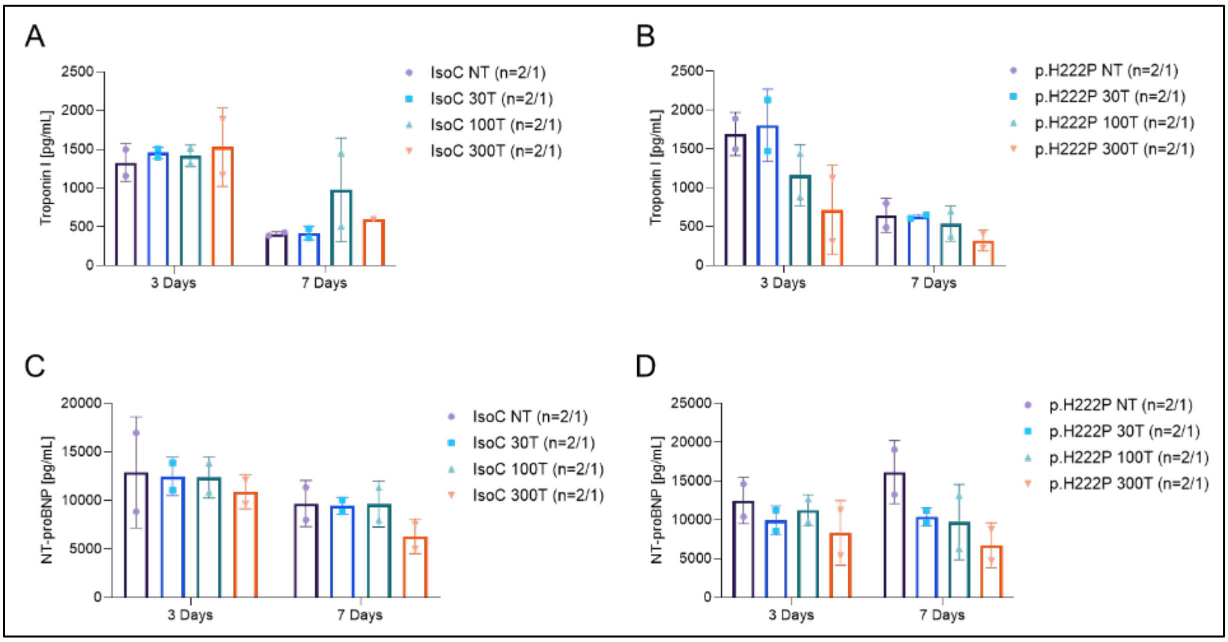

Figure 54 Concentration of cardiac troponin I or N-terminal prohormone of brain natriuretic peptide (NT-proBNP; y-axis) in EHT media of p.H222P or IsoC EHTs either 3 days or 7 days (x-axis) after GT of MOI ranging from 30,000 (30T) to 300,000 (300T) or NT. n=number of EHTs / batches.

The next step was to examine the effect of GT on the proteomic profile. Therefore, unlabelled mass spectrometry (MS) was performed on NT and GT IsoC and p.H222P samples transduced with the different MOIs. As expected, lamin A abundance increased with higher MOIs in both groups (Figure 55 A). While the increase in lamin A in p.H222P started already at MOI 30,000 (~2-fold) and then levelled off (Figure 55 A), it started in IsoC only at MOI 100,000 and then steeply increased with MOI 300,000 (to ~6-fold). Unsupervised clustering of the total proteome resulted mainly in clustering according to the genotype, i.e., the p.H222P groups clustered together and the IsoC groups (Figure 55 B). Interestingly, however, p.H222P EHTs transduced at an MOI of 300,000 clustered closer with IsoC samples that were transduced at MOIs of 30,000 and 100,000 (Figure 55 B), indicating some potential reversion of the p.H222P phenotype by overexpression of lamin A.

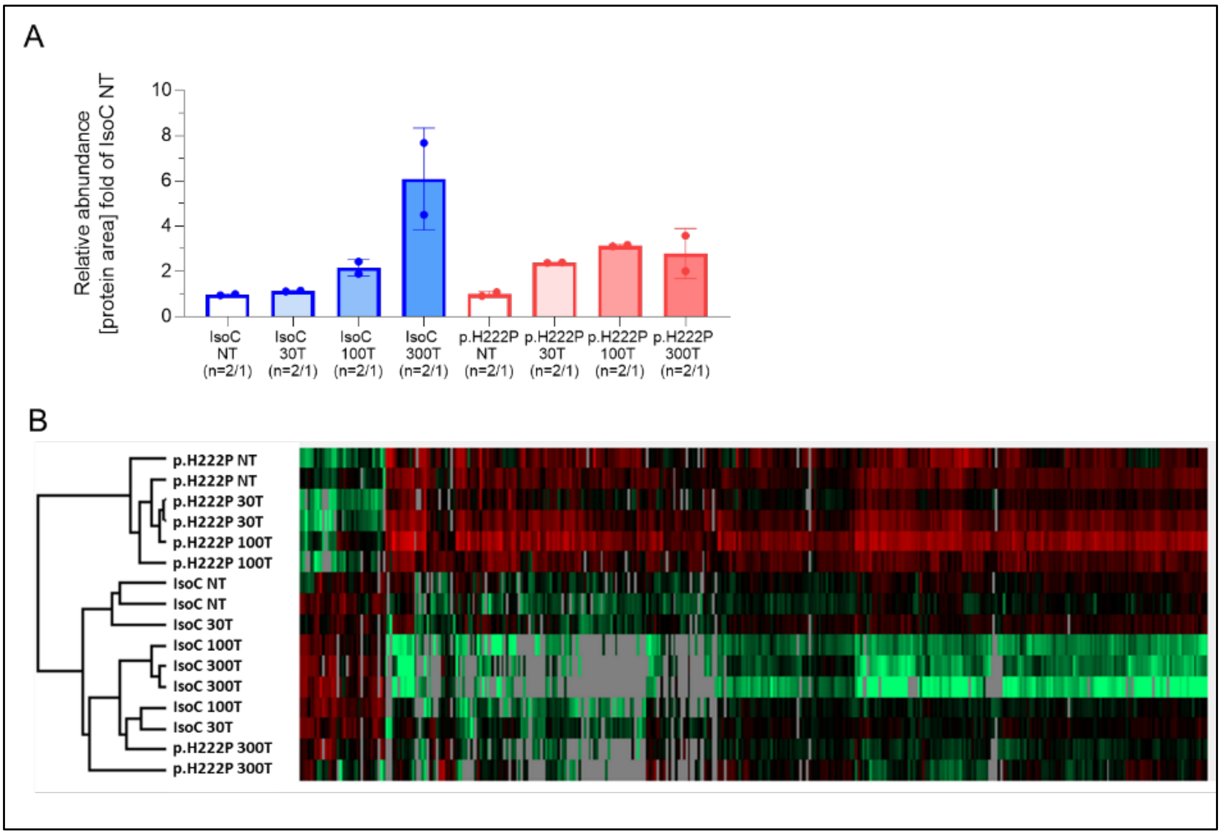

Figure 55 **A** Quantification of lamin A abundance in p.H222P and IsoC EHTs either NT or transduced with GT of different MOIs ranging from 30,000 (30T) to 300,000 (300T) on 15 days in culture via MS (protein area as fold of IsoC NT; y-axis). n=number of EHTs / batches. **B** Unsupervised clustering of the proteome profile, showing proximities of the different transduced groups.

4.4.5.3 Long-term toxicity study in unrelated control cell line

To follow up on the negative effect of GT on force development of p.H222P and IsoC EHTs, EHTs of an unrelated control cell line, UKEi3, were transduced with *AAV6-pCMV-GFP-2A-cLMNA* (GT; Figure S 1) or *AAV6-pCMV-GFP* (GFP; Figure S 2) on day 28 of culture. Their force was tracked over 90 days after casting, to distinguish between a possible toxic effect of GFP or lamin. In stark contrast to the previous experiments, no drop in force was observed for either construct, even at MOI 300,000 (Figure 56 B).

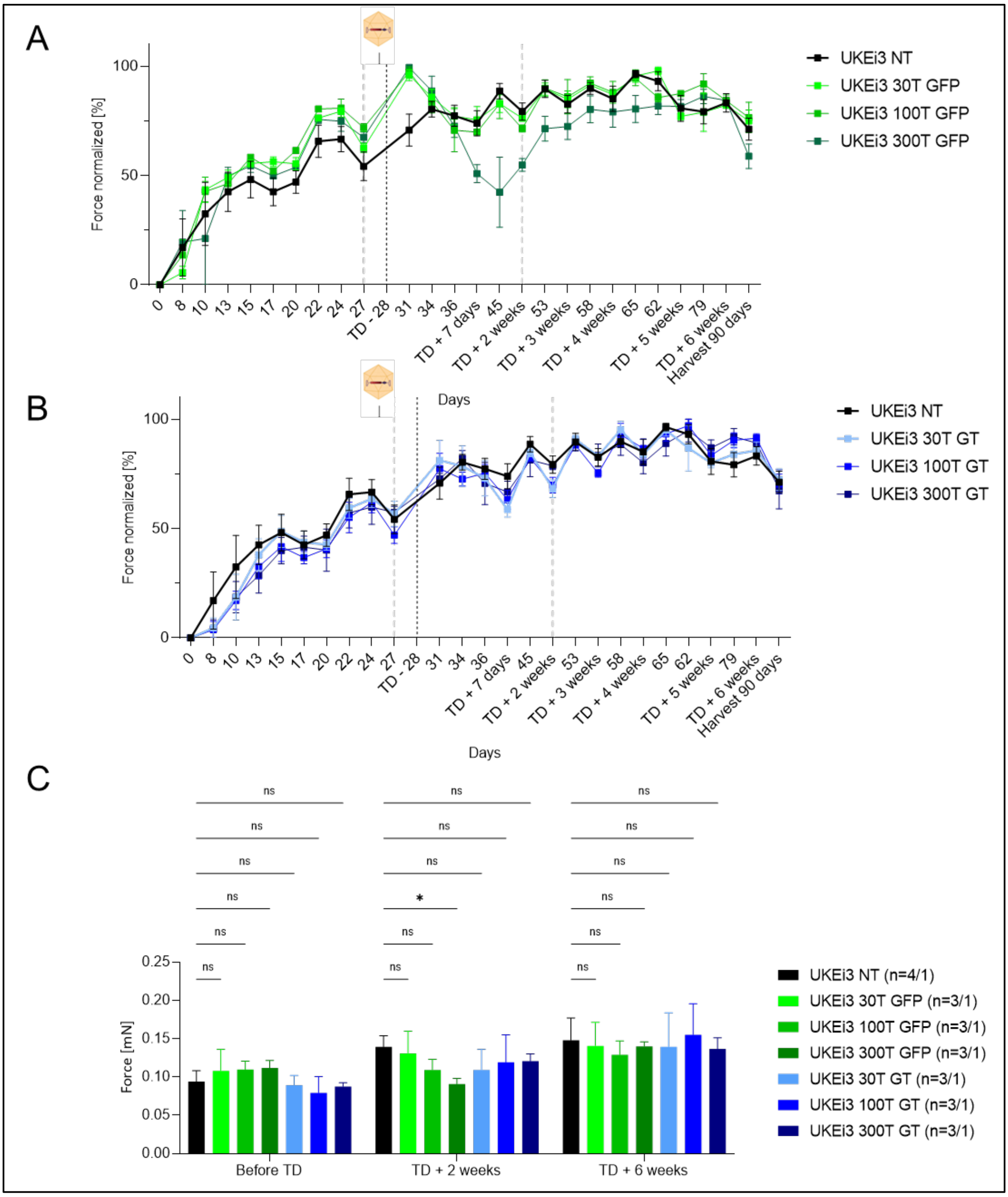

Figure 56 EHTs of an unrelated control cell line UKEi3 and their force normalised to the maximum force over the period of culture time. EHTs were transduced with an AAV6 either carrying **A** GFP (*AAV6-pCMV-GFP)* only or the **B** *AAV6-pCMV-GFP-2A-cLMN*A of different MOIs pre and post transduction (TD). **C** Absolute forces of day before TD, 2 weeks and 6 weeks after TD. ** p <0.005, 2-way ANOVA. n=number of EHTs / batches.

4.4.6 Transcriptomic changes in LMNA-KO model and therapeutic effects

To analyse the consequences of the absence of A-type lamins and its overexpression of lamin A by GT, EHTs were subjected to bulk RNA sequencing. The PCA of the data revealed a closer clustering of LMNA-KO and LMNA-KO GT, but a shift of LMNA-KO GT samples towards IsoC on component 2 (Figure 57 A). Remarkably, LMNA-KO versus IsoC exhibited 3486 DEGs, LMNA-KO GT versus IsoC 3300 DEGs, but LMNA-KO versus LMNA-KO GT resulted only in 759 DEGs (Figure 57 B).

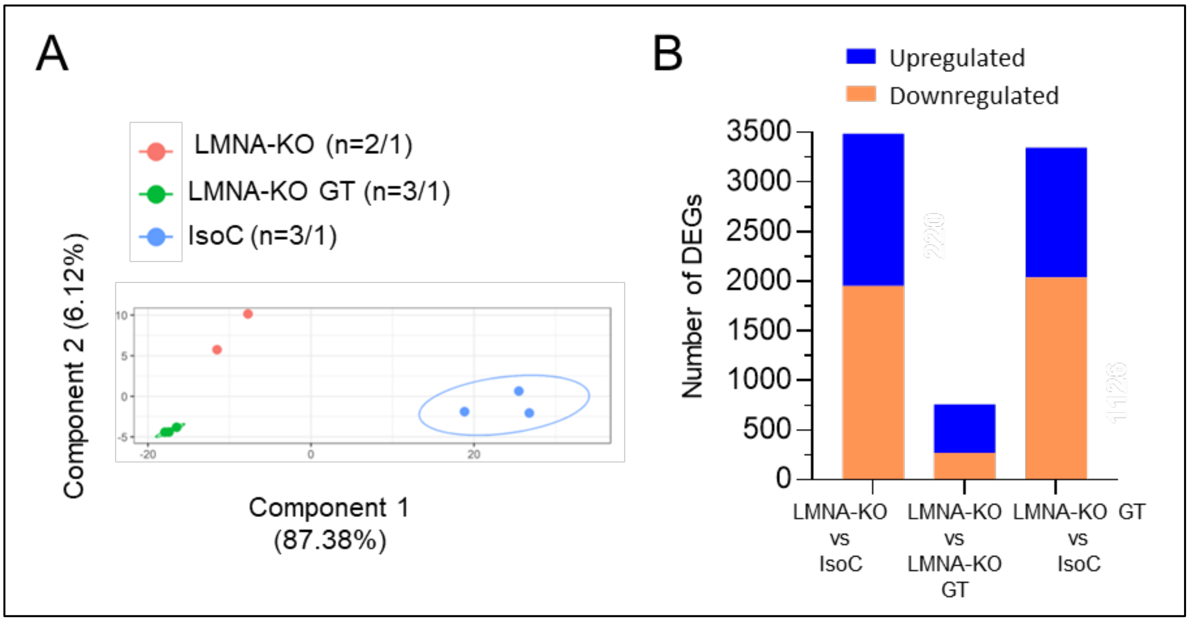

Figure 57 Bulk RNA sequencing of LMNA-KO, LMNA-KO transduced with GT and IsoC EHTs on day 30 in culture **A** PCA of samples each dot representing one EHT. n= EHTs/batch. Circles indicates genotype. **B** Number of significantly differentially expressed genes (DEGs), up- (blue) and downregulated (orange) when comparing different groups (FDR <0.05).

GO enrichment analyses of the DEGs between LMNA-KO versus IsoC indicated that a total of 329 GO pathways “biological function” were significantly enriched (false discovery rate [FDR] <0.05). The majority of pathways could be classified into chromosomal organisation, DNA replication and cell cycle (Figure 58 A). Other pathways were grouped into cardiac contraction and muscle development, microtubules and cardiac electrophysiology and conduction (Figure 58 A). A fundamental question was to what extent the DEGs overlap between the different comparisons. This analysis revealed that 2005 DEGs were shared between LMNA-KO versus IsoC and LMNA-KO GT versus IsoC, indicating unaltered genes upon therapeutic intervention (Figure 58 B). However, a LMNA-KO GT Enrichment Set was identified, consisting of 2524 genes which were found in LMNA-KO to be altered by GT intervention towards IsoC (Figure 58 B). Out of the 2524 genes, 1043 genes belonged still to the significantly DEGs between LMNA-KO GT and IsoC (Figure 58 B), indicating incomplete correction. GO enrichment analysis of the DEGs in the LMNA-KO GT Enrichment Set, demonstrate that mainly pathways involved in the regulation of cardiac sarcomere/contraction, oxidative metabolism and electrophysiology were corrected upon GT (Figure 58 C).

Figure 58 **A** GO Enrichment analysis of differentially expressed genes (DEGs) comparing LMNA-KO and IsoC. Manual classification of the 329 downregulated pathways: (i) chromosome organisation, DNA replication, cell cycle, (ii) cardiac contraction, muscle development, (iii) microtubules, (iv) cardiac electrophysiology, conduction (n=3 EHTs from one batch/ cell line, FDR <0.05). **B** Venn diagram showing the overlap (shaded; upper panel) of DEGs between LMNA-KO versus IsoC (blue; upper panel) and LMNA-KO GT versus IsoC (orange; upper and lower panel; P_{adj}-value <0.05). Comparing in total 3486 DEGs LMNA-KO versus IsoC, 2524 genes were corrected upon LMNA-KO GT towards IsoC ‘LMNA-KO GT Enrichment Set’ (blue; lower panel). Out of them, 1043 genes belong to the 3343 DEGs in LMNA-KO GT versus IsoC (shaded; lower panel). **C** DEGs of the LMNA-KO GT Enrichment Set were analysed for enrichment of GO terms of biological processes (electrophysiology in orange, oxidative metabolism in light blue, contraction in dark blue; normalised enrichment score [NES]; FDR < 0.05).

4.4.7 Proteomic analyses in LMNA-KO model and therapeutic effects

Next, the impact of the therapeutic intervention on the proteomic profile was assessed. Therefore, EHT samples of IsoC NT, LMNA-KO NT and LMNA-KO GT were subjected to quantitative MS analysis. This method allowed an exact quantification of A-type lamin peptides normalised to total peptides detected, which verified the complete absence of A-type lamins in LMNA-KO NT and restoration of lamin A to almost physiological level in LMNA-KO GT EHTs (Figure 59 A). Of note, this result differs considerably to that of the Western blot analysis (see Figure 46). Clustering of the overall proteome according to PCA showed proximity of the two LMNA-KO groups (NT and GT) and a shift of LMNA-KO GT towards IsoC on component 2 (Figure 59 B), very similar to the PCA of the transcriptome (Figure 57)

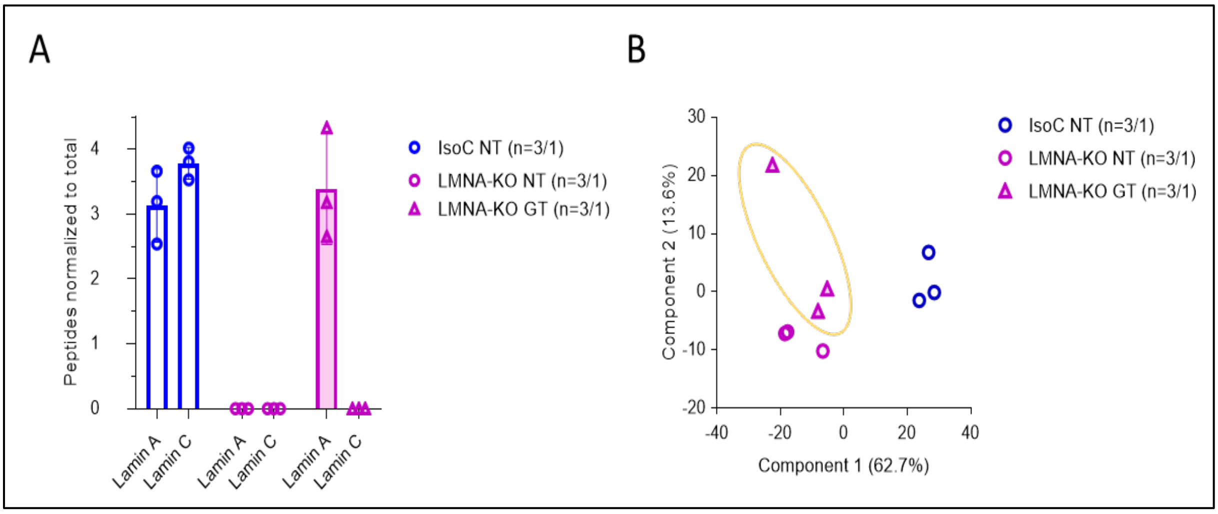

Figure 59 **A** Differential quantitative proteomics in EHT samples showing quantified lamin A and C peptides (n=EHTs/batches) normalised to total peptides of each sample. **B** PCA of MS analysis of IsoC NT (blue), LMNA-KO NT (purple circles) and LMNA-KO GT (purple rectangles in yellow circle) EHTs. Each symbol represents an EHT (n=EHTs/batches).

The MS proteome profile of single EHT samples was analysed in a supervised clustering on the basis of differentially expressed proteins in LMNA-KO NT versus LMNA-KO GT. Overall, the similarity between LMNA-KO NT and GT and the dissimilarity to IsoC prevailed. However, some clusters of LMNA-KO GT showed a shift towards the expression pattern of IsoC samples (Figure 60).

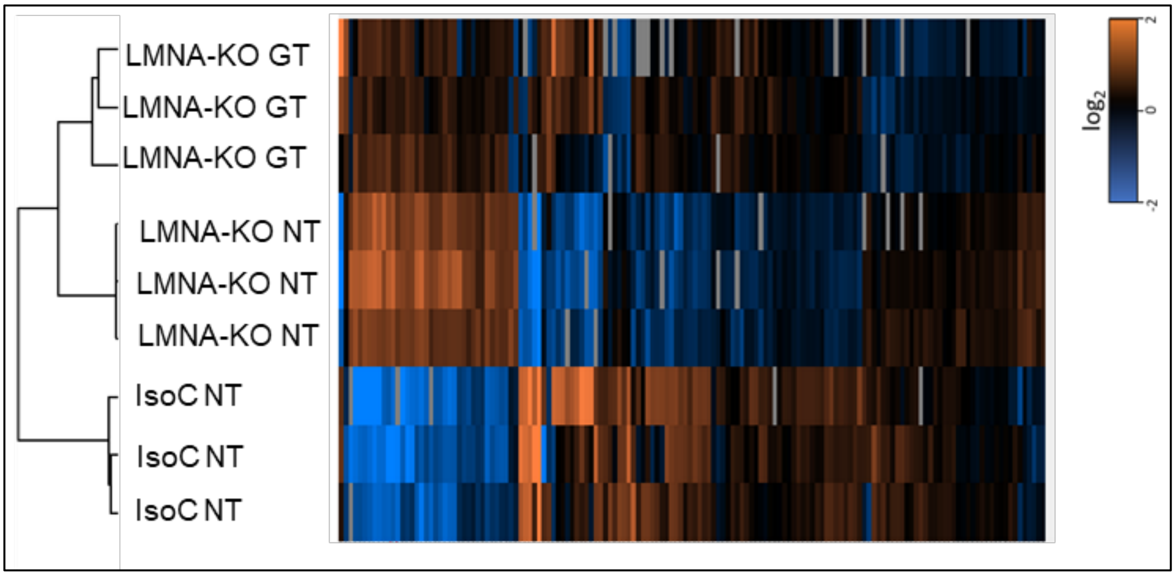

Figure 60 Supervised clustering shown as a heatmap indicating Log$_2$ values (LMNA-KO vs LMNA-KO GT) of differential quantitative MS of IsoC, LMNA-KO and LMNA-KO GT EHTs (FDR<0.05). 3 EHTs of one batch per genotype and intervention.

To investigate the consequence of the absence of A-type lamins on their interaction partners, the abundance of selected partners (Carmosino *et al.*, 2014; Brayson and Shanahan, 2017; Donnaloja *et al.*, 2020) was compared between the three groups (Figure 61 A). The majority of the interaction partners were less abundant in the two LMNA-KO groups, but several were partially restored in LMNA-KO GT (*e.g.,* lamin B, emerin; Figure 61 A). To explore whether similar effects occurred in pathways identified in the transcriptome GT enrichment set before (*e.g.*, cardiac contraction, electrophysiology; Figure 58 C), the corresponding protein abundance was compared between the three groups (Figure 61 B). The majority of these proteins was downregulated (blue) in LMNA-KO NT versus IsoC and indeed partially normalised in LMNA-KO GT (Figure 61 B), well corresponding to similar changes of the transcriptome.

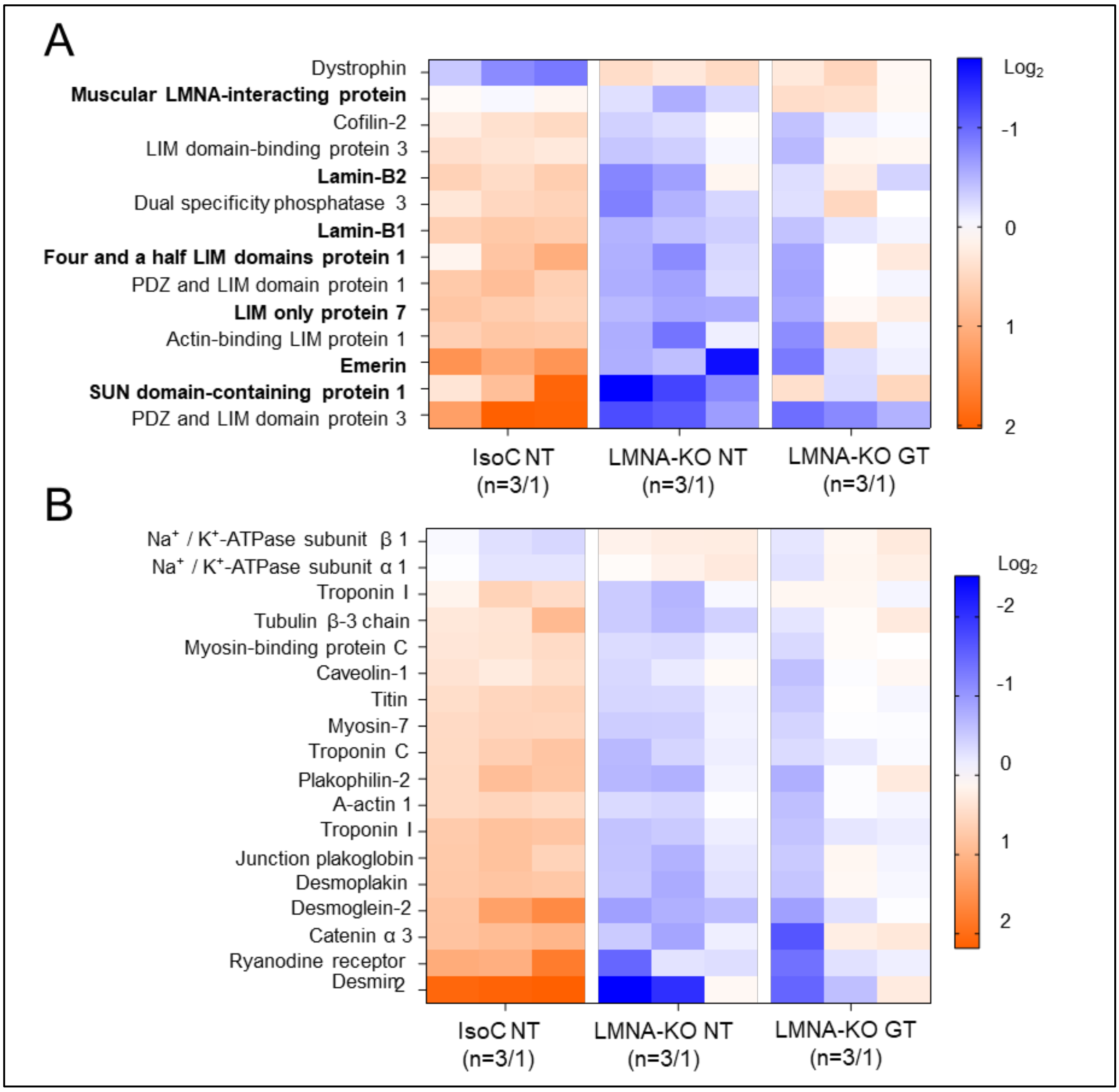

Figure 61 Selected proteins of the proteome profile of single EHTs of IsoC NT, LMNA-KO NT and LMNA-KO GT classified into **A** known interaction partners of lamin (Carmosino *et al.*, 2014; Brayson and Shanahan, 2017; Donnaloja *et al.*, 2020) and **B** important proteins involved in cardiac excitation-contraction coupling (Log_2 fold change from mean of all groups). Direct lamin A and C interactions partners are presented in bold (n=number of EHTs / batches; LMNA-KO NT versus IsoC NT p-value < 0.05, t-test).

4.4.8 Consequence of LMNA-KO on morphological level

The absence and the restoration of lamin A upon GT, respectively, was further explored by immunostaining of fixed tissues (day 30 or 31 of culture). Staining for lamin A and C demonstrated a nuclear-restricted signal in IsoC with a preferential localisation at the nuclear membrane as expected (Figure 62). Staining for α-actinin-2 showed the expected striated pattern with mainly longitudinally oriented cells. The pattern was similarly observed in IsoC transduced with *AAV6-pCMV-GFP-2A-cLMN*A. In addition, staining of GFP showed successful transduction. In contrast to IsoC, no lamin A signal was detected in LMNA-KO, verifying the absence of the protein. This was accompanied by lower cell density, nuclear fragmentation as a sign of apoptosis and an incomplete sarcomeric organisation of α-actinin-2 in the few cells remaining. This picture was largely normalised in LMNA-KO GT with canonical nuclear membrane staining of lamin and a well-developed sarcomere structure of the cells. Quantification of positively stained nuclei was conducted on the basis of positive stained area due to the nuclear fragmentation in LMNA-KO which would result in higher numbers of lamin negative nuclei. Of note, not all cells stained positive for lamin (mean 45%; area of lamin A positive staining normalised to area of Hoechst positive staining; Figure 62 B) and GFP (mean 15% area with positive GFP signal normalised to area with positive α-actinin-2 signal; Figure 62 C). GFP signal might have been lower due to the fixation process prior to imaging, but lamin A staining indicates incomplete normalisation. For more representative GFP quantification a staining with anti-GFP might enhance the signal.

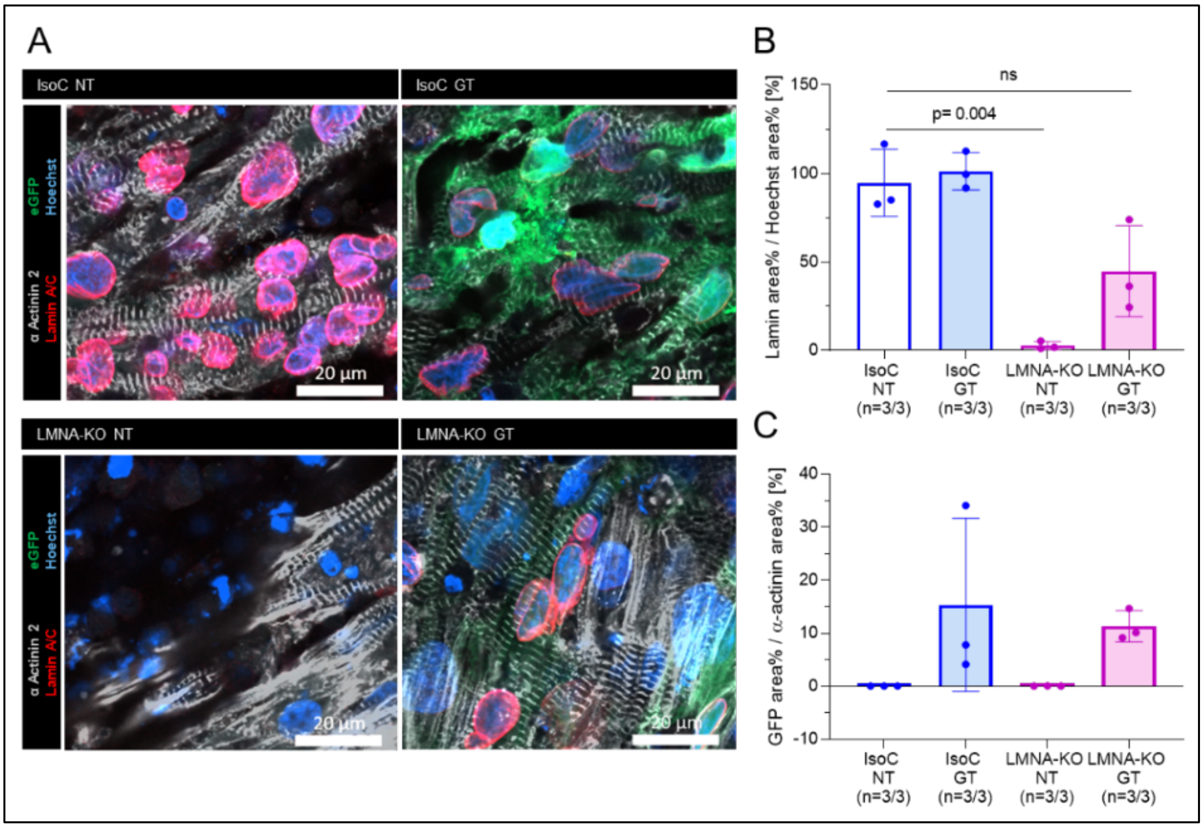

Figure 62 **A** Immunostaining of human α-actinin-2 (grey), lamin A/C (red) and nuclei (Hoechst, blue; scale 20 µm) on fixed EHTs from IsoC, IsoC GT, LMNA-KO and LMNA-KO GT EHTs. Representativ images of 3 EHTs. **B** Lamin A quantification by measuring the lamin A and Hoechst positive area and subsequent normalisation to Hoechst area (y-axis; %). Statistics were calculated by two-way ANOVA and Tukey's post-test. **C** GFP quantification by measuring the lamin A and α-actinin-2 positive area and subsequent normalisation to α-actinin-2 area (y-axis; %).

LMNA-KO EHTs showed a tendency towards a reduced remodelling capacity (Figure 49) as well as the loss of cellular integrity (Figure 62). To follow up on these findings, tissues were imaged as whole mounts. Stitching of confocal images of fixed and stained tissues confirmed a lower cell density in LMNA-KO NT EHTs compared to the other three groups (Figure 63). Moreover, cells appeared less well developed and longitudinally oriented in LMNA-KO. Staining of lamin A (not shown) was quantified in three EHTs per group of three independent batches. The area of lamin A positive staining was normalised to the area of Hoechst positive staining. Quantification of lamin A area resulted in approximately in 3% in LMNA-KO NT and in 30% in LMNA-KO GT EHTs, which confirmed only partial restoration of lamin A (Figure 63 B). GFP staining allowed an approximate evaluation of the transduction efficiency in the two GT groups, which amounted to 35% in LMNA-KO GT and 43% in IsoC GT (Figure 63 C).

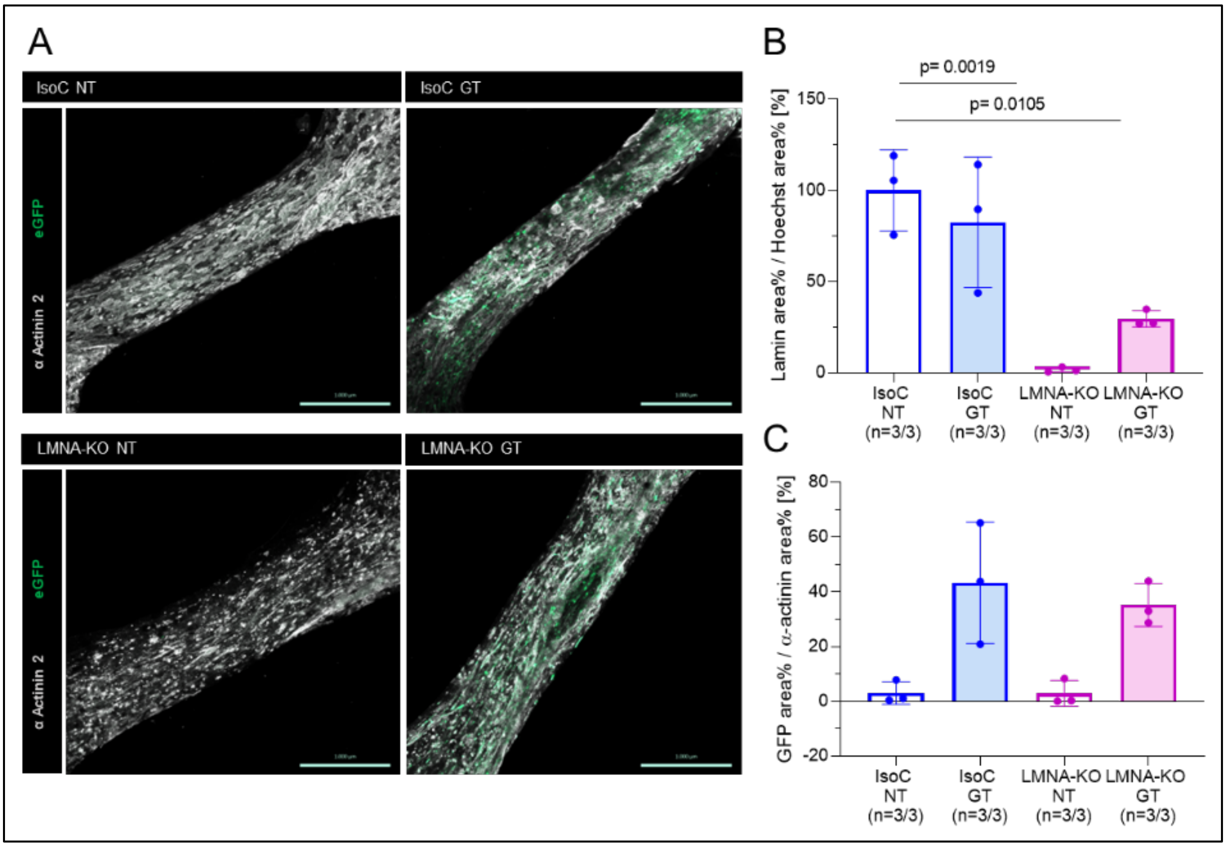

Figure 63 Representative stitched confocal images of fixed IsoC NT, IsoC GT, LMNA-KO NT and LMNA-KO GT EHTs stained for human α-actinin-2 (grey) and detection of GFP after 30 days in culture (scale 1,000 µm). Statistics were calculated with two-way ANOVA.

To further investigate whether the absence of A-type lamins also affected known interaction partners on the protein level and their localisation (Figure 61), 2D cultured hiPSC-CMs were stained for the nuclear envelope protein emerin. Corresponding to the low abundance in the whole EHT proteome (Figure 61), no emerin signal was detected in the canonical nuclear localisation in LMNA-KO NT hiPSC-CMs. Upon therapeutic intervention, emerin expression and localisation were restored. Representative images are shown in Figure 64. Counting Hoechst- and emerin- stained nuclei (solely red circular staining) in a blinded manner in several samples verified the complete absence of emerin in LMNA-KO NT and partial restoration in LMNA-KO GT (Figure 64 B).

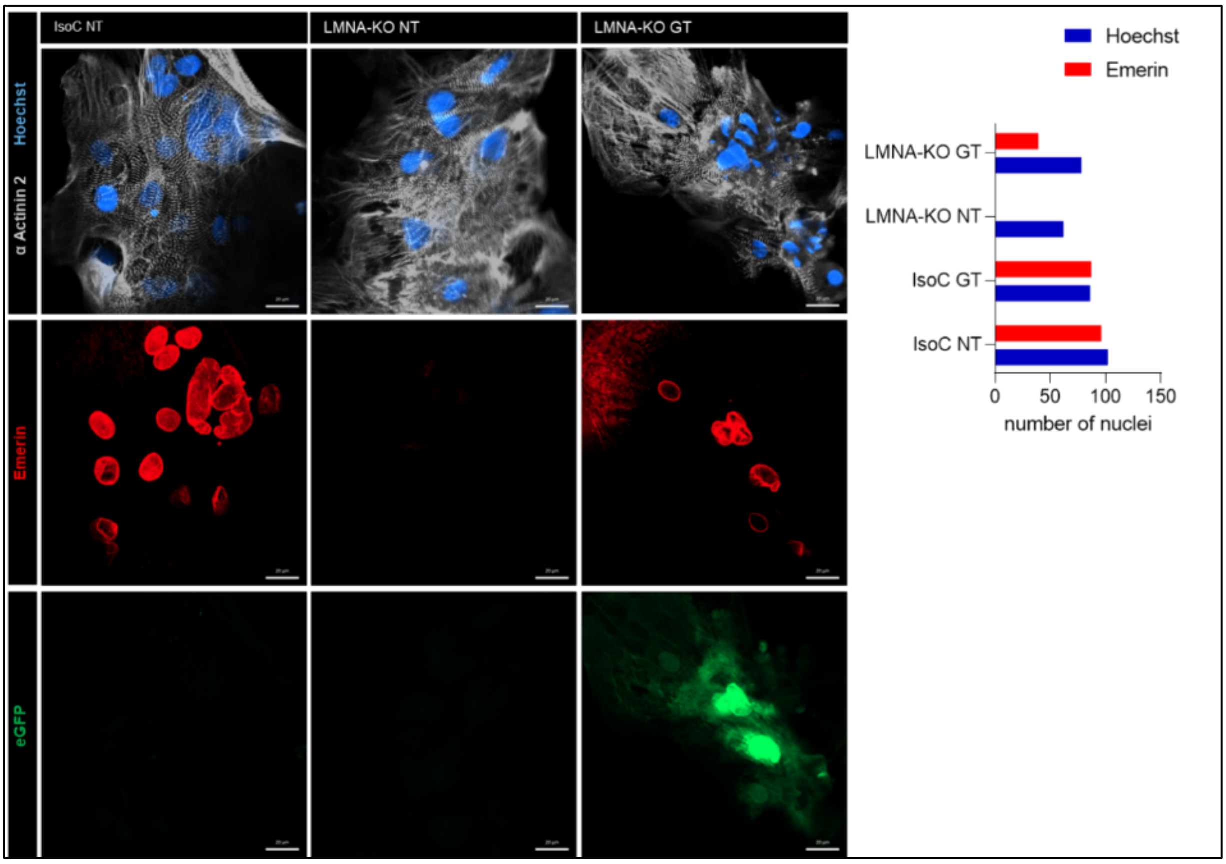

Figure 64 **A** Representative confocal images of fixed 2D-cultured hiPSC-CMs of IsoC NT, LMNA-KO NT and LMNA-KO GT stained for human α-actinin-2 (grey), nuclei (Hoechst, blue) and the nuclear envelope protein emerin (red; scale 20 µm). **B** Quantification of emerin (red) and Hoechst (blue) positive nuclei in a blinded manner.

4.4.9 Towards optimisation of the therapeutic strategy

Given the only partial functional and molecular rescue by GT, further experiments are required to increase the therapeutic effects.

4.4.9.1 Functional verification of an endogenous *LMNA* promotor

The clear toxicity of lamin A overexpression in some of the experimental series (Figure 52 and Figure 53) points to the need to better control the level of overexpression. A possible modification to achieve this goal with GT, would be the substitution of the strong promotor *CMV*, which is used in the current construct, by the endogenous *LMNA* promotor. *In silico* analysis, which was performed by the company Genecopoia, predicted a partial region upstream of the transcriptional start site of the *LMNA* gene to act as a promotor of the gene. The promotor sequence was purchased from Genecopoia and cloned into an AAV6 construct, in which the putative promotor was driving GFP expression. Transduction of IsoC EHTs with the *AAV6-pLMNA-GFP* (Figure S 3) at an MOI of 30,000 and 100,000 showed dose-dependent increases in GFP fluorescence that was absent in non-transduced EHT. The data indicate that the selected sequence acts as a promotor in hiPSC-derived CMs (Figure 65). Obviously, more experiments are needed to examine its regulation.

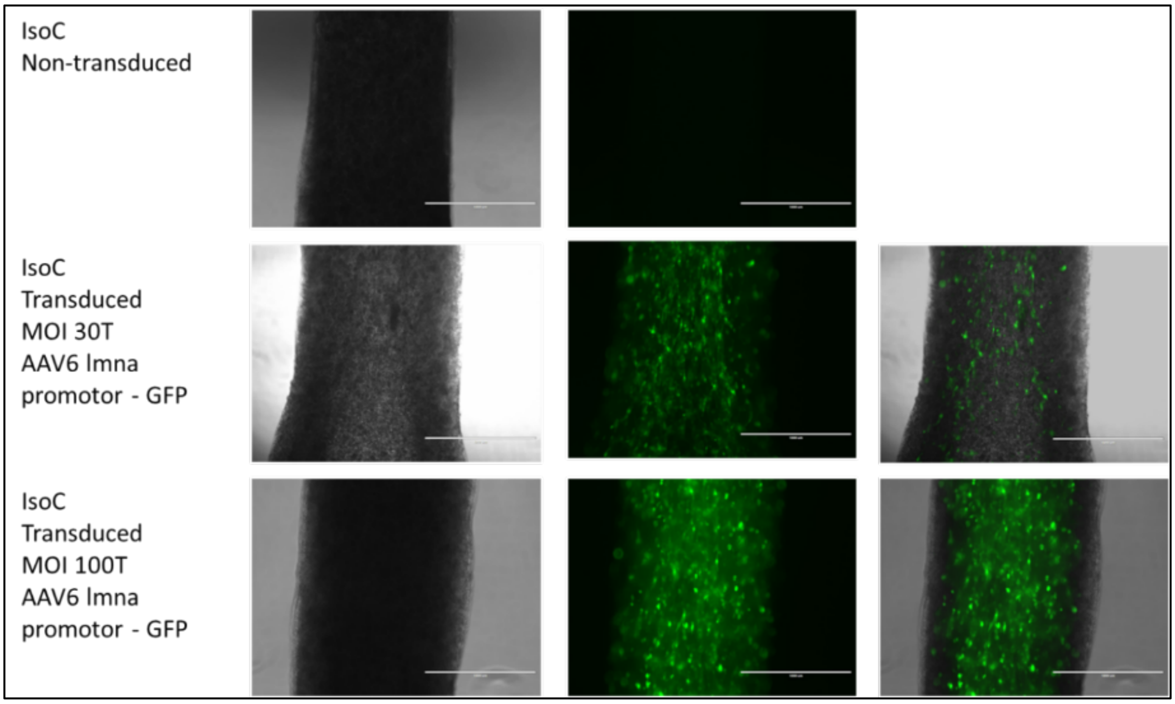

Figure 65 Bright field, GFP and overlay images of IsoC EHTs transduced with an AAV6 construct carrying GFP driven by a subset of *in silico* analysed lmna promotor at different MOIs (30,000 and 100,000; scale 1,000 µm).

5 Discussion

The overall objectives of this thesis were to (i) establish and (ii) characterise a laminopathy model in order to (iii) test novel therapeutic strategies. The main findings of this thesis were achieved in two different models:

1. A patient-derived, heterozygous *LMNA* p.H222P hiPSC line. CMs and EHTs from this line showed mild contractile dysfunction, electrophysiological abnormalities and elongated nuclei compared to CMs and EHTs of a CRISPR/Cas9-derived isogenic control line in which the mutation was corrected. The phenotype was exaggerated by mechanical stress, indicating altered mechanotransduction in p.H222P.

2. A CRISPR/Cas9-derived derivative of the p.H222P line with a homozygous truncating mutation in exon 4 and complete absence of full-length lamin A and C. CMs and EHTs from this line showed a severe, time-dependent loss of contractile force development, associated with signs of cell death and structural disintegration. This pathological phenotype could be partially prevented by AAV6-mediated expression of a lamin A cDNA.

5.1 Generation of a stable laminopathy disease model

This thesis employed hiPSC reprogramming of patient cells, cardiac differentiation of hiPSC *in vitro*, and CRISPR/Cas9 gene-editing to establish laminopathy disease models. Even though these new technologies are principally straightforward (Bassett, 2017), they still pose numerous obstacles, which had to be tackled following different strategies.

5.1.1 CRISPR/Cas9 gene editing of laminopathy patient line

Fibroblasts of a male patient heterozygous for p.H222P could be successfully reprogrammed with Sendai virus-mediated overexpression of the four pluripotency markers (Oct3/4, Sox2, Klf4, Myc) into hiPSCs. The quality of reprogramming was demonstrated by the strong expression of pluripotency markers and the ability to differentiate into all germ layers under suitable conditions. To properly study solely the effect of the mutation in this line, the mutation was corrected via CRISPR/Cas9 gene-editing. This is current standard in the field (Denning *et al.*, 2016; Salvarani *et al.*, 2019; Cuello *et al.*, 2021; Zech *et al.*, 2022) and is expected to create an isogenic control line that differs from the parental diseased line only by the absence of the mutation. The correction of the mutation p.H222P was not that straight forward as the strategy described in literature (Bassett, 2017).

First of all, it took three different gRNAs, predicted from the CRISPOR tool. The first gRNA, used in two independent runs, resulted in editing of the wrong (WT) allele as shown by the presence of the silent PAM mutation and the p.H222P mutation in several clones. The second gRNA, which had the second-best score according to CRISPOR did not result in a significant Cas9 activity at all, as no Indels were detected. Only the third gRNA resulted in the intended editing activity of around 86%. A high editing activity, i.e., high incidence of DSBs, is required since HDR occurs rarely. Underlying causes for the failure of the first two gRNAs were not investigated. Expression level and chromatin accessibility of the gene of interest plays an important role in CRISPR/Cas9 cleavage activity (Daer *et al.*, 2017). Thus, the identification of a suitable gRNA might have been more challenging since A-type lamins are expressed at low levels in human ESCs (Constantinescu *et al.*, 2006).

Second, the repair template for HDR, here a ssODN, required optimisation. It is hypothesised that unwanted secondary folding interferes with the HDR machinery, especially with varying length (Wang *et al.*, 2016). The corresponding template for gRNA 3 was therefore redesigned based on a prediction tool for secondary structures (see Figure 14) with the intention of a lower probability for a loop around the ROI. The redesign seemed to have had an impact on the HDR efficiency, represented by the PAM insertion. In addition to the theory of secondary folding, a higher HDR efficiency might have occurred due to the length of the template. A shorter (60 nucleotides) ssODN template lowers the HDR efficiency in comparison to a length of 120 nucleotides (Boel *et al.*, 2018). Indeed, the first template was 60 nucleotides long, whereas the second and successful one consisted of 113 nucleotides (see Table 4). Nevertheless, design experiences just led to assumptions since there was no head-to-head comparison nor testing in different gene loci.

The third challenge was the occurrence of a large deletion in one clone, which was first interpreted as a potential correction. This assumption was based on the promising absence of the mutation in the standard PCR (1,000 bp) sequencing analyses (see Figure 12 and Figure 13). However, also the expected silent PAM mutation was absent, raising suspicions whether HDR indeed occurred. Finally, a long-range PCR showed that clone #1 carried a large deletion at the ROI, which was not covered by the regular PCR amplification. Thus, loss of the allele with the original mutation gave rise to a standard PCR product that looked like homozygous WT, while functionally it was a heterozygous KO. Initially, the

CRISPR/Cas9 strategy was thought to be very precise without major adverse effect. Recent studies, however, discovered that large deletions and genome reorganisations are more frequent than initially expected (Kosicki, Tomberg and Bradley, 2018). Our own experiments underpin that CRISPR/Cas9 results have to be interpreted with caution. The absence of the mutation in a short-range PCR of the ROI does not suffice as evidence for the correction of the mutation. PCR products of regular size (*e.g.* 1,000 bp), can easily lie within the larger deletion site. Here, several large fragment PCRs were performed shifting up- and downstream of the target size to test whether a large deletion had occurred. Southern blots are an alternative method.

To conclude, optimisations for tracrRNA and ssODN sequences of the CRISPR/Cas9 were required to correct the p.H222P mutation in patient derived hiPSC. For future projects, prime editing might be a suitable alternative to circumvent major side effects. Prime editing makes use of catalytically inactive Cas9 which is fused to a reverse transcriptase (Anzalone *et al.*, 2019). In this case, the prime editing guide RNA consists a sequence for the target size and for the intended edit (Anzalone *et al.*, 2019). Thus, prime editing allows to bypass problematic genomic reorganisations since it does not induce DSBs.

5.1.2 Differentiation efficiency instabilities

Another challenge in setting up this disease model was the instability of cardiac differentiation efficiencies. The EHT model depends on a high quantity (1 million cells per EHT) and high quality (>75% cTnT positive cells) of hiPSC-CMs. Lamin A and C, however, are involved in the differentiation process and cells carrying a *LMNA* mutation showed different potential for cell fate commitment (Park *et al.*, 2009; Kubben *et al.*, 2011; Bertrand *et al.*, 2012). Mechanistically, it was reported that this stems from the function of A-type lamins to recruit and stabilise heterochromatin (Park *et al.*, 2009). Mutations in *LMNA* seem to affect the formation of LADs, allowing gene programmes of other lineages, such as neuronal, to be misexpressed (Shah *et al.*, 2021). Inadequate upregulation of neuronal pathways on the mRNA level have been also reported for another A-type lamin mutation in hiPSC-CMs (Bertero *et al.*, 2019).

Interestingly, in our study the p.H222P line showed much larger variability in differentiation efficiency than LMNA-KO (Figure 20). This was unexpected given the expected larger severity of molecular alterations in the LMNA-KO line, but six independent differentiation runs of LMNA-KO (and many more in p.H222P and IsoC) should be sufficient to yield valid results. Indeed, the difference in cardiac differentiation efficiency between p.H222P and LMNA-KO was highly significant (Figure 20) and genotype-dependent. Similar data have been reported by others (Guénantin *et al.*, 2021; Wang *et al.*, 2022). A recent study reported that a loss of a histone H3K4me1 on enhancers for genes important for epithelial-to-mesenchymal transition and cardiogenesis caused cardiac differentiation deficiency at the stage of mesodermal induction in p.H222P mouse ESCs (Guénantin *et al.*, 2021). Another publication compared different lamin A/C mutational consequences for differentiation success (Wang *et al.*, 2022). This study revealed that lamin A/C represses cardiac-specific genes during the embryonic stage, and loss of A-type lamins in mouse ESCs caused the release and subsequent expression of these genes, which resulted in a high differentiation efficiency (Wang *et al.*, 2022). In the same study mouse ESCs carrying the p.H222P mutation exhibited a cardiac differentiation deficiency, putatively caused by gain of function, e.g. stronger binding of cardiac-specific genes to the nuclear periphery (Wang *et al.*, 2022).

Nevertheless, successful, high purity differentiation is required to study p.H222P in our EHT system. Therefore, a head-to-head comparison of IsoC and p.H222P for different conditions of mesodermal induction has been tested. Interestingly, almost all conditions were sufficient for high purity cardiac differentiation of IsoC, but only one condition for p.H222P (see Figure 21). The much larger variability in differentiation efficiency between the various conditions in p.H222P than IsoC confirms the interpretation that the mutated A-type lamin negatively affects cardiac differentiation. It also demonstrates the general need to adjust cardiac differentiation parameter for different cell lines (Kattman *et al.*, 2011; Sa and McCloskey, 2012).

5.2 Patient-specific laminopathy model p.H222P

The successful gene-editing and cardiomyocyte differentiation was the basis to understand the pathogenic consequence of p.H222P mutation by comparing the *in vitro* phenotype of diseased and isogenic hiPSC-CM EHTs. In mice, p.H222P is a well-studied lamin mutation (Crasto, My and Di Pasquale, 2020). The clinical relevance has though not been fully confirmed according to the database ClinVar (Landrum *et al.*, 2018). Nevertheless, there is a familiar study pointing towards arrhythmias and muscular disorders (Bonne *et al.*, 2000). Thus, both contractile behaviour under basal and stressed condition, and electrophysiological parameters were of special interest.

5.2.1 Contractile phenotype in p.H222P

Laminopathy-associated DCM encompasses several ventricular defects, which include impaired ventricular contraction (Fatkin *et al.*, 1999). The cardiac differentiation protocols we used to set up our laminopathy model give rise to mainly ventricular CMs (Breckwoldt *et al.*, 2017; Mosqueira *et al.*, 2018). Several contractile parameters of EHTs derived from p.H222P and IsoC hiPSC ventricular CMs have been analysed, making use of the optical recording unit. However, the mean of all batches showed only a tendency towards lower force of contraction. Further there was one batch of p.H222P, which was a clear outlier (see Figure 22 A; beige-coloured) and one of IsoC (see Figure 22 A; dark turquoise). Interestingly, the IsoC batch, which exhibited lower force showed also a lower cTnT positivity in hiPSC-CM population, which might be a confounder (Figure S 8). Such a variation is not surprising since it has been described already on the functional level in this format for different control lines (Mannhardt *et al.*, 2020). The variation in differentiation success in p.H222P as discussed above (see section 5.1.2) might multiply the batch-to-batch variations.

Interestingly, despite the scattering of different parameters between batches, it is clear that the relaxation time ($RT_{80\%}$) was significantly shorter and the BPM significantly higher in p.H222P than in IsoC EHTs (see Figure 22 C). A shortened relaxation time can be explained by the phenomenon of frequency-dependent acceleration of relaxation (P. B. Chung et al., 2016). However, the shorter relaxation time was also found when only analysing EHTs in the same frequency range of both genotypes (Figure 24). Thus, the shortening of the relaxation time is not likely to be caused exclusively by the higher frequency.

Instead, the reduced relaxation time in p.H222P could also be due to a lower calcium sensitivity of myofilament, linked to an increased dissociation rate constant (Chung *et al.*, 2016; Mannhardt *et al.*, 2016). Indeed, p.H222P EHTs exhibited significantly lower sensitivity to external calcium than IsoC. Of note, the EC_{50} value of 0.54 mM in p.H222P was close to the EC_{50} values of 0.6 mM calcium in an unrelated control line (Mannhardt et al., 2016), while the EC_{50} for IsoC deviated with a value of 0.08 mM calcium (see Figure 26). Reasons are unknown. While this points to altered calcium sensitivity in p.H222P hiPSC-CM EHTs, a calcium sensitivity of the myofilaments analysed in skinned EHTs (Chung *et al.*, 2016) would be the optimal method to differentiate between altered myofilament calcium sensitivity and altered calcium handling as the underlying reason for the differences. Thus, with the existing data the hypothesis of a lower myofilament calcium sensitivity causing the shortened relaxation time in p.H222P is highly speculative.

Other reasons can be lower expression of L-type calcium- or sodium channel or higher expression of potassium channels (Mannhardt *et al.*, 2016) that can shorten the APD and subsequently the relaxation time. RNA expression analysis under condition I indeed revealed differential expression of multiple respective ion channels (Figure 32). Calcium channels were downregulated, and several potassium channels were more abundant in p.H222P (Figure 66). In the same condition, also APs were measured, and indeed there was a non-significant tendency towards APD shortening (Figure 27), pointing to alterations in calcium handling to at least participate in the shorter relaxation time in p.H222P. A recently published hiPSC-CM p.K219T model exhibited a lower *SCN5A* transcript level, which resulted in lower density of Nav1.5 channels (Salvarani *et al.*, 2019). This explanation for a shorter APD is unlikely to apply to our model since *SCN5A* transcript levels did not differ between p.H222P and IsoC.

The simultaneous pharmacological inhibition of voltage-activated potassium rectifiers by 4-AP and activation of L-type calcium channel by Bay-K confirmed the higher repolarisation reserve and lower depolarisation current in one batch p.H222P EHTs (Figure 25).

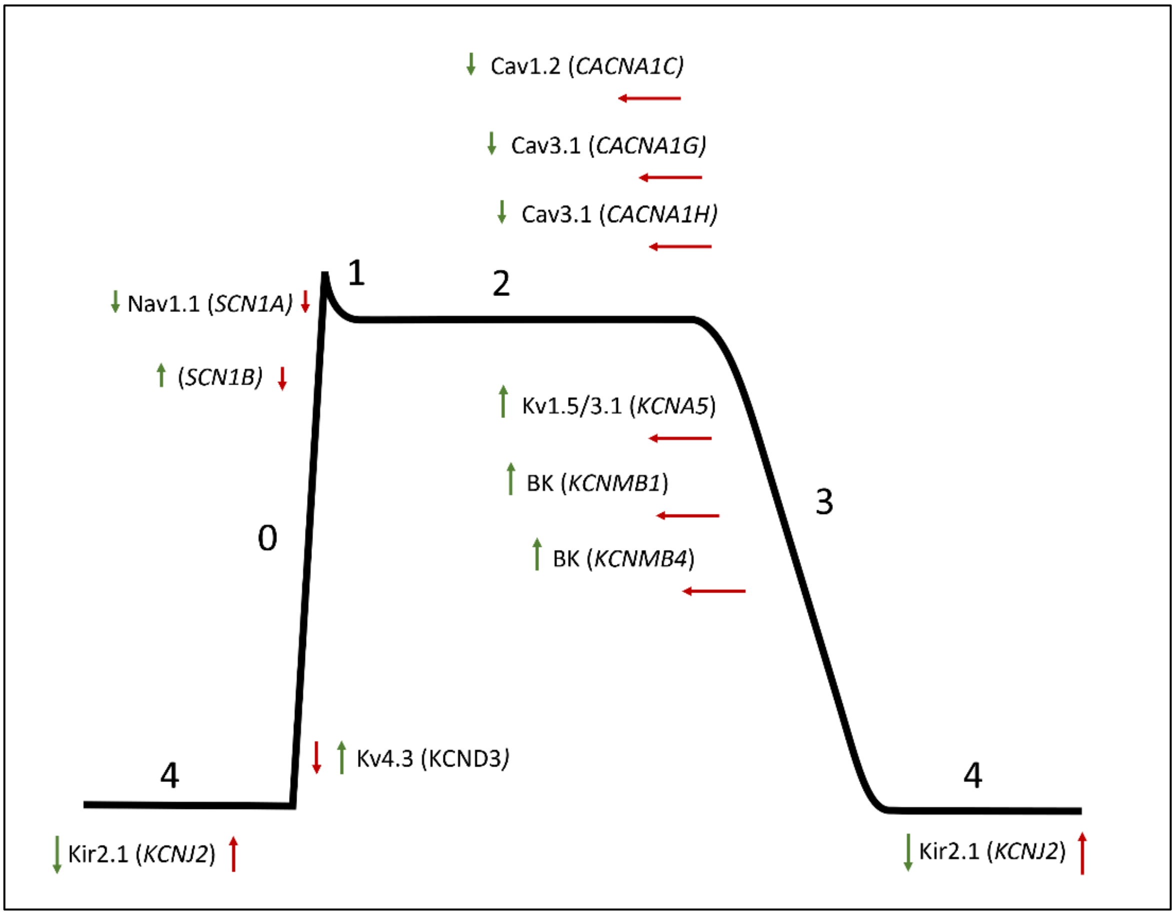

Figure 66 Altered gene expression of several ion channels (green arrow) in p.H222P EHTs and their theoretical consequences (red arrow) on the ventricular action potential in the different phases (1 to 4).

Comparing the results of the gene expression data in this thesis with existing studies, a mixed, often contradictory, picture appears. Two studies reported higher calcium currents and a prolonged APD in lamin mutated hiPSC-CMs (Bertero *et al.*, 2019; Shemer *et al.*, 2021), opposing to the p.H222P model. One of the two studies, explained the prolongation of APD by misexpression of neuronal genes, such as *CACNA1A*. Interestingly, another p.K219T mutation resulted in shorter APD, lower APA and upstroke velocity (Salvarani *et al.*, 2019) and thus strengthens the observation in our model. Several studies draw different conclusions with regard to the electrophysiological phenotype and underlying pathomechanisms already on cellular based assays. *SCN5A*, which is reported to be involved in the p.K219T pathomechanism, is a classical gene associated to the Brugada syndrome (Van Berlo, Duboc and Pinto, 2004). Laminopathy cardiac defects are common, but often not recognised in such detail as an *SCN5A* linked Brugada syndrome due to their diverse phenotype and complex clinical characterisation (Van Berlo, Duboc and Pinto, 2004;

Van Berlo *et al.*, 2005). Typically, laminopathy patients have lower P wave, prolonged PR interval with a short QRS complex on the ECG (Van Berlo *et al.*, 2005). Only recently a laminopathy patient (p.R216C) has been associated to a Brugada syndrome in a case report (Armaroli *et al.*, 2020), which exemplifies the diverse affection. Taken together, electrophysiological phenotypes are a common part of laminopathies, but the individual alterations differ.

While there are clearly electrophysiological differences observed in p.H222P, the question remains whether these might represent the mechanism underlying arrhythmias seen in patients. A shorter APD predicts a shorter absolute and relative refractory period, which is a well-known risk factor for re-entry arrhythmias (Eisner, Dibb and Trafford, 2009). Clinical studies observed that patients with short QT intervals, which are due to shorter APDs, exhibited short refractory periods with higher occurrence of arrhythmic events (Gussak *et al.*, 2000; Gaita *et al.*, 2003; Priori *et al.*, 2012). In a study on *LMNA* mutation carriers, 60% presented ventricular arrhythmias (Hasselberg *et al.*, 2018). A meta-analysis of 27 DCM studies confirmed the occurrence for ventricular arrhythmias in 50% of *LMNA* patients (Kayvanpour *et al.*, 2017). Thus, the observed shorter APD and relaxation time might be in line with an elevated risk of ventricular arrhythmia.

Nevertheless, no obvious arrhythmias were detected in p.H222P EHTs. One reason for this might be the less than adult maturation status of hiPSC-CMs, even in the EHT model (Mannhardt *et al.*, 2016). Another cause for the absence of arrhythmia can be the strip-shaped format and the small size of the EHTs, which may not be best suited for the detection of re-entry. For example, a hiPSC-CM 2D sheet model being circular and with a larger dimension allowed the observation of re-entry arrhythmias due to shorter APDs by optical mapping (Shinnawi *et al.*, 2019). It should also be noted that the clinical phenotype of patients with the p.H222P mutation has not been elaborated in much detail yet, specifically in terms of arrhythmia (Bonne *et al.*, 2000; Landrum *et al.*, 2018). Heterozygous p.H222P mice did not give rise to any cardiac phenotype over 1 year of lifespan. Homozygous p.H222P mice, however, exhibited a longer PR interval, pointing to atrio-ventricular conduction defect at three months of age and a prolonged QRS complex underlining a intraventricular conduction defect at 5 months age (Arimura *et al.*, 2005). The finding in homozygous p.H222P mice underline a ventricular involvement in arrhythmia. Still, it is not clear how much arrhythmia was to be expected in this line, given the incomplete clinical data of the patients with the p.H222P mutations.

To conclude, the underlying mechanism of the arrhythmias that are frequently observed in laminopathy patients is a remaining question. The overall range of affected ion channel genes suggests that the underlying mechanisms are rather more complex than explainable by one specific gene. The reported studies, which attempted to validate hiPSC-CMs as a model to study electrophysiology, outlined differences between hiPSC-CMs and human adult CMs such as the unexpected and batch-dependent expression of BK_{Ca} (*KCNMA1)*. This expression was associated with a typical notch, prolongation and early after depolarisation in ventricular AP recordings (Horváth *et al.*, 2020). Further, ion channel expression can be dependent on culture conditions (Feyen *et al.*, 2020), which was observed in our RNA sequencing data sets, too. Thus, the electrophysiological analysis in hiPSC-CMs has to be interpreted with caution.

5.2.2 Acute AE exaggerates contractile and transcriptomic phenotype

Patient-specific p.H222P EHTs showed only a tendency towards lower systolic force under baseline conditions (Figure 22 A). Thus, afterload was acutely increased (to 1.68-fold stiffness) by inserting short metal braces into hollow posts. FS dropped significantly to -28.8% in p.H222P EHTs after 4 hours of intervention, but non-significantly in IsoC EHTs when normalising to its baseline values (-17.2%; Figure 28). In a similar study, afterload was gradually increased in rat EHTs, but with a magnetic platform up to 7.5-fold over 7 days. In this study, FS did not decrease in rat EHTs until an increase of afterload up to 2.7-fold (Rodriguez *et al.*, 2019).

The role of mechanical stress and the proposed coupling defect in laminopathy was already investigated in different mouse studies. Mice carrying a heterozygous frameshift mutation $LMNA^{+/\Delta 8\text{-}11}$ were admitted to mechanical stress (regular moderate exercise for 6 weeks from 12 weeks age on) and did not develop any hallmarks of DCM (Chandar *et al.*, 2010). In contrast, $LMNA^{+/\Delta K32}$ mice subjected to an exercise schedule for 5 weeks starting from 17 weeks of age on had an earlier onset of ventricular dilation and decreased FS than the non-exercise group (Cattin *et al.*, 2016). Differences between the studies could be mutation-specific or due to the different starting point for the exercise experiments. Mutations might affect the physical properties and structural arrangement of the lamina differently (Makarov *et al.*, 2019; Donnaloja *et al.*, 2020). In one study, all investigated *LMNA* mutations, except p.H222P, resulted in increased nuclear rupture and DNA damage in skeletal muscle cells upon nuclear migration (Earle *et al.*, 2020). This study underlines a potential mutation-specificity in the mechanical phenotype. Further, atomic force microscopy unravelled a mechanical coupling defect in neonatal rat ventricular myocytes (NRVMs) that carried a p.D192G missense mutation in *LMNA* (Lanzicher *et al.*, 2015). The mutated NRVMs exhibited a lower probe-to-cell membrane adhesion, which was probably caused by the disruption of the actin cytoskeleton (Lanzicher *et al.*, 2015). This study strengthens the mechanical decoupling hypothesis in laminopathies.

Cellular lamin A and C protein levels can reflect a cell's state of mechanical stress (González-Cruz, Dahl and Darling, 2018). In p.H222P EHTs, lamin A and C protein were less abundant than in IsoC, but only low sample numbers were analysed. Lower lamin A was also confirmed on mRNA level in p.H222P EHTs by quantifying the transcripts of one bulk RNA sequencing experiment. Lamin A has been reported to directly account for a mechano-protective role, by being stabilised at the INM and preventing DNA damage upon external stiffer stimuli and stretching procedure (Cho *et al.*, 2019). Thus, lower abundance of A-type lamins in p.H222P might be in line with a mechanical coupling defect on functional level. Given the low sample number, more experiments and a probably more precise quantification method, such as MS, would give insights if the mechanical stress is reaching the nucleus and subsequently altering lamin A and C regulation in p.H222P. Lamin A and C protein levels are supposed to serve as a marker for mechano-phenotype (González-Cruz, Dahl and Darling, 2018). Lower lamin A and C levels in p.H222P EHTs might indeed serve as a marker for a mechano-phenotype and thus further evaluation of protein levels and subsequent correlation to functional data would be of interest in this model.

Given the failure of p.H222P to contract against the mechanical load and the role of A-type lamins in genome organisation, bulk RNA sequencing was performed in AE EHTs. Interestingly, a four-hour long AE resulted in 401 DEGs in p.H222P EHTs (minimum 1.5-fold change; p.H222P 4h vs p.H222P TC). The effect of AE on the transcriptome is in line with a study that tried to tackle the question of what exactly occurs in the nucleus as a response to mechanical stretch. NRVMs were stretched also for four hours, and their transcriptomic changes resulted in 579 DEGs with a minimum of 1.5-fold change (Rysä, Tokola and Ruskoaho, 2018). Thus, the number of DEGs confirm the success of our mechanical stress assay to reach the nucleus. Further, p.H222P EHTs responded with 829 DEGs in total (without fold change criteria) to mechanical stress and thus differed drastically from IsoC EHTs that responded with only 107 DEGs. This difference already hints towards p.H222P CMs to attempt to compensate the strain with a higher gene expression response. In comparison to IsoC, p.H222P EHTs exhibited already under baseline conditions DEGs belonging to proliferation, migration, differentiation and transcriptional GO pathways already. The DEGs in stretched NRVMs belonged to GO pathways concurrent with the findings in our study (Rysä, Tokola and Ruskoaho, 2018). One GO pathway, the PDGF pathway, was upregulated in p.H222P under all conditions, baseline and AE (Figure 30, Figure 37 and Figure 38). Interestingly, the PDGF pathway has been described as a mechanical stress response in vascular smooth muscle cells (Hu *et al.*, 1998), and was also identified as an upstream regulator in stretched NRVMs (Rysä, Tokola and Ruskoaho, 2018). Upregulation of the PDGF pathway has been identified already in a p.K117fs hiPSC-CM laminopathy model (Lee *et al.*, 2019), but has not been investigated in any mechano-context. Thus, the upregulation of the PDGF pathway has been described to play a role in mechano-transduction and was found to be altered in a laminopathy model. Overall, the transcriptomic profile might reflect that p.H222P hiPSC-CMs are already at an increased mechanical stress status under baseline conditions, which is further exaggerated by AE.

In addition to the identification of the PDGF pathway, different YAP1 targets were upregulated in p.H222P under baseline conditions (Figure 39). Certain YAP1 targets were even more abundant in p.H222P AE EHTs versus TC (Figure 39). Two studies, which were both conducted in muscle precursors, revealed a mechano-sensing defect in combination with elevated YAP1 signalling in several laminopathy mutations, but not for p.H222P (Bertrand *et al.*, 2014; Owens *et al.*, 2020). Nevertheless, there might be a discrepancy due to the different cell-types for the p.H222P mutation. YAP1, plays a central in the transduction of mechanical cues from the ECM along the intercalated disc, cytoskeleton, microtubular network and finally via the LINC complex into the nucleus (Dupont *et al.*, 2011; Driscoll *et al.*, 2015; Martino *et al.*, 2018). In the dephosphorylated state, YAP1 enters the nucleus and activates transcription of gene programmes for cell proliferation and regulation of actin polymerisation (Panciera *et al.*, 2017), which might explain the upregulated GO pathways in p.H222P. An elevated YAP1 translocation would underpin the hypothesis of an exaggerated mechanical stress signalling.

According to literature, YAP1 enters the nucleus by NPCs, which is facilitated by flattening of the nucleus and thus stretching of the pores (Elosegui-Artola *et al.*, 2017). In an initial experiment, p.H222P EHTs exhibited elongated nuclei in comparison to EHTs of an unrelated control line (Figure 42). This is concurrent with several studies that observed elongated nuclei in laminopathy cells compared to WT (Maffioletti *et al.*, 2018). Evaluation in comparison to IsoC would validate this preliminary finding. Given the role of lamin A and C in the organisation and localisation of NPCs (Guo and Yixian, 2015) and the observed elongated nuclei in laminopathy (Wu *et al.*, 2011), YAP1 might enter the nucleus more easily and often. Thus, the transcriptome data in p.H222P EHTs and the preliminary data on nuclear elongation support the hypothesis of elevated YAP1 nuclear translocation. Further experiments such as transmission electron microscopy could answer the question whether nuclear pores are also stretched in p.H222P EHTs. In addition, an actual elevated nuclear translocation of YAP1 in p.H222P EHTs has to be validated, which can be pursued by 3D imaging or Western blot quantification in cytosolic and nuclear fractions. The hypothesis can be further tested in AE versus TC under blockage of YAP1 translocation through NPCs. This translocation can be blocked by inhibiting the importin-β receptor with Importazole (Owens *et al.*, 2020). Subsequent assessment of YAP1 localisation and analysis of YAP1 target transcripts could be then used as a readout. Interestingly, disruption of the LINC complex rescued the cardiac phenotype in a laminopathy mouse model (Chai *et al.*, 2021). It can be speculated that this a priori surprising effect is due to the inability of YAP1 to enter the nucleus without the LINC complex (Driscoll *et al.*, 2015)

Another role of YAP1 is the regulation of actin polymerisation and degradation by promoting gene expression (Morikawa *et al.*, 2015; Ali, Braga and Giacca, 2020). One of the targets of YAP1 is cofilin-1, which is responsible for the filamentous actin (F-actin) disassembly to globular actin (G-actin). Further, increased cofilin-1 phosphorylation via ERK1/2 has been found to contribute to the laminopathy phenotype in p.H222P mouse CMs (Chatzifrangkeskou *et al.*, 2018). Therefore, it would be interesting to investigate whether YAP1 and altered cofilin-1 expression and its phosphorylation affected the actin dynamics in p.H222P hiPSC-CM. This question could be tackled by investigating the ratio of F-actin to globular (G-actin) under different YAP1 interventions.

5.2.3 Conclusion and outlook

To sum up, p.H222P EHTs showed a mild contractile under baseline conditions, which is a hallmark of DCM. The lower force of contraction was unmasked upon AE in p.H222P EHTs, reflected by decreased fractional shortening. This relatively mild phenotype matches the not so evident phenotype of p.H222P in mice and clinics. Despite the functional phenotype, p.H222P EHTs showed a strong alteration on the transcriptome which was exaggerated in response to mechanical stress, which might imply the primary consequence of laminopathies. Pathways of DNA synthesis, mitosis, contractile components, and electrophysiology were differentially expressed in p.H222P EHTs very well matching the *LMNA*-DCM phenotype. AP recordings were concurrent with altered ion channel expression in p.H222P EHTs, but the so evident arrhythmia in p.H222P laminopathy patients were not observed in this model. This might have been due to the absence of fibrosis, maturation status or geometry and dimension of the tissues. Transcriptomic analysis unravelled the potential involvement of YAP1 in a mechanical coupling defect.

Further studies to deduce the mechanism that result in lower fractional shortening and altered gene expression unravelling the role of mechanotransducer YAP1 will be of great interest. Therefore, studying the genome architecture might tackle the question of an altered genome organisation, before or up on mechanical stress applied to cells. This study would serve as a steppingstone to finally unravel the interplay between gene expression and mechanical stress hypotheses and putatively explain as in why mostly tissues underlying mechanical strain are affected in laminopathies.

5.3 Characterisation and partial rescue of the human LMNA-KO model

Several therapeutic strategies for *LMNA*-associated DCM are intensively explored and results showed partial recovery in different mouse models. Two pharmacological examples consist of inhibition of BET bromodomain-containing proteins (Auguste *et al.*, 2020) or inhibition of MEK1/2 signalling pathway (Muchir *et al.*, 2014). Other examples are following a strategy of overexpression of the cardiac chaperone αB-crystallin or RNA trans-splicing (Azibani *et al.*, 2018; Galata *et al.*, 2018). Given the diverse affection of downstream pathways in *LMNA* mutations (Gerbino *et al.*, 2018) and the low efficiency of trans-splicing approaches (Azibani *et al.*, 2018), other therapeutic approaches are of great interest. Here, we developed a gene replacement therapy and tested it in a newly created and characterised homozygous LMNA-KO hiPSC-CM model.

5.3.1 Functional and morphological phenotype in LMNA-KO EHTs

Full-length A-type lamin knockout was assessed on transcriptomic and proteomic level and faint bands were observed in some samples on cDNA levels and lower bands on Western blots. Still, MS analysis and confocal microscopy validated the absence of A-type lamins (Figure 59). Stitched confocal images of the whole EHTs (consisting initially of 1 million hiPSC-CMs) showed a very small number of A-type lamin positive nuclei (Figure 63), which indicates that some cells expressed lamin and their nuclei remained intact. However, a complete knockout is difficult to guarantee, since it is reported that 50% of cell lines carrying a nonsense mutation still express some protein, *e.g.* as a result of exon-skipping (Tuladhar *et al.*, 2019). Further, NMD does not work 100% efficiently, which results in partial expression of the mutated protein (Bassett, 2017). In the LMNA$^{\Delta K32/+}$ mouse model, dysfunctional UPS over the course of time resulted in the re-occurrence of mutated lamin A and C (Cattin *et al.*, 2013), but this aspect has not been assessed in this model. Even though some nuclei stained positive in LMNA-KO EHTs (1 million hiPSC-CMs), the number of cells remained very little and A-type lamins were not detectable by MS, thus LMNA-KO EHTs represent a knockout. Despite the problem to create a full knockout by nonsense mutations, there is no optimal strategy to establish and investigate a 100% efficient knockout. A large deletion of the ROI would be an alternative strategy, but can include a deletion of regulatory regions for distant genes, and thus induce unknown effects (Bassett, 2017). Thorough investigation needs to be performed to verify either complete absence or investigate regulatory function of the removed sequence, to ensure solely studying a complete knockout. Further, the aim of this project was to set up a laminopathy model with a truncating mutation that is more comparable to patients carrying nonsense mutations rather than examining a large deletion with unintended deletions of probable regulatory elements.

After successful validation and cardiac differentiation EHTs were casted and their developed forces were tracked over time. Initially LMNA-KO forces were similar to IsoC, but after three weeks in culture, a pronounced decrease in force for LMNA-KO EHTs was observed (Figure 50). To date, the only patient reported with a homozygous nonsense mutation exhibited severe growth retardation, poor striated muscles and died at birth (Van Engelen *et al.*, 2005). This nonsense mutation is only 36 AA downstream of the here investigated mutation in LMNA-KO. The contractile deterioration in LMNA-KO EHTs might be very well in line with the patient report. Given the final contractile dysfunction, other functional parameters were evaluated already after 19 or 20 days in culture, representing a short plateau phase of force in LMNA-KO force. Interestingly, there were more parameters and with a higher significance altered in LMNA-KO versus IsoC EHTs, than in p.H222P versus IsoC EHTs. For example, a stronger effect of the mutation can be seen in lower force (p value 0.0089 vs 0.2974), lower contraction velocity (p value 0.0406 vs 0.1915) and shorter relaxation time (RT80; p value 0.0169 vs 0.0251) for LMNA-KO and p.H222P, respectively. Further, both lines presented a higher frequency than IsoC, which might be due to a less mature state. The stronger phenotype of LMNA-KO in the EHT format might be due to the more severe molecular consequence of the mutation in comparison to a missense mutation of p.H222P, which was also found in mice (reviewed and compared in section 1.2.4). The observed shorter relaxation time and lower force of contraction underpin the strength and probably more global description of a contractile laminopathy phenotype in this EHT model since one is based on a heterozygous missense and the other on a homozygous nonsense mutation.

Arrhythmias are one of the key features of laminopathies, which were again not detected in LMNA-KO EHTs similar to the p.H222P model. The absence of arrhythmic events in the LMNA-KO model might be due to the type and homozygosity of the mutation, since arrhythmia were also not reported, in homozygous LMNA-KO mice or patients (Van Engelen *et al.*, 2005; Kubben *et al.*, 2011). All members of a five generations family that carried the heterozygous p.Y259X showed a definite cardiac phenotype including arrhythmias. In contrast to this, no cardiac characterisation has been reported for the family member that carried the p.Y259X mutation in the homozygous state (Van Engelen *et al.*, 2005). Further, one mouse model underpins the potential role of the type of the mutation. An often used and formerly termed homozygous LMNA knockout, the LMNA$^{\Delta 8\text{-}11}$ mouse model, developed AV conduction defects and atrial arrhythmias, and retrospectively was reported to carry a frameshift mutated protein instead of being a knockout (Kubben *et al.*, 2011; Frock *et al.*, 2012). A more stringent argument for the absence of arrhythmias could be the severity of the cellular consequence *e.g.,* loss of cellular integrity, overwriting the long-term aspect of DCM. Furthermore, as discussed in section 5.2.1, the model might lack a certain state of maturation, as well as not having a suitable size of tissue or wrong type of CMs (ventricular instead of atrial).

The EHT format also allows assessment on morphological level, which revealed a reduced remodelling capacity of LMNA-KO EHTs. Given the role of lamin A in a mechano-induced response, it can be hypothesised that mechanical coupling and thus tension induced remodelling of the tissue were affected by absence of A-type lamins in this model. Further, cell density and sarcomere structures were poor in LMNA-KO EHTs, putatively contributing to mediocre tissue formation.

In conclusion, this model resembled, with the deterioration of contractile force, reduced remodelling capacity and cellular integrity, closely the description of the human case report carrying a similar homozygous truncating mutation in the homozygous state (Van Engelen *et al.*, 2005).

5.3.2 Transcriptomic and proteomic phenotype

Molecular consequences of *LMNA* knockout in CM EHTs were examined on transcriptomic and proteomic level in order to understand the observed functional phenotype, especially considering the role of A type lamins in nuclear gene expression regulation. When classifying manually the GO pathways affected on RNA level upon *LMNA* knockout, mainly four groups were identified being related to (i) chromosome organization, DNA replication and mitosis, (ii) cardiac contraction, (iii) electrophysiology and (iv) microtubules. All four groups affected are compatible with functions of A-type lamins (Carmosino *et al.*, 2014; Brayson and Shanahan, 2017; Donnaloja *et al.*, 2020), hallmarks of laminopathy associated DCM and the functional and morphological phenotype of lamin knockouts. For example, there is a strong and important interaction of the microtubular network with the nuclear lamina in CMs (Heffler *et al.*, 2020). Further, assessing altered biological processes in LMNA-KO, pathways involved in muscle contraction (5 in the top-15) were one of the most significant hits (see Figure 58). These transcriptomic pathways are concurrent with the finding of several proteins being dysregulated on protein level belonging to cardiac contraction components (see Figure 61) and the contractile dysfunction.

5.3.3 Partial rescue upon lamin A replacement

Given the lack of a therapeutic strategy to treat laminopathies by targeting the underlying pathogenic mechanism, a lamin A replacement therapy was tested. The severity of this model served as a basis to test the therapeutic effects. The deterioration of contractile force, one of the most relevant *in vitro* disease phenotypes, was partially rescued upon restoration of normal lamin A protein levels through AAV6-mediated gene transfer on day 15 in culture. Along the rescue of collapse in contractile force, GO pathways related to cardiac contractility, electrophysiology and mitochondrial function were partially restored in LMNA-KO GT EHTs.

Even though the therapeutic effect was significant, it remained partial, which might be due to the strategy of solely replacing lamin A. Most studies focussed and thus mainly suggest a predominant role of lamin A, but recent findings indicate an independent importance of lamin C, for example in ensuring positioning of the NPCs (Xie *et al.*, 2016; González-Cruz, Dahl and Darling, 2018). The strong expression of lamin C on mRNA and protein level also in our hiPSC-CM/EHT model argues for an important role of this variant. Furthermore, it is suggested that non-farnesylated lamin C has a modulatory role, especially in mechanical cue transduction (González-Cruz, Dahl and Darling, 2018). Thus, it can be hypothesised that lamin A expression is not sufficient to cope with the molecular and cellular consequence of complete absence of endogenous A-type lamins. To this point, the collected data cannot exclude whether the lamin C deficiency is an underlying cause for the only partial recovery in GT-treated LMNA-KO EHTs. Experiments for comparing the effects of simultaneous and exclusive overexpression of lamin A and or C in this model would address this question in the future.

Exogenous lamin A overexpression restored the morphological phenotype in LMNA-KO EHTs. Cellular and nuclear integrity of CMs were restored in GFP positive cells detected by genomic DNA and sarcomeric staining. Further, the complete absence of nuclear emerin in 2D cultured LMNA-KO CMs was reversed by GT. This is very well in line with the reported absence of emerin in fibroblasts of the patient with the homozygous mutation p.Y259X, which was also reversed by transfection of *LMNA* cDNA (Muchir *et al.*, 2003). Thus, a severe consequence on chromatin organisation in LMNA-KO CM nuclei can be assumed, due to the role of emerin to recruit chromatin to the nuclear periphery (Wilson *et al.*, 2005).

That the replacement strategy only achieved a partial restoration effect is not surprising, considering similar effect in rescuing a DCM phenotype in LMNA$^{\Delta 8\text{-}11}$ mice expressing transgenic CM-specific lamin A (Frock *et al.*, 2012). In our study, roughly 35 to 45% of hiPSC-CMs were lamin A positive (Figure 62 and Figure 63), which is comparable with the quantifications that resulted only in 35% positive CMs in the mouse study (Frock *et al.*, 2012). Partial success in our study might be due to imperfect dosage. Single cells might be heavily transduced, whereas others remain non-transduced, leaving optimisation in balancing expression strength and overall transduction efficiency. Another reason for the incomplete rescue might be timing. Recent data in a progeria mouse model revealed that only the correction (by base-editing) at an early time point restored the laminopathy phenotype, while a delayed therapy had no or only a minor effect (Koblan *et al.*, 2021). A too strong genetic background or compensation mechanism of mutated cells might be difficult to correct in other strategies and thus be the bottleneck of therapeutic approaches. The same was seen in another study using CRISPR/Cas9 (Sánchez-López *et al.*, 2021). In the present study, EHTs were transduced on day 15, a time when force development peaked, but pathology had likely already started. Together with the fact that AAV6-mediated gene transfer requires some days to reach full expression this might participate in the lack of full rescue.

5.3.4 *LMNA* dosing and toxicity

Manipulating A-type lamin levels artificially might be critical for normal cellular function given their important roles to define cell types and properties (Swift *et al.*, 2013). Levels of other proteins such as components of the sarcomere underlie a stringent stoichiometric control (Palermo *et al.*, 1996; Mearini *et al.*, 2014). Up until now, no such regulation upon exogenic expression has been described for A-type lamins. However, dosing of A-type lamins is not only important in normal cells, but pathogenicity also seems to correlate with lamin levels. Early and severe phenotype at almost foetal stage in mice and humans have been associated with complete lack of A-type lamins (Van Engelen *et al.*, 2005; Kubben *et al.*, 2011). In contrast, patients with a haploinsufficiency (roughly 50% WT lamin) typically exhibit laminopathy-associated DCM with conduction defects and mild limb girdle muscular dystrophy phenotype (Bécane *et al.*, 2000; Van Engelen *et al.*, 2005). These reports underpin a role of haploinsufficiency next to the poison peptide as the pathogenic mechanism. Moreover, this assumption also supports the strategy for a gene replacement reaching at least 50% of normal lamin A and C level. The true level of lamin A upon GT has not been solved in this study yet. As discussed above, a discrepancy was noted between MS quantification (WT level) and western blot (8-fold higher) analysis. The exact reason is not clear, but in principle, MS should be the more reliable method. Further, at higher MOIs the lamin signal increased also according to MS quantification, but not as strong as seen by Western blot analysis. A possible reason for the discrepancy is a differential post-translational modification (PTM) such as phosphorylation, ubiquitination, acetylation, or others. Such modifications can affect antibody binding, but likely not MS-based detection efficacy. It appears likely that PTMs of the exogenous protein induced by the GT differ from those of the endogenous lamin A protein, but more work is needed to answer this question.

To address the question of lamin A toxicity, different experiments were set up. First, in three independent batches of IsoC treated with the same dose GT as LMNA-KO GT (MOI 30,000), A-type lamin overexpression did not affect any of the 11 contractile parameters (see Figure 51). This encouraging result contrasts with the clear evidence for a dose-dependent toxicity in the second series. Here, transduction with different doses of *AAV6-pCMV-GFP-2A-cLMNA* in IsoC and also p.H222P induced a time- and dose-dependent decrease of contractile force in a low sample number (n=2), but transduction was assessed via MS. In the third series, the same intervention exerted no apparent effect in an unrelated control line (UKEi3). Given that the *AAV6-pCMV-GFP-2A-cLMNA* also contained GFP, which itself might exert cardiac toxicity (Huang *et al.*, 2000), a GFP-only construct was tested in parallel and also had no apparent toxicity. The exact reasons for the discrepant results in the different experimental series have not been resolved. One possibility is that the transduction efficiency in the different series differed, which has not been fully assessed. MS was only performed in the IsoC and p.H222P series which both showed a dose-dependent decrease in contractile force. On the other hand, the data could also point to batch-to-batch differences, *e.g.,* a different compensation reserve of the EHTs of the different series. In any case, the data raise caution and underscore the need for further improvements of this therapeutic approach.

To conclude, we examined the question of lamin A dosing in a hiPSC-CM model for the first time and until now found no apparent and definite sign of toxicity, neither on functional nor on structural level, in three independent experiments of IsoC. However, indications for dose dependent toxic effects were observed in one batch with low sample number. Subsequent experiments to analyse and correlate the true level of lamin with the functional data are required.

5.3.5 Therapeutic coverage and optimisation perspectives

Regarding the high number of different *LMNA* mutations, the therapeutic coverage is the main bottleneck considering gene therapies. According to the ClinVar database, 112 mutations that are classified as being pathogenic, result in a frameshift or nonsense mutation (Landrum *et al.*, 2018). Out of 498 mutations reported in another database without a filter for the record of confirmed pathogenicity, around one third (159 mutations) result in a premature stop of translation (http://www.umd.be/LMNA/; accessed 2022-10-05). Nonsense and frameshift mutations in *LMNA* are all expected to result in haploinsufficiency, because one allele is functionally inactive. The respective studies in experimental models confirm this assumption (Ito *et al.*, 2017; Bertero *et al.*, 2019; Lee *et al.*, 2019). Of note, also missense laminopathy mutations can rarely cause haploinsufficiency via NMD (Kato *et al.*, 2020). Thus, the diversity of potential pathomechanisms emphasise the need to specifically examine whether or not a mutation results in haploinsufficiency or rather a poison peptide mechanism before deciding on a specific therapeutic strategy.

To proceed further with the here discussed therapeutic strategy and aiming for clinical translation, different optimisations have to be taken into consideration. The definition of the “therapeutic index” of virus-mediated overexpression of wild-type A-type lamins. The present results have been obtained with a non-cell-specific, strong promotor (*CMV*), which is unlikely to be optimal. A cardiomyocyte-specific promoter would probably cause less unwanted effects in the body. Moreover, a promotor that is subjected to physiological regulatory mechanisms would probably reduce unwanted effects of over-dosing. This study therefore did first experiments with a promoter consisting of sequence fragments upstream of the endogenous *LMNA* gene. The fact that this construct successfully drove GFP expression in hiPSC-CM EHTs shows principal proof of activity. Further studies to determine a similar expression pattern to that of *LMNA* in different cell types would be of interest. Further improvements might be achieved by not only expressing lamin A, but also lamin C, e.g. by using respective constructs that allow endogenous splicing. Finally, it will be critical to start corrective therapies early, i.e. before structural and likely irreversible changes in the heart.

5.3.6 Conclusion and outlook

Laminopathy patients face a severe form of DCM accompanied by a poor prognosis. Up until now, there are only symptomatic treatments, thus there is a large clinical unmet need for the development of a curative therapeutic strategy. All other studies tested signalling inhibition, which covers however only one downstream aspect and lacks precision. This study could recapitulate a severe form of *LMNA* associated DCM *in vitro* in hiPSC-CM EHTs to test a replacement therapy *in vitro*. These functional, structural and molecular aspects of DCM were partially rescued by restoring lamin A expression. Despite being homozygous, while almost all patients present heterozygous *LMNA* mutations, this cellular model is of interest, since one third of reported *LMNA* mutations lead to a premature stop in translation of lamin A and C and haploinsufficiency. Thus, they putatively represent the target patient group for this gene replacement therapy.

Future experiments need to tackle questions for clinical applications, *e.g.,* of correct dosing, timing, the role of lamin C, liver toxicity and long-term toxicity. This can be either in the here described model or in additional models *e.g.,* in animal experiments. Further therapeutic interventions should be tested in a model carrying a heterozygous nonsense mutation to better reflect haploinsufficiency. For the remaining missense mutations, probably caused by a poison-peptide, gain-of-function mechanism, a suppression-replacement gene therapy (Sánchez-López *et al.*, 2021) or one of the various gene-editing approaches (Santiago-Fernández *et al.*, 2019; Koblan *et al.*, 2021) might be the right option.

6 Summary

The two isoforms lamin A and C, A-type lamins, encoded by the gene *LMNA* via alternative splicing, are located at the inner nuclear membrane, and play pivotal roles in shaping the mechanical properties of the nucleus, in regulating gene expression and sensing and responding to extracellular mechanical cues. Given the complex roles of A-type lamins, mutations can cause a diverse picture range of affected tissues, phenotypes and molecular consequences, very often accompanied by a severe form of dilated cardiomyopathy (DCM). The broad range of molecular consequences makes a causative therapy for DCM challenging, leaving heart transplantation the only option at end-stage of the disease. Here, we investigated in human induced pluripotent stem cell derived cardiomyocytes (hiPSC-CMs) engineered heart tissues (EHTs) the functional and molecular consequences of (i) a heterozygous missense *LMNA* mutation (p.H222P) and (ii) a homozygous premature stop-codon resulting in complete *LMNA* knockout (LMNA-KO). (iii) A lamin A gene replacement therapy (*AAV6-pCMV-GFP-2A-cLMNA*) was tested in the LMNA-KO EHT model.

P.H222P hiPSCs revealed an instable cardiac differentiation capacity compared to IsoC hiPSCs. Successful differentiated CMs of p.H222P casted to EHTs revealed shorter relaxation time and a tendency towards lower force development than IsoC. Contractile function further deteriorated in p.H222P upon acute afterload enhancement (AE), but not in IsoC EHTs. The transcriptomic profile was altered in p.H222P EHTs and further exaggerated by AE. Interestingly, p.H222P showed a much larger gene expression response to AE than IsoC, suggesting a mechanical coupling defect as a putatively global pathogenic mechanism.

The LMNA-KO EHT model revealed a severe, time-dependent functional phenotype including marked force deterioration. Relaxation time, contraction velocity, contractile force and resting length were also significantly altered. Cellular and nuclear integrity as well as tissue remodelling capacity were disturbed in LMNA-KO EHTs. Transcriptomic and proteomic analyses revealed alterations of typical DCM pathways and lamin interaction partners. Adeno-associated virus mediated restoration of lamin A (*AAV6-pCMV-GFP-2A-cLMNA*) expression and localisation in the nuclear lamina resulted in the partial rescue of the functional, structural, transcriptomic and proteomic phenotype. While parallel treatment of IsoC EHTs with *AAV6-pCMV-GFP-2A-cLMNA* with the same dose did not exert signs of toxicity, other series of experiments in different hiPSC lines showed evidence for a dose-dependent decrease of contractile function.

In summary, two novel laminopathy hiPSC-CM EHT models were established. (i) A heterozygous p.H222P model recapitulated a mechanical decoupling phenotype and (ii) a homozygous LMNA-KO showed severe contractile dysfunction that was partially rescued by lamin A overexpression. The p.H222P model might serve as a basis for studying the interplay of altered gene expression and mechanical stress in a human laminopathy cardiac background. Thus, this model might enable to investigate a more global underlying mechanism. The LMNA-KO model addresses the second challenge for laminopathy research, elucidating a therapeutic strategy. One third of the laminopathy patients carry a nonsense mutation resulting in a premature stop of translation and putatively in a haploinsufficiency. This model might serve as a steppingstone to test the therapeutic window and assess further cardiac toxicity of the gene replacement therapy.

7 Zusammenfassung

Das Gen *LMNA* kodiert durch alternatives Spleißen die Isoformen Lamin A und C, zusammengefasst A-Typ Lamine. A-Typ Lamine befinden sich an der inneren Kernmembran und spielen eine zentrale Rolle bei der Genomorganisation, bei der Beeinflussung der mechanischen Eigenschaften des Zellkerns und bei der Weiterleitung und Reaktion auf extrazelluläre mechanische Reize. Angesichts der komplexen Rolle der A-Typ-Lamine betreffen Mutationen im Gen *LMNA* eine Vielzahl von Gewebetypen, welche in unterschiedlichen Phänotypen und unterschiedlichen molekularen Folgen resultieren. Dennoch gehen *LMNA*-assoziierte Krankheiten, so genannte Laminopathien, meistens mit einer schweren Form der dilatativen Kardiomyopathie (DCM) einher. Das breite Spektrum der molekularen Folgen macht eine Therapie für *LMNA* assoziierte DCM schwierig, so dass im Endstadium der Krankheit meist eine Herztransplantation die einzige Option ist. Hier wurden (i) die funktionellen und molekularen Folgen einer *LMNA missense* Mutation (p.H222P) in aus menschlichen induzierten pluripotenten Stammzellen abgeleiteten Kardiomyozyten (*hiPSC-CM*) im künstlichen Herzmuskelgewebe (EHT) und im Vergleich zur isogenen Kontrolllinie (IsoC) untersucht. Darüber hinaus wurde (ii) eine Zelllinie, mit einem homozygoten vorzeitigen Stopp-Codon, das zu einem *Knockout* von *LMNA* führt (LMNA-KO) im hiPSC-CM EHT Format untersucht, und eine Lamin-A-Gentherapie in diesem Modell getestet.

Bei der Etablierung des p.H222P Laminopathie-Krankheitsmodells zeigten die hiPSCs im Vergleich zu IsoC hiPSCs eine hohe Varianz im kardialen Differenzierungsvermögen. Die erfolgreich differenzierten CMs von p.H222P wiesen im EHT-Format eine kürzere Relaxationszeit, eine Tendenz zu einer geringeren Kontraktionskraft im Vergleich zu IsoC-EHTs und Veränderungen des Aktionspotentials auf. Die kontraktile Funktion fiel bei p.H222P unter akuter Nachlasterhöhung (AE) ab, nicht aber bei IsoC-EHTs. Eine Transkriptom-Analyse zeigte, dass sich das Expressionsprofil von p.H222P EHTs stark von IsoC unterschied. p.H222P EHTs reagierten auf eine durch erhöhte AE induzierte mechanische Belastung deutlich stärker mit einer Veränderung der Genexpression als IsoC. Die Ergebnisse sprechen zusammengenommen für einen Defekt der mechanischen Kopplung, welcher mutmaßlich als globaler pathogener Mechanismus in diesem Laminopathie Modell und darüber hinaus verstanden werden kann.

Das LMNA-KO-EHT-Modell zeigte im Vergleich zu p.H222P einen schwereren funktionellen Phänotyp auf, der zu einem zeitabhängigen Einbruch in der Kontraktionskraft führte. Die Relaxationszeit, die Kontraktionsgeschwindigkeit, die Kontraktionskraft und die Ruhelänge

waren alle samt signifikant verändert. Das Fehlen der A-Typ-Lamine führte zu fehlender zellulärer und nukleärer Integrität sowie einer eingeschränkten Fähigkeit zum *Remodelling* im EHT. Die Expression von typischen DCM-Signalwegen und Lamin-Interaktionspartnern war in der Transkriptom- und Proteom-Analyse in LMNA-KO-EHTs verändert. Die durch ein Adeno-assoziiertes Virus vermittelte Expression von Lamin A führte zu einem Einbau von Lamin A in die Kernmembran und einer teilweisen Verbesserung des funktionellen und strukturellen Phänotyps, sowie partiell des Transkriptoms und Proteoms. Während die parallele Behandlung von IsoC-EHTs mit *AAV6-pCMV-GFP-2A-cLMNA* bei gleicher Dosis keine Anzeichen von Toxizität aufwies, zeigten andere Versuchsreihen in verschiedenen hiPSC-Linien Hinweise auf eine dosisabhängige Abnahme der kontraktilen Funktion.

Zusammengefasst wurden zwei neue Laminopathie-hiPSC-CM-EHT-Modelle etabliert: (i) EHTs mit einer heterozygoten p.H222P Mutation wiesen Zeichen einer mechanischen Entkopplung als grundlegenden Krankheits-Phänotyp auf, und (ii) EHTs mit einem homozygoten LMNA-KO zeigten eine schwere kontraktile Dysfunktion, die durch exogene Lamin-A-Expression teilweise behoben werden konnte. Das p.H222P-Modell kann als Grundlage für die Untersuchung des Zusammenspiels von veränderter Genexpression und mechanischer Belastung im humanen kardialen Laminopathie-Kontext dienen. Dieses Modell könnte es ermöglichen, einen globaleren zugrunde liegenden Mechanismus zu ermitteln. Das LMNA-KO-Modell stellt die Basis für die Untersuchung der zweiten Herausforderung für die Laminopathie-Forschung, der Ermittlung einer therapeutischen Strategie, dar. Ein Drittel der Laminopathie-Patienten trägt eine *nonsense* Mutation, die zu einem vorzeitigen Translationsstopp und dadurch vermutlich zu einer Haploinsuffizienz führen. Dieses Modell könnte als erster Ansatz für die Ermittlung eines therapeutischen Fensters und die Testung kardialer Toxizität der Genersatztherapie dienen.

8 Literature

Al-Saaidi, R. and Bross, P. (2015) ‘Do lamin A and lamin C have unique roles?’, *Chromos*, 124, pp. 1–12. doi: 10.1007/s00412-014-0484-7.

Ali, H., Braga, L. and Giacca, M. (2020) ‘Cardiac regeneration and remodelling of the cardiomyocyte cytoarchitecture’, *The FEBS Journal*. Blackwell Publishing Ltd, 287(3), pp. 417–438. doi: 10.1111/febs.15146.

Anders, S., Pyl, P. T. and Huber, W. (2015) ‘HTSeq—a Python framework to work with high-throughput sequencing data’, *Bioinformatics*. Oxford Academic, 31(2), pp. 166–169. doi: 10.1093/BIOINFORMATICS/BTU638.

Antzelevitch, C. *et al.* (2007) ‘Loss-of-Function Mutations in the Cardiac Calcium Channel Underlie a New Clinical Entity Characterized by ST-Segment Elevation, Short QT Intervals, and Sudden Cardiac Death’, *Circulation*. Lippincott Williams & Wilkins, 115(4), pp. 442–449. doi: 10.1161/CIRCULATIONAHA.106.668392.

Anzalone, A. V. *et al.* (2019) ‘Search-and-replace genome editing without double-strand breaks or donor DNA’, *Nature 2019 576:7785*. Nature Publishing Group, 576(7785), pp. 149–157. doi: 10.1038/s41586-019-1711-4.

Arbustini, E. *et al.* (2002) ‘Autosomal Dominant Dilated Cardiomyopathy With Atrioventricular Block: A Lamin A/C Defect-Related Disease’. doi: 10.1016/S0735-1097(02)01724-2.

Arimura, T. *et al.* (2005) ‘Mouse model carrying H222P-Lmna mutation develops muscular dystrophy and dilated cardiomyopathy similar to human striated muscle laminopathies’, *Human Molecular Genetics*, 14(1), pp. 155–169. doi: 10.1093/hmg/ddi017.

Armaroli, A. *et al.* (2020) ‘Lamin A/C Missense Mutation R216C Pinpoints Overlapping Features between Brugada Syndrome and Laminopathies’, *Circulation: Genomic and Precision Medicine*. Lippincott Williams and Wilkins, pp. 90–92. doi: 10.1161/CIRCGEN.119.002751.

Auguste, G. *et al.* (2020) ‘BET bromodomain inhibition attenuates cardiac phenotype in myocyte-specific lamin A/C-deficient mice’, *Journal of Clinical Investigation*, 130(9), pp. 4740–4758. doi: 10.1172/JCI135922.

Azibani, F. *et al.* (2018) ‘Gene Therapy via Trans -Splicing for LMNA -Related Congenital Muscular Dystrophy’, 10(March), pp. 376–386. doi: 10.1016/j.omtn.2017.12.012.

Bassett, A. R. (2017) ‘Editing the genome of hiPSC with CRISPR/Cas9: disease models’, *Mammalian Genome 2017 28:7*. Springer, 28(7), pp. 348–364. doi: 10.1007/S00335-017-

9684-9.

Bécane, H. M. *et al.* (2000) ‘High incidence of sudden death with conduction system and myocardial disease due to lamins A and C gene mutation’, *Pacing and clinical electrophysiology : PACE*. Pacing Clin Electrophysiol, 23(11 Pt 1), pp. 1661–1666. doi: 10.1046/J.1460-9592.2000.01661.X.

Van Berlo, J. H. *et al.* (2005) ‘Meta-analysis of clinical characteristics of 299 carriers of LMNA gene mutations: Do lamin A/C mutations portend a high risk of sudden death?’, *Journal of Molecular Medicine*, 83(1), pp. 79–83. doi: 10.1007/s00109-004-0589-1.

Van Berlo, J. H., Duboc, D. and Pinto, Y. M. (2004) ‘Often seen but rarely recognised: cardiac complications of lamin A/C mutations’, *European Heart Journal*. Oxford Academic, 25(10), pp. 812–814. doi: 10.1016/J.EHJ.2004.03.007.

Bernasconi, P. *et al.* (2018) ‘Elevated TGF b2 serum levels in Emery-Dreifuss Muscular Dystrophy: Implications for myocyte and tenocyte differentiation and fibrogenic processes’. doi: 10.1080/19491034.2018.1467722.

Bertero, A. *et al.* (2019) ‘Chromatin compartment dynamics in a haploinsufficient model of cardiac laminopathy’, *The Journal of cell biology*, 218(9), pp. 2919–2944. doi: 10.1083/jcb.201902117.

Bertrand, A. T. *et al.* (2012) ‘DelK32-lamin A/C has abnormal location and induces incomplete tissue maturation and severe metabolic defects leading to premature death’, *Human Molecular Genetics*, 21(5), pp. 1037–1048. doi: 10.1093/hmg/ddr534.

Bertrand, A. T. *et al.* (2014) ‘Cellular microenvironments reveal defective mechanosensing responses and elevated YAP signaling in LMNA-mutated muscle precursors’, *Journal of Cell Science*, 127, pp. 2873–2884. doi: 10.1242/jcs.144907.

Bione, S. *et al.* (1994) ‘Identification of a novel X-linked gene responsible for Emery-Dreifuss muscular dystrophy’, *Nature Genetics 1994 8:4*. Nature Publishing Group, 8(4), pp. 323–327. doi: 10.1038/ng1294-323.

Boel, A. *et al.* (2018) ‘CRISPR/Cas9-mediated homology-directed repair by ssODNs in zebrafish induces complex mutational patterns resulting from genomic integration of repair-template fragments’, *Disease Models & Mechanisms*. Company of Biologists, 11(10). doi: 10.1242/DMM.035352.

Bolger, A. M., Lohse, M. and Usadel, B. (2014) ‘Trimmomatic: a flexible trimmer for Illumina sequence data’, *Bioinformatics*. Oxford Academic, 30(15), pp. 2114–2120. doi: 10.1093/BIOINFORMATICS/BTU170.

Bonne, G. *et al.* (1999) 'Mutations in the gene encoding lamin A/C cause autosomal dominant Emery-Dreifuss muscular dystrophy', *Nature Genetics 1999 21:3*. Nature Publishing Group, 21(3), pp. 285–288. doi: 10.1038/6799.

Bonne, G. *et al.* (2000) 'Clinical and molecular genetic spectrum of autosomal dominant Emery-Dreifuss muscular dystrophy due to mutations of the lamin A/C gene', *Annals of Neurology*, 48(2), pp. 170–180. doi: 10.1002/1531-8249(200008)48:2<170::AID-ANA6>3.0.CO;2-J.

Brayson, D. and Shanahan, C. M. (2017) 'Current insights into LMNA cardiomyopathies: Existing models and missing LINCs', *Nucleus*, 8. doi: 10.1080/19491034.2016.1260798.

Breckwoldt, K. *et al.* (2017) 'Differentiation of cardiomyocytes and generation of human engineered heart tissue', *Nature Protocols*. doi: 10.1038/nprot.2017.033.

Brenière-Letuffe, D. *et al.* (2018) 'Clonal dynamics studied in cultured induced pluripotent stem cells reveal major growth imbalances within a few weeks', *Stem cell research & therapy*. NLM (Medline), 9(1), p. 165. doi: 10.1186/S13287-018-0893-2/FIGURES/4.

Brull, A. *et al.* (2018) 'The Pathogenesis and Therapies of Striated Muscle Laminopathies', *Frontiers in Physiology*. Frontiers, 0(OCT), p. 1533. doi: 10.3389/FPHYS.2018.01533.

Bruyneel, A. A. N. *et al.* (2018) 'Using iPSC Models to Probe Regulation of Cardiac Ion Channel Function', *Current Cardiology Reports 2018 20:7*. Springer, 20(7), pp. 1–12. doi: 10.1007/S11886-018-1000-0.

Burridge, P. W. *et al.* (2007) 'Improved human embryonic stem cell embryoid body homogeneity and cardiomyocyte differentiation from a novel V-96 plate aggregation system highlights interline variability', *Stem cells (Dayton, Ohio)*. Stem Cells, 25(4), pp. 929–938. doi: 10.1634/STEMCELLS.2006-0598.

Burridge, P. W. *et al.* (2014) 'Chemically Defined and Small Molecule-Based Generation of Human Cardiomyocytes', *Nature methods*. NIH Public Access, 11(8), p. 855. doi: 10.1038/NMETH.2999.

Carmosino, M. *et al.* (2014) 'Role of nuclear Lamin A/C in cardiomyocyte functions', *Biology of the Cell*, 106(10), pp. 346–358. doi: 10.1111/boc.201400033.

Cattin, M.-E. *et al.* (2013) 'Heterozygous Lmna delK32 mice develop dilated cardiomyopathy through a combined pathomechanism of haploinsufficiency and peptide toxicity', *Human Molecular Genetics*, 22(15), pp. 3152–3164. doi: 10.1093/hmg/ddt172.

Cattin, M. E. *et al.* (2016) 'Mutation in lamin A/C sensitizes the myocardium to exercise-induced mechanical stress but has no effect on skeletal muscles in mouse', *Neuromuscular*

Disorders, 26(8), pp. 490–499. doi: 10.1016/j.nmd.2016.05.010.

Chai, R. J. *et al.* (2021) ‘Disrupting the LINC complex by AAV mediated gene transduction prevents progression of Lamin induced cardiomyopathy’, *Nature Communications*. Springer US, 12(1), pp. 1–16. doi: 10.1038/s41467-021-24849-4.

Chandar, S. *et al.* (2010) ‘Effects of mechanical stress and carvedilol in lamin A/C-deficient dilated cardiomyopathy’, *Circulation Research*, 106(3), pp. 573–582. doi: 10.1161/CIRCRESAHA.109.204388.

Chatzifrangkeskou, M. *et al.* (2016) ‘ERK1/2 directly acts on CTGF/CCN2 expression to mediate myocardial fibrosis in cardiomyopathy caused by mutations in the lamin A/C gene’, *Human Molecular Genetics*, 25(11), pp. 2220–2233. doi: 10.1093/hmg/ddw090.

Chatzifrangkeskou, M. *et al.* (2018) ‘Cofilin-1 phosphorylation catalyzed by ERK1/2 alters cardiac actin dynamics in dilated cardiomyopathy caused by lamin A/C gene mutation’, *Original Article Human Molecular Genetics*. Advance Access Publication Date, 27(5), pp. 3060–3078. doi: 10.1093/hmg/ddy215.

Chen, L., Sampson, K. J. and Kass, R. S. (2016) ‘Cardiac Delayed Rectifier Potassium Channels in Health and Disease’, *Cardiac electrophysiology clinics*. NIH Public Access, 8(2), p. 307. doi: 10.1016/J.CCEP.2016.01.004.

Cho, S. *et al.* (2019) ‘Mechanosensing by the Lamina Protects against Nuclear Rupture, DNA Damage, and Cell-Cycle Arrest’, *Developmental Cell*. Elsevier Inc., 49(6), pp. 920-935.e5. doi: 10.1016/j.devcel.2019.04.020.

Choi, J. C. *et al.* (2012) ‘Dual specificity phosphatase 4 mediates cardiomyopathy caused by lamin A/C (LMNA) gene mutation’, *Journal of Biological Chemistry*, 287(48), pp. 40513–40524. doi: 10.1074/JBC.M112.404541.

Choi, J. C. and Worman, H. J. (2013) ‘Reactivation of autophagy ameliorates LMNA cardiomyopathy’, *Autophagy*, 9(1), pp. 110–111. doi: 10.4161/auto.22403.

Chung, J.-H. *et al.* (2016) ‘Myofilament calcium sensitivity: Role in regulation of in vivo cardiac contraction and relaxation’, *Frontiers in Physiology*. Frontiers Media SA, 7(DEC), p. 562. doi: 10.3389/FPHYS.2016.00562.

Constantinescu, D. *et al.* (2006) ‘Lamin A/C expression is a marker of mouse and human embryonic stem cell differentiation’, *Stem cells (Dayton, Ohio)*. Stem Cells, 24(1), pp. 177–185. doi: 10.1634/STEMCELLS.2004-0159.

Crasto, S., My, I. and Di Pasquale, E. (2020) ‘The Broad Spectrum of LMNA Cardiac Diseases: From Molecular Mechanisms to Clinical Phenotype’, *Frontiers in Physiology*.

Frontiers Media S.A. doi: 10.3389/fphys.2020.00761.

Cuello, F. *et al.* (2021) ‘Impairment of the ER/mitochondria compartment in human cardiomyocytes with PLN p.Arg14del mutation’, *EMBO Molecular Medicine*. John Wiley & Sons, Ltd, 13(6), p. e13074. doi: 10.15252/EMMM.202013074.

Daer, R. M. *et al.* (2017) ‘The Impact of Chromatin Dynamics on Cas9-Mediated Genome Editing in Human Cells’, *ACS synthetic biology*. ACS Synth Biol, 6(3), pp. 428–438. doi: 10.1021/ACSSYNBIO.5B00299.

Dechat, T. *et al.* (2008) ‘Nuclear lamins: major factors in the structural organization and function of the nucleus and chromatin’, *Genes & development*. doi: 10.1101/gad.1652708.

Deltcheva, E. *et al.* (2011) ‘CRISPR RNA maturation by trans-encoded small RNA and host factor RNase III’, *Nature 2011 471:7340*. Nature Publishing Group, 471(7340), pp. 602–607. doi: 10.1038/nature09886.

Denning, C. *et al.* (2016) ‘Cardiomyocytes from human pluripotent stem cells: From laboratory curiosity to industrial biomedical platform ☆’. doi: 10.1016/j.bbamcr.2015.10.014.

Donnaloja, F. *et al.* (2020) ‘Lamin A/C Mechanotransduction in Laminopathies’, *Cells 2020, Vol. 9, Page 1306*. Multidisciplinary Digital Publishing Institute, 9(5), p. 1306. doi: 10.3390/CELLS9051306.

Dotzler, S. M. *et al.* (2021) ‘Suppression-Replacement KCNQ1 Gene Therapy for Type 1 Long QT Syndrome’, *Circulation*. Lippincott Williams and Wilkins, 143(14), pp. 1411–1425. doi: 10.1161/CIRCULATIONAHA.120.051836.

Le Dour, C. *et al.* (2017) ‘Decreased WNT/b-catenin signalling contributes to the pathogenesis of dilated cardiomyopathy caused by mutations in the lamin a/C gene’, *Human Molecular Genetics*, 26(2), pp. 333–343. doi: 10.1093/hmg/ddw389.

Driscoll, T. P. *et al.* (2015) ‘Cytoskeletal to Nuclear Strain Transfer Regulates YAP Signaling in Mesenchymal Stem Cells’, *Biophysical Journal*. Biophysical Society, 108(12), pp. 2783–2793. doi: 10.1016/j.bpj.2015.05.010.

DuBose, A. J. *et al.* (2018) ‘Everolimus rescues multiple cellular defects in laminopathy-patient fibroblasts.’, *Proceedings of the National Academy of Sciences of the United States of America*. National Academy of Sciences, 115(16), pp. 4206–4211. doi: 10.1073/pnas.1802811115.

Dupont, S. *et al.* (2011) ‘Role of YAP/TAZ in mechanotransduction’, *Nature*, 474(7350), pp. 179–184. doi: 10.1038/nature10137.

Earle, A. J. *et al.* (2020) ‘Mutant lamins cause nuclear envelope rupture and DNA damage in skeletal muscle cells’, *Nature Materials*, 19(4), pp. 464–473. doi: 10.1038/s41563-019-0563-5.

Eder, A. *et al.* (2014) ‘Effects of proarrhythmic drugs on relaxation time and beating pattern in rat engineered heart tissue’. Available at: https://www.ncbi.nlm.nih.gov/pmc/articles/PMC4160570/pdf/395_2014_Article_436.pdf (Accessed: 11 January 2018).

Eijgenraam, T. R., Silljé, H. H. W. and de Boer, R. A. (2020) ‘Current understanding of fibrosis in genetic cardiomyopathies’, *Trends in Cardiovascular Medicine*. Elsevier, 30(6), pp. 353–361. doi: 10.1016/J.TCM.2019.09.003.

Eisner, D. A., Dibb, K. M. and Trafford, A. W. (2009) ‘The mechanism and significance of the slow changes of ventricular action potential duration following a change of heart rate’, *Experimental Physiology*. John Wiley & Sons, Ltd, 94(5), pp. 520–528. doi: 10.1113/EXPPHYSIOL.2008.044008.

Elosegui-Artola, A. *et al.* (2017) ‘Force Triggers YAP Nuclear Entry by Regulating Transport across Nuclear Pores’, *Cell*. Cell Press, 171(6), pp. 1397-1410.e14. doi: 10.1016/j.cell.2017.10.008.

Van Engelen, B. G. M. *et al.* (2005) ‘The lethal phenotype of a homozygous nonsense mutation in the lamin A/C gene’, *Neurology*, 64(2), pp. 374–376. doi: 10.1212/01.WNL.0000149763.15180.00.

Eschenhagen, T. *et al.* (1997) ‘Three-dimensional reconstitution of embryonic cardiomyocytes in a collagen matrix: a new heart muscle model system.’, *FASEB journal : official publication of the Federation of American Societies for Experimental Biology*, 11(8), pp. 683–94. doi: 10.1096/fasebj.11.8.9240969.

Eschenhagen, T. and Carrier, L. (2019) ‘Cardiomyopathy phenotypes in human-induced pluripotent stem cell-derived cardiomyocytes-a systematic review’, *European Journal of Physiology*, 471, pp. 755–768. doi: 10.1007/s00424-018-2214-0.

Eser, G. and Topaloğlu, H. (2022) ‘Current Outline of Exon Skipping Trials in Duchenne Muscular Dystrophy’, *Genes*, 13(7). doi: 10.3390/genes13071241.

Fatkin, D. *et al.* (1999) ‘Missense Mutations in the Rod Domain of the Lamin A/C Gene as Causes of Dilated Cardiomyopathy and Conduction-System Disease’, *New England Journal of Medicine*. Massachusetts Medical Society, 341(23), pp. 1715–1724. doi: 10.1056/NEJM199912023412302.

Feyen, D. A. M. *et al.* (2020) 'Metabolic Maturation Media Improve Physiological Function of Human iPSC-Derived Cardiomyocytes', *Cell Reports*. Elsevier B.V., 32(3). doi: 10.1016/J.CELREP.2020.107925.

Frank, S. *et al.* (2012) 'Small Molecule-Assisted, Line-Independent Maintenance of Human Pluripotent Stem Cells in Defined Conditions', *PLoS ONE*, 7(7), p. 41958. doi: 10.1371/journal.pone.0041958.

Frock, R. L. *et al.* (2012) 'Cardiomyocyte-specific expression of lamin A improves cardiac function in Lmna-/- mice', *PLoS ONE*, 7(8). doi: 10.1371/journal.pone.0042918.

Gaita, F. *et al.* (2003) 'Short QT Syndrome', *Circulation*. Lippincott Williams & Wilkins, 108(8), pp. 965–970. doi: 10.1161/01.CIR.0000085071.28695.C4.

Galata, Z. *et al.* (2018) 'Amelioration of desmin network defects by αB-crystallin overexpression confers cardioprotection in a mouse model of dilated cardiomyopathy caused by LMNA gene mutation', *Journal of Molecular and Cellular Cardiology*. Elsevier, 125(June), pp. 73–86. doi: 10.1016/j.yjmcc.2018.10.017.

Gerbino, A. *et al.* (2018) 'Role of Lamin A/C Gene Mutations in the Signaling Defects Leading to Cardiomyopathies', *Frontiers in Physiology*. Frontiers, 9, p. 1356. doi: 10.3389/fphys.2018.01356.

Gesson, K. *et al.* (2016) 'A-type lamins bind both hetero- and euchromatin, the latter being regulated by lamina-associated polypeptide 2 alpha', *Genome research*. Genome Res, 26(4), pp. 462–473. doi: 10.1101/GR.196220.115.

Gilbert, G. *et al.* (2021) 'Incomplete Assembly of the Dystrophin-Associated Protein Complex in 2D and 3D-Cultured Human Induced Pluripotent Stem Cell-Derived Cardiomyocytes', *Frontiers in Cell and Developmental Biology*. Frontiers Media S.A., 9, p. 2869. doi: 10.3389/FCELL.2021.737840/BIBTEX.

González-Cruz, R. D., Dahl, K. N. and Darling, E. M. (2018) 'The Emerging Role of Lamin C as an Important LMNA Isoform in Mechanophenotype', *Frontiers in Cell and Developmental Biology*. Frontiers Media SA, 6(NOV). doi: 10.3389/FCELL.2018.00151.

Goswami, R. *et al.* (2019) 'Gene Therapy Leaves a Vicious Cycle', *Frontiers in Oncology*. Frontiers, 9, p. 297. doi: 10.3389/fonc.2019.00297.

Grant, A. O. (2009) 'Cardiac Ion Channels', *Circulation: Arrhythmia and Electrophysiology*. Lippincott Williams & Wilkins, 2(2), pp. 185–194. doi: 10.1161/CIRCEP.108.789081.

Gruenbaum, Y. and Foisner, R. (2015) 'Lamins: Nuclear Intermediate Filament Proteins with Fundamental Functions in Nuclear Mechanics and Genome Regulation', *Annual Review of*

Biochemisty. doi: 10.1146/annurev-biochem-060614-034115.

Gruenbaum, Y. and Medalia, O. (2015) ‘Lamins: The structure and protein complexes’, *Current Opinion in Cell Biology*. Elsevier Ltd, 32, pp. 7–12. doi: 10.1016/j.ceb.2014.09.009.

Guénantin, A. C. *et al.* (2021) ‘Targeting the histone demethylase LSD1 prevents cardiomyopathy in a mouse model of laminopathy’, *Journal of Clinical Investigation*. American Society for Clinical Investigation, 131(1). doi: 10.1172/JCI136488.

Guo, Y. and Pu, W. T. (2020) ‘Cardiomyocyte Maturation’, *Circulation Research*. Lippincott Williams & WilkinsHagerstown, MD, pp. 1086–1106. doi: 10.1161/CIRCRESAHA.119.315862.

Guo, Y. and Yixian, Z. (2015) ‘Lamins position the nuclear pores and centrosomes by modulating dynein’, *Molecular Biology of the Cell*. American Society for Cell Biology, 26(19), p. 3379. doi: 10.1091/MBC.E15-07-0482.

Gussak, I. *et al.* (2000) ‘Idiopathic Short QT Interval:A New Clinical Syndrome?’, *Cardiology*. Karger Publishers, 94(2), pp. 99–102. doi: 10.1159/000047299.

Hansen, A. *et al.* (2010) ‘Development of a drug screening platform based on engineered heart tissue’, *Circulation Research*, 107(1), pp. 35–44. doi: 10.1161/CIRCRESAHA.109.211458.

Hasselberg, N. E. *et al.* (2018) ‘Lamin A/C cardiomyopathy: Young onset, high penetrance, and frequent need for heart transplantation’, *European Heart Journal*, 39(10), pp. 853–860. doi: 10.1093/eurheartj/ehx596.

Haurwitz, R. E. *et al.* (2010) ‘Sequence- and structure-specific RNA processing by a CRISPR endonuclease’, *Science*. American Association for the Advancement of Science, 329(5997), pp. 1355–1358. doi: 10.1126/SCIENCE.1192272/SUPPL_FILE/HAURWITZ-SOM.PDF.

Heald, R. and McKeon, F. (1990) ‘Mutations of phosphorylation sites in lamin A that prevent nuclear lamina disassembly in mitosis’, *Cell*. Cell, 61(4), pp. 579–589. doi: 10.1016/0092-8674(90)90470-Y.

Heffler, J. *et al.* (2020) ‘A Balance Between Intermediate Filaments and Microtubules Maintains Nuclear Architecture in the Cardiomyocyte’, *Circulation Research*. Lippincott Williams & WilkinsHagerstown, MD, pp. E10–E26. doi: 10.1161/CIRCRESAHA.119.315582.

Hershberger, R. E. *et al.* (2021) ‘The Complex and Diverse Genetic Architecture of Dilated Cardiomyopathy’, *Circulation Research*. Lippincott Williams and Wilkins, pp. 1514–1532. doi: 10.1161/CIRCRESAHA.121.318157.

Hershberger, R. E., Hedges, D. J. and Morales, A. (2013) 'Dilated cardiomyopathy: the complexity of a diverse genetic architecture', *Nature Reviews Cardiology 2013 10:9*. Nature Publishing Group, 10(9), pp. 531–547. doi: 10.1038/nrcardio.2013.105.

Hershberger, R. E., Morales, A. and Siegfried, J. D. (2010) 'Clinical and genetic issues in dilated cardiomyopathy: a review for genetics professionals.', *Genetics in medicine : official journal of the American College of Medical Genetics*. NIH Public Access, 12(11), pp. 655–67. doi: 10.1097/GIM.0b013e3181f2481f.

Hirt, M. N. *et al.* (2012) 'Increased afterload induces pathological cardiac hypertrophy: a new in vitro model', *Basic Research in Cardiology*, 107(6), pp. 1–16. doi: 10.1007/s00395-012-0307-z.

Hirt, M. N. *et al.* (2014) 'Functional improvement and maturation of rat and human engineered heart tissue by chronic electrical stimulation', *Journal of Molecular and Cellular Cardiology*. Academic Press, 74, pp. 151–161. doi: 10.1016/j.yjmcc.2014.05.009.

Höger, T. H. *et al.* (1990) 'Characterization of a second highly conserved B-type lamin present in cells previously thought to contain only a single B-type lamin', *Chromosoma*, 99(6), pp. 379–390. doi: 10.1007/BF01726689.

Horváth, A. *et al.* (2020) 'Case Report on: Very Early Afterdepolarizations in HiPSC-Cardiomyocytes—An Artifact by Big Conductance Calcium Activated Potassium Current (Ibk,Ca)', *Cells 2020, Vol. 9, Page 253*. Multidisciplinary Digital Publishing Institute, 9(1), p. 253. doi: 10.3390/CELLS9010253.

Hu, Y. *et al.* (1998) 'Activation of PDGF receptor alpha in vascular smooth muscle cells by mechanical stress', *FASEB journal : official publication of the Federation of American Societies for Experimental Biology*. FASEB J, 12(12), pp. 1135–1142. doi: 10.1096/FASEBJ.12.12.1135.

Huang, W. Y. *et al.* (2000) 'Transgenic expression of green fluorescence protein can cause dilated cardiomyopathy', *Nature Medicine 2000 6:5*. Nature Publishing Group, 6(5), pp. 482–483. doi: 10.1038/74914.

Hwang, H. S. *et al.* (2015) 'Comparable calcium handling of human iPSC-derived cardiomyocytes generated by multiple laboratories', *Journal of Molecular and Cellular Cardiology*. Academic Press, 85, pp. 79–88. doi: 10.1016/J.YJMCC.2015.05.003.

Ito, K. *et al.* (2017) 'Identification of pathogenic gene mutations in *LMNA* and *MYBPC3* that alter RNA splicing', *Proceedings of the National Academy of Sciences*, 114(29), pp. 7689–7694. doi: 10.1073/pnas.1707741114.

Jahn, D. *et al.* (2012) ‘A truncated lamin A in the Lmna -/- mouse line: implications for the understanding of laminopathies.’, *Nucleus (Austin, Tex.)*. doi: 10.4161/nucl.21676.

Jain, S. *et al.* (2021) ‘TALEN outperforms Cas9 in editing heterochromatin target sites’, *Nature Communications 2021 12:1*. Nature Publishing Group, 12(1), pp. 1–10. doi: 10.1038/s41467-020-20672-5.

Jiang, C. L. *et al.* (2022) ‘Cell type determination for cardiac differentiation occurs soon after seeding of human-induced pluripotent stem cells’, *Genome Biology*. BioMed Central Ltd, 23(1), pp. 1–29. doi: 10.1186/S13059-022-02654-6/FIGURES/5.

Jinek, M. *et al.* (2013) ‘RNA-programmed genome editing in human cells’, *eLife*, 2. doi: 10.7554/eLife.00471.

Jordan, E. *et al.* (2021) ‘Evidence-Based Assessment of Genes in Dilated Cardiomyopathy’, *Circulation*. Lippincott Williams & WilkinsHagerstown, MD, 144(1), pp. 7–19. doi: 10.1161/CIRCULATIONAHA.120.053033.

Judge, D. P. *et al.* (2022) ‘Long-Term Efficacy and Safety of ARRY-371797 (PF-07265803) in Patients With Lamin A/C–Related Dilated Cardiomyopathy’, *American Journal of Cardiology*. Elsevier Inc., 183, pp. 93–98. doi: 10.1016/j.amjcard.2022.08.001.

Kaese, S. and Verheule, S. (2012) ‘Cardiac electrophysiology in mice: A matter of size’, *Frontiers in Physiology*. Frontiers, 3 SEP, p. 345. doi: 10.3389/FPHYS.2012.00345/BIBTEX.

Kane, G. C. *et al.* (2006) ‘KCNJ11 gene knockout of the Kir6.2 K ATP channel causes maladaptive remodeling and heart failure in hypertension’, *Human Molecular Genetics*. Oxford Academic, 15(15), pp. 2285–2297. doi: 10.1093/HMG/DDL154.

Kato, K. *et al.* (2020) ‘ LMNA Missense Mutation Causes Nonsense-mediated mRNA Decay and Severe Dilated Cardiomyopathy ’, *Circulation: Genomic and Precision Medicine*. Ovid Technologies (Wolters Kluwer Health). doi: 10.1161/circgen.119.002853.

Kattman, S. J. *et al.* (2011) ‘Stage-Specific Optimization of Activin/Nodal and BMP Signaling Promotes Cardiac Differentiation of Mouse and Human Pluripotent Stem Cell Lines’, *Cell Stem Cell*. Cell Press, 8(2), pp. 228–240. doi: 10.1016/J.STEM.2010.12.008.

Kayvanpour, E. *et al.* (2017) ‘Genotype-phenotype associations in dilated cardiomyopathy: meta-analysis on more than 8000 individuals’, *Clinical Research in Cardiology*. Springer Berlin Heidelberg, 106(2), pp. 127–139. doi: 10.1007/s00392-016-1033-6.

Kehat, I. *et al.* (2001) ‘Human embryonic stem cells can differentiate into myocytes with structural and functional properties of cardiomyocytes’, *The Journal of Clinical Investigation*. American Society for Clinical Investigation, 108(3), pp. 407–414. doi: 10.1172/JCI12131.

Kim, D., Langmead, B. and Salzberg, S. L. (2015) ‘HISAT: a fast spliced aligner with low memory requirements’, *Nature Methods 2015 12:4*. Nature Publishing Group, 12(4), pp. 357–360. doi: 10.1038/nmeth.3317.

Kim, Y. *et al.* (2016) ‘The Generation of Human Induced Pluripotent Stem Cells from Blood Cells: An Efficient Protocol Using Serial Plating of Reprogrammed Cells by Centrifugation’. doi: 10.1155/2016/1329459.

Kim, Y., Jeong, J. and Choi, D. (2020) ‘Small-molecule-mediated reprogramming: a silver lining for regenerative medicine’, *Experimental & Molecular Medicine 2020 52:2*. Nature Publishing Group, 52(2), pp. 213–226. doi: 10.1038/s12276-020-0383-3.

King, N. M. P. and Perrin, J. (2014) ‘Ethical issues in stem cell research and therapy’, *Stem Cell Research and Therapy*. BioMed Central Ltd., 5(4), pp. 1–6. doi: 10.1186/SCRT474/METRICS.

Kirby, T. J. and Lammerding, J. (2018) ‘Emerging views of the nucleus as a cellular mechanosensor’, *Nature Cell Biology*. doi: 10.1038/s41556-018-0038-y.

Koblan, L. W. *et al.* (2021) ‘In vivo base editing rescues Hutchinson–Gilford progeria syndrome in mice’, *Nature 2020 589:7843*. Nature Publishing Group, 589(7843), pp. 608–614. doi: 10.1038/s41586-020-03086-7.

Köhne, M. *et al.* (2022) ‘A potential future Fontan modification: preliminary in vitro data of a pressure-generating tube from engineered heart tissue’, *European Journal of Cardio-Thoracic Surgery*. Oxford Academic, 62(2), pp. 1–8. doi: 10.1093/EJCTS/EZAC111.

Kosicki, M., Tomberg, K. and Bradley, A. (2018) ‘Repair of double-strand breaks induced by CRISPR–Cas9 leads to large deletions and complex rearrangements’, *Nature Biotechnology*. doi: 10.1038/nbt.4192.

Kosmidis, G. *et al.* (2016) ‘Readthrough-promoting drugs gentamicin and PTC124 Fail to Rescue Na v 1.5 function of human-induced pluripotent stem cell-derived cardiomyocytes carrying nonsense mutations in the sodium channel gene SCN5A’, *Circulation: Arrhythmia and Electrophysiology*. Lippincott Williams and Wilkins, 9(11). doi: 10.1161/CIRCEP.116.004227.

Kubben, N. *et al.* (2011) ‘Post-natal myogenic and adipogenic developmental’, *Nucleus*. Taylor & Francis, 2(3), pp. 195–207. doi: 10.4161/nucl.2.3.15731.

Lammerding, J. *et al.* (2006) ‘Lamins a and C but not lamin B1 regulate nuclear mechanics’, *Journal of Biological Chemistry*. Elsevier, 281(35), pp. 25768–25780. doi: 10.1074/jbc.M513511200.

Landrum, M. *et al.* (2018) *ClinVar: improving access to variant interpretations and supporting evidence.*, *Nucleic Acids Res .* Available at: http://www.ncbi.nlm.nih.gov/clinvar/?term=LMNA (Accessed: 19 October 2022).

Lanzicher, T. *et al.* (2015) 'The Cardiomyopathy Lamin A/C D192G Mutation Disrupts Whole-Cell Biomechanics in Cardiomyocytes as Measured by Atomic Force Microscopy Loading-Unloading Curve Analysis', *Scientific Reports 2015 5:1*. Nature Publishing Group, 5(1), pp. 1–14. doi: 10.1038/srep13388.

Lee, J. *et al.* (2019) 'Activation of PDGF pathway links LMNA mutation to dilated cardiomyopathy', *Nature 2019 572:7769*. Nature Publishing Group, 572(7769), pp. 335–340. doi: 10.1038/s41586-019-1406-x.

Lee, J. H. *et al.* (2017) 'Human Pluripotent Stem Cell-Derived Atrial and Ventricular Cardiomyocytes Develop from Distinct Mesoderm Populations', *Cell Stem Cell*. Cell Press, 21(2), pp. 179-194.e4. doi: 10.1016/J.STEM.2017.07.003.

Lemoine, M. D. *et al.* (2017) 'Human iPSC-derived cardiomyocytes cultured in 3D engineered heart tissue show physiological upstroke velocity and sodium current density', *Scientific Reports*. Nature Publishing Group, 7(1), p. 5464. doi: 10.1038/s41598-017-05600-w.

Li, H. (2011) 'A statistical framework for SNP calling, mutation discovery, association mapping and population genetical parameter estimation from sequencing data', *Bioinformatics*. Oxford Academic, 27(21), pp. 2987–2993. doi: 10.1093/BIOINFORMATICS/BTR509.

Lin, F. and Worman, H. J. (1993) 'Structural organization of the human gene encoding nuclear lamin A and nuclear lamin C', *Journal of Biological Chemistry*. Elsevier, 268(22), pp. 16321–16326. doi: 10.1016/S0021-9258(19)85424-8.

Liu, G. *et al.* (2019) 'Modulating chromatin accessibility by transactivation and targeting proximal dsgRNAs enhances Cas9 editing efficiency in vivo', *Genome Biology*. BioMed Central Ltd., 20(1), pp. 1–11. doi: 10.1186/S13059-019-1762-8/FIGURES/7.

Long, X. *et al.* (2009) 'The Smooth Muscle Cell-restricted KCNMB1 Ion Channel Subunit Is a Direct Transcriptional Target of Serum Response Factor and Myocardin', *The Journal of Biological Chemistry*. American Society for Biochemistry and Molecular Biology, 284(48), p. 33671. doi: 10.1074/JBC.M109.050419.

Love, M. I., Huber, W. and Anders, S. (2014) 'Moderated estimation of fold change and dispersion for RNA-seq data with DESeq2', *Genome Biology 2014 15:12*. BioMed Central, 15(12), pp. 1–21. doi: 10.1186/S13059-014-0550-8.

Lu, J. T. *et al.* (2011) 'LMNA cardiomyopathy: cell biology and genetics meet clinical medicine', *Disease Models & Mechanisms*, 4(5), pp. 562–568. doi: 10.1242/dmm.006346.

Macquart, C. *et al.* (2018) 'Microtubule cytoskeleton regulates Connexin 43 localization and cardiac conduction in cardiomyopathy caused by mutation in A-type lamins gene', *Human Molecular Genetics*. doi: 10.1093/hmg/ddy227.

Maffioletti, S. M. *et al.* (2018) 'Three-Dimensional Human iPSC-Derived Artificial Skeletal Muscles Model Muscular Dystrophies and Enable Multilineage Tissue Engineering', *Cell Reports*, 23(3), pp. 899–908. doi: 10.1016/j.celrep.2018.03.091.

Maier, S. K. G. *et al.* (2004) 'Distinct subcellular localization of different sodium channel alpha and beta subunits in single ventricular myocytes from mouse heart', *Circulation*. Circulation, 109(11), pp. 1421–1427. doi: 10.1161/01.CIR.0000121421.61896.24.

Makarov, A. A. *et al.* (2019) 'Lamin A molecular compression and sliding as mechanisms behind nucleoskeleton elasticity', *Nature Communications 2019 10:1*. Nature Publishing Group, 10(1), pp. 1–17. doi: 10.1038/s41467-019-11063-6.

Makita, N., Bennett, P. B. and George, A. L. (1996) 'Molecular determinants of β1 subunit-induced gating modulation in voltage-dependent Na+ channels', *Journal of Neuroscience*. Society for Neuroscience, 16(22), pp. 7117–7127. doi: 10.1523/jneurosci.16-22-07117.1996.

Mannhardt, I. *et al.* (2016) 'Human Engineered Heart Tissue: Analysis of Contractile Force', *Stem cell reports*, 7, pp. 29–42. doi: 10.1016/j.stemcr.2016.04.011.

Mannhardt, I. *et al.* (2020) 'Comparison of 10 Control hPSC Lines for Drug Screening in an Engineered Heart Tissue Format', *Stem Cell Reports*. Cell Press, 15(4), pp. 983–998. doi: 10.1016/J.STEMCR.2020.09.002.

Maron, B. J. *et al.* (2006) 'Contemporary Definitions and Classification of the Cardiomyopathies', *Circulation*. Lippincott Williams & Wilkins, 113(14), pp. 1807–1816. doi: 10.1161/CIRCULATIONAHA.106.174287.

Martino, F. *et al.* (2018) 'Cellular Mechanotransduction: From Tension to Function', *Frontiers in Physiology*. Frontiers, 9, p. 824. doi: 10.3389/fphys.2018.00824.

Mathews, D. H., Turner, D. H. and Zuker, M. (2007) 'RNA Secondary Structure Prediction', *Current protocols in nucleic acid chemistry*. NIH Public Access, CHAPTER 11, p. Unit. doi: 10.1002/0471142700.NC1102S28.

Matsa, E. *et al.* (2014) 'Allele-specific RNA interference rescues the long-QT syndrome phenotype in human-induced pluripotency stem cell cardiomyocytes', *European Heart Journal*. Oxford Academic, 35(16), pp. 1078–1087. doi: 10.1093/EURHEARTJ/EHT067.

McDonagh, T. A. *et al.* (2021) '2021 ESC Guidelines for the diagnosis and treatment of acute and chronic heart failureDeveloped by the Task Force for the diagnosis and treatment of acute and chronic heart failure of the European Society of Cardiology (ESC) With the special contribution of the Heart Failure Association (HFA) of the ESC', *European Heart Journal*. Oxford Academic, 42(36), pp. 3599–3726. doi: 10.1093/EURHEARTJ/EHAB368.

Mearini, G. *et al.* (2014) 'Mybpc3 gene therapy for neonatal cardiomyopathy enables long-term disease prevention in mice', *Nature Communications*. Nature Publishing Group, 5(1), p. 5515. doi: 10.1038/ncomms6515.

Meera, P., Wallner, M. and Toro, L. (2000) 'A neuronal β subunit (KCNMB4) makes the large conductance, voltage- and Ca2+-activated K+ channel resistant to charybdotoxin and iberiotoxin', *Proceedings of the National Academy of Sciences of the United States of America*. National Academy of Sciences, 97(10), pp. 5562–5567. doi: 10.1073/PNAS.100118597/ASSET/BA07E016-5C37-4651-A064-D228BE3CF81D/ASSETS/GRAPHIC/PQ1001185005.JPEG.

Milani-Nejad, N. and Janssen, P. M. L. (2014) 'Small and large animal models in cardiac contraction research: Advantages and disadvantages', *Pharmacology & Therapeutics*. Pergamon, 141(3), pp. 235–249. doi: 10.1016/J.PHARMTHERA.2013.10.007.

Morales Rodriguez, B. *et al.* (2020) 'Activation of sarcolipin expression and altered calcium cycling in LMNA cardiomyopathy', *Biochemistry and Biophysics Reports*, 22(April), pp. 1–10. doi: 10.1016/j.bbrep.2020.100767.

Morikawa, Y. *et al.* (2015) 'Actin cytoskeletal remodeling with protrusion formation is essential for heart regeneration in Hippo-deficient mice', *Science Signaling*. American Association for the Advancement of Science, 8(375), pp. ra41–ra41. doi: 10.1126/scisignal.2005781.

Mosqueira, D. *et al.* (2018) 'CRISPR/Cas9 editing in human pluripotent stem cell-cardiomyocytes highlights arrhythmias, hypocontractility, and energy depletion as potential therapeutic targets for hypertrophic cardiomyopathy', *European Heart Journal*, 39(43), pp. 3879–3892. doi: 10.1093/eurheartj/ehy249.

Muchir, A. *et al.* (2003) 'Nuclear envelope alterations in fibroblasts from LGMD1B patients carrying nonsense Y259X heterozygous or homozygous mutation in lamin A/C gene', *Experimental Cell Research*, 291(2), pp. 352–362. doi: 10.1016/j.yexcr.2003.07.002.

Muchir, A. *et al.* (2007) ‘Activation of MAPK pathways links LMNA mutations to cardiomyopathy in Emery-Dreifuss muscular dystrophy’, 117(5). doi: 10.1172/JCI29042DS1.

Muchir, A. *et al.* (2009) ‘Inhibition of extracellular signal-regulated kinase signaling to prevent cardiomyopathy caused by mutation in the gene encoding A-type lamins’, *Human Molecular Genetics*, 18(2), pp. 241–247. doi: 10.1093/hmg/ddn343.

Muchir, A. *et al.* (2012) ‘Abnormal p38α mitogen-activated protein kinase signaling in dilated cardiomyopathy caused by lamin A/C gene mutation’, *Human Molecular Genetics*, 21(19), pp. 4325–4333. doi: 10.1093/hmg/dds265.

Muchir, A. *et al.* (2014) ‘Mitogen-activated protein kinase kinase 1/2 inhibition and angiotensin II converting inhibition in mice with cardiomyopathy caused by lamin A/C gene mutation’, *Biochemical and Biophysical Research Communications*. doi: 10.1016/j.bbrc.2014.09.020.

Mummery, C. *et al.* (2002) ‘Cardiomyocyte differentiation of mouse and human embryonic stem cells’, *Journal of Anatomy*. Wiley-Blackwell, 200(3), p. 233. doi: 10.1046/J.1469-7580.2002.00031.X.

Mummery, C. L. *et al.* (2012) ‘Differentiation of Human Embryonic Stem Cells and Induced Pluripotent Stem Cells to Cardiomyocytes’, *Circulation Research*. Lippincott Williams & WilkinsHagerstown, MD, 111(3), pp. 344–358. doi: 10.1161/CIRCRESAHA.110.227512.

Musunuru, K. *et al.* (2018) ‘Induced Pluripotent Stem Cells for Cardiovascular Disease Modeling and Precision Medicine: A Scientific Statement From the American Heart Association’, *Circulation. Genomic and precision medicine*. NIH Public Access, 11(1), p. e000043. doi: 10.1161/HCG.0000000000000043.

Nardone, G. *et al.* (2017) ‘YAP regulates cell mechanics by controlling focal adhesion assembly’, *Nature Communications*. Nature Publishing Group, 8(1), pp. 1–13. doi: 10.1038/ncomms15321.

Nichols, C. G. (2016) ‘ATP-sensitive Potassium Currents in Heart Disease and Cardioprotection’, *Cardiac electrophysiology clinics*. NIH Public Access, 8(2), p. 323. doi: 10.1016/J.CCEP.2016.01.005.

Nikolova, V. *et al.* (2004) ‘Defects in nuclear structure and function promote dilated cardiomyopathy in lamin A/C–deficient mice’, *Journal of Clinical Investigation*, 113(3), pp. 357–369. doi: 10.1172/JCI19448.

Okumura, T. *et al.* (2019) ‘Robust and highly efficient hiPSC generation from patient non-mobilized peripheral blood-derived CD34+ cells using the auto-erasable Sendai virus vector’, *Stem Cell Research and Therapy*. BioMed Central Ltd., 10(1), pp. 1–16. doi: 10.1186/S13287-019-1273-2/FIGURES/5.

Ono, K. and Iijima, T. (2010) 'Cardiac T-type Ca(2+) channels in the heart', *Journal of molecular and cellular cardiology*. J Mol Cell Cardiol, 48(1), pp. 65–70. doi: 10.1016/J.YJMCC.2009.08.021.

Owens, D. J. *et al.* (2020) 'Lamin Mutations Cause Increased YAP Nuclear Entry in Muscle Stem Cells', *Cells*, 9(4), p. 816. doi: 10.3390/cells9040816.

Palermo, J. *et al.* (1996) 'Transgenic remodeling of the contractile apparatus in the mammalian heart', *Circulation Research*, 78(3), pp. 504–509. doi: 10.1161/01.RES.78.3.504.

Panciera, T. *et al.* (2017) 'Mechanobiology of YAP and TAZ in physiology and disease', *Nature Reviews Molecular Cell Biology*. Nature Publishing Group, pp. 758–770. doi: 10.1038/nrm.2017.87.

Park, Y. E. *et al.* (2009) 'Nuclear changes in skeletal muscle extend to satellite cells in autosomal dominant Emery-Dreifuss muscular dystrophy/limb-girdle muscular dystrophy 1B', *Neuromuscular Disorders*. Elsevier, 19(1), pp. 29–36. doi: 10.1016/j.nmd.2008.09.018.

Paull, D. *et al.* (2015) 'Automated, high-throughput derivation, characterization and differentiation of induced pluripotent stem cells', *Nature Methods*. Nature Publishing Group, 12(9), pp. 885–892. doi: 10.1038/nmeth.3507.

Peric-Hupkes, D. *et al.* (2010) 'Molecular Maps of the Reorganization of Genome-Nuclear Lamina Interactions during Differentiation', *Molecular Cell*, 38, pp. 603–613. doi: 10.1016/j.molcel.2010.03.016.

Perovanovic, J. *et al.* (2016) 'Laminopathies disrupt epigenomic developmental programs and cell fate', *Science Translational Medicine*, 8(335). Available at: http://stm.sciencemag.org/content/scitransmed/8/335/335ra58.full.pdf (Accessed: 8 January 2018).

Peter, M. *et al.* (1991) 'Disassembly of in vitro formed lamin head-to-tail polymers by CDC2 kinase', *The EMBO Journal*, 10(1), pp. 535–1. Available at: https://www.ncbi.nlm.nih.gov/pmc/articles/PMC452817/pdf/emboj00104-0227.pdf (Accessed: 8 March 2018).

Pfizer to Discontinue Development Program for PF-07265803 for LMNA-Related Dilated Cardiomyopathy (2022). Available at: https://www.pfizer.com/news/announcements/pfizer-discontinue-development-program-pf-07265803-lmna-related-dilated.

Priori, S. G. *et al.* (2012) 'Risk Stratification in Brugada Syndrome: Results of the PRELUDE

(PRogrammed ELectrical stimUlation preDictive valuE) Registry', *Journal of the American College of Cardiology*. Elsevier, 59(1), pp. 37–45. doi: 10.1016/J.JACC.2011.08.064.

Prondzynski, M. *et al.* (2017) 'Evaluation of MYBPC3 trans-Splicing and Gene Replacement as Therapeutic Options in Human iPSC-Derived Cardiomyocytes', *Molecular Therapy - Nucleic Acids*. Cell Press, 7, pp. 475–486. doi: 10.1016/J.OMTN.2017.05.008.

Prondzynski, M. *et al.* (2019) 'Disease modeling of a mutation in α-actinin 2 guides clinical therapy in hypertrophic cardiomyopathy', *EMBO Molecular Medicine*. John Wiley & Sons, Ltd, 11(12), p. e11115. doi: 10.15252/EMMM.201911115.

Prondzynski, M., Mearini, G. and Carrier, L. (2019) 'Gene therapy strategies in the treatment of hypertrophic cardiomyopathy', *Pflugers Archiv European Journal of Physiology*. Pflügers Archiv - European Journal of Physiology, 471(5), pp. 807–815. doi: 10.1007/s00424-018-2173-5.

Querdel, E. *et al.* (2021) 'Human Engineered Heart Tissue Patches Remuscularize the Injured Heart in a Dose-Dependent Manner', *Circulation*. Wolters Kluwer Health, 143(20), p. 1991. doi: 10.1161/CIRCULATIONAHA.120.047904.

Ran, F. A. *et al.* (2013) 'Genome engineering using the CRISPR-Cas9 system', *Nature Protocols 2013 8:11*. Nature Publishing Group, 8(11), pp. 2281–2308. doi: 10.1038/nprot.2013.143.

Rao, L., Perez, D. and White, E. (1996) 'Lamin proteolysis facilitates nuclear events during apoptosis.', *Journal of Cell Biology*. The Rockefeller University Press, 135(6), pp. 1441–1455. doi: 10.1083/JCB.135.6.1441.

Redwood, A. B. *et al.* (2011) 'A dual role for A-type lamins in DNA double-strand break repair', *Cell Cycle*. Taylor & Francis, 10(15), p. 2549. doi: 10.4161/CC.10.15.16531.

Rodriguez, M. L. *et al.* (2019) 'Magnetics-Based Approach for Fine-Tuning Afterload in Engineered Heart Tissues', *ACS Biomaterials Science and Engineering*. American Chemical Society, 5(7), pp. 3663–3675. doi: 10.1021/ACSBIOMATERIALS.8B01568/ASSET/IMAGES/LARGE/AB-2018-01568R_0007.JPEG.

Rysä, J., Tokola, H. and Ruskoaho, H. (2018) 'Mechanical stretch induced transcriptomic profiles in cardiac myocytes', *Scientific Reports*. Nature Publishing Group, 8(1), pp. 1–14. doi: 10.1038/s41598-018-23042-w.

Sa, S. and McCloskey, K. E. (2012) 'Activin A and BMP4 Signaling for Efficient Cardiac Differentiation of H7 and H9 Human Embryonic Stem Cells', *Journal of Stem Cells &*

Regenerative Medicine. German Society for Stem Cell Research, 8(3), p. 198. doi: 10.46582/JSRM.0803013.

Saleem, U. *et al.* (2020) ‘Force and Calcium Transients Analysis in Human Engineered Heart Tissues Reveals Positive Force-Frequency Relation at Physiological Frequency’, *Stem Cell Reports*. ElsevierCompany., 14(2), pp. 312–324. doi: 10.1016/j.stemcr.2019.12.011.

Salvarani, N. *et al.* (2019) ‘The K219T-Lamin mutation induces conduction defects through epigenetic inhibition of SCN5A in human cardiac laminopathy’, *Nature Communications*. Nature Publishing Group, 10(1), p. 2267. doi: 10.1038/s41467-019-09929-w.

Sánchez-López, A. *et al.* (2021) ‘Cardiovascular Progerin Suppression and lamin A Restoration Rescues Hutchinson-Gilford Progeria Syndrome.’, *Circulation*. Lippincott Williams & Wilkins Hagerstown, MD . doi: 10.1161/CIRCULATIONAHA.121.055313.

Santiago-Fernández, O. *et al.* (2019) ‘Development of a CRISPR/Cas9-based therapy for Hutchinson–Gilford progeria syndrome’, *Nature Medicine 2019 25:3*. Nature Publishing Group, 25(3), pp. 423–426. doi: 10.1038/s41591-018-0338-6.

Schaaf, S. *et al.* (2011) ‘Human Engineered Heart Tissue as a Versatile Tool in Basic Research and Preclinical Toxicology’, *PLOS ONE*. Public Library of Science, 6(10), p. e26397. doi: 10.1371/JOURNAL.PONE.0026397.

Scharner, J. *et al.* (2015) ‘Ameliorating pathogenesis by removing an exon containing a missense mutation: a potential exon-skipping therapy for laminopathies’, *Gene Therapy 2015 22:6*. Nature Publishing Group, 22(6), pp. 503–515. doi: 10.1038/gt.2015.8.

Schlaeger, T. M. *et al.* (2014) ‘A comparison of non-integrating reprogramming methods’, *Nature Biotechnology 2014 33:1*. Nature Publishing Group, 33(1), pp. 58–63. doi: 10.1038/nbt.3070.

Schreiber, K. H. and Kennedy, B. K. (2013) ‘When Lamins Go Bad: Nuclear Structure and Disease’, *Cell*. Cell Press, 152(6), pp. 1365–1375. doi: 10.1016/J.CELL.2013.02.015.

Schubert, M. S. *et al.* (2021) ‘Optimized design parameters for CRISPR Cas9 and Cas12a homology-directed repair’, *Scientific Reports 2021 11:1*. Nature Publishing Group, 11(1), pp. 1–15. doi: 10.1038/s41598-021-98965-y.

Schultheiss, H.-P. *et al.* (2019) ‘Dilated cardiomyopathy’, *Nature Reviews Disease Primers 2019 5:1*. Nature Publishing Group, 5(1), pp. 1–19. doi: 10.1038/s41572-019-0084-1.

Shah, P. P. *et al.* (2021) ‘Pathogenic LMNA variants disrupt cardiac lamina-chromatin interactions and de-repress alternative fate genes’, *Cell Stem Cell*. Elsevier Inc., 28(5), pp. 938-954.e9. doi: 10.1016/j.stem.2020.12.016.

Shemer, Y. *et al.* (2021) ‘Investigating LMNA-related dilated cardiomyopathy using human induced pluripotent stem cell-derived cardiomyocytes’, *International Journal of Molecular Sciences*. MDPI, 22(15). doi: 10.3390/IJMS22157874/S1.

Shibamiya, A. *et al.* (2020) ‘Cell Banking of hiPSCs: A Practical Guide to Cryopreservation and Quality Control in Basic Research’, *Current Protocols in Stem Cell Biology*. Blackwell Publishing Inc., 55(1), p. 127. doi: 10.1002/cpsc.127.

Shinnawi, R. *et al.* (2019) ‘Modeling Reentry in the Short QT Syndrome With Human-Induced Pluripotent Stem Cell–Derived Cardiac Cell Sheets’, *Journal of the American College of Cardiology*. Elsevier, 73(18), pp. 2310–2324. doi: 10.1016/J.JACC.2019.02.055.

Soheilypour, M. *et al.* (2016) ‘On the Nuclear Pore Complex and Its Roles in Nucleo-Cytoskeletal Coupling and Mechanobiology’, *Cellular and Molecular Bioengineering*. Springer New York LLC, 9(2), pp. 217–226. doi: 10.1007/S12195-016-0443-X.

Stoehr, A. *et al.* (2014) ‘Automated analysis of contractile force and Ca2+ transients in engineered heart tissue.’, *American journal of physiology. Heart and circulatory physiology*. American Physiological Society, 306(9), pp. H1353-63. doi: 10.1152/ajpheart.00705.2013.

Stuurman, N., Heins, S. and Aebi, U. (1998) ‘Nuclear lamins: Their structure, assembly, and interactions’, *Journal of Structural Biology*, 122(1–2), pp. 42–66. doi: 10.1006/jsbi.1998.3987.

Subramanian, A. *et al.* (2005) ‘Gene set enrichment analysis: A knowledge-based approach for interpreting genome-wide expression profiles’, *Proceedings of the National Academy of Sciences*. National Academy of Sciences, 102(43), pp. 15545–15550. doi: 10.1073/PNAS.0506580102.

Sullivan, T. *et al.* (1999) ‘Loss of A-type Lamin Expression Compromises Nuclear Envelope Integrity Leading to Muscular Dystrophy’, *The Journal of Cell Biology*, 147(5), pp. 913–919. Available at: http://www.jcb.org (Accessed: 16 September 2022).

Swift, J. *et al.* (2013) ‘Nuclear Lamin-A Scales with Tissue Stiffness and Enhances Matrix-Directed Differentiation’, *Science*, 341. Available at: http://science.sciencemag.org/content/sci/341/6149/1240104.full.pdf (Accessed: 24 January 2018).

Swift, J. and Discher, D. E. (2014) ‘The nuclear lamina is mechano-responsive to ECM elasticity in mature tissue’, *Journal of Cell Science*, 127, pp. 3005–3015. doi: 10.1242/jcs.149203.

Szklarczyk, D. *et al.* (2021) ‘The STRING database in 2021: customizable protein–protein networks, and functional characterization of user-uploaded gene/measurement sets’, *Nucleic*

Acids Research. Oxford Academic, 49(D1), pp. D605–D612. doi: 10.1093/NAR/GKAA1074.

Taapken, S. M. *et al.* (2011) ‘Karotypic abnormalities in human induced pluripotent stem cells and embryonic stem cells’, *Nature biotechnology*. Nat Biotechnol, 29(4), pp. 313–314. doi: 10.1038/NBT.1835.

Takahashi, K. *et al.* (2007) ‘Induction of Pluripotent Stem Cells from Adult Human Fibroblasts by Defined Factors’, *Cell*. Elsevier, 131(5), pp. 861–872. doi: 10.1016/j.cell.2007.11.019.

Takahashi, K. and Yamanaka, S. (2006) ‘Induction of Pluripotent Stem Cells from Mouse Embryonic and Adult Fibroblast Cultures by Defined Factors’, *Cell*. Elsevier, 126(4), pp. 663–676. doi: 10.1016/j.cell.2006.07.024.

Taylor, M. R. . *et al.* (2003) ‘Natural history of dilated cardiomyopathy due to lamin A/C gene mutations’, *Journal of the American College of Cardiology*. Elsevier, 41(5), pp. 771–780. doi: 10.1016/S0735-1097(02)02954-6.

Thomson, J. A. *et al.* (1998) ‘Embryonic Stem Cell Lines Derived from Human Blastocysts’, *Science*. American Association for the Advancement of Science, 282(5391), pp. 1145–1147. doi: 10.1126/SCIENCE.282.5391.1145.

Tuladhar, R. *et al.* (2019) ‘CRISPR-Cas9-based mutagenesis frequently provokes on-target mRNA misregulation’, *Nature Communications*. Springer US, 10(1), pp. 1–10. doi: 10.1038/s41467-019-12028-5.

Ulmer, B. M. *et al.* (2018) ‘Contractile Work Contributes to Maturation of Energy Metabolism in hiPSC-Derived Cardiomyocytes.’, *Stem cell reports*. Elsevier, 10(3), pp. 834–847. doi: 10.1016/j.stemcr.2018.01.039.

Ulmer, B. M. and Eschenhagen, T. (2020) ‘Human pluripotent stem cell-derived cardiomyocytes for studying energy metabolism’, *Biochimica et biophysica acta. Molecular cell research*. Biochim Biophys Acta Mol Cell Res, 1867(3). doi: 10.1016/J.BBAMCR.2019.04.001.

Uusi-Mäkelä, M. I. E. *et al.* (2018) ‘Chromatin accessibility is associated with CRISPR-Cas9 efficiency in the zebrafish (Danio rerio)’, *PLOS ONE*. Public Library of Science, 13(4), p. e0196238. doi: 10.1371/JOURNAL.PONE.0196238.

Uzun, A. U. *et al.* (2016) ‘Ca2+-currents in human induced pluripotent stem cell-derived cardiomyocytes effects of two different culture conditions’, *Frontiers in Pharmacology*. Frontiers Media S.A., 7(SEP), p. 300. doi: 10.3389/FPHAR.2016.00300/BIBTEX.

Vignier, N. *et al.* (2009) ‘Nonsense-Mediated mRNA Decay and Ubiquitin–Proteasome System Regulate Cardiac Myosin-Binding Protein C Mutant Levels in Cardiomyopathic Mice’, *Circulation Research*. Lippincott Williams & Wilkins, 105(3), pp. 239–248. doi: 10.1161/CIRCRESAHA.109.201251.

Wang, K. *et al.* (2016) 'Efficient Generation of Orthologous Point Mutations in Pigs via CRISPR-assisted ssODN-mediated Homology-directed Repair', *Molecular Therapy. Nucleic Acids*. American Society of Gene & Cell Therapy, 5(11), p. e396. doi: 10.1038/MTNA.2016.101.

Wang, Y. *et al.* (2022) 'Lamin A/C-dependent chromatin architecture safeguards naïve pluripotency to prevent aberrant cardiovascular cell fate and function', *Nature Communications 2022 13:1*. Nature Publishing Group, 13(1), pp. 1–24. doi: 10.1038/s41467-022-34366-7.

Warnecke, N. *et al.* (2021) 'Generation of bi-allelic MYBPC3 truncating mutant and isogenic control from an iPSC line of a patient with hypertrophic cardiomyopathy', *Stem Cell Research*. Elsevier, 55, p. 102489. doi: 10.1016/J.SCR.2021.102489.

Wenzel, K. *et al.* (2021) 'A Transgenic Mouse Model of Eccentric Left Ventricular Hypertrophy With Preserved Ejection Fraction Exhibits Alterations in the Autophagy-Lysosomal Pathway', *Frontiers in Physiology*. Frontiers, 0, p. 524. doi: 10.3389/FPHYS.2021.614878.

Wilson, K. L. *et al.* (2005) 'Nuclear Membrane Protein Emerin: Roles in Gene Regulation, Actin Dynamics and Human Disease', *Novartis Foundation Symposium*. John Wiley & Sons, Ltd, 264, pp. 51–62. doi: 10.1002/0470093765.CH5.

Wolf, C. M. *et al.* (2007) 'Lamin A/C haploinsufficiency causes dilated cardiomyopathy and apoptosis-triggered cardiac conduction system disease'. doi: 10.1016/j.yjmcc.2007.11.008.

Wu, W. *et al.* (2010) 'Pharmacological inhibition of c-Jun N-terminal kinase signaling prevents cardiomyopathy caused by mutation in LMNA gene', *Biochimica et Biophysica Acta (BBA) - Molecular Basis of Disease*. Elsevier, 1802(7–8), pp. 632–638. doi: 10.1016/J.BBADIS.2010.04.001.

Wu, W. *et al.* (2011) 'Mitogen-Activated Protein Kinase Inhibitors Improve Heart Function and Prevent Fibrosis in Cardiomyopathy Caused by Mutation in Lamin A/C Gene', *Circulation*. Lippincott Williams & WilkinsHagerstown, MD, 123(1), pp. 53–61. doi: 10.1161/CIRCULATIONAHA.110.970673.

Xie, W. *et al.* (2016) 'A-type Lamins Form Distinct Filamentous Networks with Differential Nuclear Pore Complex Associations', *Current Biology*. Cell Press, 26(19), pp. 2651–2658. doi: 10.1016/j.cub.2016.07.049.

Zech, A. T. L. *et al.* (2022) ‘ACTN2 Mutant Causes Proteopathy in Human iPSC-Derived Cardiomyocytes’, *Cells 2022, Vol. 11, Page 2745*. Multidisciplinary Digital Publishing Institute, 11(17), p. 2745. doi: 10.3390/CELLS11172745.

Zhou, T. *et al.* (2011) ‘Generation of Induced Pluripotent Stem Cells from Urine’, *Journal of the American Society of Nephrology : JASN*. American Society of Nephrology, 22(7), p. 1221. doi: 10.1681/ASN.2011010106.

Zimmermann, W. H. *et al.* (2000) ‘Three-Dimensional Engineered Heart Tissue from Neonatal Rat Cardiac’, *Biotechnology and Bioengineering*, 68(1), pp. 106–114.

9 Supplementary

9.1 Supplementary figures and tables

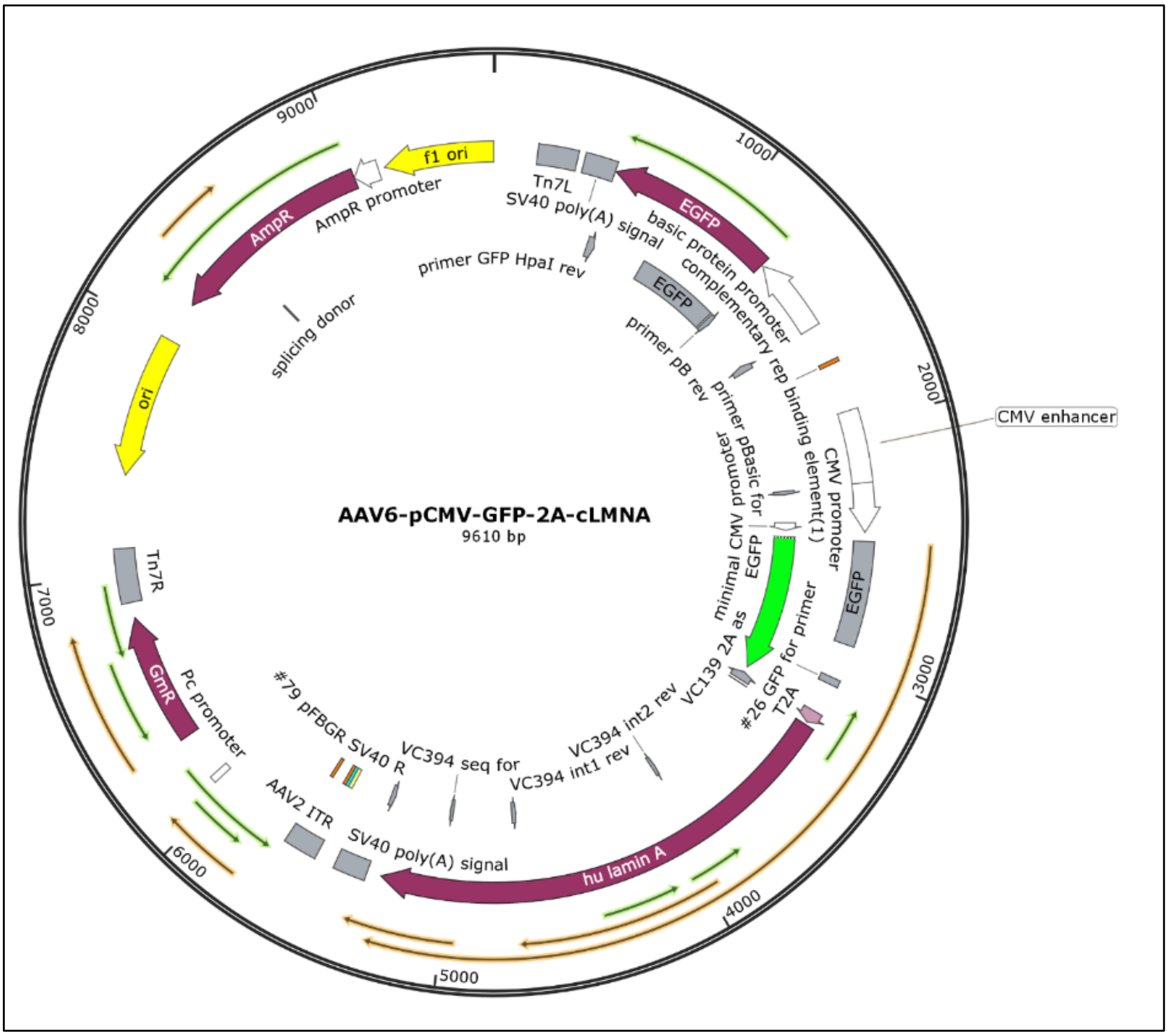

Figure S 1 Vector map of the *AAV6-pCMV-GFP-2A-cLMNA* plasmid used for AAV6 particle production and subsequent gene replacement therapy. The plasmid carried a Cytomegalovirus (CMV) promoter driving enhanced green fluorescent protein (GFP) expression and human lamin A cDNA divided by a 2A peptide signal.

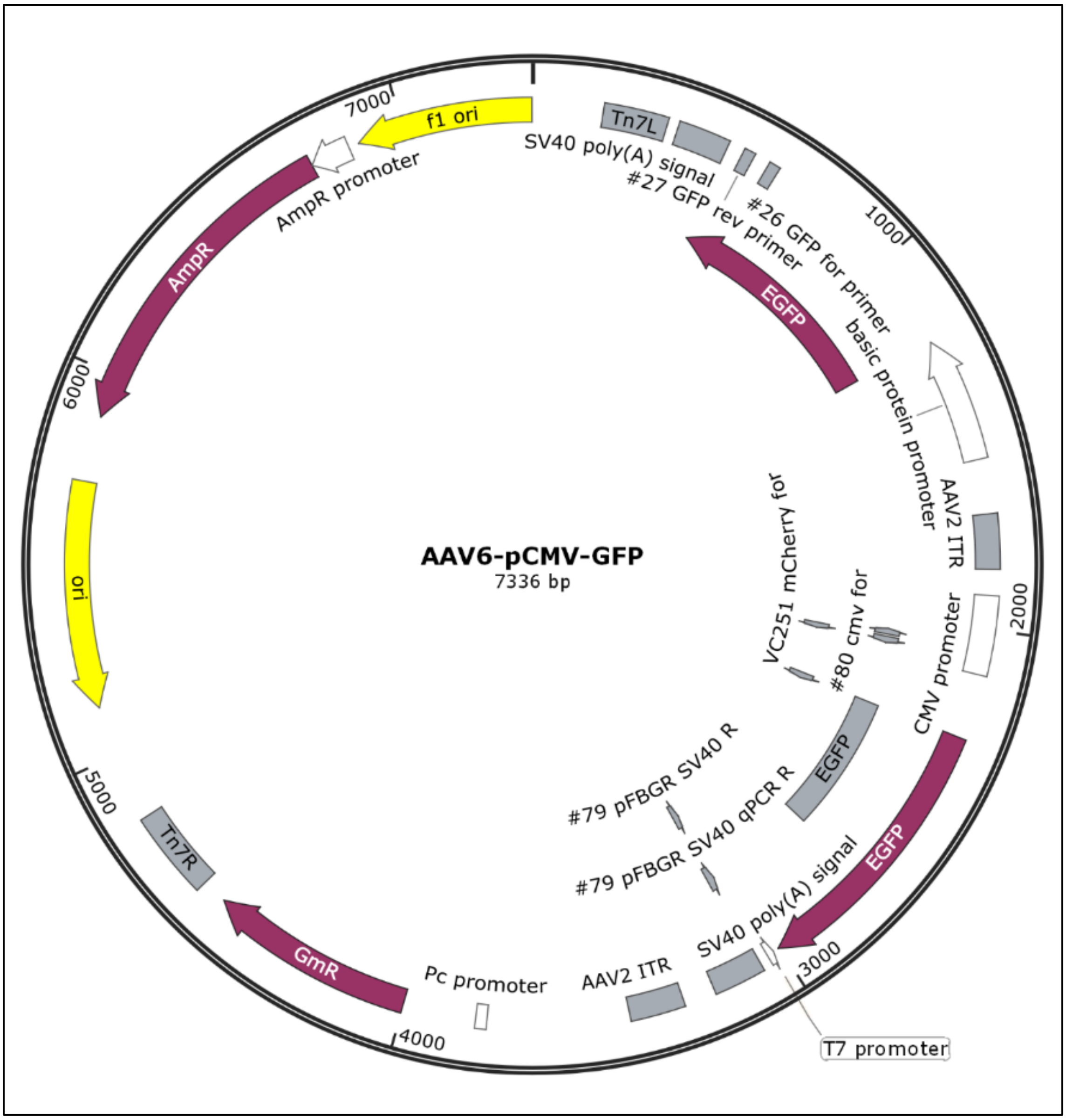

Figure S 2 Vector map of the *AAV6-pCMV-GFP* plasmid used for AAV6 particle production and used as a green fluorescent protein (GFP)-only control driven by the Cytomegalovirus (CMV) promoter.

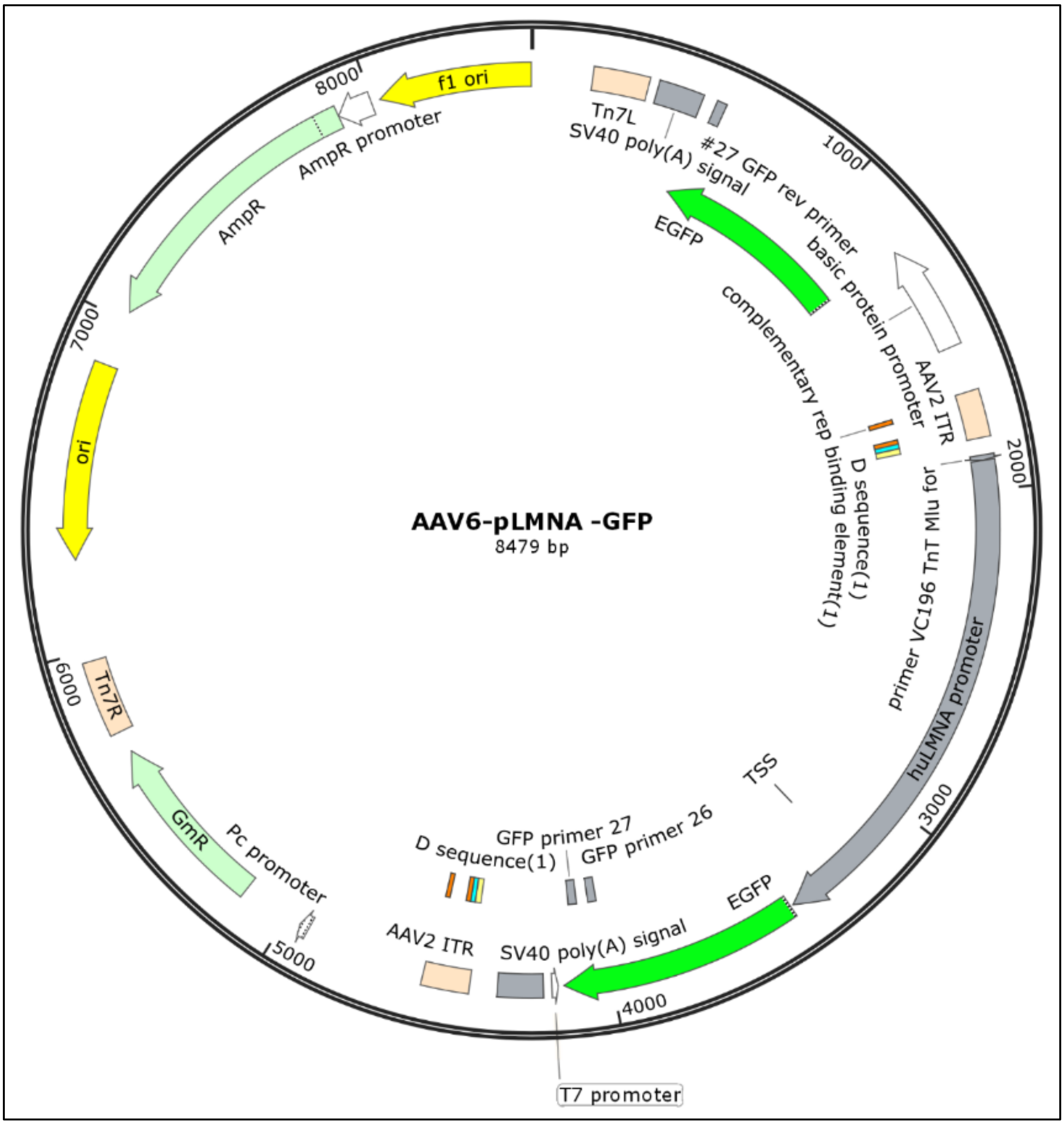

Figure S 3 Vector map of the *AAV6-pLMNA-GFP* plasmid used for AAV6 particle production that carried exerts of endogenous *LMNA* promotor and the green fluorescent protein (GFP) sequence.

Table S 1 Predicted OT sequences of gRNA 3 by *in silico* tool CRISPOR

offtargetSeq (5‘-3‘)	**mismatchPos**	**mismatchCount**	**mitOfftargetScore**	**cfdOfftargetScore**	**chrom**	**start**	**end**	**strand**	**locusDesc**
TCGGGTCCTATGACAGCTCTGGG	.......**.....*..*..	4	0.04591849	0.54901961	chr9	32668781	32668803	+	intergenic:RP11-555J4.4-AL157884.1
TACTGATGGAAATTGACATTGGG	*....*....*.......*.	4	0.17690259	0.53846154	chr11	73870615	73870637	+	intergenic:MRPL48-COA4
CCACCAGCAGGGTCTCATGTAGG	.......**..........*	3	0.75758263	0.51428571	chr7	131897237	131897259	-	intergenic:AC008085.1-AC009518.4
AGTGTCAGTCACCACCAGTCTGG	.*.....*..*.........	3	1.48312236	0.462	chr19	57265212	57265234	+	intergenic:CTC-444N24.8-CTC-444N24.6
GGACTGGAGGAGAATGACAAGGG	*......*.....*......	3	0.44303599	0.45217391	chr5	78638671	78638693	+	intron:LHFPL2
ATTGTCAATTTACACCATTCAGG	.........*.*.....*..	3	0.23733665	0.44817927	chr2	172486981	172487003	-	intron:ITGA6
ATTGGTAGTCTCCACAAGTCTGG	....**.*.......*....	4	0.14888102	0.43580952	chr4	122829526	122829548	-	intergenic:FGF2/AC021205.1-FGF2
GATGGCTAATCTCCACCAGTTGG	*..*.**.............	4	0.56401473	0.42150445	chr2	88280915	88280937	-	intergenic:THNSL2-AC012671.1
TTTGTCAATTTGCACAAGTCAGG	*........*.*...*....	4	0.12340295	0.41830065	chr4	104624836	104624858	+	intergenic:AC004063.1-AC004053.1
GATTGTCAATCCCCAAAAGTGGG	*..........*...**...	4	0.05158538	0.40366133	chr1	235100139	235100161	-	intergenic:LINC01348-RP4-597N16.4

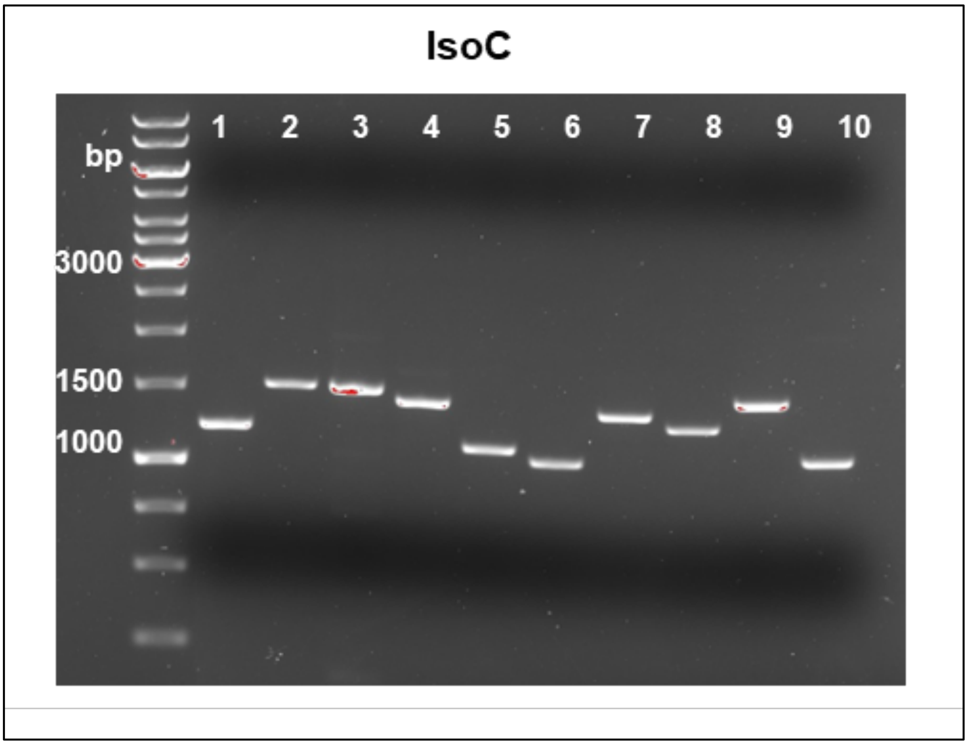

Figure S 4 Agarose gel electrophoresis of PCR product on 10 most likely OT sequences of gRNA from IsoC derived gDNA.

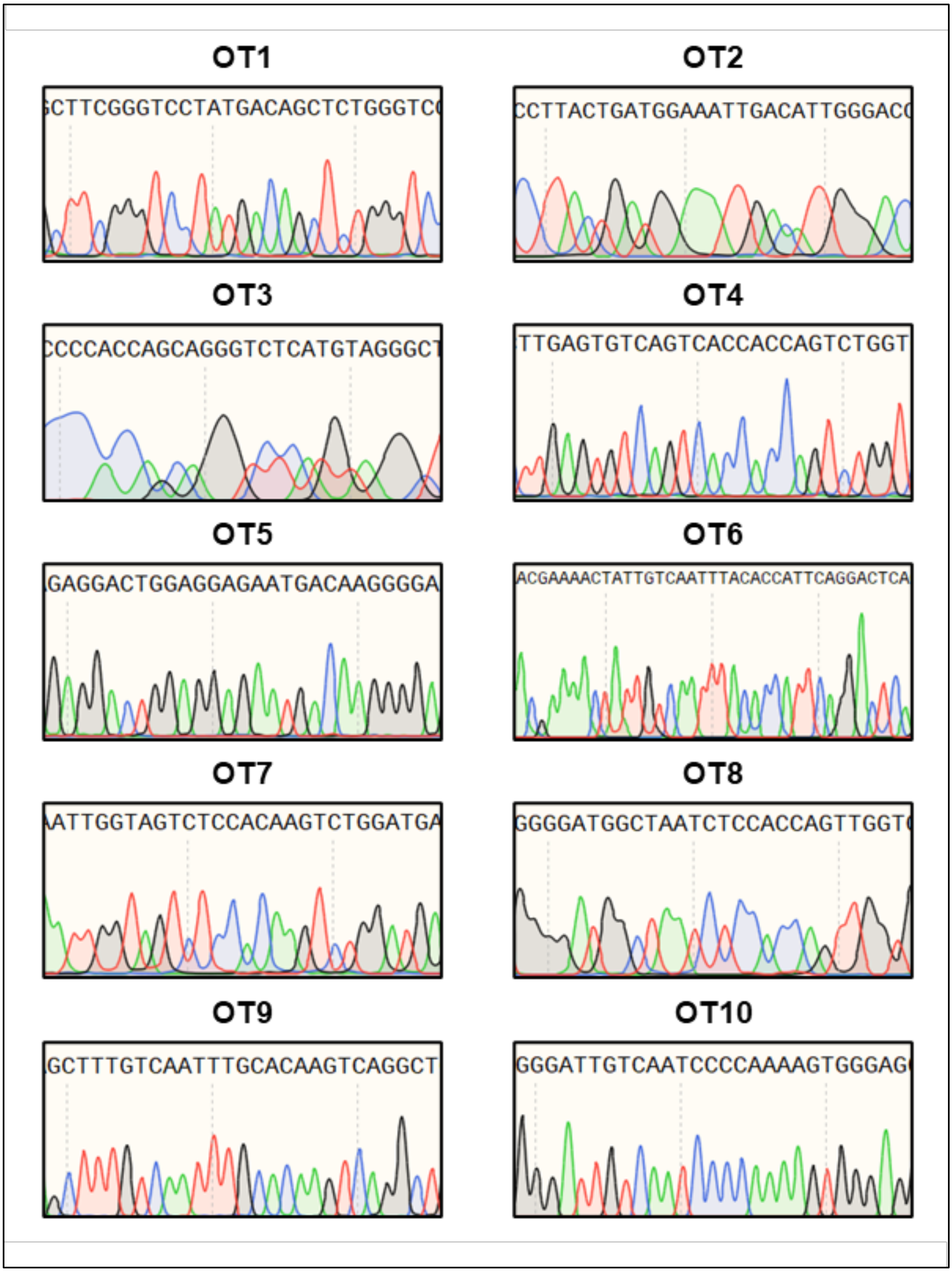

Figure S 5 Sanger sequencing traces of PCR products from IsoC gDNA for 10 most likely OT sequences of gRNA 3.

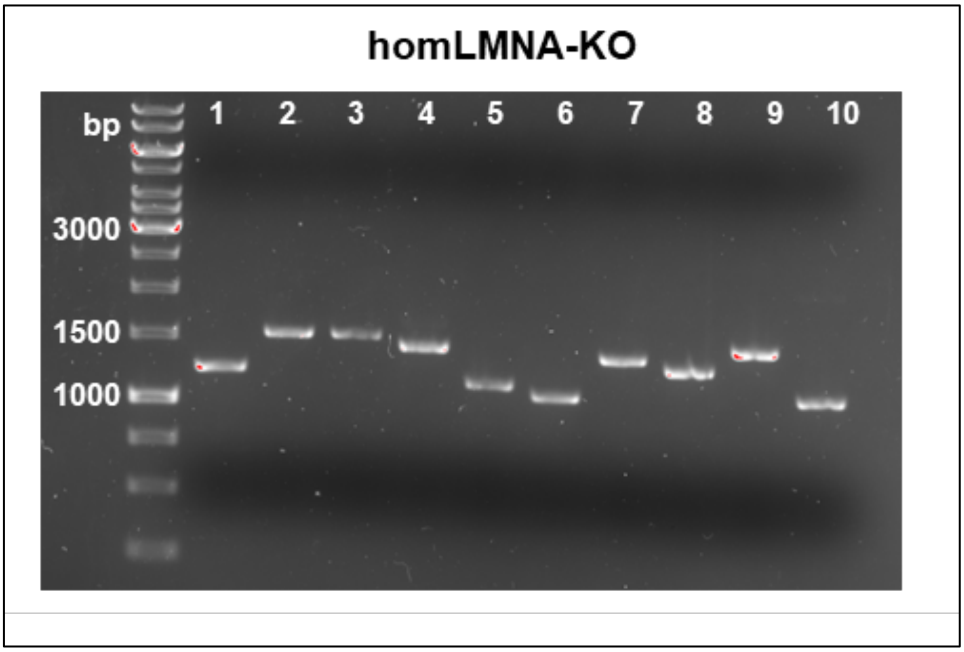

Figure S 6 Agarose gel electrophoresis of PCR product on 10 most likely OT sequences of gRNA from LMNA-KO derived gDNA.

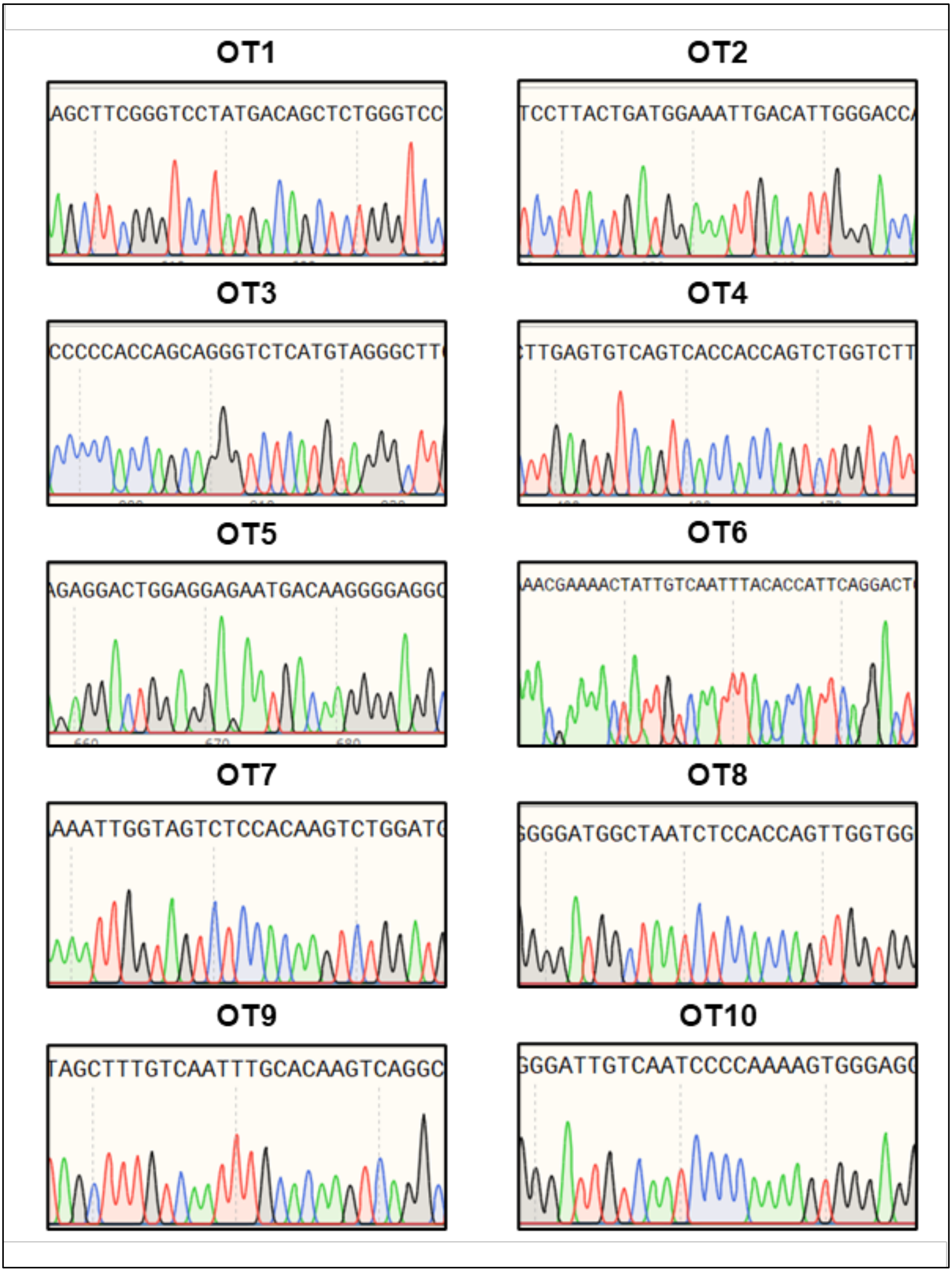

Figure S 7 Sanger sequencing traces of PCR products from LMNA-KO gDNA for 10 most likely OT sequences of gRNA 3.

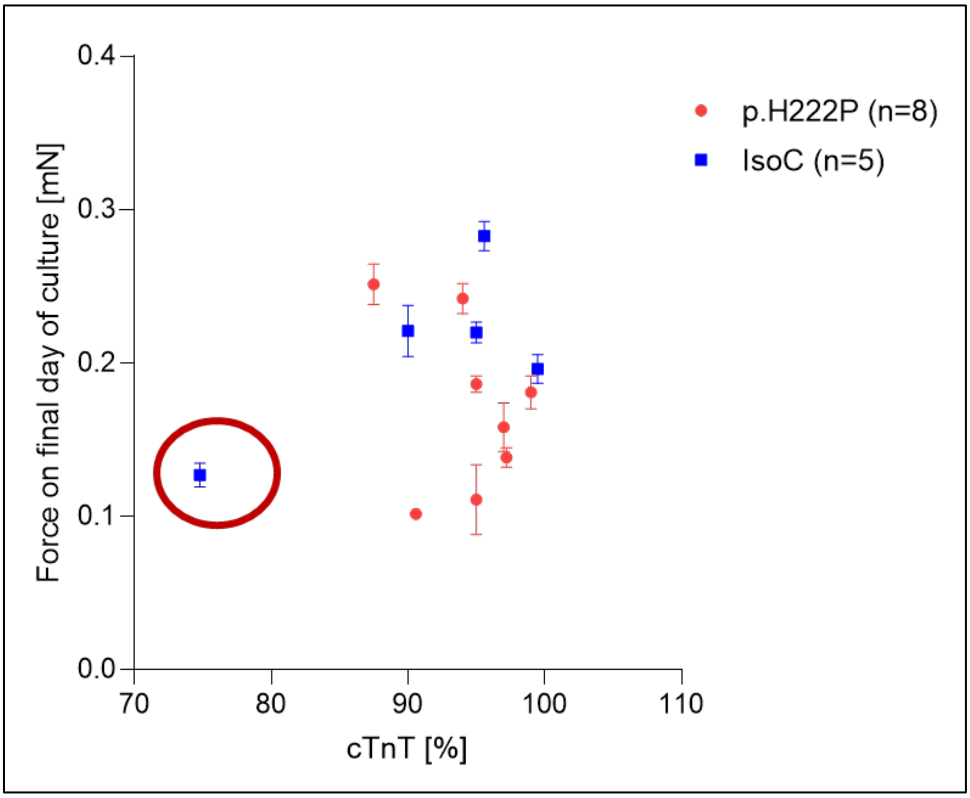

Figure S 8 Mean force of contraction (mN; y-axis) and the corresponding cardiac Troponin T positivity in hiPSC-CMs (%; x-axis) of casted p.H222P and IsoC batches. Red circle indicates a potential outlier batch of IsoC. N= number of batches.

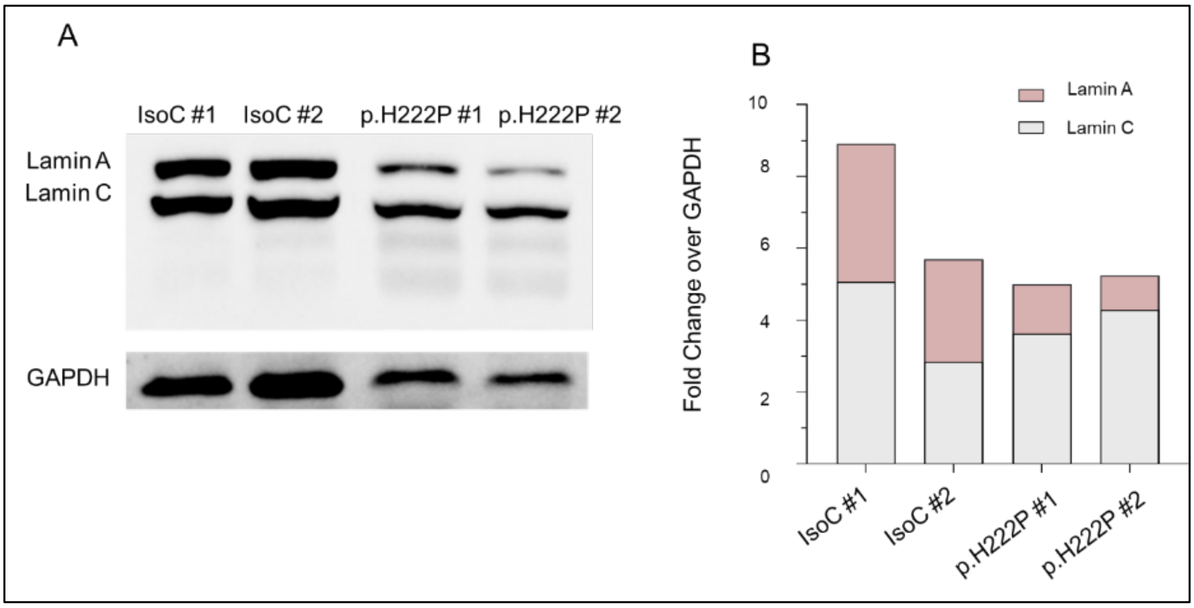

Figure S 9 **A** Western blot experiment of IsoC and p.H222P EHT protein lysates with a potential degradation of lamin in p.H222P sample. Stained for lamin A/C and GAPDH as a loading control. **B** Quantification of lamin A (red) and C (grey) signal normalised to the loading control GAPDH.

Table S 2 Primers for genomic loci in the gene *LMNA*

Experiment/ target	**Primer name**	**Primer sequence (5’-3’)**
Exon 4 to 10 / Allelic discrimination	Exon-4-in-Fwd	GTC CCT GGG TCT TGG CCT CC
	SNP-Rev	GTTCCCTGTTCAAGGTATAGG
Exon 4 / CRISPR experiment	Exon-3-in-Fwd	ttcttgtgttctgtgacccctt
	Exon-5-in-Rev	TGCATCCGGCCCAGACTCTA
Exon 3 to 5 / Large fragment PCR	Intronic-Fwd-1	gctggtcttgaactcctggctg
	Exon-5-in-Rev	TGCATCCGGCCCAGACTCTA
Lamin A transcript	LMN_Fwd	CCTGATAGCTGCTCAGGCTC
	LMNA_Rev	GAGTGACCGTGACACTGGAG
Lamin C transcript	LMN_Fwd	CCTGATAGCTGCTCAGGCTC
	LMNC_Rev	AGATTTTTGGCACGGGGAGG

Table S 3 PCR Primers for OT region of gRNA 3

Off-Target	**Forward Primer (5'-3')**	**Reverse Primer (5'-3')**	**Length (bp)**
OT1	GTGCTGAAAAACCACTGGGG	TCTGGGGGCAAAACATTGGT	1207
OT2	TACTGGGCAACAGATGCTTGT	AAAGTACCTGGAAGCCACCAA	1496
OT3	AGCAGAGGAGGGGAAGGTTT	CAGATAGGTGCCTTCCCCAA	1481
OT4	CAGACATCCAAGGGACCACTG	AACTGAAGCCAAGGGCACAG	1406
OT5	TTGTCTTGGGGCCAGATCAC	TCTGACCAGCCATGTTAGGC	1117
OT6	TTGGAGCCAAATTATCTTGATTGCT	TGTGTGGAATAGCCAGTCACC	1051
OT7	AAAGCATCCCTCCCCAAACT	ATCTCAGCTGACAAGGGCAAG	1362
OT8	GTCAGTGGGGCTTAAGCTGT	AGTACAGACTGGAGCCAGGA	1273
OT9	TGCTGAAGGTCAAACGACCA	AGCACAATCAGGTTGCCTCT	1460
OT10	GGATCAGCTGTTGACCCCAA	AGTAATGCTGAGACCGAGCC	1082

9.2 List of abbreviations

A	
AA	Amino acids
AAV	Adeno-associated virus
ACM	Arrhythmogenic right ventricular cardiomyopathy
ACTA1	Actin Alpha 1, Skeletal Muscle
ACTN1	Alpha-actinin 1
ACTN4	Alpha-actinin 4
ADAMTS8	ADAM Metallopeptidase With Thrombospondin Type 1 Motif 8
AE	Afterload enhancement
ANOVA	Analysis of variance
AP	Action potential
APA	Action potential amplitude
APD	Action potential duration
AV	Atrioventricular
B	
BAF	Barrier of autointegration factor
BCAR1	Breast cancer anti-estrogen resistance protein 1
bFGF	Basic fibroblast growth factor
BKCa	Large-conductance voltage- and Ca2+-activated potassium channel
bMHC	Beta myosin heavy chain
BMP4	Bone morphogenetic protein 4
bp	Base pair
BPM	Beats per minute
C	
CACNA1A	Calcium channel, voltage-dependent, P/Q
CACNA1C	Calcium channel, voltage-dependent, L type, alpha 1C subunit
CACNA1G	Calcium channel, voltage-dependent, T type, alpha 1G subunit
CACNA1H	Calcium channel, voltage-dependent, T type, alpha 1H subunit
CAV1	Caveolin 1
CBD	Chromatin binding domain
Cdc2	Cell cycle dependent kinase 2
CDH1	E-cadherin
cDNA	Complementary DNA

CDM	Conditioned medium
CM	Cardiomyocytes
CMV	Cytomegalovirus
c-Myc	Cellular myelocytomatosis
COL12A1	Collagen, type XII, alpha 1
CRISPR	Clustered regularly interspaced short palindromic repeats
crRNA	CRISPR-RNA
C-terminal	Carboxyl-terminal
CTGF	Connective tissue growth factor
cTnI	Cardiac troponin I
cTnT	Cardiac troponin T
D	
DCM	Dilated cardiomyopathy
DEG	Differentially expressed genes
DMEM	Dulbecco's Modified Eagle Medium
DMSO	Dimethyl sulfoxide
DNA	Deoxyribonucleic acid
dNTPs	Deoxy-nucleoside triphosphate
DSB	Double strand break
dsODN	Double-stranded oligonucleotides
DTT	Dithiothreitol
E	
EB	Embryoid bodies
EC_{50}	Mean effective concentration
ECM	Extracellular matrix
EDMD	Emery-Dreifuss muscular dystrophy
EDTA	Ethylenediaminetetraacetic acid
EHT	Engineered heart tissue
ERK1/2	Extracellular signal-regulated kinases 1/2
ESC	Embryonic stem cells
F	
FA	Formic acid
FBS	Foetal bovine serum
FC	Flow cytometry
FCS	Foetal calf serum

FDA	Food and Drug Administration
FDR	False discovery rate
FHL1	Four and a half LIM domains protein 1
FLNA	Filamin A
FNT	Farnesyltransferase
FS	Fractional shortening
FSC	Forward scatter
FTDA	bFGF, TGFβ1, dorsomorphin and activin A-based hiPSC culture medium
G	
gDNA	Genomic deoxyribonucleic acid
GFP	Green fluorescent protein
GO	Gene ontology
gRNA	Guide RNA
GT	Gene replacement therapy
H	
HCM	Hypertrophic cardiomyopathy
HDR	Homology directed repair
HEPES	4-(2-hydroxyethyl)-1-piperazineethanesulfonic acid
HF	Heart failure
hiPSC	Human induced pluripotent stem cells
HR	Homologous recombination
I	
ICD	Intracardiac defibrillator/cardioverters
ICMT	Isoprenylcysteine
IEPT	Institute of Experimental Pharmacology and Toxicology
IF	Immunoflourescence
Ig	Immunoglublin
I_{K1}	Inwardly rectifying potassium current I (K1)
Ikr	Rapid delayed rectifier potassium current
Iks	Slow delayed rectifier potassium current
IKur	Ultra-rapidly activating delayed rectifier K+ current
Indels	Insertion-deletion
INM	Inner nuclear membrane
iPSC	Induced pluripotent stem cells

IsoC	Isogenic control line
ITGAM	Integrin Subunit Alpha M
ITGB1	Integrin Subunit Beta 1
ITGB5	Integrin Subunit Beta 5
ITGB6	Integrin Subunit Beta 6
Ito,f	Fast transient outward potassium current
J	
JNK	c-Jun N-terminal kinase
K	
KCNA5	Potassium voltage-gated channel, shaker-related subfamily, member 5
KCND2	Potassium voltage-gated channel subfamily D member 2
KCND3	Potassium voltage-gated channel subfamily D member 3
KCNH2	human Ether-à-go-go-Related Gene (hERG)
KCNJ11	Potassium inwardly rectifying channel subfamily J member 11
KCNJ2	Potassium inwardly rectifying channel subfamily J member 2
KCNJ8	Potassium inwardly rectifying channel subfamily J member 8
KCNK1	Potassium Two Pore Domain Channel Subfamily K Member 1
KCNK6	Potassium Two Pore Domain Channel Subfamily K Member 6
KCNMB1	Calcium-activated potassium channel subunit beta 1
KCNMB4	Calcium-activated potassium channel subunit beta 4
KCNQ1	Potassium voltage-gated channel subfamily Q member 1
Kir2.1	Potassium inwardly rectifying channel subfamily J member 2
Kir6.1	Potassium inwardly rectifying channel subfamily J member 8
Kir6.2	Potassium inwardly rectifying channel subfamily J member 11
Klf4	Kruppel-like factor 4
Kv1.5	Potassium voltage-gated channel, shaker-related subfamily, member 5
Kv7.1	Potassium voltage-gated channel subfamily Q member 1
L	
LADs	Lamin-associated domains
LAMA2	Laminin subunit alpha-2
LAMB3	Laminin Subunit Beta 3
LAP2α	Lamina-associated polypeptide 2α
LINC	Linker of nucleoskeleton and cytoskeleton

LMNA	Lamin A and C
LMNA-KO	LMNA knockout
LMNB1	Lamin B1
LMNB2	Lamin B2
LOXL4	Lysyl oxidase like 4
LV	Left ventricle
LVFS	Left ventricular fractional shortening
M	
MAPK	Mitogen activated protein kinase
MCB	Master cell bank
MKI67	Antigen Ki-67
MMP14	Matrix metallopeptidase 14
MMP16	Matrix metallopeptidase 16
MOI	Multiplicity of infection
mRNA	Messenger ribonucleic acid
MS	Mass spectometry
MYBPC3	Myosin binding protein C
MYH7	Myosin heavy chain 7
N	
NANOG	Nanog homeobox
Nav1.1	Sodium voltage-gated channel protein subunit alpha 1
Nav1.5	Sodium voltage-gated channel protein subunit alpha 5
NCAM1	Neural cell adhesion molecule 1
NHEJ	Non-homologous end joining
NLS	Nuclear localisation sequence
NMD	Nonsense-mediated mRNA decay
NPC	Nuclear pore complex
NRVM	Neonatal rat ventricular myocytes
NT	Non-transduced
N-terminal	Amino-terminus
NT-proBNP	N-terminal prohormone of brain natriuretic peptide
O	
Oct4	Octamer binding transcription factor 4
ONM	Outer nuclear membrane
OT	Off-target

P	
PAGE	Polyacrylamide gel electrophoresis
PAM	Protospacer adjacent motif
PAX6	Paired box 6
PBMC	Peripheral blood mononuclear cells
PBS	Phosphate-buffered saline
PCA	Principal component analysis
PCR	Polymerase chain reaction
PDGF	Platelet-derived grwoth factor
PFA	Paraformaldehyde
PRC2	Polycomb repressive complex 2
PTM	Post-translational modification
Q	
qPCR	Quantitave polymerase chain reaction
R	
RCE1	RAS-converting enzyme
REA	Recombinant engineered antibodies
RMP	Resting membrane potential
RNA	Ribonucleic acid
RNP	Ribonucleoprotein complex
ROI	Region of interest
RPMI	Roswell Park Memorial Institute
RR-scatter	Variability of R-R/beat-to-beat distance
RT	Relaxation time
S	
SCN1A	Sodium voltage-gated channel protein subunit alpha 1
SCN1B	Sodium voltage-gated channel subunit beta 1
SCN3B	Sodium voltage-gated channel subunit beta 3
SCN4B	Sodium voltage-gated channel subunit beta 4
SCN5A	Sodium voltage-gated channel protein subunit alpha 5
SD	Standard deviation
SDC	Sodium deoxycholate
SDS	Sodium dodecyl sulphate
SEM	Standard error of mean
SERCA	Sarcoplasmic reticulum calcium ATPase

SGCE	Epsilon-sarcoglyca
SNP	Single nucleotide polymorphism
SOX17	SRY-box 17
Sox2	Sex determining region Y-box 2
SPARC	Osteonectin
SPP1	Osteopontin
SR	Sarcoplasmic reticulum
SSC	Sideward scatter
SSEA3	Stage-specific embryonic antigen 3
ssODN	Single-stranded oligonucleotides
T	
TAE	Tris acetate EDTA
TAZ	WW-domain-containing transcription regulator 1
TBS	Tris-buffered saline
TBS-T	Tris-buffered saline-Tween
TC	Time-matched control
TD	Transduction
TEAB	Triethylamonium bicarbonat
TEAD	Transcriptional enhancer factor domain
TGFβ	Transforming growth factor beta
THBS1	Thrombospondin 1
TIMP2	Tissue inhibitor of metalloproteinase 2
TPM	Transcripts per million reads
tracrRNA	Trans-activating crRNA
TTP	Time to peak
U	
UE	Unedited
UKE	University medical centre Eppendorf
UPLC	Ultra-performance liquid chromatography
UPS	Ubiquitin proteasome system
V	
VASP	Vasodilator stimulated phosphoprotein
VCAN	Versican
VCL	Vinculin
Vs	Versus

VTN	Vitronectin
W	
WB	Western blot
WCB	Working cell bank
Wnt	Wingless-related integration site
WT	Wild-type
Y	
YAP1	Yes-activated protein 1
Z	
ZMPSTE24	Zinc metalloprotease
ZYX	Zyxin
αB-Cry	αB-chain crystallin
4-AP	4-Aminopyridine

9.3 Devices, materials & substances

9.3.1 List of primers

Table S 4 Primer sequences for quality control experiments

Target	Primer name	Primer sequence (5’-3’)
NANOG (stem cell)	Forward	GATTTGTGGGCCTGAAGAAA
	Reverse	AAGTGGGTTGTTTGCCTTTG
SOX2 (stem cell)	Forward	AGTCTCCAAGCGACGAAAAA
	Reverse	TTTCACGTTTGCAACTGTCC
SOX17 (endodermal)	Forward	CGCACGGAATTTGAACAGTA
	Reverse	GGATCAGGGACCTGTCACAC
PAX6 (ectodermal)	Forward	TGGGCAGGTATTACGAGACTG
	Reverse	ACTCCCGCTTATACTGGGCTA
NCAM1 (ectodermal)	Forward	ATGGAAACTCTATTAAAGTGAACCTG
	Reverse	TAGACCTCATACTCAGCATTCCAGT
GUSB (housekeeping)	Forward	AAACGATTGCAGGGTTTCAC
	Reverse	CTCTCGTCGGTGACTGTTCA
Sendai vector	Forward	GGATCACTAGGTGATATCGAGC
	Reverse	ACCAGACAAGAGTTTAAGAGATATGTATC
Mycoplasma	Forward	TGCACCATCTGTCACTCTGTTAACCTC
	Reverse	ACTCCTACGGGAGGCAGCAGTA

9.3.2 Antibodies

Table S 5 List of antibodies

Antibody	**Species**	**Application and dilution**	**Company (catalogue number)**
Primary antibodies			
anti-lamin A/C	Mouse	WB: 1:500; IF: 1:500	Santa Cruz (sc-376248; E-1)
anti-α-actinin2	Rabbit	IF: 1:800	Sigma Aldrich (SAB2108642)
anit-YAP1 Alexa Fluor 647	Mouse	IF: 1:200	Santa Cruz (sc-376830; G-6)
anti-Hu Ki-67	Rat	IF 1:1000	Thermo Fisher Scientific (14-5698-82)
anti-emerin	Mouse	IF: 1:100	Novocastra (4G5)
anti-MYBPC3	Mouse	WB: 1:1000	Santa Cruz (sc-137181; F-1)
anti-GFP	Rabbit	WB: 1:2000	Abcam (ab290)
Secondary antibodies			
anti-mouse Alexa Fluor 633		IF: 1:800	Thermo Fisher Scientific (A-21052)
anti-rabbit Alexa Fluor 546		IF: 1:800	Thermo Fisher Scientific (A-11035)
anit-rat Alexa Fluor 488		IF: 1:800	Thermo Fisher Scientific (A-11006)
anti-mouse peroxidase-conjugated		WB: 1:6000	Sigma Aldrich (A9044)
anti-rabbit peroxidase-conjugated		WB: 1:5000	Sigma Aldrich (A0545)
Flow cytometry antibodies			
Anti-cardiac troponin T FITC		FC: 1:50	Miltenyi Biotec (130-119-674)
REA Control (I)-FITC		FC: 1:50	Miltenyi Biotec (130-120-709)
Rat Anti-Human SSEA-3 Antibody PE Conjugated		FC: 1:50	BD Biosciences (560237)
Rat IgM, κ Isotype Control Antibody PE Conjugated		FC: 1:50	Biosciences (553943)

9.3.3 Buffers and solutions

Buffer/ solutions	**Components**
Activin A (157 µg/mL)	1 mg Activin A
	in 6.369 mL 4 mM HCl (sterile)
Agar plates	15 g/L Bacto Agar,
	10 g Bacto Tryptone
	5 g Basto Yeast Extract
	10 g NaCl
	autoclaved and casted into TC dish 100
Agarose for EHT casting	2% (w/v) Agarose
	300 mL 1xPBS
	Sterilized by autoclaving before storage at 60 °C
Aprotinin	33 mg/mL Aprotinin
	in aqua ad injectabilia
	250 µL aliquots, stored at -20 °C for up to one year
bFGF (100 µg/mL)	1 mg bFGF
	0.1% BSA
	in PBS
Blocking solution	5% Milk powder
	in TBS-T
1x Blotting buffer I	400 mL 5x Blotting buffer
	400 mL Methanol
	Fill up to 2 L with ddH2O
5x Blotting buffer I	29 g Trizma base (125 mM)
	145 g Glycine (950 mM)
	in 2 L ddH2O
BMP4 (50 µg/mL)	1 mg BMP4
	in 20 mL 0.1% BSA 4mM HCl
BTS solution	30 mM BTS
	in DMSO
	250 µL aliquots, stored at -20 °C for up to one year
Collagenase dissociation buffer	200 U/mL Collagenase II

	1 mM HEPES 10 µM Y-27632 30 µM BTS in HBSS (-) calcium/magnesium
DNase solution	100 mg DNase II in 50 mL PBS 2 mL aliquots, stored at -20 °C for up to six months
EDTA	0.5 mM EDTA in PBS Stored at 4 °C
FACS buffer	5% (v/v) FCS 0.5% (w/v) Saponin 0.05% (v/v) Sodium azide in PBS
Fibrinogen	200 mg/mL Fibrinogen 100 µg/mL Aprotinin 0.9%-NaCl solution
HEPES stock	1 M HEPES in 1xPBS (pH 7.4 adjusted with potassium hydroxide) Stored at 4 °C for up to one year
Kranias buffer	2 mL Tris (1.5 M, pH 8.8) 1 mL EDTA (0.5 M) 6 mL NaF (500mM) 15 mL SDS (20%) 10 mL Glycerol in 100 mL ddH2O
Laemmli buffer (6x)	1.2 g SDS 6 mg Bromophenol blue 6 g Glycerol 1.2 mL of 0.5 M Tris (pH 6.8) 0.93 g DTT in ddH2O
LB- medium	10 g Bacto Tryptone

	5 g Basto Yeast Extract
	10 g NaCl
	1 L ddH20, pH7.4
Blocking buffer (IF)	3% (w/v) Skim milk powder
	0.1% (v/v) Triton X-100
	in PBS
Phosphoascorbate (250 mM)	1 g Phosphoascorbate
	12.4 mL PBS
Pluronic F-127 solution	1% (w/v) Pluronic F-127
	in PBS
	Stored at 4 °C for up to one year.
50x Polyvinyl alcohol	20 g polyvinyl alcohol
	in 100 mL ddH2O
	Stored at 4 °C for up to one year
10x SDS-PAGE electrophoresis buffer	30.2 g Trizma base (250 mM)
	10 g SDS (1%) or 50 mL of 20% SDS
	144 g Glycine (1.92 M)
	in 1 L ddH2O
50x TAE-buffer (agarose gel electrophoresis)	242 g Trizma base
	37.2 g Titriplex III (EDTA)
	57.1 mL concentrated acetic acid
	1 L ddH2O (pH 8.5)
10xTBS	121.1 g Trizma base (1 M)
	87.66 g NaCl (1.5 M)
	in ddH2O (pH 7.5, adjusted with 37% HCL)
TBS-T	100 mL TBS
	900 mL ddH2O
	1 mL Tween20 (0.1%)
TGFß1 (20 µg/mL)	100 µg TGFß1
	in 0.1% HSA-solution
Thrombin	100 U/mL Thrombin
	60% (v/v) PBS
	40% (v/v) Aqua ad iniectabilia
Transferrin-selenite solution	100 mg Transferrin
	dissolved in 2 mL sodium selenite (382 µM)

	Stored at -80 °C for up to six months
0.5 M Tris (pH 6.8)	60.6 g Trizma base
	in 1 L ddH2O
1.5 M Tris (pH 8.8)	181.7 g Trizma base
	in 1 L ddH2O
XAV 939 (10 mM)	50 mg XAV 939
	in 14.3 mL DMSO

9.3.4 Kits and enzymes

AmaxaTM P4 Primary Cell 4D-Nucleofector X Kit L (Lonza, V4XP-4024)
BspHI (FastDigest PagI; Thermo Fisher, FD1284)
CloneJET PCR Cloning Kit (Thermo Fisher Scientific, K1232)
DNeasy® Blood & Tissue Kit (QIAGEN, 69504)
DreamTaq Green DNA Polymerase (Thermo Fisher Scientific, EP0711)
DreamTaq Green PCR Master Mix (Thermo Fisher Scientific, K1081)
Maxima SYBR Green/ROX qPCR Master Mix (2x; Thermo Fisher Scientific, K0222)
NucleoSpin Plasmid Miniprep Kit (Macherey-Nagel, 740588.25)
P3 Primary Cell 4D-Nucleofector X Kit L (Lonza, V4XP-3024)
Phusion HF (Thermo Fisher Scientific, F531L)
PrimeSTAR HS DNA polymerase (Takara, R010A)
QIAamp® 96 DNA QIAcube® HT kit (Qiagen, 51331)
QIAGEN Plasmid Mini Kit (QIAGEN, 12125)
QIAquick PCR Purification Kit (QIAGEN, 28104)
QIAquick® PCR Purification Kit (Qiagen, 28104)
Qubit Protein Assay Kit (Thermo Fisher Scientific, Q33212)
RNeasy Plus® Mini Kit (Qiagen, 74134)
SuperscriptTM IV (Thermo Fisher Scientific, 18091050)
TRIzol Reagent (Life Technologies, 15596026)

9.3.5 Reagents

1,4-Dithiothreitol (DTT, Roth, 6908.2)
1-Thioglycerol (Sigma-Aldrich, M6145)
2-Mercaptoethanol (Sigma-Aldrich, M6250)
2-Propanol (Merck Millipore, 107022)
4-Aminopyridine (Sigma Aldrich, A78403)

6x DNA loading dye (Thermo Fisher Scientific, R0611)
Accutase® Cell Dissociation Reagent (Sigma-Aldrich, A6964)
Activin A (R&D Systems, 338-AC)
Agarose (Invitrogen, 15510-027)
Alt-R® Cas9 Electroporation Enhancer, (IDT®, 1075916)
Alt-R® CRISPR-Cas9 tracrRNA, ATTO™550, (IDT®, 1075927)
Alt-R® S.p. Cas9 Nuclease 3NLS, (IDT®, 1081058)
Ammoniumpersulfate (APS, Bio-Rad Laboratories, 161-0700)
Ampicillin trihydrate (SERVA, 13397.01)
Aprotinin (Sigma-Aldrich, A1153)
Aqua ad iniectabilia (Baxter S.A., 001428)
B27 Plus Insulin (Gibco, 17504-044)
BactoTM Agar (BD, 214010)
BactoTM Tryptone (BD, 211705)
BactoTM Yeast Extract (BD, 212750)
Bay K-8644 Tocris, 1544
bFGF (basic FGF, R&D Systems, 233-FB)
BIOMYC-1 PromoCell, PK-CC03-036-1B
BIOMYC-2 PromoCell, PK-CC03-037-1B
BMP4 (R&D Systems, 314-BP)
Bromphenol blue (Merck, 108122)
BSA (Sigma-Aldrich, A3059)
BTS (N-Benzyl-p-Toluenesulfonamide, TCI, B3082-25G)
Chlororform/trichloromethane (Roth, 4432.1)
Clarity™ Western ECL Substrate (Bio-Rad, 170-5061)
Collagenase II (Worthington, LS004176)
cOmplete, Mini, EDTA-free Protease Inhibitor (Roche, 04693159001)
DMSO (Sigma-Aldrich, D4540)
DNase (Sigma-Aldrich, D8764)
Dorsomorphin (Abcam, ab120843 or Tocris, 3093)
Dulbecco's Phosphate-Buffered Saline (PBS; Gibco 14040-133)
EDTA (Roth, 8043.2)
Ethanol, absolute (Chemsolute, 2246.1000)
Fibrinogen (Sigma-Aldrich, F8630)
Geltrex® (Gibco, A1413302)
GeneRuler 1 kb DNA Ladder (Thermo Fisher Scientific, SM0313)

GeneRuler 100 bp DNA Ladder (Thermo Fisher Scientific, SM0243)
Glycerol (Merck 1.04092)
Glycine (Roth, 3790.2)
HBSS (-) Ca2+/Mg2+ (Gibco, 14175-053)
HEPES (Roth, 9105.4)
Hoechst 33258 (1:1,000; Thermo Fisher, #33258;)
Human serum albumin (Biological Industries, 05-720-1B)
Hydrochloric acid, 37% solution (Merck, 1.00317)
Hydrocortisone (Sigma-Aldrich, H4001)
Insulin (Sigma-Aldrich, I9278)
L-Glutamine (Gibco, 25030-081)
Lipidmix (Sigma-Aldrich, L5146)
Matrigel® Basement Membrane Matrix (Corning, 354234)
Matrigel® Growth Factor Reduced Basement Membrane Matrix (Corning, 354230)
Methanol (J. Baker, 8045)
Midori Green (Biozym, 617004)
N,N,N',N'-Tetramethylethylenediamine (TEMED, Bio-Rad, 161-0801)
Na-Selenite (Sigma-Aldrich, T8158)
Nitrogen, liquid (TMG)
Non-essential amino acids (Gibco, 11140)
PageRuler Plus Prestained Protein Ladder (Thermo Fisher Scientific, 26619)
Penicillin/Streptomycin (Gibco, 15140)
PFA (Thermo Scientific, 28908)
Phosphoascorbate (2-Phospho-L-ascorbic acid trisodium salt, Sigma-Aldrich, 49752)
Pluronic F-127 (Sigma-Aldrich, P2443)
Polyvinyl alcohol (Sigma-Aldrich, P8136)
Ponceau S solution (Sigma-Aldrich, P7170)
Precision Plus Protein Dual Color (Bio-Rad, 161-0394)
Pursept (Schülke, 230125)
PVA (Sigma-Aldrich, P8136)
Roti®-Histofix 4% (Roth, P087.3)
S.O.C. medium (Thermo Fisher Scientific, 15544034)
Saponin (Merck, 558255)
Skim milk powder (Roth, T145.2)
Sodium azide (Sigma-Aldrich, 71290)
Sodium chloride solution 0.9% (B. Braun, 3570210)

Sodium dodecyl sulphate (SDS pellets; Roth, CN30.3)
TBS (Sigma-Aldrich, T6664)
TGFß1 (Peprotech, 100-21)
Thrombin (Sigma-Aldrich, T7513)
TOP10 chemically competent E. coli (Thermo Fisher Scientific, C404010)
Transferrin (Sigma-Aldrich, S5261)
Triton X-100 (Roth, 3051.3)
Trizma® base (Sigma-Aldrich, T1503)
TRIzol (Life Technologies, 15596026)
Trypan Blue (Biochrom, L 6323)
Tween 20 (Sigma-Aldrich, P1379)
UltraPure DTT (Sigma, 17-1318-02)
XAV-939 (Tocris, 3748)
Y-27632 (Biaffin, PKI-Y27632-010)

9.3.6 Consumables

250 mL Vacuum Filtration "rapid"-Filtermax (TPP, 99250)
500 mL Vacuum Filtration "rapid"-Filtermax (TPP, 99500)
Aspiration pipette 2 mL (Sarstedt, 86.1252.011)
Cell culture flask T175 (Sarstedt, 83.3911.002)
Cell culture flask T75 and T175 for suspension culture (Sarstedt, 83.3911.502 / 83.3912.502)
Cell culture flask T80 (Nunc, 178905)
Cell culture microplate 96 well µClear® black CELLSTAR® (Greiner Bio-One, 655090)
Cell culture plate 6 / 12 / 24-well (Nunc)
Cell scraper (Sarstedt, 83.1830)
Cell strainer 30 µm (Sysmex, 04-004-2326)
Cryovial CryoPure 1.6 mL (Sarstedt, 72.380)
Flow cytometry tubes (Sarstedt, 55.1579)
Neubauer counting chamber (Karl-Hecht KG)
Omnifix-Fluer Solo 0.01 ml - 1 ml (B.Braun, 9161406V)
Pacing adapter/cables (EHT Technologies GmbH, P0002)
Pacing electrode carbon (EHT Technologies GmbH, P0001)
Pipette tips (Sarstedt)
Pipette tips with Biosphere filter (Sarstedt)
Reaction tube graduated 15 mL (Sarstedt, 62.554.502)
Reaction tubes conical 15 / 50 mL (Sarstedt)

Reaction tubes Safe Lock 0.2 – 2 mL (Eppendorf)
Round bottom tube 12 mL (Greiner Bio-One, 163160)
Serological pipettes 1 / 2 / 5 / 10 / 25 / 50 mL (Sarstedt)
Silicone rack (EHT Technologies GmbH, C0001)
Spinner flasks 500 / 1000 mL (Integra Biosciences, 182101 / 182051)
Sterican 0.4 mm x 20 mm BL/LBneedle (B.Braun)
Sterican 0.9 mm x 70 mm BL/LBneedle (B.Braun)
Syringe filtration unit Filtropur S 0.2 µm (Sarstedt, 83.1826.001)
Teflon Spacer (EHT Technologies GmbH, C0002)

9.3.7 Devices

4D-Nucleofector Core Unit and X Unit (Lonza)
ABI PRISM 7900HT Sequence Detection System (Applied Biosystems)
Analytic Scale Genius (Sartorius AG)
BD FACS Canto II flow cytometer (BD Biosciences)
C25 Incubator Shaker (New Brunswick Scientific)
Cell culture incubator CB 220 (Binder)
Cell culture incubators MCO-19M & MCO-20AIC (Sanyo)
Cell culture incubators S2020 1.8, HERAcell 240 & 150i (Thermo Fisher Scientific)
Centrifuge Avanti JXN 26 (Beckmann Coulter)
Centrifuge J-6B (Beckmann Coulter)
Centrifuges 5415 R & 5810 R (Eppendorf)
Centrifuges Rotanta/RP & Universal 30 RF (Hettich)
ChemiDocTM Touch Imaging System (Bio-Rad)
Confocal microscope (LSM800, Zeiss)
Cryopreservation system Asymptote EF600M (Grant Instruments)
Electrophoretic Transfer Cell Mini Trans-Blot cell (Bio-Rad)
Gel electrophoresis cell Mini-PROTEAN 3 Cell (Bio-Rad)
Gel electrophoresis tank Sub-cell® GT (Bio-Rad)
HERAcell 150i (Thermo Fisher Scientific)
HERAcell 240 (Thermo Fisher Scientific)
HeraSafe (Heraeus)
Ice machine (Scotsman)
LSM 800 Airyscan (Zeiss)
Magnetic stirring and heating plate IKA Combimag RET (Janke & Kunkel & Co KG)
Magnetic stirring plate Variomag / Cimarec Biosystem 4 Direct (Thermo Fisher Scientific)

Magnetic stirring plate Variomag / Cimarec Biosystem Direct (Thermo Fisher Scientific)
Microscope Axioskop 2 with AxioCam Color (Zeiss)
Microscope Axiovert 25 with ProgRes Speed XT core 5 camera (Jenoptik)
Microscope EVOS FL Cell Imaging System (Thermo Fisher Scientific)
Microwave (Sharp)
NanoDrop ND-1000 Spectrophotometer (Thermo Fisher Scientific)
nCounter® SPRINT (NanoString)
Pipette controller Accu-jet® pro (Brand)
Pipettes 10 / 100 / 1000 µL (Eppendorf)
Portable balance Scout Pro (Ohaus)
Power supply PowerPac Bacic (Bio-Rad Laboratories)
Power supply PowerPac Basic (Bio-Rad)
Precision Advanced Scale (Ohaus)
QExactive HFx mass spectrometer (Thermo Electron)
QIAcube HT System (Qiagen)
Qubit 3.0 Fluorometer (Thermo Fisher Scientific)
S88X dual output square pulse stimulator (Grass)
Safety workbench HeraSafe (Heraeus)
Safety workbench Safe 2020 (Thermo Fischer Scientific)
Thermal cycler Hybaid PCR Sprint (Thermo Fisher Scientific)
Thermal cycler vapo.protect (Eppendorf)
Thermomixer comfort (Eppendorf)
TubeRoller (Benchmark)
Ultimate 3000 nano-LC system (Thermo Fisher Scientific)
Video-optical EHT analysis system (EHT Technologies GmbH)
Vortexer Vibrofix VF1 (Janke & Kunkel GmbH)
Warming cabinet Kelvitron® (Heraeus)
Water bath 25900 (Medax)

9.3.8 Software

Axio Vision Rel. 4.8.2 (Zeiss)
CTMV
FACSDiva (BD Biosciences)
FlowJo 10 (BD Biosciences)
Image Lab Version 5.2.1 (Bio-Rad)
ImageJ 1.52n (Wayne Rasband)

Imaris 9.3.0 (Bitplane)
Prism 8.3.0. (GraphPad)
SDS 2.4.1 (Applied Biosystems)
SnapGene 5.0.1. (GSL Biotech LLC)
STRING database 11.5
ZEN 2012 (Zeiss) ZEN 2.3 (Zeiss)

9.4 Financial support

This project was funded by the ERA-CVD as part of Variation consortium, the Werner-Otto-Stiftung (1860/100) and British Heart Foundation (80714/162).

9.5 Publications

Antonia T. L. Zech, Maksymilian Prondzynski, Sonia R. Singh, Ellen Orthey, Erda Alizoti, Josefine Busch, Alexandra Madsen, **Charlotta S. Behrens**, Moritz Meyer-Jens, Giulia Mearini, Marc D. Lemoine, Elisabeth Krämer, Diogo Mosqueira, Sanamjeet Virdi, Daniela Indenbirken, Maren Depke, Manuela Gesell Salazar, Uwe Völker, Ingke Braren, William T. Pu, Thomas Eschenhagen, Elke Hammer, Saskia Schlossarek, Lucie Carrier. (2022). **ACTN2 Mutant Causes Proteopathy in Human iPSC-Derived Cardiomyocytes.** Cells. 11

Maria Köhne, **Charlotta Sophie Behrens**, Tim Stüdemann, Constantin von Bibra, Eva Querdel, Aya Shibamiya, Birgit Geertz, Jakob Olfe, Ida Hüners, Stefan Jockenhövel, Michael Hübler, Thomas Eschenhagen, Jörg Siegmar Sachweh, Florian Weinberger, Daniel Biermann. (2022). **A potential future Fontan modification: preliminary in vitro data of a pressure-generating tube from engineered heart tissue**. European Journal of Cardio-Thoracic Surgery. Ezac111.

Nele Annika Warnecke, Bärbel M Ulmer, Sandra D Laufer, Aya Shibamiya, Elisabeth Krämer, Christiane Neuber, Sophia Hanke, **Charlotta Behrens**, Malte Loos, Julia Münch, Jirko Kühnisch, Sabine Klaassen, Thomas Eschenhagen, Monica Patten-Hamel, Lucie Carrier, Giulia Mearini. (2021) **Generation of bi-allelic MYBPC3 truncating mutant and isogenic control from an iPSC line of a patient with hypertrophic cardiomyopathy**. Stem Cell Research. 21

Aya Shibamiya, Elisabeth Schulze, Dana Krauß, Christa Augustin, Marina Reinsch, Mirja Loreen Schulze, Simone Steuck, Giulia Mearini, Ingra Mannhardt, Thomas Schulze, Birgit Klampe, Tessa Werner, Umber Saleem, Anika Knaust, Sandra D. Laufer, Christiane Neuber, Marta Lemme, **Charlotta Sophie Behrens**, Malte Loos, Florian Weinberger, Sigrid Fuchs, Thomas Eschenhagen, Arne Hansen, Bärbel Maria Ulmer. (2020) **Cell Banking of hiPSCs: A Practical Guide to Cryopreservation and Quality Control in Basic Research. Current Protocols in Stem Cell Biology**. 55. e127

Dries A.M. Feyen, Wesley L. McKeithan, Arne A.N. Bruyneel, Sean Spiering, Larissa Hörmann, Bärbel Ulmer, Hui Zhang, Francesca Briganti, Michaela Schweizer, Bence Hegyi, Zhandi Lia, Risto-Pekka Pölönen, Kenneth S. Ginsburg, Chi Keung Lam, Ricardo Serrano, Christine Wahlquist, Alexander Kreymerman, Michelle Vu, Prashila L. Amatya, **Charlotta S. Behrens**, Sara Ranjbarvaziri, Renee G.C. Maas, Matthew Greenhaw, Daniel Bernstein, Joseph C. Wu, Donald M. Bers, Thomas Eschenhagen, Christian M. Metallo, Mark Mercola. (2020) **Metabolic Maturation Media Improve Physiological Function of Human iPSC-Derived Cardiomyocytes.** Cell Reports. 32

9.6 Congress participations

06/2018	Precision Medicine Summit on Cardiomyopathies & Heart Failure, Heidelberg, Germany
02/2019	DGK/ DZHK Gene Editing Workshop, Berlin, Germany
05/2019	Indivumed Symposium, Hamburg Germany Oral presentation: “Modeling Lamin A/C mutations in hiPSC-CM”
05/2019	ERA-Net on Cardiovascular Diseases (ERA-CVD), Riga, Latvia Poster presentation: “Modelling of LMNA-cardiomyopathy in human iPSC-derived engineered heart tissue for testing novel therapies”
06/2019	European Meeting on Intermediate Filaments, Turku, Finland Poster presentation: “Modelling of LMNA-cardiomyopathy in human iPSC-derived engineered heart tissue”
06/2019	NCCR Retreat, Tremsbüttel, Germany Poster presentation: “Modelling of LMNA-cardiomyopathy in human iPSC-derived engineered heart tissue”
12/2019	Technobeat Symposium, Hanover, Germany Poster presentation: “Modelling of LMNA-cardiomyopathy in human iPSC-derived engineered heart tissue for testing novel therapies”

01/2020	Heart Failure Association Winter Meeting 2020, Les Diablerets, Switzerland Poster presentation: “Patient-specific human iPSC-derived engineered heart tissue recapitulate structural and contractile phenotype of LMNA-cardiomyopathy”
07/2021	International Society of Stem Cell Research, Virtual Poster presentation: “Modelling LMNA-cardiomyopathy with patient-specific human iPSC-derived engineered heart tissue demonstrates a structural and mechanical coupling defect”
06/2022	International Society of Heart Research, Berlin, Germany Poster presentation: “Modelling LMNA-cardiomyopathy with patient-specific human iPSC-derived engineered heart tissue and a partial rescue by gene replacement the

10 Acknowledgements

After writing up the projects of the last three and half years in lab and one year whilst on parental leave, I would like to thank the people who've supported me the most:

Firstly, I would like to thank Prof. Dr. Thomas Eschenhagen, who has been a great supervisor throughout all the years. I'm more than grateful to have worked on such an exciting topic that allowed me to learn all the technologies. It's been the right balance of working independently but being able to consult you at any time with your tremendous experience and knowledge. I especially enjoyed the *Jour fixe*, when we discussed the data and that you would always suggest new scientific ideas.

I would also like to thank Prof. Dr. Thomas Dobner for taking the time to co-supervise and his interest in this thesis.

A special thanks goes to Bärbel Ulmer. I learnt a lot from you; you encouraged me in many aspects during the last years and especially throughout the last weeks. I enjoyed being in your team. Even though you left the IEPT some time ago, I still feel that I can contact you anytime. The Spätzle evenings and your garden will remain as good memories for me.

I'm very grateful to have started this thesis at the same time as Malte Loos. All beginnings are tough, especially when you must learn so many new biological techniques. Thank you for your support over the years, whether that was in the lab or during discussions at lunch time. And thanks to Nele Warnecke, who has been working with us a lot during the first year of PhD, it was plenty of fun.

One special part of my thesis was supervising Julia Freese in the lab. With you I could finally work as a team and share the thrill of the projects, which have benefited a lot from your support. I thoroughly enjoyed our team spirit and I do not know how I could thank you for staying on this project for such a long time. Further, I would like to thank Maximilian Kolbe for your support in the lab. I benefited a lot from your medical perspective when you joined the lamin team.

Furthermore, I would like to thank Antonia Zech and Maria Köhne. You have supported me with chocolate and mentally a lot over the past few years. I'm happy that I found so good friends with whom I could share every thought.

I would like to thank Tamara Glawe, who is kind of family, too. I’ve shared with you many struggles and joy throughout the past 17 years. Thank you for all your motivating words.

A very special thanks goes to my family. Firstly, thanks to my parents and grandparents for supporting my studies, even abroad. I really enjoyed discovering the world of science, which made it possible to conduct this PhD project. You supported me in every way I could think of, giving me time to work on this thesis whilst being a mother. Particular thank goes to Moritz Förster and my daughter Henriette Behrens, without whom I would have not come this far. You cheered me up every day and gave me laughs and motivation. Thank you for your patience these last few months, that’s something I definitely should learn from you. I’m so excited about all the chapters which are ahead of us.

11 Declaration of academic honesty – Eidesstattliche Erklärung

I hereby declare that the present thesis with the title: "Modeling of LMNA-cardiomyopathy in human iPSC-derived engineered heart tissue for testing novel therapies"

was written independently by myself. No further sources or aids other than those indicated were used. The submitted written form of the thesis complies with the electronic version. This thesis was not handed in any other form for another examination procedure.

Hamburg, 22.11.2022

Ich erkläre hiermit, dass die vorliegende Arbeit mit dem Titel: "*Modeling of LMNA-cardiomyopathy in human iPSC-derived engineered heart tissue for testing novel therapies*"

von mir selbständig verfasst wurde. Andere Quellen und Hilfsmittel als die, die genannt wurden, wurden nicht verwendet. Die eingereichte schriftliche Form der Arbeit entspricht derjenigen auf der elektronischen Version. Diese Arbeit wurde in keiner anderen Form zu einem anderen Prüfungsverfahren eingereicht.

Hamburg, 22.11.2022